THE DESIGN AND DEVELOPMENT OF HYDROGEN ISOTOPE EXTRACTION TECHNOLOGIES FOR A LiMIT-STYLE LIQUID LITHIUM LOOP

BY

MICHAEL PETER CHRISTENSON

DISSERTATION

Submitted in partial fulfillment of the requirements
for the degree of Doctor of Philosophy in Nuclear, Plasma, and Radiological Engineering
in the Graduate College of the
University of Illinois at Urbana-Champaign, 2018

Urbana, Illinois

Doctoral Committee:

Professor David N. Ruzic, Chair
Professor Jean Paul Allain
Assistant Professor Caleb Brooks
Dr. Daniel Andruczyk
Assistant Professor Jessica Krogstad

ABSTRACT

As lithium has grown in popularity as a plasma-facing material, efforts have been placed on examining its viability as a first wall candidate. Lithium has proven over numerous studies to improve core confinement, while allowing access to operational regimes previously unattainable while using solid, high-Z divertor and limiter modules. These benefits are due to the fuel retention capabilities of lithium, which allow it to be an almost ideally absorbing boundary, which is both beneficial and problematic. While lithium exhibits a number of other advantages and disadvantages as a plasma-facing material, none is more important than the tritium retention problem. As such, extraction technologies must be constructed and verified within the scope of larger scale lithium loop systems that separate lithium impurities, recover deuterium and tritium, and recycle clean liquid lithium back to the plasma-material interface.

Laboratory-scale and pilot-scale studies have been conducted at the Center for Plasma-Material Interactions at the University of Illinois to investigate a number of phenomena that influence the recovery of entrained tritium from lithium. While the ultimate goal is to develop a fully-functional liquid lithium loop for the Lithium Metal Infused Trenches plasma-facing component, complete with efficient hydrogen reclamation technologies, there exists a lack in understanding within the community of the thermochemical fundamentals that are envisioned to drive tritium reclamation. Of specific interest are the evolution fluxes of hydrogen isotopes from solutions of various concentrations of hydrogen in lithium, and the associated temperatures. The knowledge of how the isotopic fraction affects recovery is pivotal to determining the appropriate thermal treatment technique.

The laboratory-scale experiments in this report aimed at filling in the knowledge gaps in the literature with regards to the thermochemistry of the hydrogen-lithium system. In all cases, hydrogen was used as an isotopic surrogate for deuterium and tritium. Success was based on an individual samples ability to evolve molecular hydrogen at rates that would match or exceed in-vessel wall losses, determined from a simulated Lithium-Walled International Thermonuclear Experimental Reactor scenario. The hydrogen degassing of pure lithium hydride was observed to exceed fuel loss by a factor of two or greater, at temperatures near the melting point for hydride.

Samples of both solid and liquid lithium were subjected to different hydrogen environments under a variety of exposure conditions. During plasma exposures, evidence of saturation, where hydride layers are formed at or near the sample surface and inhibit hydrogen absorption, was witnessed for solid lithium samples. Liquid samples exhibited this behavior to a lesser degree; however, mass diffusion was able to transport the insulating species away from the surface and absorption was able to continue, albeit to a lesser extent than was initially detected. The sub-surface chemistry was found to still be limited by the thermodynamic solubility thresholds in a plasma environment, meaning enhanced hydrogen dissolution was not witnessed at ion energies relevant to these experiments. The presence of a plasma, however, did appear to enhance absorption rates above and beyond what was capable with hydrogen gas alone. During these tests, hydrogen evolution rates from the dissolved phase never approached the point of being able to balance losses at the plasma-material interface, being always less by a factor of two or more. It was therefore determined that supplementary methods were required to enhance thermal-based recovery in solutions with hydrogen molar ratios less than the solubility limits.

This work culminated in the design, development, construction, and proof-of-concept testing of a distillation column. Envisioned to be an integrated treatment method in a fully functional lithium loop, the column was developed based on the need to recover tritium and recycle fresh lithium back into the reactor. The novelty in this design was in its use of induction heating drive and condensation stages. Proof-of-concept tests were performed in the fully constructed prototype with solutions of lithium and lithium hydride at various molar ratios. The system was observed to operate as intended during these initial runs, but requires further testing; however, the column marks the first system constructed for the sole purpose of recovering tritium from a lithium-walled reactor. Such a system will prove most effective if upstream separation and purification techniques are present to divert the lithium deuteride and lithium tritide-rich streams to the column for thermal decomposition and degassing.

In the case where upstream purification modules are absent from the lithium loop, the column alone will be hard pressed to achieve recovery rates in far-from-saturated solutions that balance wall losses. A technique to supplement the induction heating drive was therefore proposed. Ultrasonic degassing of liquid metals is an industry-tested technique used to rid melts of dissolved gases by taking advantage of acoustically-induced cavitation. This process was theoretically

applied to the hydrogen-lithium system, displaying evidence that degassing is most effective in the presence of heat, ultrasonic waves, and vacuum. This work laid the theoretical groundwork for future application.

The results presented in this report show that using the appropriate combination of treatment methods, hydrogen, and by extension deuterium and tritum, can be recovered from lithium at rates that balance in-vessel wall loss. Future work will be needed to then integrate these methods into a fully functional liquid lithium loop.

To my advisor, thank you for your counsel and guidance.
To my friends and peers, thank you for all of your help and support.
To my family, thank you for making me the man I am.
To my wife, thank you for being my foundation. You are everything to me

TABLE OF CONTENTS

LIST OF FIGURES

LIST OF TABLES

ABBREVIATIONS AND SYMBOLS

D	Deuterium
T	Tritium
α	Alpha particle
n	Neutron
n_i	Number density of species 'i'
T_i	Temperature of species 'i'
τ_E	Confinement time
P_j	Power gained or lost in process 'j'
R	Radiation parameter OR resistance OR range OR bubble radius
$< \sigma v >$	Thermonuclear reactivity
ε	Energy released per fusion event
Z	Atomic number
Γ_i	Flux of species 'i'
v_i	Velocity of species 'i'
x_i	Molar fraction of species 'i'
T_M	Monotectic temperature
ΔG_f^0	Standard Gibbs free energy of formation
K_j	Reaction constant for process 'j'
κ_0	Prefactor in Sieverts' constant
σ	Reaction cross-section OR conductivity OR surface site availability OR surface tension
M_i	Molecular weight of species 'i'
E_j	Energy for process 'j'
α	Reacted fraction OR dissolved phase lithium hydride
$\Re$	Universal gas constant
β	Temperature ramp rate OR solid phase lithium hydride
Θ	Surface coverage fraction OR constant in Rayleigh-Plesset analysis
Δf	Change in oscillator frequency
C_f	Constant defined as crystal sensitivity factor
Δm	Change in mass

ρ_i	Density of species or phase 'i'
μ_q	Shear modulus of quartz
χ_i	Volume fraction of species 'i'
ω_i	Mass fraction of species 'i'
ρ	Resistivity
R_p	Projected Range
$S_n(E)$	Nuclear stopping function
a_{TF}	Thomas-Fermi radius
γ	Reduced mass OR ratio of specific heats
u_j	Velocity magnitude for process 'j'
Ha	Hartmann number
S_i	Absolute Seebeck coefficient of species 'i'
B	Magnetic field
P_i	Pressure of species 'i'
k_i	Thermal conductivity of species 'i'
$\varphi(z)$	Particle flux profile along length 'z'
C_p	Constant pressure heat capacity
ω	frequency
ϵ_0	Vacuum permittivity
ϵ_r	Relative permittivity
A	Magnetic vector potential
μ_0	Vacuum permeability
μ_r	Relative permeability
J_e	Induced current density
E	Electric Field
H	Auxiliary Field
ω_N	Natural bubble frequency
η	Polytropic constant
α_i	Thermal diffusivity of species 'i'
μ_i	Dynamic viscosity of species 'i'
c	Dissolved gas concentration
C_s	Sound speed in liquid medium

k	Wave vector
S	Entropy
$\forall$	Volume
ζ	Volume viscosity OR constant
D	Mass diffusion
A_i^n	Variable 'A' at grid point 'i' and time step 'n'
P_A	Acoustic pressure amplitude
$\dot{m}$	Rate of mass transfer
J	Nucleation bubble production rate
LCFS	Last Closed Flux Surface
SOL	Scrape-Off Layer
PFC	Plasma-facing Component
ITER	International Thermonuclear Experimental Reactor
NBI	Neutral Beam Injector
LHCD	Lower Hybrid Current Drive
ICRH	Ion Cyclotron Resonance Heating
W	Tungsten
Mo	Molybdenum
ELM	Edge Localized Mode
EAST	Experimental Advanced Superconducting Tokamak
DEMO	Demonstration Power Station
CPS	Capillary Porous System
FLiLi	Flowing Liquid Lithium Limiter
LiMIT	Lithium Metal Infused Trenches
CPMI	Center for Plasma-Material Interactions
MHD	Magnetohydrodynamics
TEMHD	Thermoelectric Magnetohydrodynamics
Li	Lithium
LiH	Lithium Hydride
LiD	Lithium Deuteride
LiT	Lithium Tritide
Li_2O	Lithium Oxide

LiOH	Lithium Hydroxide
H	Atomic Hydrogen
D	Atomic Deuterium
T	Atomic Tritium
H_2	Molecular Hydrogen
D_2	Molecular Deuterium
T_2	Molecular Tritium
NSTX	National Spherical Torus Experiment
IFMIF	International Fusion Materials Irradiation Facility
TDS	Thermal Desorption Spectroscopy
TPD	Temperature-Programmed Desorption
PPPL	Princeton Plasma Physics Laboratory
RLLD	Radiative Liquid Lithium Divertor
ARLLD	Active Radiative Liquid Lithium Divertor
RGA	Residual Gas Analyze
QMS	Qaudrupole Mass Spectrometer
LiHDE	Lithium Hydride Degassing Experiment
QCM	Quartz Crystal Microbalance
XPS	X-ray Photoelectron Spectroscopy
LEISS	Low-energy Ion Scattering Spectroscopy
TUFCON	Tungsten Fuzz Characterization of Nanofeatures
MD	Molecular Dynamics
BCA	Binary Collision Approximation
SRIM	Stopping and Range of Ions in Matter
TRIM	Transport of Ions in Matter
TRIDYN	Dynamic TRIM
OES	Optical Emission Spectroscopy
HIDRA	Hybrid Illinois Device for Research and Application
AMU	Atomic Mass Units
ODE	Ordinary Differential Equation
IGNIS	Ion-Gas-Neutrals Interactions with Surfaces

CHAPTER 1: INTRODUCTION

1.1 Fusion Basics

As the world approaches the point in which non-renewable resources are no longer a sustainable source of energy, humanity must turn to alternative sources to meet future power demands. Energy production through controlled nuclear fusion is often considered one of the most attractive alternative solutions due to the high abundance of fuel, minimal ecological impact, and the potential for high efficiency.

Nuclear fusion is characterized by the collision between two light atomic species that produces a heavier atomic species. Energy is also released during the reaction, owing to the mass difference between the new, heavier product and the sum of the masses of the lighter reactants. This mass difference is converted to energy. Fusion reactions require substantial energy input, either from an external source or, in the case of sustainable fusion, from the energy released by previous nuclear interactions. This energy input is necessary to overcome the repulsive Coulombic forces that would otherwise inhibit nuclear interactions.

A number of reactions have been considered for the production of energy from nuclear fusion. These mechanisms are often characterized by their ability to produce neutrons, with neutronic reactions having neutrons as a product and aneutronic reactions being absent of neutrons in their products. While each mechanism has its benefits and flaws, the most widely accepted and researched reaction pathway is that which occurs between deuterium and tritium:

$$D + T \rightarrow \alpha + n + 17.6\ MeV \tag{1.1}$$

where D is deuterium, T is tritium, α is an alpha particle (or a charged He nucleus), and n is a neutron. This reaction mechanism is the primary focus of the fusion community because it has a relatively high reaction cross section at low energies and the fuel species are more abundant than in other proposed mechanisms.

Many techniques have been studied to harness the energy released during fusion reactions, but the most promising of these deals with magnetically confining the extremely energetic fusion plasma. Magnetic confinement in a torus has been found to be the most energetically favorable orientation and has led to the creation of two separate concepts: the stellarator and the tokamak.

For either of these cases to succeed at generating net power, the operating condition of the device must be optimized with respect to the ion density (n_i), the ion temperature (T_i), and the energy confinement time (τ_E). Formally, these parameters are lumped together to form the triple product ($n_i T_i \tau_E$), which must meet or surpass the standard known as the Lawson criterion [1] in order to achieve a sustainable, power-producing fusion reaction. For a system that uses deuterium and tritium as the fuel source, the Lawson criterion is defined as [1]:

$$n_i T_i \tau_E \geq 3.21 \; x \; 10^{21} \frac{keV \cdot s}{m^3} \tag{1.2}$$

Considered to be the most thoroughly researched of the magnetic confinement fusion concepts, the tokamak uses the combination of a toroidal and poloidal magnetic field component to generate what is referred to as a rotational transform. This field arrangement generates flux surfaces to which charged particles are confined and can gain enough kinetic energy for the ions to overcome the repulsive Coulombic forces and undergo nuclear collisions. Closed flux surfaces do not extend out to the confining wall, but instead have a transition between the Last Closed Flux Surface (LCFS) and the Scrape-Off Layer (SOL). The SOL is characterized by open field lines and plays a pivotal role in the plasma-material interactions, since particle flow along this surface is directed toward the plasma-facing components (PFCs) [2]. Emitted particles from PFC surfaces can also migrate along the SOL [3]. Figure 1.1 illustrates how the magnetic field structure is set up in a classical tokamak configuration. The tokamak will be the primary fusion system considered in this report; however, many of the same issues and benefits resulting from the work described here can be extended to alternative solutions that utilize magnetic confinement.

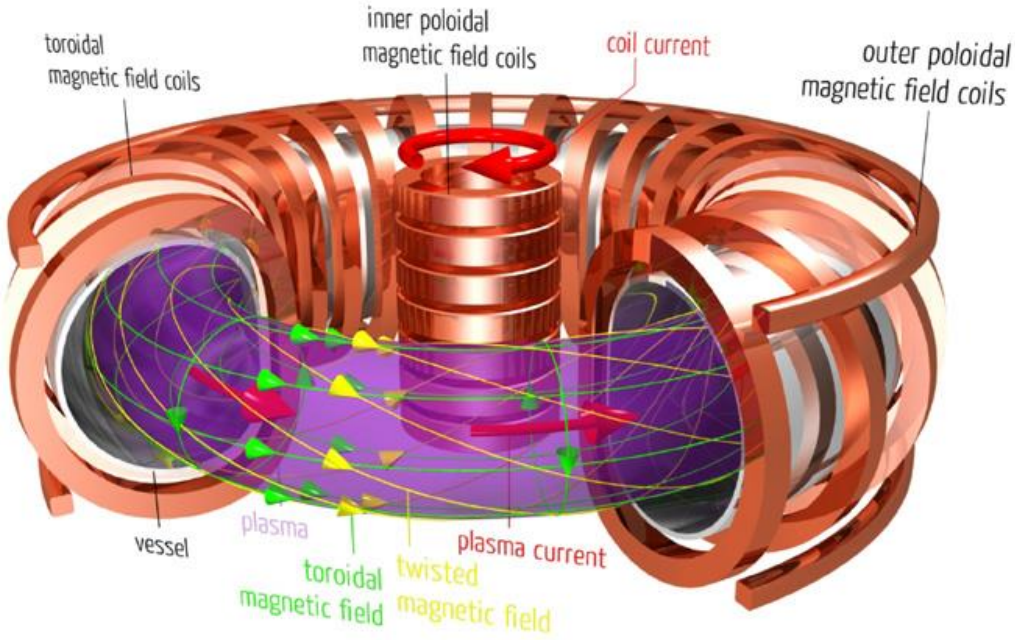

Figure 1.1: An illustration of the field configuration in a classical tokamak device [4].

1.1.1 Plasma Shaping

In order for fusion plasmas to reach the condition known as ignition, the plasma must be heated to a temperature in excess of 10 keV [5]. This temperature is characteristic of the energy distribution of the plasma, which must be achieved in order for an appreciable number of fusion events to occur in the high-energy tail of this distribution. The products, carrying with them the released energy of these fusion events then drive the fusion chain reaction. As would be expected from such high-energy interactions, the materials confining this plasma are subjected to very extreme conditions. Exhausted heat fluxes may bombard PFCs with values that are projected to surpass 10 MW/m^2 [6] in the International Thermonuclear Experimental Reactor (ITER), and may even reach as high as 20 MW/m^2 during steady-state operation.

Originally, fusion experiments were set up in a limiter configuration, where materials were placed inside the vessel at key positions to prevent plasma expansion from reaching the first wall. From a contamination point-of-view, since the limiter localizes the particle and heat exhaust, it is also meant to localize the emitted particle flux and particle recycling from the surface of the

limiting PFC. The functionality of the limiter requires careful consideration of the plasma-facing material. Limiters must be able to handle thermal shocks and cyclical thermal loading, be made of low atomic-number material or have low sputtering yields (or a combination of both), and have good thermal conductivity [1]. Realizing all of these criteria in a single material is extremely challenging, oftentimes leading to a relaxation in one requirement in order to strengthen another. Limiter configurations are plagued by impurity penetration into the core of the plasma, leading to an increase in the effective atomic number (Z_{eff}) in the plasma. This increases power losses and leads to minimal confinement times.

The response to the issues facing fusion experiments operating solely in the limiter regime came in 1982, when the ASDEX device in Germany used magnetic shaping to divert the particle and heat exhaust to an area farther from the plasma core than in any limiter scenario [7]. The material planes specified to handle these fluxes were officially titled the divertor, and a new confinement regime was achieved. Discharges in this new confinement regime were dubbed high-confinement mode (H-mode) operations, and were accompanied by higher densities and temperatures, longer confinement times, and large density and temperature gradients at the plasma boundary known as the pedestal. Since the divertor was located at distances much further from the plasma core than any limiter could be, the emitted particle flux from these divertor materials was less damaging to core confinement. It has since been proven on ASDEX and other machines that because of the inhibition of particle transport across the pedestal, the confinement is thereby strongly influenced by the height and gradient of the density and temperature pedestal [8 – 11]. While operating in the new confinement mode has its benefits, the plasmas are subject to new transient instabilities that can exterminate the plasma and dump excessive heat loads on the divertor over very short timespans. As such, the material candidacy requirements for divertors are similar to those for limiters. In fact, power handling may be even more important for divertor materials, since the exhausted particle flux is spread over a much smaller strike point than in a limiter setting. The difference between the two classical tokamak shaping scenarios is illustrated in Figure 1.2.

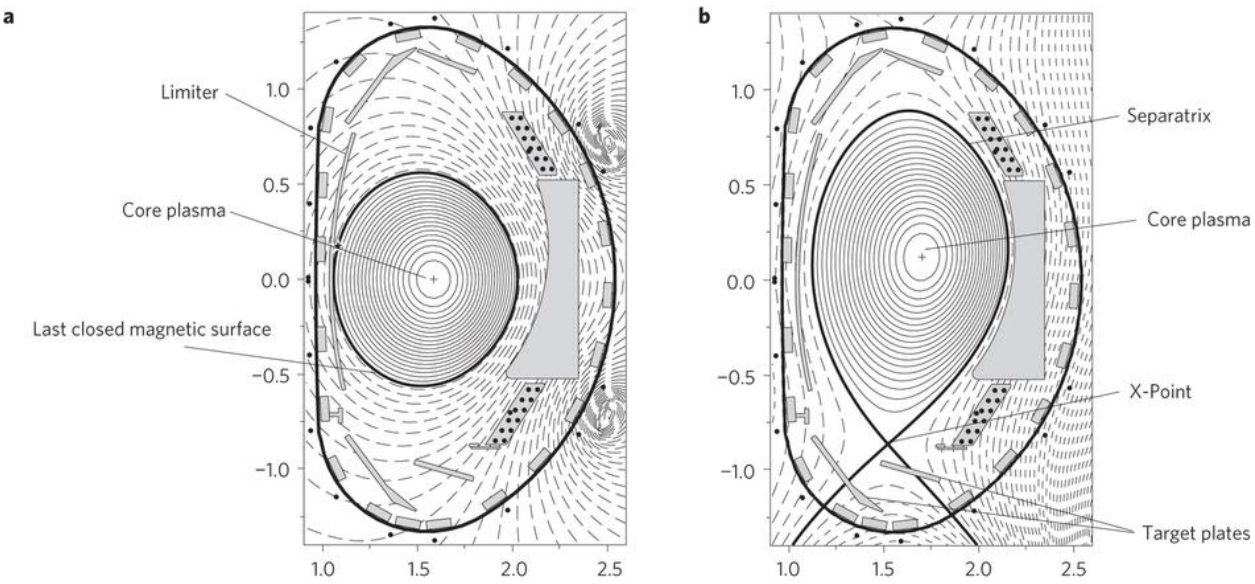

Figure 1.2: The two ways in which a tokamak plasma is shaped and confined [12]. In image a, the plasma is confined using only limiters, where the plasma edge is in direct contact with the material surface. In image b, the plasma does not directly interact with the wall materials and is magnetically shaped so that the plasma-material boundary is shifted toward the divertor plates, labeled as the "Target plates". Axes units are in meters.

The helical field shaping of the plasma within the tokamak is achieved in three startup phases [13]. The first portion of plasma startup is defined by breakdown of a relatively low temperature deuterium or D-T plasma, which is induced by the current through the central solenoid. Similarly, the plasma current is driven by this induction, which increases as the current through the central solenoid is ramped in the final phase. During this time, the poloidal coils which surround the chamber torus are synchronized to generate a poloidal field null. The second portion of the discharge is characterized by radiative losses to low-Z impurities, which is important to prevent particle diffusion back toward the core in later stages. To overcome these expected power losses, external power is used to maintain the discharge. The final startup phase is identified by the controlled ramp-up of the current through the central solenoid as well as the external coils. The flux surfaces and helical field structure are fully formed, and the plasma current reaches its maximum value. It is also during this phase that high-power heating schemes can be used to supply energy to the plasma, such as: Neutral Beam Injection (NBI), Lower Hybrid Current Drive

(LHCD), and Ion Cyclotron Resonance Heating (ICRH). The most important resulting structures in terms of core confinement, particle transport, and plasma-material interactions are the previously described Last Closed Flux Surface (LCFS) and Scrape-Off Layer (SOL).

1.2 Material Candidacy

The decision for the material of a plasma-facing component is dependent on the function of the component during operation and how the plasma will interact with the material. Generally speaking, the ideal material must be able to withstand thermal shocks and thermal cycling, have good thermal conductivity for rapid heat transfer, be a low-atomic number material to prevent major power losses, and be erosion resistant to prevent core contamination. Since such a material currently does not exist, candidates are typically chosen that have weaknesses in one of these areas, but make up for these weaknesses in the remaining areas. Two alternate schools of thought arose from the need to reduce wall impurities able to travel to the plasma core: high-Z refractory metals and alloys and low-Z materials. Researchers in these opposing camps must also consider the fuel retention characteristics, which could eventually make or break the ability to produce net power. The PFC material decision is critical to the advancement of the fusion energy field and has been an active area of meticulous research for decades.

1.2.1 High-Z Materials

The first school of thought that arose from the need to reduce plasma impurities generated at the PFC surface focused on the use of carbon, discussed in the following section. Complications with carbon led to the use of low-sputtering yield, refractory metals to mitigate power losses. Physical sputtering is the process in which energetic atoms or ions bombard a material surface and, depending on the angle and energy, initiate a displacement cascade within the first few nanometers of the material resulting in the expulsion of atoms from the surface as the crystal structure reorganizes [14]. The dependence on the energy and angle of the incident particle gives rise to a sputtering threshold, below which sputtering is so unlikely that the yield (the number of ejected particles over the number of incident particles) is considered negligible.

Researchers focusing on the high-Z solution look at refractory metals, such as tungsten (W) and molybdenum (Mo), and their alloys as PFC options. While a few of the properties of these high-Z choices differ, they all have very high melting temperatures, low sputtering yields, and high thermal conductivities [15]. While these metals have low erosion rates, both from a microscopic and macroscopic standpoint, these rates are still non-zero and are exacerbated during transient events like Edge Localized Modes (ELMs) or disruptions. A few of these released particles can then travel to the core, being only partially ionized along the way, and act as energy sinks that take power away from the plasma. Power loss to impurities is defined as [1]:

$$P_R = n_e n_I R \tag{1.3}$$

where P_R is the radiated power loss, n_e is the electron number density, n_I is the impurity number density, and R is the radiation parameter that is a function of the electron temperature, seen in Figure 1.3. Knowing a simplified form for the thermonuclear power produced (P_{Th}), the fraction of power lost to impurities (F) can be directly calculated. Assuming a 50% - 50% deuterium-tritium fuel mixture, this fraction can be calculated as [1]:

$$n_D = n_T = n \tag{1.4.1}$$

$$P_{Th} = \frac{1}{4} n_D n_T < \sigma v > \varepsilon = \frac{1}{4} n^2 < \sigma v > \varepsilon \tag{1.4.2}$$

$$F = \frac{n_e n_I R}{\frac{1}{4} n^2 < \sigma v > \varepsilon} = \frac{(1 + f\bar{Z}) f R}{\frac{1}{4} < \sigma v > \varepsilon} \tag{1.4.3}$$

where n_D is the deuterium number density, n_T is the tritium number density, $< \sigma v >$ is the thermonuclear reactivity as a function of the reactant energies, ε is the energy released per fusion reaction (17.6 MeV per D-T fusion reaction), f is the fraction of impurities to hydrogenic species ($\frac{n_I}{n}$), and $\bar{Z}$ is a mean value for the distribution of charge states for the impurity species.

Even if one of these high-Z impurity particles manages to become fully stripped as it travels to the plasma core, the presence of this impurity raises the Z_{eff} of the plasma. Collisional power losses to electrons with these high-Z ions enhances the Bremsstrahlung radiation, and is described in terms of the effective Z of the plasma [1]. Bremsstrahlung losses scale as a function of the square of Z_{eff}, but these losses are not as dramatic as the direct losses to impurities in the core.

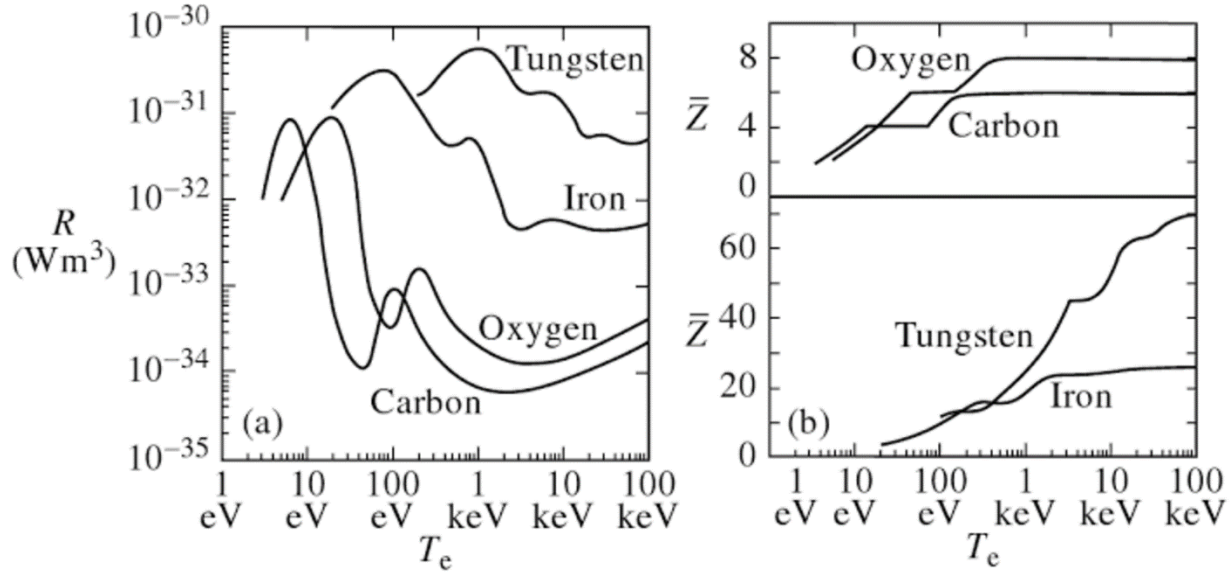

Figure 1.3: The radiation parameter, R, and the mean charge state, $\bar{Z}$, as a function of the electron temperature [1]. Low-Z impurities, like carbon and oxygen, peak in R at low temperatures because less energy is required to fully strip these species as they travel to the core. Fully stripped particles contribute more so to Bremsstrahlung losses, whereas high-Z impurities, like tungsten and iron, are still direct energy sinks even at core temperatures.

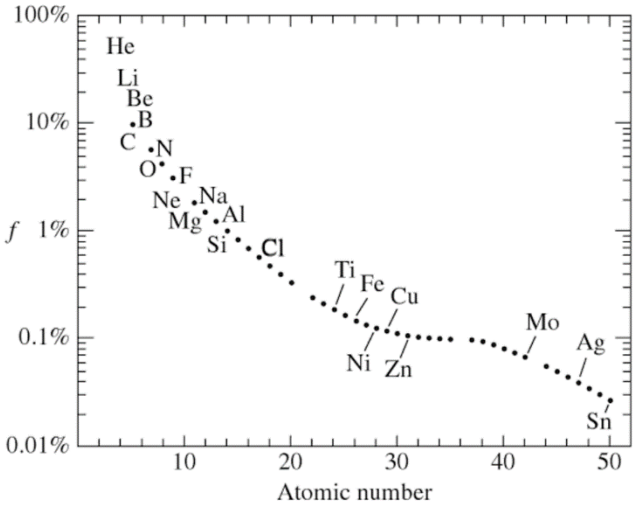

Figure 1.4: A graphic illustrating what plasma impurity fraction a given species needs to achieve in order to radiate away 10% of the thermonuclear power [1].

Besides their direct implications on plasma performance, high-Z materials also suffer in a number of other areas that either directly or indirectly impact operation. During operation, transient events that expel high energy densities from the core to the divertor may erode [16], modify [17, 18], or even melt the refractory solids at the plasma-surface interface [19, 20]. This is especially true in the chamfers and edges between monoblocks because the heat flux at the edges is amplified by the infinitesimally small area over which the energetic particles are striking. Growing concerns about the radioactive tritium inventory for solid refractory PFCs have also become increasingly important. Hydrogenic species implanted in solid walls prove difficult to remove and tritium captured by solid dust is a very real concern for long-term, large-scale device operation [19, 21-23]. Despite a variety of drawbacks, future fusion machines will more than likely feature, at least in part, solid refractory PFCs. To counteract a number of the aforementioned problems, wall conditioning techniques such as boronization [24] and lithiation [25] have been implemented and proven effective. Methods also exist that promote smaller, more manageable core impurity fractions (less than 0.001 %) of high-Z materials, such as detached divertor operation [26 – 28] and magnetic field sweeping [29]. While the application of these methods will allow for reactor-scale operation with the use of high-Z wall materials, the use of these materials is based on scale. Large, complex machines will not be financially viable, which is why the low-Z alternative is so attractive. The low-Z approach to the PFC material candidacy questions may prove to resolve many of the issues plaguing high-Z components.

1.2.2 Low-Z Materials

The opposing approach to minimize core contamination was to develop low-Z material walls that could withstand extreme conditions. Taking this approach would mean that even eroded particles that were able to migrate to the core plasma would not greatly affect the Z_{eff} of the core and would excite fewer pressure and current-driven instabilities. Originally, solid carbon PFCs in the form of graphite monoblocks or carbon fiber composites [30, 31] were considered for this approach, but it was soon discovered that the fuel retention in such structures would be prohibitive from both an operational and safety standpoint [32]. Carbon is also highly susceptible to erosion through chemical sputtering [33], and suffers from a phenomenon known as wall fueling, where retained fuel can desorb from the surface. While this lowers the need for external fueling [34], the

release of these retained fuel particles negatively impacts plasma confinement in terms of power loss.

As another solid, low-Z alternative wall material, beryllium has also been investigated due to its good thermal conductivity, low fuel retention, and ability to remove unwanted oxygen impurities from the plasma [35]. Beryllium, however, has a low melting point compared to graphite. Beryllium melts at 1287 °C, whereas graphite nominally undergoes a phase transition at 3257 °C [36, 37]. This limits the use of beryllium in first wall components on toroidal devices to areas other than the divertor. Beryllium is also problematic in that its dust is very toxic and bulk material is likely to erode, both at the micro- and macro-scale, in extreme conditions [38].

Even in the case of high-Z PFC use, lithium is still often used as a discharge pre-conditioner. This is because lithium has proven itself as a suitable PFC in its ability to "getter" impurities from the plasma [39], improve confinement times [40, 41], and limit the amount of retained fuel it recycles back into the plasma edge [42]. Some of the most recent results on the Experimental Advanced Superconducting Tokamak (EAST) show that with numerous lithium injection techniques, H-mode discharges can reach confinement times greater than 30 seconds [43]. Granted, the EAST device can use magnetic shaping techniques [44] that other devices cannot to help mitigate the effects of major instabilities, but these high-confinement, long-duration pulses would not be possible without the use of lithium. An in-vacuo image of one of these long-duration pulses can be seen in Figure 1.5.

Lithium is so advantageous for operations that alloys of it and other high-Z materials have been proposed for PFC use. Various alloys and eutectic compositions of tin and lithium are the most widely studied of these mixtures [45 – 48]. Originally thought to be an alternative for a tritium breeder blanket material in fusion reactors, the tin-lithium system offers a number of benefits over other metals and alloys. The combination of heating and ion bombardment causes lithium to diffuse to the surface through Gibbsian segregation [48], allowing plasma operation to benefit from all of the properties of lithium while preventing the high-Z tin from eroding and transporting into the plasma. Eutectics of this mixture have also shown to have a lithium vapor pressure lower than that of pure lithium by a factor of approximately 1000 [46]. The energy needed to liberate lithium from the surface is much higher in these alloys. If implemented properly, tin-lithium could be a very plausible candidate for PFCs in future machines.

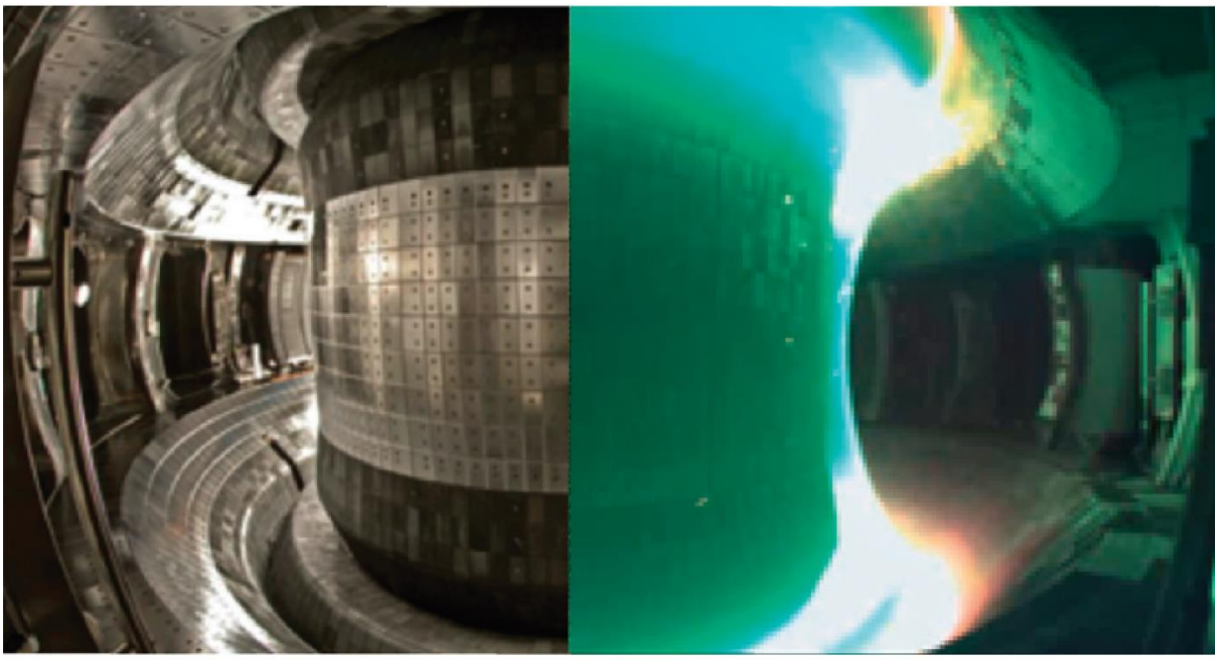

Figure 1.5: An internal view of the EAST machine [43]. The left portion shows the configuration of the tiles on the walls (molybdenum) and divertors (carbon). The right portion displays a discharge with walls pre-conditioned with lithium. The green glow at the plasma-material interface is characteristic of lithium emission and lithium is actively being injected from the top of the machine.

In general, the fusion community must address power handling at the walls in order to advance toward future reactor scenarios. The high-Z and low-Z materials previously described all rely on the use of solid tiles or solid composites in plasma-facing positions. Without significant active cooling behind these structures, especially for those materials at the divertor strike points, mass-scale erosion can occur that will greatly affect plasma performance and confinement time. The use of liquid metals in the place of solid PFCs may be the answer to many of the power-handling problems the community faces.

1.3 Liquid Metals

Even tungsten, with the highest melting point of all refractory metals, will undergo melting and mass scale erosion in the cases of ITER [49, 50] and DEMOnstration Power Station (DEMO) [51]. Such catastrophic events produced with solid PFC operations can be avoided by using liquid metals in place of solid metals, simply by virtue of the fact that this phase is amorphous and self-healing. Even the effects of extremely energetic, transient events can be mitigated by the fact that liquids will rearrange to their equilibrium state after the event happens. The problem with using liquid metals in general for both the high-Z and low-Z materials previously described is that all of them require extremely high temperatures to maintain their liquid state. Tungsten's melting point, at 3422 °C [36, 37], prohibits it from being held by nearly any other material. Molybdenum and the other high-Z options are all similarly limited to the solid phase, so it stands to reason that liquid metal PFCs must come from the low-Z approach.

Carbon and beryllium are not adequate candidates for the liquid low-Z approach, as they both have high melting points along with a few other detrimental qualities. While still low-Z, boron also has a high melting point at 2076 °C, meaning it also is impractical to maintain as a liquid. Lithium, on the other hand, is a brilliant candidate for a liquid, low-Z material since its melting point is much lower than all other low-Z materials at 180.5 °C [36, 37]. As mentioned in the previous section, lithium is also beneficial for a number of other reasons, and pre-conditioning high-Z walls with lithium coatings is fairly common practice.

1.3.1 Liquid Lithium as a PFC

As a low-Z alkali metal, lithium has exhibited numerous benefits over high-Z, and even other low-Z, material alternatives. Since it has such a low melting point when compared to other PFCs, it is much more feasible to maintain it in its liquid form throughout the duration of a pulse, than for other metals. As a liquid, it can be flowed through sections of a reactor to both conduct and convect heat away from sections exposed to the highest heat loads. This is most important in the divertor. A secondary benefit to lithium is that even if vaporized, the cloud that persists directly in front of the lithium strike point can be used to disperse the incoming particle and heat fluxes and minimize the effective burden on the bulk surface [52, 53]. If some of this cloud is able to be

transported to the core through the SOL, lithium is easily ionized and subsequently transported away from the core [54]. The ease of ionization also affects the sputtering characteristics of lithium, demonstrated by Allain [55, 56] and László and Eckstein [57]. Sputtered lithium neutrals appear to re-ionize quite easily, with the total lithium yield being observed to be two thirds ions and only one third neutrals [55]. This is important because the high ion fraction limits lithium transport to the core. Two categories of liquid lithium use as a PFC have been proposed based on the flow characteristics of lithium through various liquid-confining structures.

1.3.1.1 Slow-flow Liquid Lithium Systems

In the case of systems where liquid lithium flows through its confining structure very slowly (essentially maintaining a static supply of lithium at the plasma-facing surface), the most thoroughly investigated are those that use capillary forces in the liquid metal to drive movement. The Capillary Porous System (CPS) [58, 59] takes advantage of the surface tension and capillary action of liquid lithium to constantly replenish the lithium on the surface that gets eroded at the plasma-material interface. As mentioned before, the lithium that erodes establishes a vapor cloud directly above the structure that helps to disperse incoming particle and heat fluxes. The CPS containment structure is also actively cooled to help reduce the impact of both steady-state and transient heat loads. A diagram in Figure 1.6 illustrates how the CPS system provides a constant, static, lithium surface at the plasma interface in a reactor setting.

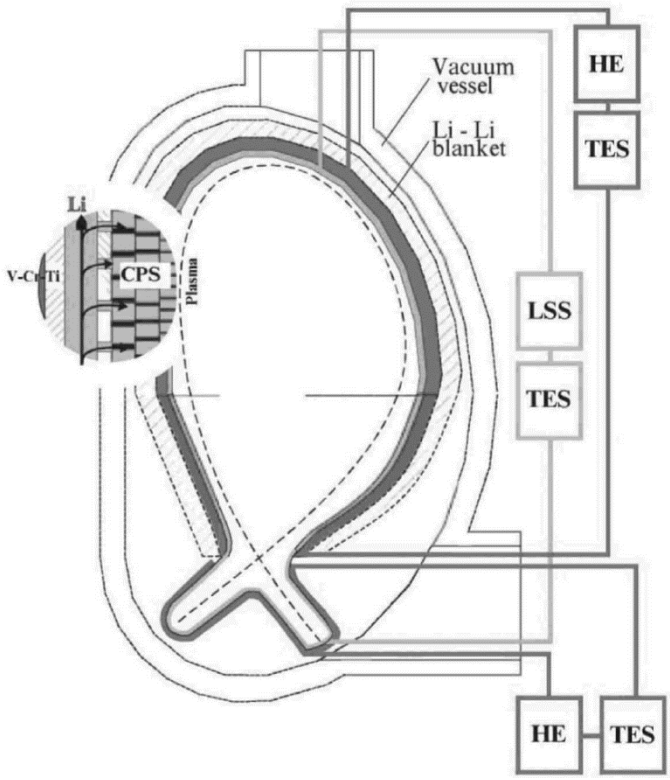

Figure 1.6: An image depicting how the CPS system would work in a classical fusion reactor system, like that of the T-11M tokamak [60]. Lithium will flow along a back channel, but will be forced through narrowing capillary channels as lithium surface layers are eroded. The acronyms HE, TES, and LSS stand for Heat Exchanger, Tritium Extraction System, and Lithium Supply System, respectively. Two separate collection loops are depicted for the first wall vs. divertor components.

Critics of the CPS system are concerned with a few items that proponents of the structure need to address before applying it to large-scale devices. First, lithium passivates quickly in the presence of impurities like oxygen, nitrogen, carbon, and hydrogen [61]. Passivation of a static surface like that provided by the CPS system can inhibit flow and nullify the benefits provided by clean lithium. Research has been done on how the impurity levels within the Li of a CPS system affects the interfacial properties, and proponents have concluded that the presence of oxygen is necessary for minimizing fuel recycling [61, 62]. Local and global re-deposition of lithium is also a concern because numerous surfaces within the vessel would be obstructed by the presence of lithium, if the entire vessel was not already covered in lithium. Finally, deuterium and tritium

retention is the greatest concern for this type of PFC. Lithium and its impurity products (lithium hydride, lithium oxide, lithium hydroxide, etc.) are efficient at retaining hydrogenic species [63 – 66]. Future reactors will have limitations on their total on-site tritium inventories, so tritium fuel captured in a slow-flow lithium system negatively impacts this inventory since the system was designed to contain the lithium entirely within the vessel. The supply of tritium is also limited globally, where on-site inventories are meant to reflect resource limits. To recycle the tritium, the reactor will have to undergo a maintenance period to degas the entrained fuel, which will be costly for a power-producing utility. It is also impractical to heat the entire vessel to the temperatures needed to desorb the fuel during maintenance, since by the time the maintenance period would occur, the fuel species would have likely been converted to the hydride form.

1.3.1.2 Medium-flow Liquid Lithium Systems

To combat the problems surrounding the removal of fuel entrained in lithium within the reactor, devices that flow lithium past the plasma strike point at velocities much greater than what can be provided by capillary forces have been proposed, constructed, and tested in a variety of machines. The two concepts that have undergone the highest degree of experimental verification are the Flowing Liquid Lithium (FLiLi) concept [67] from the Princeton Plasma Physics Laboratory (PPPL) and the Lithium Metal Infused Trenches (LiMIT) concept [68, 69] from the Center for Plasma-Material Interactions at the University of Illinois.

The FLiLi concept operates on the basis of flowing a very thin sheet of liquid lithium over a solid backing plate. Lithium reaching the bottom of the plate will then theoretically go through a purification process before being recycled back to the distribution manifold at the top of the plate. Since FLiLi operates on the fundamental principles of surface tension and gravity to drive flow across the solid surface, it is subject to magnetohydrodynamic (MHD) instabilities in the lithium excited by currents in the lithium interacting with the strong fields at the edge of the reactor. FLiLi has also been observed to undergo dryout in the plasma strike zone, leading to direct plasma impingement on the backing plate. Finally, issues with blockages and fouling in the manifold distribution system has led to uneven coverage across the solid surface, again exposing the backing plate directly to the plasma. Because of apprehensions surrounding the dryout issue to which FLiLi

is prone, the device is only meant to be operated as a limiter and only for the intention of lowering fuel recycling at the edge.

The LiMIT device attempts to address a number of issues with FLiLi operation. Instead of being inhibited by the MHD forces that generate turbulence in flowing a thin sheet of lithium over a solid surface, LiMIT utilizes those same forces to help propel lithium along a series of containing trenches. LiMIT operates under the principles of thermoelectric magnetohydrodynamics (TEMHD) [70 – 72]. By establishing a thermal gradient through the lithium between the plasma-facing surface and the bottom of the trench using active cooling through the middle of the confining trench structure, a current is generated between the dissimilar metals of the lithium and the trench material at the side walls. In an ideal case, a thin layer of lithium will also be covering the tops of the trench walls. Using the toroidal field, a Lorentz force of the cross product of the current and magnetic field (JxB) is generated that drives lithium flow without the use of a mechanical pump. A diagram of how lithium flow is created in a trench structure can be seen in Figure 1.7. While envisioned to replace solid divertors in large devices, LiMIT has only been observed to be able to handle heat fluxes up to 3 MW m^{-2}. ITER is expected to have steady-state heat fluxes to the divertor in excess of 10 MW m^{-2} and transient heat fluxes in excess of 20 MW m^{-2} [73]. Apart from its heat flux handling capabilities, opponents of LiMIT, and medium-flow liquid lithium systems in general, are concerned with fuel retention. Specifically, extraction of entrained fuel and recycling of the fuel species and clean lithium are collectively considered to be one of the biggest roadblocks to widespread deployment of medium-flow liquid lithium PFCs.

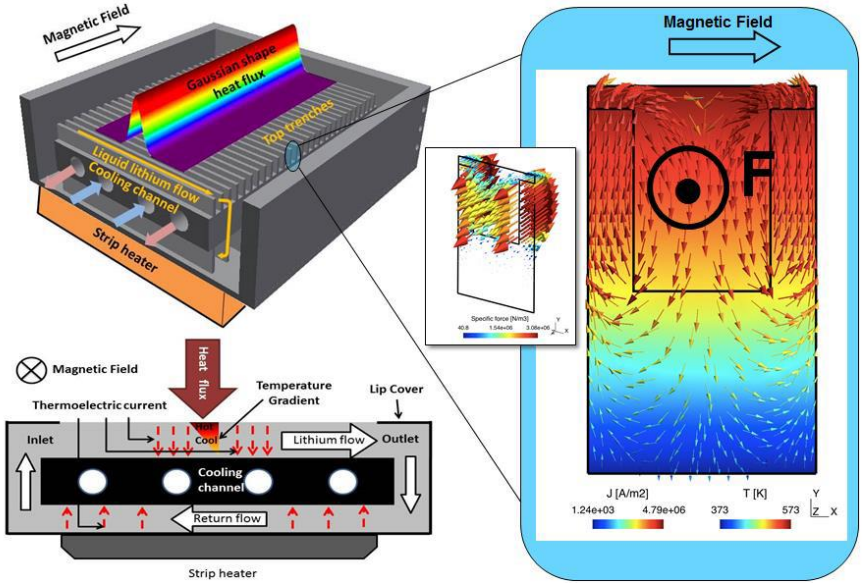

Figure 1.7: Images that illustrate the driving forces for lithium flow in the LiMIT channels [72]. The top left image shows the full structure with the cooling channels, direction of the magnetic field, and the Gaussian heat flux profile along the center of the trenches. The right image shows how the thermoelectric currents are generated in an individual trench, with typical gradients through the trench reaching values exceeding 1000 K m^{-1}. The bottom left image combines the effects in the other two diagrams to explain the flow direction of lithium in a single trench.

This thesis aims to prove that there exist hydrogenic fuel reclamation technologies that will counteract the worries and claims of those who believe that widespread Li wall deployment is unfeasible. In order for these technologies to be quantified as successful or not, a metric, or standard of comparison, must be defined. The metric for success, along with more detail surrounding the fuel retention capabilities and general use of liquid lithium in the fusion environment, will be expanded upon in the following chapter. The next chapter will also elaborate on how fuel retention and reclamation will affect LiMIT use in a reactor scenario.

1.4 References

[1] J. Wesson, *Tokamaks*. No. 149 in International series of monographs on physics, New York, NY: Oxford University Press, 4th ed., 2011.

[2] J. P. Freidberg, *Plasma physics and fusion energy*. Cambridge: Cambridge University Press, 2007.

[3] R. A. Pitts, J. P. Coad, D. P. Coster, G. Federici, W. Fundamenski, J. Horacek, K. Krieger, A. Kukushkin, J. Likonen, G. F. Matthews, M. Rubel, J. D. Strachan, and J.-E. contributors, "Material erosion and migration in tokamaks", *Plasma Phys. Cont. Fus.* 47 (2005) B303.

[4] Classical tokamak magnetic field structure (image available for download; original produced by Abteilung Öffentlichkeitsarbeit – Max-Planck Institut für Plasmaphysik). Available from: https://www.laetusinpraesens.org/docs10s/radexis.php [accessed: December 14, 2016].

[5] J.D. Lawson, "Some criteria for a power producing thermonuclear reactor," *Proc. Phys. Soc.* 70 (1957).

[6] H. Bolt, V. Barabash, G. Federici, J. Linke, A. Loarte, J. Roth, K. Sato "Plasma facing and high heat flux materials-needs for ITER and beyond", *J. Nucl. Mat.* 307-311 (2002) 43.

[7] F. Wagner, et al., "Regime of improved confinement and high beta in neutral-beam-heated divertor discharges of the asdex tokamak", *Phys. Rev. Lett.* 49 (1982) 1408.

[8] J.R. Walk, P.B. Snyder, J.W. Hughes, J.L. Terry, A.E. Hubbard, P.E. Phillips, "Characterization of the Pedestal in Alcator C-Mod ELMing H-Modes and Comparison of the EPED Model", *Nucl. Fus.* 52 (2012) 063011.

[9] E.J. Doyle, et al., "ITPA Transport Physics Topical Group, ITPA confinement Database, Modelling Topical Group, ITPA Pedestal, and Edge Topical Group", *Nucl. Fus.* 47 (2007) S18.

[10] M. Greenwald, R.L. Bolvin, F. Bombarda, P.T. Bonoli, C.L. Fiore, D. Garnier, J.A. Goetz, S.N. Golovato, M.A. Graf, R.S. Granetz, "H mode confinement in alcator c-mod," *Nucl. Fus.* 37 (1997) 793.

[11] A.E. Hubbard, et al., "Measurements of the high confinement mode pedestal region on alcator c-mod", *Phys. Plasmas* 5 (1998) 1744.

[12] J. Ongena, R. Koch, R. Wolf, and H. Zohm, "Magnetic-confinement fusion", *Nat. Phys.* 12 (2016) 398.

[13] D. Mueller, "The physics of tokamak start-up", *Phys. Plasmas* 20 (2013) 058101.

[14] P. Sigmund, "Theory of Sputtering. I. Sputtering Yield of Amorphous and Polycrystalline Targets", *Phys. Rev. Lett.* 184 (1969) 383.

[15] R.F. Mattas, B. Misra, D.L. Smith, G.D. Morgan, M. Delaney, and R.E. Gold, "MATERIALS SELECTION FOR THE U.S. INTOR DIVERTOR COLLECTION PLATE", *J. Nucl. Mat.* 103-104 (1981) 217.

[16] S. Kajita, N. Ohno, S. Takamura, "Tungsten blow-off in response to the ignition of arcing: Revival of arcing issue in future fusion devices", *J. Nucl. Mat.* 415 (2011) S42.

[17] P. Fiflis, D. Curreli, and D.N. Ruzic, "Direct time-resolved observation of tungsten nanostructured growth due to helium plasma exposure", *Nucl. Fus.* 55 (2015) 033020.

[18] P. Fiflis, N. Connolly, and D.N. Ruzic, "Experimental mechanistic investigation of the nanostructuring of tungsten with low energy helium plasmas", *J. Nucl. Mat.* 482 (2016) 201-209.

[19] R.A. Pitts, S. Carpentier, F. Escourbiac, T. Hirai, V. Komarov, S. Lisgo, A.S. Kukushkin, A. Loarte, M. Merola, A. Sashala Maik, R. Mitteau, M. Sugihara, B. Bazylev, and P.C. Stangeby, "A full tungsten divertor for ITER: Physics issues and design status", *J. Nucl. Mat.* 438 (2013) S48.

[20] K. Tobita, S. Nishio, S. Konishi, M. Sato, T. Tanabe, K. Masaki, N. Miya, "First wall issues related with energetic particle deposition in a tokamak fusion power reactor", *Fus. Eng. and Des.* 65 (2003) 561.

[21] M. Desecures, L. El-Guebaly F. Druyts, P. Van Iseghem, V Massaut, G. Van Oost, "Study of radioactive inventory generated from W-based components in ITER and PPCS fusion designs", *Fus. Eng. and Des.* 88 (2013) 2674.

[22] C. Sang, J. Sun, X. Bonnin, S. Dai, W. Hu, D. Wang, "Numerical study of the effects of physical parameters on the dynamic fuel retention in tungsten materials", *J. Nucl. Mat.* 455 (2014) 111.

[23] H. Bolt, V. Barabash, W. Krauss, J. Linke, R. Neu, S. Suzuki, N. Yoshida, ASDEX Upgrade Team, "Materials for plasma-facing components of fusion reactors", *J. Nucl. Mat.* 329-333 (2004) 66.

[24] O. Buzhinskij and Y. Semenets, "Review of in situ boronization in contemporary tokamaks", *Fus. Tech.* 32 (1997) 1.

[25] R. Maingi, et. al., "Continuous improvement of H-mode discharge performance with progressively increasing lithium coatings in the National Spherical Torus Experiment", *Phys. Rev. Lett.* 107 (2011).

[26] Y. Homma, et al., "Numerical analysis of tungsten erosion and deposition processes under a DEMO divertor plasma", *Nucl. Mater. & Energ.* 12 (2017) 323.

[27] X. Bonnin, R.A. Pitts, V. Komarov, F. Escourbiac, M. Merola, L. Bo, L. Wei, L. Pan, and A.S. Kukushkin, "ITER divertor plasma response to time-dependent impurity injection", *Nucl. Mater. & Energ.* 12 (2017) 1100.

[28] S.I. Krasheninnikov and A.S. Kukushkin, “Physics of ultimate detachment of a tokamak divertor plasma”, *J. Plasma Phys.* 83 (2017) 1.

[29] S.A. Silburn, et al., “Mitigation of divertor heat loads by strike point sweeping in high power JET discharges”, *Phys. Scr.* T170 (2017) 014040.

[30] F.W. Meyer, H.F. Krause, L.I. Vergara, “Measurements of chemical erosion of ATJ graphite by low energy D2+ impact”, *J. Nucl. Mat.* 337 (2005).

[31] G.F. Counsell and C.H. Wu, “In-situ detection and removal of carbon debris - a challenge for the next step fusion device” *Phys. Scr.* T91 (2001).

[32] R.A. Causey, M.I. Baskes, K.L. Wilson, “The retention of deuterium and tritium in POCO AXF-5Q graphite”, *J. Vac. Sci. Tech. A* 4 (1986).

[33] J. Roth, “Chemical erosion of carbon based materials in fusion devices”, *J. Nuc. Mat.* 266 (1999).

[34] R. Kaita, et. al., “Low recycling and high power density handling physics in the Current Drive Experiment Upgrade with lithium plasma facing components”, *Phys. Plasmas* 14 (2007).

[35] R.W. Conn, R.P. Doerner, J. Won, “Beryllium as the plasma facing material in fusion energy systems - experiments, evaluation, and comparison with alternative materials”, *Fus. Eng. and Des.* 37 (1997).

[36] A.M. James and M.P. Lord, *Macmillan's Chemical and Physical Data*, Macmillan: London, UK, 1992.

[37] G.W.C. Kaye and T.H. Laby, *Tables of physical and chemical constants*, Longman: London, UK, 15th edition, 1993.

[38] G.F. Matthews, M. Beurskens, S. Brezinsek, M. Groth, E. Joffrin, A. Loving, M. Kear, M.-L. Mayoral, R. Neu, P. Prior, “JET ITER-like wall - overview and experimental programme”, *Phys. Scr.* T145 (2011) 014001.

[39] R. Majeski, S. Jardin, R. Kaita, T. Gray, P. Marfuta, J. Spaleta, J. Timberlake, L. Zakharov, G. Antar, R. Doerner, S. Luckhardt, R. Seraydarian, V. Soukhanovskii, R. Maingi, M. Finkenthal, D. Stutman, D. Rodgers, and S. Angelini, “Recent liquid lithium limiter experiments in CDX-U”, *Nucl. Fus.* 45 (2005) 519.

[40] G. Mazzitelli, M.L. Apicella, V. Pericoli Ridolfini, G. Apruzzese, R. De Angelis, D. Frigione, E. Giovannozzi, L. Gabellieri, G. Granucci, C. Mazzotta, M. Marinucci, A. Romano, O. Tudisco, A. Alekseyev, I. Ljublinski, A. Vertkov, ECRH Team, “Review of FTU results with the liquid lithium limiter”, *Fus. Eng. and Des.* 85 (2010) 896.

[41] G.S. Zuo, B.N. Wan, J.G. Li, X.Z. Gong, J.S. Hu, J.F. Shan, H. Li, D.K. Mansfield, D.A. Humphreys, V. Naulin, EAST Team, "Study on H-mode access at low density with lower hybrid current drive and lithium-wall coatings on the EAST superconducting tokamak", *Nucl. Fus.* 51 (2011) 072001.

[42] R. Majeski, R. Doerner, T. Gray, R. Kaita, D. Mansfield, J. Spaleta, V. Soukhanovskii, J. Timberlake, L. Zakharov. "Enhanced energy confinement and performance in a low-recycling tokamak", *Phys. Rev. Lett.* 97 (2006) 075002.

[43] J. Li, et al., "A long-pulse high-confinement plasma regime in the Experimental Advanced Superconducting Tokamak", *Nat. Phys.* 9 (2013) 817.

[44] Y. Sun, et al., "Nonlinear Transition from Mitigation to Suppression of the Edge Localized Mode with Resonant Magnetic Perturbations in the EAST Tokamak", *Phys. Rev. Lett.* 117 (2016) 115001.

[45] M.A. Futterer, G. Aiello, F. Barbier, L. Giancarli, Y. Poitevin, P. Sardain, J. Szczepanski, A. Li Puma, G. Ruvutuso, and G. Vella, "On the use of tin-lithium alloys as breeder material for blankets of fusion power plants", *J. Nucl. Mat.* 283-287 (2000) 1375.

[46] K. Natesan, W.E. Ruther, "Fabrication and properties of a tin-lithium alloy", *J. Nucl. Mat.* 307-311 (2002) 743.

[47] A. Hassanein, J.P. Allain, Z. Insepov, I. Konkashbaev, "PLASMA/LIQUID-METAL INTERACTIONS DURING TOKAMAK OPERATION", *Fus. Sci. and Tech.* 47 (2005) 686.

[48] R. Bastasz, J.A. Whaley, "Surface composition of liquid metals and alloys", *Fus. Eng. and Des.* 72 (2004) 111.

[49] M.I. Guseva, V.M. Gureev, L.S. Danelyan, B.N. Kolbasov, S.N. Korshunov, Yu. V. Martynenko, V.B. Petrov, V.G. Stolyarova, B.I. Khripunov, V.I. Vasiliev, V.M. Strunnikov, "Tungsten erosion under simulation of iter divertor operation", *Plasma Dev. & Op.* 11 (2003) 141.

[50] W. Hu, C. Sang, Z. Sun, D. Wang, "Divertor tungsten tiles erosion in the region of the castellated gaps", *Fus. Eng. and Des.* 109 (2016) 330.

[51] Y. Igitkhanov, B. Bazylev, "Modeling of DEMO PFC Erosion Due to ELM Impact", *IEEE Trans. on Plasma Sci.* 42 (2014) 2284.

[52] Travis Gray, Doctoral Thesis (2009): UIUC.

[53] R.J. Goldston, R. Myers, J. Schwartz, "The lithium vapor box divertor", *Phys. Scrip.* 2016 (2016) 014017.

[54] F. Scotti, et. al., “Core transport of lithium and carbon in ELM-free discharges with lithium wall conditioning in NSTX”, *Nucl. Fus.* 53 (2013).

[55] J.P. Allain and D.N. Ruzic, “Measurements and modelling of solid phase lithium sputtering”, *Nucl. Fusion* 42 (2002) 202.

[56] J.P. Allain, D.N. Ruzic, and M.R. Hendricks, “Measurements and modeling of D, He and Li sputtering of liquid lithium”, *J. Nucl. Mater.* 290-293 (2001) 180.

[57] J. László and W. Eckstein, “Sputtering and reflection from lithium, gallium and indium”, *J. Nucl. Mater.* 184 (1991) 22.

[58] L.G. Golubchikov, V. Evtikhin, I. Lyublinski, V. Pistonovich, I. Potapov, and A. Chumanov, “Development of liquid metal fusion reactor divertor with a capillary pore system”, *J. Nucl. Mat.* 233 (1996).

[59] S. Mirnov, E. Azizov, V. Evtikhin, V. Lazarev, I. Lyublinski, A. Vertkov, D. Prokhorov, “Experiments with lithium limiter on T-11M tokamak and applications of the lithium capillary pore system in future fusion reactor devices”, *Plas. Phys. Cont. Fus.* 48 (2006).

[60] Li-CPS limiter in tokamak T-11M (PDF Download Available). Available from: https://www.researchgate.net/publication/228561617_Li-CPS_limiter_in_tokamak_T-11M [accessed Dec 14, 2016].

[61] J.P. Allain, D.L. Rokusek, S.S. Harilal, M. Nieto-Perez, C.H. Skinner, H.W. Kugel, B. Heim, R. Kaita, R. Majeski, “Experimental studies of lithium-based surface chemistry for fusion plasma-facing materials applications”, *J. Nucl. Mat.* 390-391 (2009) 942.

[62] E. Oyarzabal, A.B. Martin-Rojo, F.L. Tabarés, “Laboratory experiments of uptake and release of hydrogen isotopes in liquid lithium”, *J. Nucl. Mat.* 463 (2015) 1173.

[63] S.K. Erents, G.M. McCracken, and P. Goldsmith, “Trapping of keV deuterons in lithium”, *J. Phys. D: Appl. Phys.* 4 (1971) 672.

[64] M.J. Baldwin, R.P. Doerner, S.C. Luckhardt, and R.W. Conn, “Deuterium retention in liquid lithium”, *Nucl. Fus.* 42 (2002) 1318.

[65] M.J. Baldwin, R.P. Doerner, S.C. Luckhardt, R. Seraydarian, D.G. White, R.W. Conn, “Plasma interaction with liquid lithium: Measurements of retention and erosion”, *Fus. Eng. and Des.* 61-62 (2002) 231.

[66] R. Stubbers, W. Olczak, M. Nieto, and D.N. Ruzic, “Measurement of hydrogen absorption in flowing liquid lithium in the flowing lithium retention experiment (FLIRE)”, *J. Nucl. Mat.* 337-339 (2005) 1033.

[67] J. Ren, J.S. Hu, G.Z. Zuo, Z. Sun, J.G. Li, D.N. Ruzic, and L.E. Zakharov, “First results of flowing liquid lithium limiter in HT-7”, *Phys. Scr.* T159 (2014) 014033.

[68] D.N. Ruzic, W. Xu, D. Andruczyk, M.A. Jaworski. “Lithium-metal infused trenches (LiMIT) for heat removal in fusion devices”, *Nucl. Fus.* 51 (2011) 10200.

[69] W. Xu, D. Curreli, and D.N. Ruzic, “Computational studies of thermoelectric MHD driven liquid lithium flow in metal trenches”, *Fus. Eng. and Des.* 89 (2014) 2868.

[70] J. A. Shercliff, “Thermoelectric magnetohydrodynamics”, *J. Fluid Mech.* 91 (1979) 231.

[71] M. A. Jaworski, T. K. Gray, M. Antonelli, J. J. Kim, C.Y. Lau, M. B. Lee, M. J. Neumann, W. Xu, and D. N. Ruzic, “Thermoelectric Magnetohydrodynamic Stirring of Liquid Metals”, *Phys. Rev. Lett.* 104 (2010) 094503.

[72] W. Xu, D. Curreli, D. Andruczyk, T. Mui, R. Switts and D.N. Ruzic, “Heat transfer of TEMHD driven lithium flow in stainless steel trenches”, *J. Nucl. Mat.* 438 (2013) S422.

[73] A. Loarte, “Fusion plasmas: Chaos cuts ELMs down to size”, *Nat. Phys.* 2 (2006) 369.

CHAPTER 2: BACKGROUND AND MOTIVATION

2.1 Background

Even though lithium has been seen to be extremely beneficial to plasma performance in a number of tokamak devices, it still suffers from a number of shortcomings that prevent it from being universally considered as the PFC of choice. While both slow-flow and medium-flow liquid lithium options suffer from nearly identical problems, medium-flow devices have the distinct ability to overcome many of these complications simply by virtue of them driving lithium flow more quickly through the device. For any fast-flow alternative to be widely considered for use as a PFC, it must not be limited by: (1) droplet ejection, (2) wetting control, (3) tritium retention, and (4) heat flux handling. Steps taken to eliminate these issues in the LiMIT device are active areas of research [1 – 5]; however, little has been done to address fuel retention concerns. This is especially true with regards to the extraction of entrained fuel species in the flowing lithium. To understand how to extract entrained fuel, we must first look at the fundamental mechanisms by which fuel species become trapped within the lithium.

2.1.1 Fuel Retention in Li

As lithium has gained popularity as a plasma-facing material, research groups have begun to dedicate their efforts on examining its viability as a first wall candidate. Since the retention characteristics of lithium are both beneficial and detrimental for steady-state operation of a reactor, focus has been placed on understanding the probability with which a fuel particle striking the lithium surface will absorb or adsorb at the atomistic level, which can then be translated to a macroscopic recycling coefficient. As mentioned in Chapter 1, minimal fuel recycling from the wall can allow for future devices to operate in confinement regimes beyond those available to high-recycling, solid walls. In these regimes, machines can be built on a much smaller scale than previously imagined, meaning that the intricacies and details surrounding this recycling issue with regards to liquid lithium must be flushed out for future power-producing utilities to be economically feasible.

From a molecular level, one of the most important metrics for understanding the probability that an energetic fuel particle will be captured by lithium or lithium impurities, such as lithium

oxide (Li_2O) or lithium hydroxide (LiOH), is the cross-section for a given reaction as a function of the energy of the bombarding species. Cross-sections indicate the probability that a reaction will occur at a given energy, and can be translated to macroscopic coefficients. Lithium has a high affinity for hydrogen isotopes across a wide range of energies, but so do its impurities. A number of studies [6 – 10] have concluded that the presence of oxygen is actually more beneficial for hydrogen isotope entrapment than having pure Li. This is important to consider for future wall designs because there will always be a native oxide layer on any metallic surface. A flowing liquid metal, however, may not be able to take advantage of this since the bulk movement of the lithium carries the impurities with it as it flows. From a chemistry perspective, the Li-H-LiH system still requires further analysis since many of the fundamentals of the interaction among these species are not fully understood.

Retention of fusion fuel species, at a macroscopic scale, can be related to atomistic quantities easily by knowing the reflection probability of an individual particle at an individual energy from a lithium surface [11]. From a zeroth order approximation, the reflection probability and the capture probability at a lithium wall sum to unity, at a given energy. This assumes that the lithium surface has enough of a bulk layer underneath for a hydrogen isotope to traverse, inelastically scatter, and eventually become captured. Applying this probability over the energy distribution with which fuel species strike the wall gives a total reflection probability distribution. This kind of distribution is illustrated in Figure 2.1 for all three hydrogen isotopes.

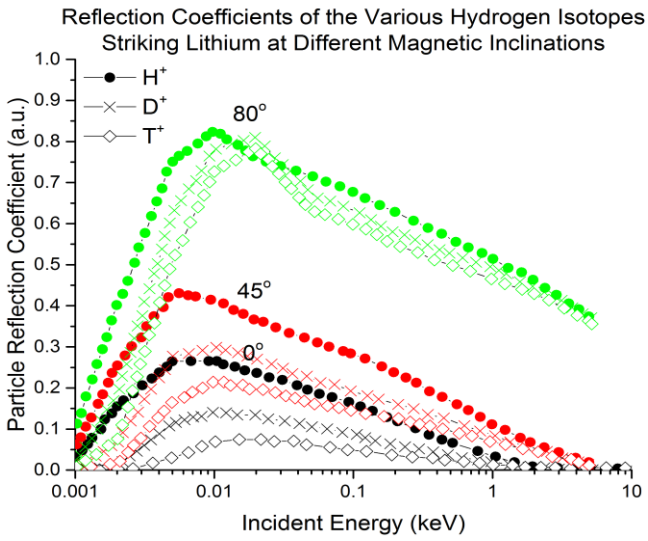

Figure 2.1: The reflection probability distributions as functions of energy for the various hydrogenic isotopes at different angles of incidence. These were calculated using SDTrimSP 4.10 and are available from the EIRENE database [12]. Differences in the reflection probabilities between isotopes are based on particle mass.

The reflection coefficients in Figure 2.1 represent those calculated using SDTrimSP, which is a Monte Carlo code that assumes an amorphous target at "zero temperature" and uses the binary collision approximation for the collision kernel. Potentials are incredibly important in evaluating these probabilities, and while the available potentials in SDTrimSP cover a wide range of nuclear and electronic interactions, they are not universally inclusive. Ab initio molecular dynamics may be able to help resolve these shortcomings with regards to the Li-H system, but are computationally intensive since they are deterministic and work off of first principles.

While the reflection probability distributions above follow well with the dependence on particle mass, laboratory experiments conducted by Erents [13] and Baldwin [14] describe deuterium uptake in bulk liquid lithium samples to be nearly 100% at ion energies in the 10's of eV to 10's of keV. This disagrees with the distributions in Figure 2.1, where capture is not considered complete at any temperature since there seems to be some probability that the particle will be reflected. Baldwin's study is more representative, however, than are the distributions, since the establishment of the sheath and the redeposition of ionized lithium are considered

experimentally. These studies also found that the presence of impurity layers, even those that potentially contain oxygen, greatly inhibits the uptake of deuterium, which is in contrast to the studies referenced previously. The difference here is that the studies previously mentioned looked primarily at the role oxide layers play on thin lithium films, whereas the work done by Baldwin and Erents look at retention in bulk liquid lithium. Differences also exist in the fact that the studies conducted by Baldwin and Erents used samples exposed to high fluences, which would probably not be the case for medium- or fast-flow systems. High retention characteristics were also observed in NSTX [15] that approach the 1:1 capture characteristic described by Baldwin. Another important conclusion that can be drawn from Baldwin's work is the fact that this 1:1 absorption ratio is only possible in the liquid phase. While this 1:1 chemical makeup occurs more so at higher fluences, it will be important for future flowing liquid lithium PFCs and fuel extraction technologies to take high LiD and LiT concentrations into account.

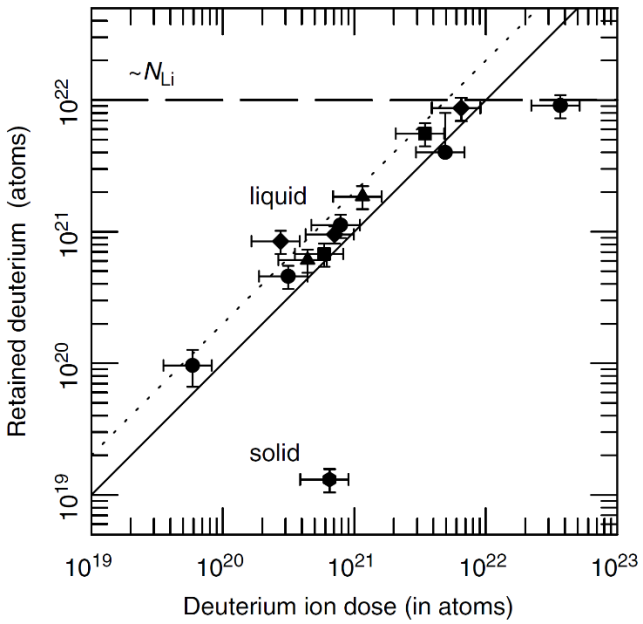

Figure 2.2: The summarizing plot from the work conducted by Baldwin [14], which illustrates how liquid lithium samples will capture deuterons (conducted in the PISCES-B experiment) with nearly 100% efficiency. The solid lithium sample is far less likely to capture incoming fuel species, possibly due to surface saturation or surface contamination.

While macroscopically it appears as if liquid Li will consume all fuel species that strike its surface, it is still unclear from the literature if the incoming ions will be more likely to covalently bond with Li or remain dissolved within the melt. Advancements in hydrogen extraction schemes require detailed knowledge of these ion-enhanced thermodynamics. The reason for this is based largely on the fundamentals of thermal diffusion and surface recombination, and will be explored later in the chapter. The next section explores the recovery time constraint that all fuel reclamation schemes operating with liquid lithium must abide by, from a theoretical point-of-view.

2.1.2 The Li-Wall Regime and the Recovery Time Constraint

The Li-Wall Regime for an ignited reactor has been studied for many years [16, 17]. In this theoretical reactor, Li covers all of the plasma-facing surfaces, as either a liquid or a replenishing solid, and acts as a perfect particle sink at the edge of the plasma cross-section. Density, temperature, power, and wall flux profiles are all calculated with respect to, at minimum, the radial dimension and time. In this scenario, it is also assumed that the lithium wall is cooled well enough such that erosion and sputtering are minimal and wall impurities do not at all interact with the core plasma. There also exists a constant particle source within the control volume, which is likely representative of a neutral beam injector (NBI). Multiple simulations have been performed, with different degrees of precision, to explain the Li-Wall Regime behavior, but what is the most important take-away from these results is the rate at which tritium will be consumed at the wall if the entire inner surface of the torus is covered in Li.

Using the density and temperature profiles calculated by Zakharov, et al., in Ref. 16 for an ITER-like scenario, a very basic time limit can be described from a particle-balance perspective. Assuming that the lithium wall is a perfect particle sink, which will not truly be the case in a real-world situation, the particle flux to the wall can easily be described by the equation:

$$\Gamma_i = < n_i v_i > \tag{2.1}$$

where Γ_i is the flux of species i, n_i is the number density of species i, and v_i is the velocity of species i. If the particle density at the wall is 2.9×10^{18} m^{-3}, and the temperature at the wall is about 7.3 keV (for a ignited Li-Wall scenario [16]), then the expected value of the particle flux to the wall will be approximately 2×10^{24} m^{-2} s^{-1}. Assuming that the net particle flux travelling to the

wall is ¼ of the calculated flux at the wall, which roughly takes into account directionality, and assuming that the divertor strike point in this scenario covers 3.5 m^2, the total amount of 1 kg of tritium will be lost in roughly 8 minutes. The resultant density and temperature profiles resulting from this simulation work can be seen in Figure 2.3.

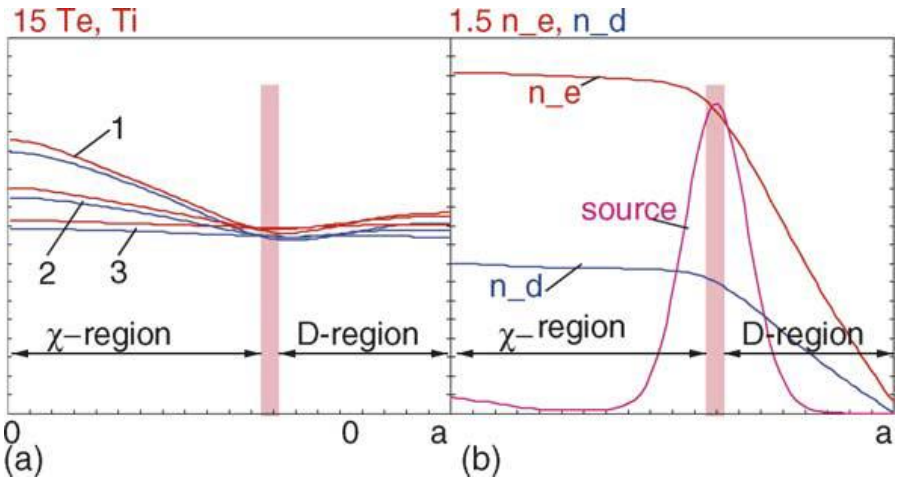

Figure 2.3: The temperature and density profiles evaluated for the Li-Wall scenario following the methodology in Ref. 16. Power loss is dominated by different diffusion mechanisms, delineated by the particle source. Here, *a* represents the full minor radius, the core electron temperature, Te(0), is 15 keV, and the core electron density, n_e(0), is approximately 1.5 x 10^{20} m^{-3}.

From this work, it seems as if tritium recycling technologies will be hard-pressed to match the wall loss rates in an ignited ITER-FEAT scenario. Work performed by Krasheninnikov, et al. [17] paints a more optimistic picture with regards to tritium retention. Like the work performed by Zakharov, Krasheninnikov's group looked at various regions of the Li-Wall scenario within the entire cross section of the tokamak that are governed by thermal vs. particle diffusivities. In this case, Bohm diffusion is also taken into account and the entire simulation is solved both in time and as a function of the radius. The results calculated by Krasheninnikov and his group are illustrated in Figure 2.4.

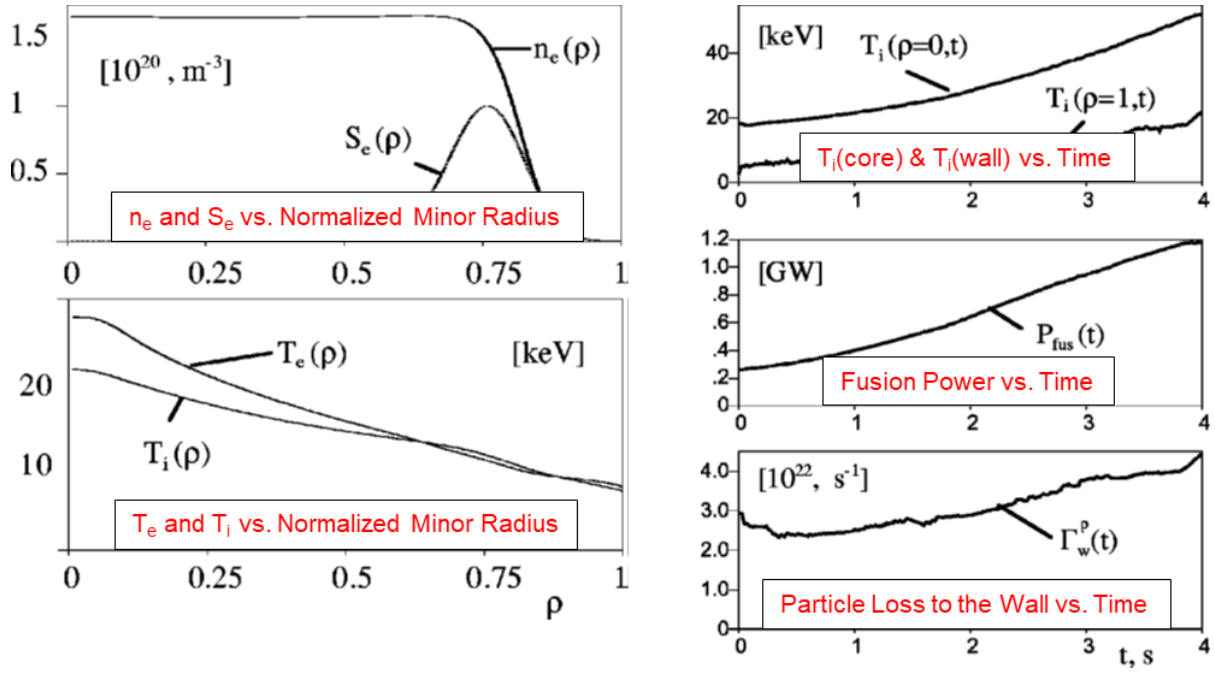

Figure 2.4: The results calculated by Krasheninnikov's group using the ASTRA transport code for an ignited Li-Wall ITER-FEAT scenario [17]. Plots on the left illustrate the density and temperature profiles as a function of the normalized minor radius, while the plots on the right look at parameters as a function of time at the wall, in the core, and averaged across the plasma cross-section.

The most important metric to take away from these results is the plot of wall particle loss rate vs. time in the bottom right of Figure 2.4. This result eliminates the need to calculate the wall flux, as was the case with Zakharov's results, and shows that the time-averages loss rate at the walls is approximately 3 x 10^{22} s^{-1}. Assuming conservatively that all of the particles lost to the walls are either D^+ or T^+ (in a 50-50 split), one can then calculate the mass loss rate of T^+ as nearly 80 mg s^{-1}. Continuing on in this calculation and assuming that the available fueling inventory of T_2 is 700 g [18], then the entire available inventory will be lost to the lithium in a little over 150 minutes (assuming negligible loss to fusion events). Apart from being significantly more reasonable, this time constraint was taken directly from Krasheninnikov's simulation results, rather than having been roughly interpreted from Zakharov's plots, lending this result more credibility than the one previously mentioned.

While it is important to consider wall retention from a theoretical point of view, it is also essential to verify these theoretical results with empirical evidence of the phenomena they describe. For the case of Zakharov [16] and Krasheninnikov [17], they predicted a drastic increase in the temperature profile across the whole minor radius and a drastic reduction in the density and, by extension, particle loss rate at the wall. Maingi, et al. [19], found similar results in NSTX after the introduction of a lithium coating on the plasma-facing components. These results can be seen in Figure 2.5.

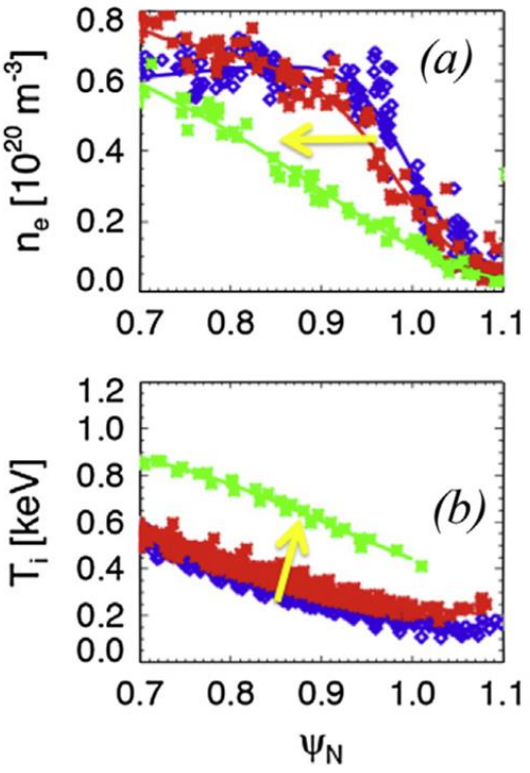

Figure 2.5: Shifts in the density and ion temperature profiles as a function of minor radius in NSTX, normalized to the outermost position of the separatrix [19]. The green trends represent the discharge with the highest amount of pre-discharge lithium coating. The variable Ψ_N is the minor radius normalized to the position of the separatrix.

The Li-Wall regime is obtainable primarily because of the ability of liquid lithium to act as a perfectly absorbing particle boundary. Other factors that help enhance plasma stability in the

Li-Wall regime are minimized core impurity transport (since Li is likely to consume many of these impurities and/or protect the high-Z structural materials) [20] and reduced excitation of peeling-ballooning and resistive-wall instabilities (since the plasma pressure is not limited by the pedestal, and Li is a highly conductive boundary) [21]. With regards to the absorbing boundary characteristic, low energy particles at the edge interact with hot, outward-diffusing ions with an almost negligible probability, so the ion temperature profiles remain elevated, in stark contrast to the H-mode discharges that use high-Z material walls. The density at the edge is reduced due to lithium's ability to absorb D^+ and T^+, along with a number of other impurity species.

The enhanced temperature profile is of greatest significance when considering future reactor scenarios. As one can see from the plot in the lower left section of Figure 2.4, the ion temperature profile does decrease with increasing minor radius, but only to the point where T_i at the wall is only slightly less than 10 keV. Because of this, an appreciable number of D-T fusion reactions can happen over the entire plasma cross-section, so a smaller vessel can theoretically produce the same P_{fus} as a larger vessel with high-Z material walls. This is important in making fusion power production economically viable.

2.1.3 The Kinetics and Thermodynamics of Isotope Recovery

While lithium PFC research is widespread due to its advantages as a plasma-facing material, little has been done to look at the tritium recycling and the associated practicality. A few studies have looked at recycling tritium through chemical [22], physical [23], or thermal [24] means, but the existing technologies have insufficient recovery rates and the proposed technologies have yet to be tested. These technologies will be discussed later in this chapter. This thesis aims to construct and test reclamation technologies that use heat as the primary driver.

In order to determine the best fuel recycling method that uses thermophysical properties of the Li-D(sol)-T(sol)-LiD-LiT matrix for recovery, one must first understand the underlying chemical thermodynamics. The thermodynamics are principally governed by the bond energies between the Li and D and between the Li and T, and what product yields the lowest energy state solution. Armed with this knowledge, the next step is to look at the kinetics for recovery while taking into account any competing reactions that may inhibit hydrogen isotope evolution.

2.1.3.1 Thermodynamics of the Li-LiH, Li-LiD, and Li-LiT Systems

Bond energies for Li-H and Li-D systems have been documented [25, 26], but little is known about the bond energy for the Li-T system, primarily because of the radioactive nature of tritium. The IUPAC standard for the bond energy is the average value for gas-phase chemical dissociation for all bonds of the same type within the same chemical species. The bond dissociation energy, on the other hand, is the energy required to break one specific type of chemical bond. For instance, the bond dissociation energy for the first C-H bond in methane, CH_4, is different than the bond dissociation energy for the second C-H bond in methane, while the bond energy for the C-H bond in CH_4 is the average of all four bond dissociation energies. Fortunately, the bond energy for singly-bonded systems such as the Li-H system are the same as the dissociation energy.

The thermodynamics for the Li-LiH and Li-LiD systems were explored by Adams, et al. [27, 28] and Veleckis, et al. [29-32] in the 1970s. Adams' group looked at the solubility dynamics for binary systems of Li-LiH and Li-LiD with low atomic fractions of hydride or deuteride [28]. To estimate the solubility of the lithium salt within the molten lithium, the group looked at the change in resistivity in these low-salt-concentration mixtures and found that miscibility in low concentrations can be directly correlated to the resistivity of the mixture up to the saturation point at various temperatures. These measurements, however, fell short when predicting the delineation of phases beyond approximately a few mol % LiH or LiD. The results of Adams' report are important for determining the fraction of absorbed D^+ or T^+ particles that remain dissolved as opposed to those that covalently bond to form the deuteride or tritide salt. Adams was able to determine a relationship between the dissolved hydrogen mole fraction and temperature based on the electrical information in his melt samples, described in Eq. 2.2, where x_h is the mole fraction of dissolved hydrogen and T is the temperature in K. The resistivity results will be discussed again in detail later in this report. An example plot illustrating a single isotherm at 400 °C relating the resistivity change vs. salt concentration can be seen in Figure 2.6.

$$log_{10}\, x_h = 1.523 - \frac{2308}{T} \tag{2.2}$$

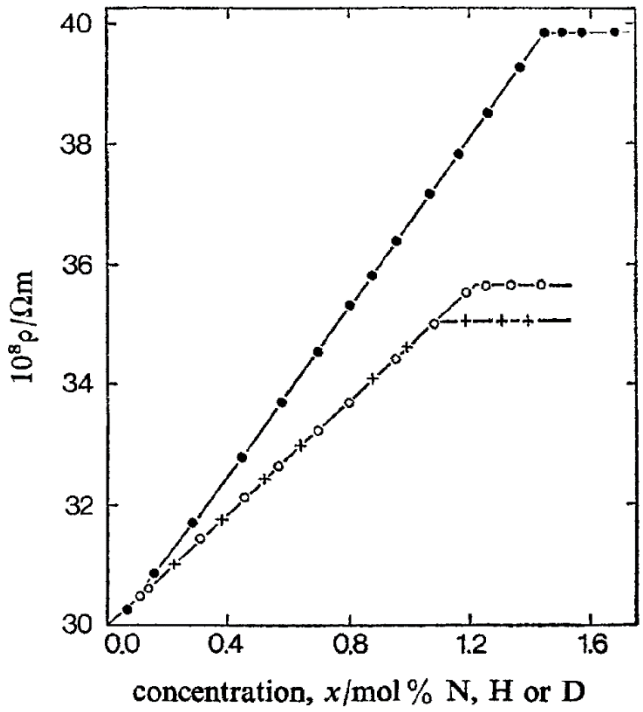

Figure 2.6: Data gathered by Adams, et al. [27] that relates the resistivity for binary mixtures of Li-Li_3N, Li-LiH, and Li-LiD. These solutions looked at the contribution of nitride (●), hydride (○), and deuteride (+) to the electrical properties of the mixture. Adams' group only looked at measuring the electrical properties of mixtures with low atomic fractions of dissolved lithium salts. The flat lines present in each trend are indicative of the saturation point in each mixture at 400 °C.

Independently of Adams' group, Katsuta's group [33] and Yakimovich's group [34] also investigated the maximum solubility concentrations for LiH and LiD in liquid Li. Katsuta used equilibrium plateau pressures as a function of temperature and correlated these values to the amount dissolved within the solution using Sieverts' Law. Their investigations also led to the determination of the thermodynamic values for the enthalpies of solution for LiH dissolved in lithium. More recently, Yakimovich's group was able to determine a more thorough relationship for the critical LiH, LiD, and LiT mole fraction for solubility, with the form [34]:

$$\ln x = A + B\left(\frac{1}{T} - \frac{1}{T_M}\right) + C\ln\left(\frac{T}{T_M}\right) \tag{2.3}$$

where x is the mole fraction of LiH, LiD, or LiT in solution, T is the temperature in K, and T_M is the monotectic temperature for the LiH, LiD, or LiT salt. The constants A, B, and C are all semi-empirical values based on which isotope is being considered. For the Li-LiH system, Yakimovich determined the constants to have the values of -1.517 for A, -3998 K^{-1} for B, and 3.004 for C, with a T_M of approximately 961 K (688 °C). The application of Yakimovich's relationships will be explained in further detail in Chapter 5.

The group led by Veleckis thoroughly investigated a number of the thermophysical properties of the Li-LiH, Li-LiD, and Li-LiT systems at Argonne National Laboratory in the 1970s [29 – 32]. For the Li-LiH and Li-LiD systems, Veleckis' group was able to determine the miscibility gap between the Li-rich and LiH-rich (or LiD-rich) solution, the equilibrium constant for the reactions described in Eqn. (2.4) and Eqn. (2.5), and the activity coefficients that correspond to the solutions for the Li-rich and LiH-rich (or LiD-rich) phases. Measurements were done in an isolated system held at constant temperature where pre-treated samples of Li were exposed to controlled H_2 or D_2 environments. Equilibrium between the gas and the solution was achieved when there was no longer a pressure drop in the sample. It is important to note that in these experiments, system temperatures were always held above the monotectic temperature in order to inhibit the formation of a limiting/shielding hydride (or deuteride) layer. While there are quite a few important points to take away from Veleckis' early work, one of the more impressive results was the determination of the miscibility gap, where two phases co-exist in a solution and the mixture is not homogeneous. The miscibility gap data can be seen in Figure 2.7.

$$\frac{1}{2}H_2\left(g, T, P_{H_2}\right) + Li\left(soln, T, P_{H_2}\right) \leftrightarrow LiH(soln, T, P_{H_2}) \tag{2.4}$$

$$\frac{1}{2}D_2\left(g, T, P_{D_2}\right) + Li\left(soln, T, P_{D_2}\right) \leftrightarrow LiD(soln, T, P_{D_2}) \tag{2.5}$$

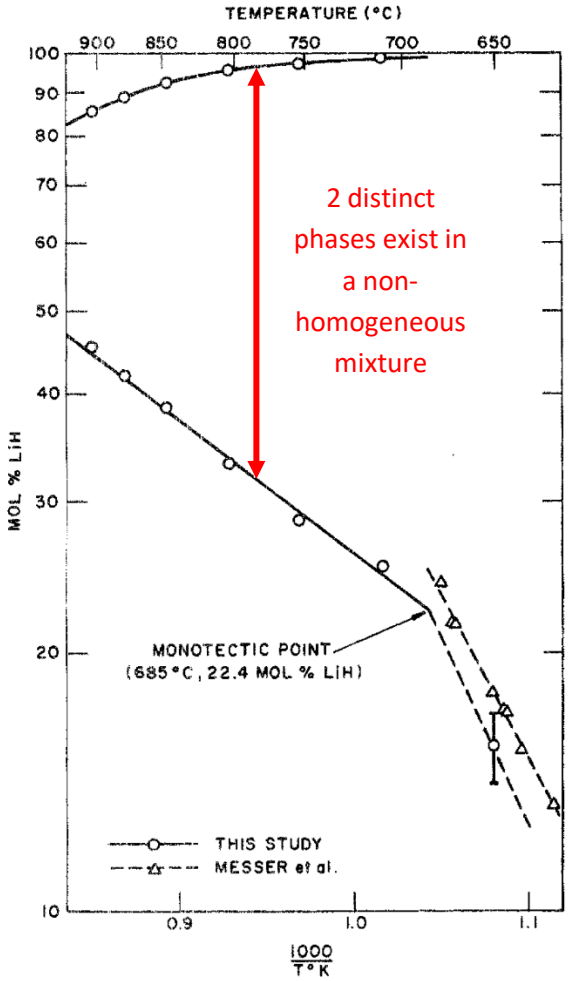

Figure 2.7: The miscibility gap in the Li-LiH system as reported by Veleckis, et al. [29]. All data reported are above the monotectic temperature for the solution. These data indicate the solubility of the dilute phase in either the Li-rich or LiH-rich phase. The two phases that exist simultaneously are the dissolved LiH in Li and the solid, precipitated LiH.

Interestingly enough from the data plotted in Figure 2.7, it appears as if even below the monotectic temperature that relatively high atomic concentrations of the hydride can remain dissolved in the mixture, contrary to the work established by Adams' group where upper solubility limitations appeared to halt the changes in resistivity. These data were not considered to be accurate by Veleckis' group, however, since shield layers of hydride on the surface of the lithium sample could impede progress toward equilibrium. Because the data presented in Veleckis' earlier work was only representative of dissolution in solutions above the monotectic temperature,

T_m, more work was required to investigate solubility limitations and phase separations below these temepratures. Veleckis' group approached this by starting with a solution at T_m with a known concentration of dissolved LiH or LiD. Melt samples were then withdrawn from the bulk at various temperatures below T_m, and the H or D concentrations were determined from thermal decomposition analysis, whereas the amount of Li in the sample was determined using titration. Figure 2.8 illustrates Veleckis' findings from these experiments as a conventional phase diagram [31]. The global eutectic for the Li-LiH and Li-LiD phase diagram shown at the temperature of 180.3 °C defines the most stable mixture of phases, but also illustrates that even in solid lithium there will remain a finite amount of hydrogen, meaning that completely pure lithium is likely impossible in systems where lithium is irradiated by hydrogen isotopes.

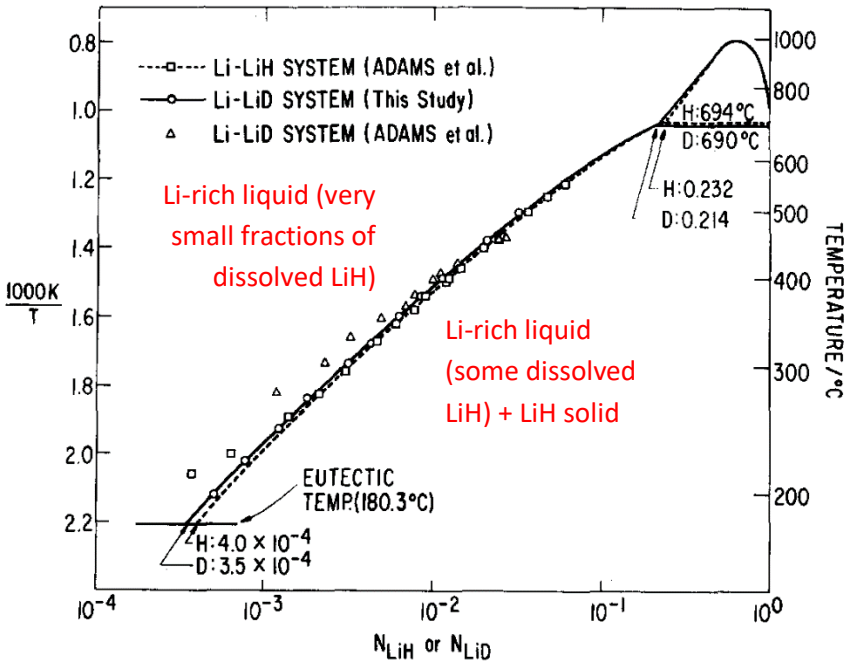

Figure 2.8: The phase diagrams for the Li-LiH and Li-LiD systems reported by Veleckis, et al. [31]. The plot is skewed toward the lower-concentration solutions by using a logarithmic abscissa, since this is the region of interest for fusion systems. Solubility data can be gathered from this plot by investigating the temperature and concentration along the liquidus curve.

During his extensive investigations, Veleckis was able to determine the standard free energies of formation for the salts of each hydrogen isotope [32]. These semi-empirical equations took on the form:

$$\Delta G_f^0(LiH) = 19.76 \times 10^{-3}\, T - 22.63$$

$$\Delta G_f^0(LiD) = 20.30 \times 10^{-3}\, T - 22.73 \qquad (2.6)$$

$$\Delta G_f^0(LiT) = 20.64 \times 10^{-3}\, T - 22.82$$

where ΔG_f^0 is the standard free energy of formation in kcal mol^{-1}, and T in K. What these values relate is how energetically favorable the formation of the salt is at any given temperature. Favorability comes with the reduction in the free energy, so as the temperature increases the production of the salt for each isotope becomes less favorable. This reduction in favorability for salt formation is what separates the dissolved phase from the precipitate, especially in the range between the eutectic and monotectic for each system.

Worth mentioning in the context of the work presented throughout this whole document is the difference between the different hydrogen isotopes. What is claimed in the body of this work is that the use of hydrogen sufficiently represents systems that are fully or partially composed of deuterium and/or tritium. What separates these three isotopes from a chemical standpoint is not only mass, but the degree at which nuclear screening affects valence chemistry. The higher the isotope mass, the more the positive charge at the nucleus is screened from the electron. This screening affects nearly all of the properties of the material. This trend is evident in Veleckis' work [32], where lithium tritide has the greatest standard free energy of formation dependence on temperature out of all three isotopes. On top of this, the monotectic temperature (T_M) for lithium tritide is lower than for lithium deuteride and lithium hydride [32]. What can be said about the use of hydrogen and lithium hydride as the surrogate is that use of this isotope will yield conservative results.

The most important conclusion to draw from this final culmination of Veleckis' work was that even at the lowest point on the phase diagram (at the eutectic), incredibly small fractions of hydrogen, deuterium, and, by extension, tritium would remain dissolved in the solution [31]. In this case, it appears that atomic fractions in excess of 100 ppm will persist even below the melting

point of pure lithium. Therefore, conventional cold traps will be hard-pressed to fully precipitate out lithium tritide and/or lithium deuteride from an effluent lithium stream, and equilibrium concentrations may need to be considered for a fully-actualized liquid lithium loop. These thermodynamic limitations will also inform treatment options for tritium recovery, specifically with regards to startup. More information on the specifics of the thermodynamic information reported in these studies is found in Ref. 29 through Ref. 32.

2.1.3.2 Absorption and Solution Kinetics

The thermodynamics of the Li-LiH, Li-LiD, and Li-LiT systems inform the kinetics based on properties such as the chemical potential and the activity coefficients. Veleckis' [31] group was able to define equilibrium coefficients for the hydride, deuteride, and, by extension, the tritide systems. These coefficients help to define the solution compositions for liquid lithium, as the solvent, exposed to reactor-scale fluences of deuterium and tritium neutrals. It is important to distinguish between previous studies that looked into studies that looked at how neutral gas molecules interact with liquid lithium and those that looked at how ionized environments modify the system dynamics. Summarizing the kinetics results of Veleckis [31, 32], one can arrive at Sieverts' Law coefficients, which relates the solubility of gas in a metal as a function of temperature, for the Li-LiH, Li-LiD, and Li-LiT system [32]:

$$\ln(K_S) = -(A' + \frac{B'}{T}) \tag{2.7}$$

where K_S is the Sieverts' coefficient in units of $atm^{-1/2}$, T is the temperature in K, and A' and B' are semi-empirical constants which define the system. For the Li-LiH system, A' was found to be 6.498 and $\frac{B'}{1000\ K}$ was found to be -6.182. For the Li-LiD system, A' was found to be 6.138 and $\frac{B'}{1000\ K}$ was found to be -5.5599. In the same report, Veleckis assumed that the square root of the isotopic mass ratio of tritium to hydrogen would yield an A' value of 6.773 and a $\frac{B'}{1000\ K}$ value of -6.182. Thus, Veleckis' group was able to extend the information on rates of solubility and the equilibrium conditions that exist between gas and lithium to all hydrogen isotopes. In equilibrium conditions these rates are defined by the rate coefficients, which are related to pressure plateaus through Sieverts' Law.

In the early works of Veleckis, Adams, Hubberstay, and others [29 – 38] it was found that by comparing the pressure drop in a system in which lithium is exposed to a controlled amount of hydrogen or deuterium gas to the amount recovered from decomposition analysis, solubility limits could be found. Exposure to the gas was often carried out for days to ensure the reaction had progressed to completion. At temperatures that approached the melting point for lithium, pressure decay ceased before the lithium had fully consumed the gas at the expected 1:1 ratio, meaning that hydride or deuteride surface insulating layers were forming along the surface and preventing absorption. These two points are important with regards to lithium samples exposed to plasmas. In regards to exposure time, discrete lithium volumes will only be exposed to deuterium and tritium plasmas for brief periods. In regards to the formation of insulating layers, static liquid samples may witness the same effect, especially due to the high surface tension in liquid lithium keeping the denser precipitate from falling through the bulk.

Questions remain as to if plasmas will enhance dissolution properties in lithium, or if they will follow the solubility limits explored in these earlier works [29 – 38] and in Yakimovich's study [34]. Materials exposed to plasmas often exhibit enhanced dissolution characteristics. This concept, for instance, is the fundamental basis for how integrated circuits function. In studies surrounding liquid metals, Mundra [39] found enhancement of species solubility in welded metals, which often required post-treatment to rid the casting of the higher concentration of dissolved impurities. His work concluded that it was the presence of energetic atomic radicals that enhanced solubility at the surface, since on impact the vibrational energy of radicalized diatoms dampens. Ions do help with enhancement, but the recombination with electrons at the surface of the floating object to produce energetic neutrals is what modifies solubility. The studies by Baldwin [14] and Erents [13], while important in understanding retention, did not fully differentiate between the two phases in solution. Plasma-enhanced solubility requires investigation, since knowing the state of the hydrogen isotope within lithium is crucial when designing recovery systems.

2.1.3.3 Desorption/Decomposition Kinetics

Numerous studies have been conducted investigating how lithium absorbs hydrogen isotopes, either from a standpoint of neutral absorption or absorption from plasmas. While absorption and retention in lithium has been at the forefront of active research, considerably less

effort has been dedicated to understanding solution chemistry and hydrogen isotope recovery. The reason for the discrepancy in roles is that from a safety standpoint, much of the active work is dedicated to understanding where tritium will be trapped within a reactor. Liquid metals and the associated loops that can be used to recover trapped tritium have only recently gained substantial support since the problem of tritium trapping plagues not only liquid metal PFCs, but solid PFCs as well.

The removal of absorbed and adsorbed fuel species from a Li-H-LiH system is a two-fold process. Extraction can be divided into two separate groups: 1) extraction of hydrogen from solid LiH and other solid lithium impurities, and 2) extraction of hydrogen dissolved in lithium. To date, the most thoroughly researched method for hydrogen isotope extraction has come from chemical separation. While these methods produced promising initial results at extremely low hydrogen concentrations, it has become quite evident that the yields required for lithium operation on reactor relevant timescales are inadequate for full-scale operation. This has generated a push to focus on physical separation techniques that rely on physical and/or thermodynamic principles.

Previous work done at the International Fusion Materials Irradiation Facility (IFMIF) aimed to simultaneously solve parts (1) and (2) mentioned above. To remove tritium generated in the $^{6}Li(n,\alpha)^{3}H$ and the $^{7}Li(d,np\alpha)^{3}H$ reactions, the facility uses yttrium (Y) to chemically extract the dissolved tritium [40 – 44]. This removal mechanism has been shown to be very effective for low concentrations of dissolved tritium, but this process is very slow, even at elevated temperatures, and requires the use of other chemical species, such as acids, in a secondary system to recover the entrained hydrogenic species from the Y. The rate of total H evolution from this system was found to be 2.8×10^{-6} mol s^{-1} [44], meaning that at maximum this system can remove from a lithium stream would be about 2.8 μg s^{-1}. It should also be mentioned that this recovery rate is for all hydrogen isotopes, and the recovery of tritium alone was found to be much lower. It is also difficult to directly compare these recovery rates to loss rates, because they need to be normalized by a volume or surface area to make any valid assessment. What has been reported, however, is completely insufficient for recycling in a steady-state reactor scenario, where direct bombardment of fuel particles at the edge will lead to much higher trapped fuel concentrations in the effluent stream.

For part (1) of the two-part process described above, work performed at Lawrence Livermore National Laboratory by Dinh's group [45] helped shed light on how hydrogen will evolve from bulk LiH samples exposed, in a controlled manner, to water and/or oxygen. While this work explained the way in which impurity layers of Li_2O and LiOH will form on the surfaces of pure LiH, how these layers interact with each other, and how the hydrogen outgassing kinetics are modified by the presence of these layers, it failed to describe rates of evolution from pure LiH samples. The kinetics and thermodynamics of such a system require investigation. While some impurity is expected, exposure to oxygen and water will be limited due to the nature of the flowing liquid. Pure lithium will also act as an oxygen and water sink, and will compete with LiH in this regard.

A number of studies have been dedicated to looking at the total evolution of hydrogen from lithium. These studies do not separate the process into two sub-categories as listed above, but instead look to understand the kinetics from a global perspective. Work done by Oyarzabal's group [46] looked at establishing degassing rates by exposing molten lithium samples and samples that had been pre-deuterated to varying pressures of hydrogen gas. Pressure decrease and thermal desorption spectroscopy (TDS) were used to look at magnitudes and rates of hydrogen uptake, but none of these samples were exposed to energetic particles. Desorption rates were also not reported in their findings. Capece's group [47] looked at how the presence of oxygen impurities on ultra-thin lithium films affects the desorption kinetics for deuterium that strike the surface as an ion beam. They found that pre-oxygenated films released hydrogen more readily at lower temperatures, showing the activation energy needed to separate hydrogen trapped or reacted by Li_2O is lower than that needed to separate hydrogen trapped by pure Li. The chemistry and diffusion properties in thin films are significantly different than in bulk systems, however, and may not hold up as applied to lithium samples greater than a few nm in thickness. Release kinetics were also not fully explored in these analyses. Capece's results are summarized in Figure 2.9.

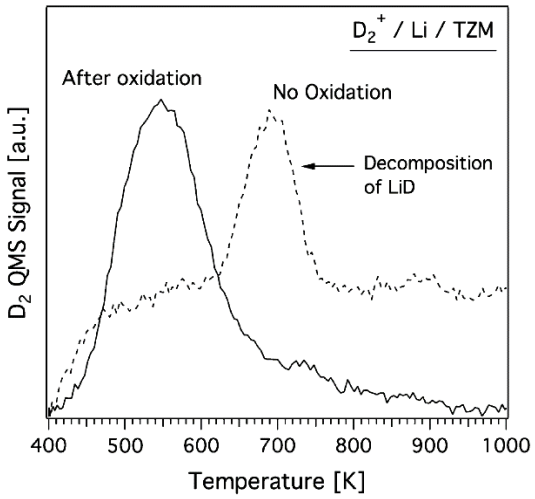

Figure 2.9: Summarizing results of the work done by Capece, et al. [47]. The presence of oxygen in these samples drastically reduces the activation energy for thermal release of deuterium.

In the work he did to evaluate the degree to which deuterium is absorbed in lithium samples in the PISCES-B experiment, Baldwin [48] also investigated evolution rates from the surfaces of these samples using TPD and decomposition analysis. The doses to the samples in this study were varied, ranging from less than 1% of the saturation value up to saturation (with saturation being defined as the point at which the atomic fractions of deuterium and lithium in the sample are equal at a 1:1 ratio), as illustrated in Figure 2.2. This allowed him to study solutions were deuterium existed in both the dissolved phase and as a precipitate. Baldwin was able to observe a clear difference in his TPD spectra between the α phase (LiD dissolved into solution) and the β phase (solid LiD precipitate). During desorption, deuterium would be released from the α phase first. Once the deuterium in this phase had been sufficiently depleted, the partial pressure would fall to a plateau where the dissolution of the β phase acted as the sole source of deuterium. These plateaus were found to be predicted by earlier works investigating the thermodynamics of Li-LiD solutions [31, 32]. An example TPD spectrum this is shown in Figure 2.10. Contrary to Capece's work [47], Baldwin also found in his studies that oxygen limited uptake and took active measures to prevent contamination.

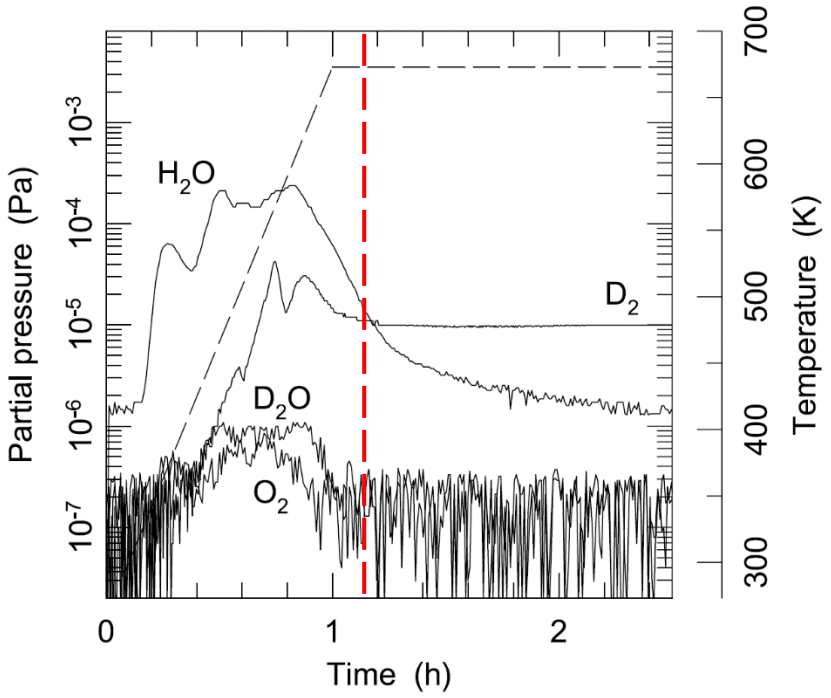

Figure 2.10: An example TPD spectrum taken by Baldwin during his investigation of the release kinetics. The vertical, dashed red line indicates the point at which Baldwin hypothesized there to be sufficient depletion of deuterium in the α phase such that the solid deuteride began to dissolve into solution, giving rise to the steady pressure plateau.

In the same study, Baldwin went on to investigate how these pressure plateaus related to deuterium liberation and the associated chemical kinetics [49]. In a single sample that had been irradiated with a dose equivalent to 80% saturation, he looked at a series of consecutive pressure plateaus at different temperatures, as illustrated in Figure 2.11. These pressure plateau values were then related to D_2 fluxes, and then to surface recombination rate coefficients through the equation [48, 49]:

$$K_r\ (m^4\ s^{-1}) = 2.63 \times 10^{24}\ (\kappa_0)^{-2}\ \sigma\ (2MT)^{-1/2}\ e^{[2(E_s - E_c)]/kT} \qquad (2.7)$$

where K_r is the surface recombination rate coefficient, κ_0 is the prefactor in Sieverts' constant, σ is a constant proportional to the surface site availability, M is the mass of the of the diffusing atomic species, T is the solution temperature, E_s is the enthalpy of solution, E_c is the activation energy for chemisorption at the surface, and k is the Boltzmann's constant.

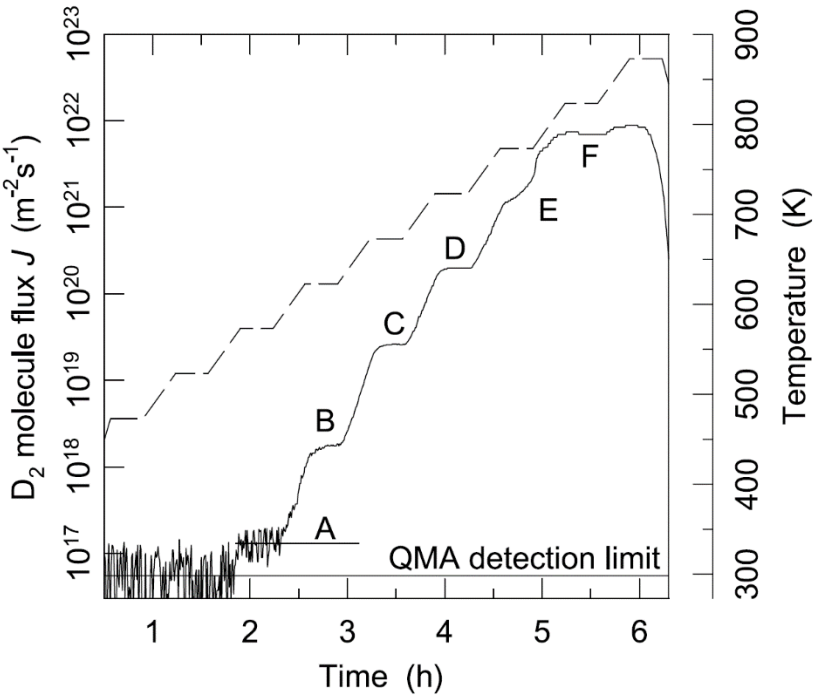

Figure 2.11: Baldwin's investigations of the constant pressure plateaus and release fluxes as functions of temperature [48].

In his conclusions, Baldwin surmised that surface recombination is the limiting factor for isotope evolution, and that only the deuterium from the α phase could be released. Rate coefficients were lower than what was predicted when assuming unity for surface site availability, but seemed relatively invariant to the chemisorption potential. While this information is quite useful from a fundamental perspective, the main take-away from this study was that in solutions where both dissolved deuterium and the deuteride salt existed, two desorption phases were witnessed – one pertaining to the release of deuterium in the α phase and one pertaining to dissociation and subsequent release from the β phase. When investigating the ability to balance loss to the wall, distinguishing between the fluxes from each phase will prove pivotal in designing recovery systems.

2.1.4 Lithium Loops and Recovery Techniques

Lithium has been considered a candidate material for a number of sub-systems in future reactors for quite some time now. Early work investigated the use of lithium as a blanket material, and has thus led to studies surrounding neutron interactions with the lithium-6 and lithium-7 isotopes, and how these interactions breed tritium [40 – 44]. Only recently has lithium garnered support throughout the community as an alternative first wall material. No matter what sub-system lithium is being used for, one thing remains clear: tritium must be separated from the lithium and recycled back into the reactor. This section will describe a few of the loop schemes that have been constructed and tested, and those that have been proposed. While tritium separation remains important in all of these devices, lithium flow velocities and characteristics were also taken into consideration.

2.1.4.1 Tested Loops and Recovery Schemes

In the case of systems where liquid lithium flows through its confining structure very slowly (essentially maintaining a static supply of lithium at the plasma-facing surface), the most thoroughly investigated are those that use capillary forces in the liquid metal to drive movement. The Capillary Porous System (CPS) [50, 51] takes advantage of the surface tension and capillary action of liquid lithium to constantly replenish the lithium on the surface that gets eroded at the plasma-material interface. As mentioned before, the lithium that erodes establishes a vapor cloud directly above the structure that helps to disperse incoming particle and heat fluxes. The CPS containment structure is also actively cooled to help reduce the impact of both steady-state and transient heat loads. A diagram in Figure 2.12 illustrates how the CPS system provides a constant, static, lithium surface at the plasma interface in a reactor setting.

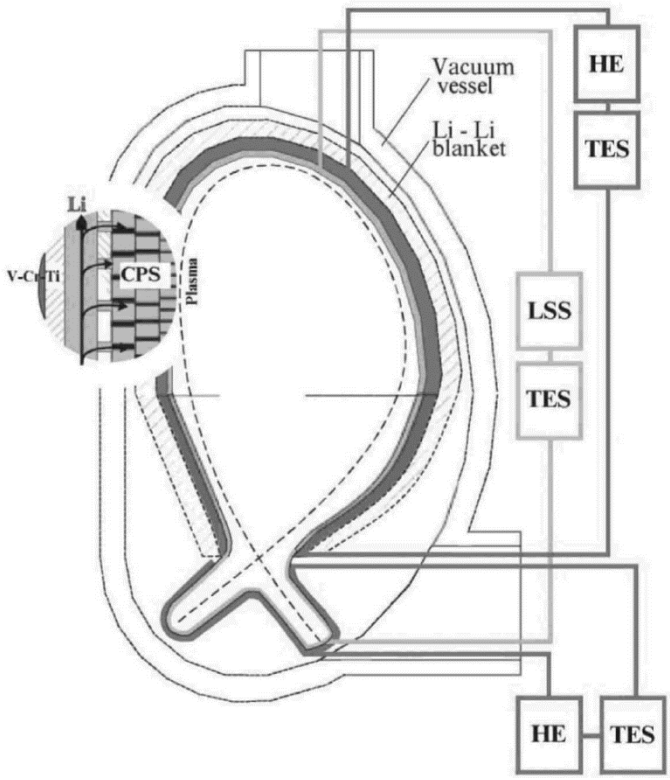

Figure 2.12: An image depicting how the CPS system would work in a classical fusion reactor system, like that of the T-11M tokamak [51]. Lithium will flow along a back channel, but will be forced through narrowing capillary channels as lithium surface layers are eroded. The acronyms HE, TES, and LSS stand for Heat Exchanger, Tritium Extraction System, and Lithium Supply System, respectively. Two separate collection loops are depicted for the first wall vs. divertor components.

Critics of the CPS system are concerned with a few items that proponents of the structure need to address before applying it to large-scale devices. First, lithium passivates quickly in the presence of impurities like oxygen, nitrogen, carbon, and hydrogen [52]. Passivation of a static surface like that provided by the CPS system can inhibit flow and nullify the benefits provided by clean lithium. Local and global re-deposition of lithium is also a concern because numerous surfaces within the vessel would be obstructed by the presence of lithium. This is true only in the case that the entire vessel wall was not already completely covered by lithium. Finally, deuterium and tritium retention is the greatest concern for this type of PFC. Lithium and its impurity products (lithium hydride, lithium oxide, lithium hydroxide, etc…) are efficient at retaining hydrogenic

species [13 – 15]. Future reactors will have limitations on their total on-site tritium inventories, so tritium fuel captured in a slow-flow lithium system negatively impacts this inventory since the system was designed to contain the lithium entirely within the vessel. The supply of tritium is also limited globally, where on-site inventories are meant to reflect resource limits. To recycle the tritium, the reactor will have to undergo a maintenance period to degas the entrained fuel, which will be costly for a power-producing utility. It is also impractical to heat the entire vessel to the temperatures needed to desorb the fuel.

A few institutions have researched and/or constructed fully circulating lithium loops either as a part of testing fast-flow lithium wall components or as a means of treating lithium blanket materials. Unfortunately, none of these loops systems have been dedicated purely to the removal of dissolved hydrogen isotopes on fusion reactor-relevant timescales. One of the most advanced and actively researched of these systems is that at IFMIF [40 – 44], introduced in Section 2.1. An overview of the IFMIF design and its validation from an engineering standpoint can be found in Ref. 44. As is the case in many of the loop designs, electro-magnetic probes are used to drive flow as fast as 15 m/s. Other aspects of this loop include lithium purifications systems, such as a mist trap, distillation columns using meshes instead of condensation stages, and an yttrium trap.

Of the loop and recovery schemes tested, the IFMIF system is widely considered to be the most established. As mentioned earlier, however, investigations on IFMIF are based entirely on the principals of neutronics and nuclear interactions, so the doses of tritium in the lithium stream are far less than those expected at the plasma-material interface within the reactor vessel. As mentioned above, tritium recovery in this system is quite limited, but chemical extraction may prove useful in far-from-saturated solutions. The effectiveness of the yttrium hot trap was explored in Ref. 43. The effectiveness of other chemical extraction techniques will be explored later in this report.

The Flowing Lithium Retention Experiment (FLiRE) [53, 54] was constructed at the Center for Plasma-Material Interactions at the University of Illinois to study helium ion and deuterium neutral retention in flowing lithium. Exposures to gas resulted in an inhibited deuterium uptake, which was considered to be limited by dissociation of the diatomic bond at the lithium surface. Since absorption kinetics were limited, deuterium recovery also suffered; however, it is worth mentioning FLiRE under the umbrella of loop and retention technologies.

The flow technology for in-vacuo, direct current, electro-magnetic pumps has been proven effective for the small lithium loop used with the Flowing Liquid Lithium (FLiLi) limiter on the EAST tokamak [55]. While the goal of the FLiLi system was to test retention characteristics for a limiter module in EAST, these results have yet to be evaluated. An assembly image of the FLiLi limiter plate with emphasis on the electromagnetic pump is shown in Figure 2.13. For a more thorough analysis of the electromagnetic drive, the author refers the reader to Ref. 56.

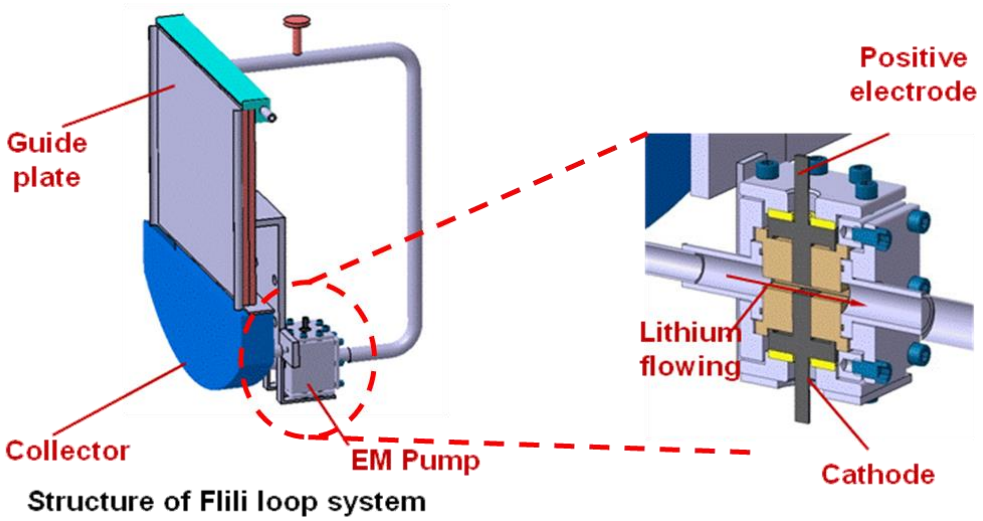

Figure 2.13: An assembly image of the FLiLi limiter PFC as it was constructed for use in the EAST tokamak [55]. Emphasis is placed on the electromagnetic drive, which will form the basis for flow in any future lithium loop system.

2.1.4.2 Proposed Loops and Recovery Schemes

Work done at the Princeton Plasma Physics Laboratory (PPPL) has assessed the efficacy of a conceptual loop design to be used in conjunction with the Radiative Liquid Lithium Divertor (RLLD) or the Active Radiative Liquid Lithium Divertor (ARLLD) [23, 56]. This assessment includes mass balance calculations, energy balance approximations, and various engineering controls for safe operation of a hypothetical tritium recovery system. The loop system proposed by Ono, et al. [57] is illustrated in Figure 2.14.

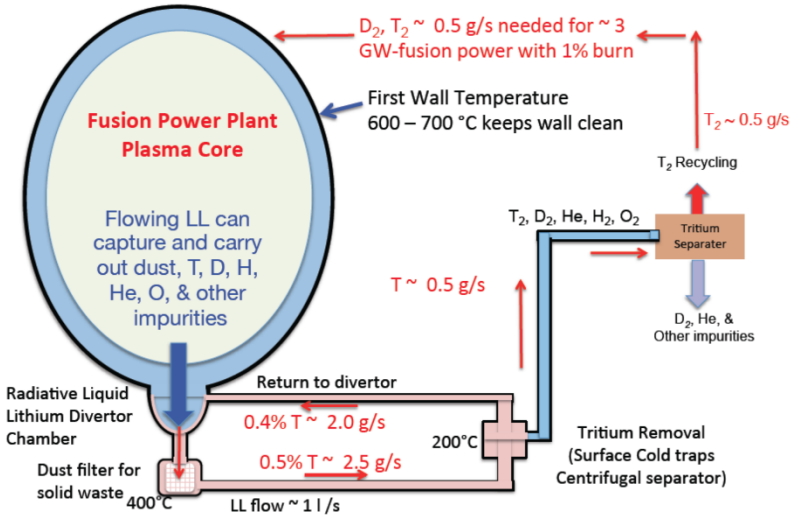

Figure 2.14: A schematic of the lithium purification loop proposed to be used in conjunction with an RLLD or ARLLD system [57].

The most important aspect of this loop design is not so much the components that make up the purification and recycling steps, but the idea that an equilibrium concentration of deuterium and tritium within the lithium must be maintained. This makes recovery more efficient, in that what is, in essence, a LiD/LiT-rich stream is being treated separately from the remaining lithium, which is recycled back to the divertor of the reactor.

The two proposed technologies for purification of the deuteride and tritide salts are a surface cold trap or a centrifugal separator, or a combination of both. Work done by Veleckis' group [32] concluded that a conventional cold trap would not be able to fully freeze out the tritide and deuteride salts. While this does remain true for far-from-saturated solutions, establishing an equilibrium concentration like that which is proposed in Figure 2.14 removes this complication, especially when the lithium is cooled to a temperature of 200 °C. To avoid issues with salt transport away from the surface cold trap, Ono [57] also proposed using a centrifuge to take advantage of the density difference between lithium and the precipitates. Centifugal separators are proven technologies and could be employed in lithium loops; however, consideration must be made for the complexity of the separator and the corrosiveness of lithium.

The use of either of these two purification techniques does not actually separate the deuterium and tritium gas that could then be used to refuel the reactor. A vital step is missing in the loop proposed in Figure 2.14, which is the principal underlying reason for the remaining body of this work. More information on the specifics of the sub-systems in Ono's loop [57] is described in Chapters 4, 5, and 6 of this report.

2.2 Motivation

While there exists a large body of research to draw from when looking at the equilibrium and chemical dynamics associated with the Li-LiH, Li-LiD, and Li-LiT systems, very little information has been gathered investigating methodologies by which entrained deuterium and tritium can be recovered and recycled back into a hypothetical fusion reactor. Lithium has already shown to be a valuable first wall material, but it will never be fully considered until research proves that tritium can be recovered from lithium at rates that balance or exceed wall losses. This fact alone is true for any wall material candidate, but liquids have a distinct advantage in this department because they can be transported away from the reactor vessel and treated externally without shutting down the reactor.

Even when focusing on liquid lithium, there exist large gaps in the fundamental knowledge of how the species that make up a plasma (ions, electrons, neutrals, and radicals) modify the surface and sub-surface chemistry for hydrogen-lithium systems. Baldwin [14], Erents [13], and Skinner [15] all showed that liquid lithium will absorb hydrogen isotopes at or near a 1:1 ratio, but these reports did not differentiate between the chemical states of the isotopes within solution. Baldwin hypothesized that the dissolved phase was the source of deuterium for evolution and the precipitate acted to replenish the deuterium lost from the dissolved phase, giving rise to the pressure plateaus described earlier. In these studies, however, very little evidence was shown that actually verified this claim and distinguished the phases. The knowledge of the solution chemistry is pivotal in understanding what loops and treatment options are required for a fully functional, lithium-walled reactor.

The primary motivation for the work presented in this report stems from the gaps in the fundamental knowledge and the necessity for the design, construction, and development of tritium

recovery technologies. The goals of this work will serve to fill, at least in part, the knowledge gaps left in previous studies, and will culminate in the design, development, construction, and proof-of-concept testing for a recovery system that uses heat as the primary driver. Results from this work will act, at minimum, as the starting point for future studies to thoroughly investigate the feasibility of recycling tritium from liquid lithium walls.

2.2.1 Primary Goals

The primary goals of this body of work are summed up in the following list, and should be considered with regards to LiMIT [1 – 5] as the plasma-facing component:

1. Investigate hydrogen release from pure lithium hydride, which will act as a surrogate material for lithium deuteride and lithium tritide. Of greatest interest are the peak evolution fluxes and the associated temperatures, activation energies for release, and information from the condensed phase that verifies these results.
2. Explore the degree by which a plasma enhances the absorption and solubility in liquid lithium, if any enhancement exists beyond that which is predicted by thermodynamic principals.
3. Identify differences between the dissolved and precipitated phases in lithium exposed to hydrogen plasmas. This also includes ascertaining what release flux pertains to each phase, and how these fluxes relate to measurable quantities during temperature-programmed desorption (TPD).
4. Design, develop, and construct a prototype hydrogen isotope recycling system that takes advantage of the thermal properties of lithium-lithium hydride solutions. The initial design will be based on the principals employed in distillation columns.
5. Explore what supplemental or alternative tritium reclamation techniques are available, apart from the yttrium hot trap used in the IFMIF facility.

2.3 References

[1] D.N. Ruzic, W. Xu, D. Andruczyk, and M.A. Jaworski. "Lithium-metal infused trenches (LiMIT) for heat removal in fusion devices," *Nucl. Fusion* 51 (2011) 10200.

[2] W. Xu, D. Curreli, D. Andruczyk, T. Mui, R. Switts and D.N. Ruzic, "Heat transfer of TEMHD driven lithium flow in stainless steel trenches", *J. Nucl. Mater.* 438(supplement) (2013) S422.

[3] W. Xu, D. Curreli, and D.N. Ruzic, "Computational studies of thermoelectric MHD driven liquid lithium flow in metal trenches," *Fusion Eng and Des.* 89 (2014) 2868.

[4] D.N. Ruzic, M. Szott, C. Sandoval, M. Christenson, P. Fiflis, S. Hammouti, K. Kalathiparambil, I. Shchelkanov, D. Andruczyk, R. Stubbers, C. Joel Foster, and B. Jurczyk, "Flowing liquid lithium plasma-facing components – Physics, technology and system analysis of the LiMIT system", *Nucl. Mater. Energy* 12 (2017) 1324.

[5] P. Fiflis, M. Christenson, M. Szott, K. Kalathiparambil, and D.N. Ruzic, "Free surface stability of liquid metal plasma facing components", *Nucl. Fusion* 56 (2016) 106020.

[6] C.N. Taylor, J.P. Allain, K.E. Luitijohan, P.S. Krstic, J. Dadras, and C.H. Skinner, "Differentiating the role of lithium and oxygen in retaining deuterium on lithiated graphite plasma-facing components", *Phys. of Plasmas* 21 (2014) 057101.

[7] C.N. Taylor, J. Dadras, K.E. Luitjohan, J.P. Allain, P.S. Krstic, and C.H. Skinner, "The role of oxygen in the uptake of deuterium in lithiated graphite", *J. Appl. Phys.* 114 (2013) 223301.

[8] P.S. Krstic, J.P. Allian, C.N. Taylor, J. Dadras, S. Maeda, K. Morokuma, J. Jakowski, A. Allouche, C.H. Skinner, "Deuterium Uptake in Magnetic-Fusion Devices with Lithium Conditioned Carbon Walls", *Phys. Rev. Lett.*, 110 (2013) 105001.

[9] T. Hino, K. Kanaya, I. Takahashi, H. Yanagihara, M. Hashiba, Y. Hirohata, K. Mori, "Gas and hydrogen ion gettering properties of lithium", *J. Nucl. Mater.* 258-263 (1998) 612.

[10] R. Kaita, et al., "Hydrogen retention in lithium on metallic walls from 'in vacuo' analysis in LTX and implications for high-Z plasma-facing components in NSTX-U," *Fusion Eng. and Des.* 117 (2017) 135.

[11] R. Majeski, "Liquid Metal Walls, Lithium, And Low Recycling Boundary Conditions In Tokamaks", *Plasma Interaction in Controlled Fusion Devices: 3rd ITER International Summer School* (2010) 122.

[12] Eirene Surface Interaction Database (particle-surface interaction data available for download). Available from: http://www.eirene.de/html/surface_data.html [accessed: January 3, 2017].

[13] S.K. Erents, G.M. McCracken, and P. Goldsmith, “Trapping of keV deuterons in lithium,” *J. Phys. D: Appl. Phys.* 4 (1971) 672.

[14] M.J. Baldwin, R.P. Doerner, S.C. Luckhardt, and R.W. Conn, “Deuterium retention in liquid lithium,” *Nucl. Fusion* 42 (2002) 1318.

[15] C.H. Skinner, J.P. Allain, W. Blanchard, H.W. Kugel, R. Maingi, L. Roquemore, V. Soukhanovskii, C.N. Taylor, “Deuterium retention in NSTX with lithium conditioning” *J. Nucl. Mater.* 415 (2011) S773.

[16] L. Zakharov, N.N. Gorelenkov, R.B. White, S.I. Krasheninnikov, and G.V. Pereversev, “Ignited spherical tokamaks and plasma regimes with LiWalls,” *Fusion Eng. Des.* 72 (2004) 149.

[17] S.I. Krasheninnikov, L.E. Zakharov, G.V. Pereverzev, “On lithium walls and the performance of magnetic fusion devices”, *Phys. of Plasmas* 10 (2003) 1678.

[18] I.R. Cristescu, I. Cristecu, L. Doerr, M. Glugla, and D. Murdoch, “Tritium inventories and tritium safety design principles for the fuel cycle of ITER”, *Nucl. Fusion* 47 (2007) S458.

[19] R. Maingi, et al., “Dependence of recycling and edge profiles on lithium evaporation in high triangularity, high performance NSTX H-mode discharges”, *J. Nucl. Mater.* 463 (2015) 1134.

[20] F. Scotti, et. al., “Core transport of lithium and carbon in ELM-free discharges with lithium wall conditioning in NSTX”, *Nucl. Fusion* 53 (2013) 083001.

[21] R. Maingi, et al., “Edge-Localized-Mode Suppression through Density-Profile Modification with Lithium-Wall Coatings in the National Spherical Torus Experiment”, *Phys. Rev. Lett.* 103 (2009) 075001.

[22] Y. Asaoka, H. Moriyama, and Y. Ito, “Equilibrium distributions of tritium in liquid lithium/molten salt systems”, *J. Nucl. Mater.* 179-181 (1991) 879.

[23] M. Ono, R. Majeski, M.A. Jaworski, Y. Hirooka, R. Kaita, T.K. Gray, R. Maingi, C.H. Skinner, M. Christenson, D.N. Ruzic, “Liquid lithium loop system to solve challenging technology issues for fusion power plant”, *Nucl. Fusion* 57 (2017) 116056.

[24] H. Moriyama, S. Tanaka, D.K. Sze, J. Reimann, and A. Terlain, “Tritium recovery from liquid metals”, *Fusion Eng. Des.* 28 (1995) 226.

[25] V.A. Zhdanov, V.V. Polyakov, and V.F. Konusov, “BOND ENERGY AND EQUATIONS OF STATE OF LITHIUM HYDRIDE”, Translated from *Teoreticheskayai Eksperimental'naya Khimiya* 10 (1974) 276.

[26] B. deB. Darwent, *National Standard Reference Data Series,* National Bureau of Standards, no. 31, Washington, 1970.

[27] P.F. Adams, M.G. Down, P. Hubberstey, R.J. Pulham, “Solutions of Lithium Salts in Liquid Lithium: The Electrical Resistivity of Solutions of Nitride, Hydride and Deuteride”, *J. Chem. Soc., Far. Trans.* 0 (1977) 230.

[28] P.F. Adams, M.G. Down, P. Hubberstey, R.J. Pulham, “SOLUBILITIES, AND SOLUTION AND SOLVATION ENTHALPIES, FOR NITROGEN AND HYDROGEN IN LIQUID LITHIUM”, *J. Less-Common Met.* 42 (1975) 325.

[29] E. Veleckis, E.H. Van Deventer, M. Blander, “The Lithium-Lithium Hydride System”, *J. Phys. Chem.* 78 (1974) 1933.

[30] E. Veleckis, R.M. Yonco, and V.A. Maroni, “SOLUBILITY OF LITHIUM DEUTERIDE IN LIQUID LITHIUM”, *J. Less-Common Met.* 55 (1977) 85.

[31] E. Veleckis, “Thermodynamics of the Lithium-Lithium Deuteride System”, *J. Phys. Chem.* 81 (1977) 526.

[32] E. Veleckis, “DECOMPOSITION PRESSURES IN THE (α + β) FIELDS OF THE Li-LiH, Li-LiD, AND Li-LiT SYSTEMS”, *J. Nucl. Mater.* 79 (1979) 20.

[33] H. Katsuta, T. Ishigai, and K. Furukawa, “Equilibrium Pressure and Solubility of Hydrogen in Liquid Lithium”, *Nucl. Technol.* 32 (1977) 297.

[34] K.A. Yakimovich and T. Biryukova, “Thermodynamic Properties of Li-LiH (LiD, LiT) Systems. The Phase Diagram” *Open J. Phys. Chem.* 2 (2012) 141.

[35] P. Hubberstey, R. J. Pulham, and A. E. Thunder, “Depression of the freezing point of lithium by nitrogen and by hydrogen”, *J. Chem. Soc. Faraday Trans.* 72 (1976) 431.

[36] C. E. Messer, "A Survey Report on Lithium Hydride." AEC Research and Developrnent Report No. NYO-9470 (1960).

[37] F. K. Heumann and O. N. Salmon, "The Lithium Hydride, Deuteride, and Tritide Systems”, USAEC Report No. KAPL-1667 (1956).

[38] E.E. Shpil’rain, K.A. Yakimovich, T.N. Medl’nikova, A. Ya. Polischuk, *Thermophysical Properties of Lithium Hydride, Deuteride and Tritide*. New York, NY: Springer Science and Business Media, 1987.

[39] K. Mundra and T. Debroy, “A General Model for Partitioning of Gases between a Metal and its Plasma Environment”, *Met. & Mat. Trans. B* 26B (1995) 149.

[40] Y. Kato, H. Katsuta, S. Konishi, M. Ogoshi, T. Hua, L. Green, and S. Cevolani, "Impurity control in liquid loop for IFMIF target facility", *J. Nucl. Mater.* 258-263 (1998) 394.

[41] J. Yagi, A. Suzuki, and T. Terai, "Nitrogen contamination effect on yttrium gettering of hydrogen in liquid lithium," *J. Nucl. Mater.* 417 (2011) 710.

[42] S. Fukada, Y. Maeda, M. Kinoshita, and T. Muroga, "Verification to recover tritium in neutron-irradiated Li by Y plate," *Fusion Eng. Des.* 82 (2007) 2152.

[43] Y. Edao, S. Fukuda, S. Yamaguchi, Y. Wu, and H. Nakamura, "Tritium removal by Y hot trap for purification of IFMIF Li target," *Fusion Eng. Des.* 85 (2010) 53.

[44] E. Wakai, et al., "Engineering validation for lithium target facility of the IFMIF under IFMIF/EVEDA project," *Nucl. Mater. Energy* 9 (2016) 278.

[45] L.N. Dinh, M.A. Schildbach, R.A. Smith, D.M. Grant, B. Balazs, and W. Mclean II, "Hydrogen Outgassing From Lithium Hydride," *Report for Lawrence Livermore National Laboratory: Nuclear Materials Research Developments* (2006).

[46] E. Oyarzabal, A.B. Martin-Rojo, and F.L. Tabarés, "Laboratory experiments of uptake and release of hydrogen isotopes in liquid lithium," *J. Nucl. Mater.* 463 (2015) 1173.

[47] A.M. Capece, J.P. Roszell, C.H. Skinner, and B.E. Koel, "Effects of temperature and surface contamination on D retention in ultrathin Li films on TZM," *J. Nucl. Mater.* 463 (2015) 1177.

[48] M.J. Baldwin, R.P. Doerner, R. Causey, S.C. Luckhardt, and R.W. Conn, "Recombination of deuterium atoms on the surface of molten Li-LiD", *J. Nucl. Mater.* 306 (2002) 15.

[49] M.A. Pick and K. Sonnenberg, "A MODEL FOR ATOMIC HYDROGEN-METAL INTERACTIONS – APPLICATION TO RECYCLING, RECOMBINATION AND PERMEATION", *J. Nucl. Mater.* 131 (1985) 208.

[50] L.G. Golubchikov, V. Evtikhin, I. Lyublinski, V. Pistonovich, I. Potapov, and A. Chumanov, "Development of liquid metal fusion reactor divertor with a capillary pore system", *J. Nucl. Mater.* 233 (1996) 667.

[51] S. Mirnov, E. Azizov, V. Evtikhin, V. Lazarev, I. Lyublinski, A. Vertkov, D. Prokhorov, "Experiments with lithium limiter on T-11M tokamak and applications of the lithium capillary pore system in future fusion reactor devices", *Plasma Phys. Control. Fusion* 48 (2006) 821.

[52] J.P. Allain, D.L. Rokusek, S.S. Harilal, M. Nieto-Perez, C.H. Skinner, H.W. Kugel, B. Heim, R. Kaita, and R. Majeski, "Experimental studies of lithium-based surface chemistry for fusion plasma-facing materials applications," *J. Nucl. Mater.* 390-391 (2009) 942.

[53] J.P. Allain, M. Nieto, M.D. Coventry, M.J. Neumann, E. Vargas-Lopez, and D.N. Ruzic, "FLIRE – flowing liquid surface retention experiment, design and testing", *Fusion Eng. Des.* 61-62 (2002) 245.

[54] R. Stubbers, W. Olczak, M. Nieto, and D.N. Ruzic, "Measurement of hydrogen absorption in flowing liquid lithium in the flowing lithium retention experiment (FLIRE)", *J. Nucl. Mater.* 337-339 (2005) 1033.

[55] J.S. Hu, et al., "First results of the use of a continuously flowing lithium limiter in high performance discharges in the EAST device", *Nucl. Fusion* 56 (2016) 046011.

[56] M. Szott (2016). Flow control and associated technologies to advance the application of TEMHD-driven liquid lithium in fusion devices (Master's Thesis). University of Illinois at Urbana-Champaign, 2016.

[57] M. Ono, M.A. Jaworski, R. Kaita, Y. Hirooka, T.K. Gray, and the NSTX-U Research Team, "Liquid lithium applications for solving challenging fusion reactor issues and NSTX-U contributions", *Fusion Eng. Des.* 117 (2017) 124.

CHAPTER 3: MOTIVATIONS AND HYPOTHESES

3.1 Motivations

As mentioned in the previous chapter, the primary motivations for this work stem from the need to recover tritium from flowing lithium at rates which balance loss within the reactor vessel at the plasma-material interface. Gaps exist in the current understanding of what the resultant surface, sub-surface, and bulk chemistry is for a lithium-hydrogen isotope system, so fundamental studies must be undertaken to aid in developing tritium recovery design criteria. Of particular interest are the fluxes of hydrogenic species emanating from the surfaces of lithium and at what temperatures the maximum of these fluxes occurs. At the end of Chapter 2, a list of goals was presented and will be re-iterated below:

1. Investigate hydrogen release from pure lithium hydride, which will act as a surrogate material for lithium deuteride and lithium tritide. Of greatest interest are the peak evolution fluxs and the associated temperatures, activation energies for release, and information from the condensed phase that verifies these results.

2. Explore the degree by which a plasma enhances the absorption and solubility in liquid lithium, if any enhancement exists beyond that which is predicted by thermodynamic principals.

3. Identify differences between the dissolved and precipitated phases in lithium exposed to hydrogen plasmas. This also includes ascertaining what release flux pertains to each phase, and how these fluxes relate to measurable quantities during temperature-programmed desorption (TPD).

4. Design, develop, and construct a prototype hydrogen isotope recycling system that takes advantage of the thermal properties of lithium-lithium hydride solutions. The initial design will be based on the principals employed in distillation columns.

5. Explore what supplemental or alternative tritium reclamation techniques are available, apart from the yttrium hot trap used in the IFMIF facility, and which of these available techniques are feasible for use in a reactor-relevant lithium loop.

While this list is not exhaustive, it does give direction to this work. The goal of constructing an isotope recovery system will act, at minimum, as the starting point for future studies to thoroughly investigate the feasibility of recycling tritium from liquid lithium walls.

3.2 Hypotheses

Based on the extensive literature review on tritium retention in and recovery from lithium in Chapter 2 and preliminary work carried out prior to the experiments in this report, a few hypotheses have been developed to guide this work. Experiments will be developed and systems will be designed with the goal of proving or disproving these claims, as will the analysis of the results. The hypotheses are:

1. *Release fluxes of molecular hydrogen from the surface of pure lithium hydride (acting as a surrogate for lithium deuteride and lithium tritide) will be high enough to compensate tritium losses at the walls of a hypothetical Li-Wall reactor.*
2. *Lithium samples exposed to hydrogen plasmas will act as perfectly absorbing boundaries, and these samples will exhibit behavior corresponding to enhanced dissolution chemistry. Condensed phase analyses will allow for the delineation between dissolved hydrogen and precipitated hydride. Recovery fluxes from the dissolved phase alone will not be high enough to compensate tritium losses at the walls of a hypothetical Li-Wall reactor.*
3. *A tritium reclamation design based on the principals of induction heating, fractional distillation, and lithium condensation stages from the Lithium Vapor Box* [1] *will be able to sufficiently recover hydrogen from lithium hydride-rich solutions fast enough for fuel replenishment. This design will be developed in the context of the lithium loop proposed by colleagues at PPPL* [2]*, along with the use of the LiMIT PFC operating as a divertor* [3].
4. *The use of techniques that either supplement or replace heat as the primary impetus for hydrogen isotope release will allow for the appropriate levels of tritium recovery from far-from-saturated lithium-hydrogen solutions.*

3.3 References

[1] R.J. Goldston, R. Myers, and J. Schwartz, "The lithium vapor box divertor", *Phys. Scripta* T167 (2016) 014017.

[2] M. Ono, R. Majeski, M.A. Jaworski, Y. Hirooka, R. Kaita, T.K. Gray, R. Maingi, C.H. Skinner, M. Christenson, and D.N. Ruzic, "Liquid lithium loop system to solve challenging technology issues for fusion power plant", *Nucl. Fusion* 57 (2017) 116056.

[3] D.N. Ruzic, W. Xu, D. Andruczyk, and M.A. Jaworski. "Lithium-metal infused trenches (LiMIT) for heat removal in fusion devices", *Nucl. Fus.* 51 (2011) 10200.

CHAPTER 4: HYDROGEN EVOLUTION FROM LITHIUM HYDRIDE

Recovery of hydrogen isotopes, such as deuterium and tritium, from liquid lithium requires knowledge of several governing physical and chemical phenomena. Because the technologies proposed in this thesis are primarily driven by thermophysical principles, it is of the utmost importance to understand what combination of liquid or liquid/solid treatment options will produce the greatest tritium recovery in the shortest amount of time. To do this, the fundamentals must be well understood, meaning that information such as solution thermodynamics, evolved gas dynamics, chemical kinetics and composition, and thermal drive must be taken into careful consideration.

One of the principle components of this research is to understand what happens to the Li-LiD-LiT-D(soln)-T(soln) when the phases are treated as separated streams and what happens when they are treated together. This chapter will focus on the evolution of hydrogen from lithium hydride as a surrogate for deuterium and tritium evolving from lithium deuteride and lithium tritide. The results from this work will help to inform tritium recovery when two distinct phases can be treated separately.

4.1 Background

In exploring tritium recovery options that are available to the fusion community, it is important to look at each from a standpoint of the extremes. The two extremes are the cases where the solution is saturated with hydrogen, as will be discussed in this chapter, and where the solution has so little hydrogen that no hydride will precipitate out no matter the phase or condition. In this chapter, the extreme that is explored is that which surrounds the recovery of hydrogen from pure lithium hydride, which acts as a surrogate for deuterium and tritium recovery from lithium deuteride and lithium tritide, respectively. While several studies have been aimed at understanding lithium-lithium hydride, lithium-lithium deuteride, and lithium-lithium tritide mixtures and their governing thermodynamics, very little has been done to take a closer look at how and at what rate hydrogen is released from pure lithium hydride as a function of temperature.

Work done in the late 1960s early into the 1970s helped to define the landscape for the systems where lithium interacted with hydrogen, deuterium, or tritium. Some of the most defining

work was published by Veleckis' group [1 – 4] at the Argonne National Laboratory, which aimed at defining the phase diagram for the lithium-lithium hydride and lithium-lithium deuteride systems above and below the monotectic temperature for each system. The work done to achieve this is essentially based on isotherms (in the pressure-phase space) collected versus composition that would then allow one to define the miscibility gap boundaries along the phase diagram. It is important to note that these isotherms were collected to determine composition above the montectic (LiH melting) temperature, whereas later work done by Veleckis' group looked at the solubility of hydrogen and deuterium gas in pure lithium using thermal decomposition analysis. Veleckis' group also compiled results from a number of other studies [5 – 15] to support their claims and to define the phase boundary illustrated in Figure 4.1.

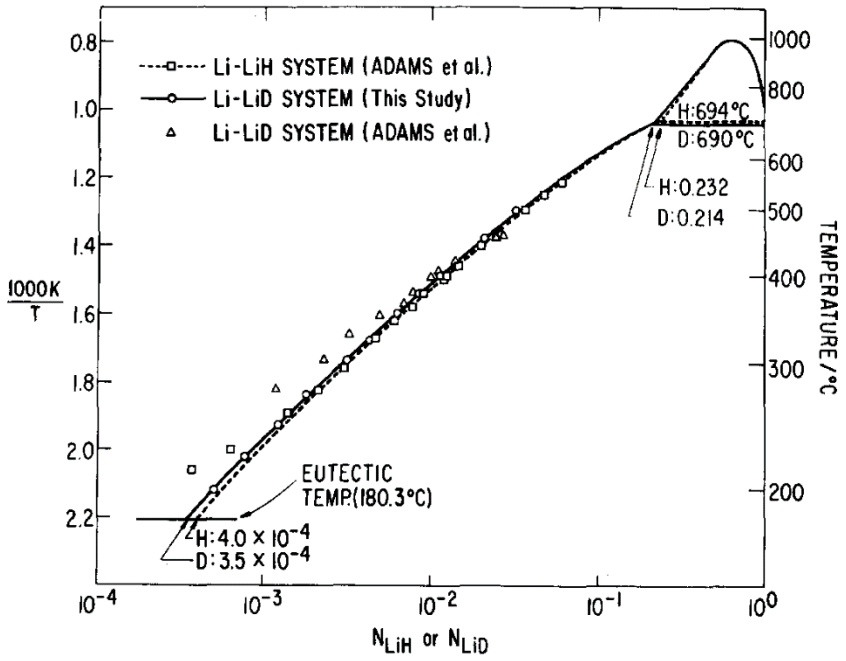

Figure 4.1: An image of the phase diagram for the lithium-lithium hydride and lithium-lithium deuteride systems with the abscissa in logarithmic scale [3].

As mentioned in Chapter 2, Adams' group looked at understanding the same phase boundary as Veleckis' group, but by using measurable quantities in the condensed phase to describe solubility limitations [16, 17]. This was done through the measurement of resistivity across a lithium sample at a given temperature mixed with various small but finite quantities of

lithium hydride. The conclusions about solubility offered by Adams' group, Veleckis' group, and all other related studies performed in these early works are important when relating melt concentration to thermal decomposition and the chemical pathways taken on the way to breaking the system down into the lithium and hydrogen, deuterium, or tritium constituents. Specifically, the conclusion described in one of Veleckis' studies [3] states that conventional cold traps will never be able to fully remove hydrogen isotopes from liquid lithium, as some will remain present within the metal matrix even well into the solid phase, as seen by the "Eutectic" line drawn in Figure 4.1. While these studies shed light on the relationship between lithium and hydrogen, deuterium, and, by extension, tritium, little is done in these studies to specifically look at decomposition rates as a function of temperature and composition.

Probably the most extensive study undertaken to investigate the thermal decomposition of lithium hydride was that performed by Dinh's group at the Lawrence Livermore National Laboratory [18]. Because nearly all metallic environments will grow a native oxide layer due to the fact that water is always present in nearly all systems (even within vacuum environments), Dinh's group set out to determine how hydrogen gas is created from samples of lithium hydride that were exposed to varying degrees of a controlled water (H_2O) atmosphere. Work done prior to that performed by Dinh's group described how lithium oxide (Li_2O) acts as a buffer layer and rests between the lithium hydride (LiH) and lithium hydroxide (LiOH) layers [19 – 22]. The formation of each of these layers and how they compete with each other can be summed up in the following chemical reaction mechanisms:

$$LiH(s) + H_2O(l) \leftrightarrow LiOH(aq) + H_2(g) + heat \tag{4.1.1}$$

$$2LiH(s) + H_2O(g) \rightarrow Li_2O(s) + 2H_2(g) + heat \tag{4.1.2}$$

$$Li_2O(s) + H_2O(g) \rightarrow 2LiOH(s) + heat \tag{4.1.3}$$

$$LiOH(s) + H_2O(g) \rightarrow LiOH \cdot H_2O + heat \tag{4.1.4}$$

$$LiOH \cdot H_2O \rightarrow LiOH(s) + H_2O(g) \tag{4.1.5}$$

$$2LiOH(s) \rightarrow Li_2O(s) + H_2O(g) \tag{4.1.6}$$

where the first reaction mechanism described in Equation (4.1.1) is the overall chemical pathway for the conversion of LiH in the presence of water and the following mechanisms describe the

competing processes that make Equation (4.1.1) an equilibrium reaction. Equations (4.1.2) through (4.1.3) describe what happens to the system with increasing water exposure, while Equations (4.1.5) and (4.1.6) describe decomposition of a few of those products in either a dry or vacuum environment.

While the hydrated hydroxide and hydroxide layers may be less likely to form, or will be more likely to decompose, in the presence of either dry or vacuum environments, the likelihood that the oxide layer will persist even under these conditions is dependent on the temperature, vacuum, and water concentration within the system. While the oxide layer is unwanted, a uniform oxide layer across the surfaces seems to impede further water interaction with the bulk LiH below. Dinh's group suggests that cleaner hydride surfaces require baking, which not only helps to remove surface water trapped within the system, but also aids in the decomposition of the surface and interfacial hydroxide and oxide layers [18].

Dinh's group went on to explain how the data collected through what is known as temperature-programmed desorption (TPR), temperature-programmed decomposition (TPD), or thermal desorption spectroscopy (TDS) can be used to measure the activation energy for thermal decomposition. It is important to note that in this report TPR, TPD, and TDS are interchangeable acronyms describing the same technique. They described a number of methods that can be used to back-calculate the activation energy for the mechanism of decomposition, which are all based on the rate equation governing solid-state reactions [23-26]:

$$\frac{d\alpha}{dt} = kf(\alpha) = \nu e^{-\frac{E}{\Re T}} f(\alpha) \tag{4.2}$$

where α is the reacted fraction (between 0 and 1), k is the rate constant, $f(\alpha)$is an analytical function determined by the rate-limiting reaction mechanism, E is the activation energy for the rate-controlling process, $\Re$ is the molar gas constant, T is the temperature, and ν is the pre-exponential factor that describes the initial state of the sample. It is important to note that any thermal decomposition process follows an Arrhenius dependence, which is present in Equation (4.2).

By knowing the temperature ramp rate, β = dT/dt, Equation (4.2) can be re-written as:

$$\frac{d\alpha}{dT} = \frac{\nu}{\beta} e^{-\frac{E}{\Re T}} f(\alpha) \tag{4.3}$$

which allows for the temperature dependence of the solid-state reaction to be much more easily manipulated. By re-arranging and taking the natural logarithm of both sides of Equation (4.2), one can arrive at:

$$\ln\left(\frac{d\alpha}{dt}\right) = \ln[\nu f(\alpha)] - \frac{E}{\Re T} \tag{4.4}$$

where plotting $\ln\left(\frac{d\alpha}{dt}\right)$ versus $\frac{1}{T}$ at different values of α will yield a slope the nature of $-\frac{E}{\Re}$ for each plot, which was first proposed by Friedman [27].

The same rate equation can be solved on an integral basis by taking Equation (4.3), re-arranging the left and right-hand sides, and integrating over an appropriate set of bounds. This is achieved in the following equation:

$$g(\alpha) = \int_0^\alpha \frac{d\alpha}{f(\alpha)} = \int_{T_0}^T \frac{\nu}{\beta} e^{-E/\Re T} dT \tag{4.5}$$

where T_0 is the temperature at which the thermal decomposition analysis begins. Using the notation where $x = E/\Re T$, one can re-write Equation (4.5) as:

$$\beta \frac{\Re}{\nu E} \int_0^\alpha \frac{d\alpha}{f(\alpha)} = \int_x^\infty x^{-2} e^{-x} dx \tag{4.6}$$

$$p(x) = \int_x^\infty x^{-2} e^{-x} dx \tag{4.7}$$

where the right-hand side of Equation (4.6) is also known as the temperature integral, $p(x)$, and does not have a closed-form solution, but must be approximated.

The Kissinger-Akahira-Sunrose approximation assumes the temperature integral to be of the form [28 – 30]:

$$p(x) \cong x^{-2} e^{-x} \tag{4.8}$$

which, after a bit of re-arranging and taking the natural logarithm of both sides of Equation (4.6), yields a functional form of:

$$\ln\left(\frac{\beta}{T^2}\right) \cong -\frac{E}{\Re T} - \ln\left[\left(\frac{E}{\Re \nu}\right) \int_0^\alpha \frac{d\alpha}{f(\alpha)}\right] \quad \left(20 < \frac{E}{\Re T} < 50\right) \tag{4.9}$$

from which one can find the activation energy, E, by plotting $\ln\left(\frac{\beta}{T^2}\right)$ versus $\frac{1}{T}$ and finding the slope for different values of α and β.

Another approximation of the temperature integral has been proposed using the Ozawa-Flynn-Wall assumption, where [28, 31 – 32]:

$$p(x) \cong -2.315 - 0.4567x \tag{4.10}$$

which, after a bit of re-arranging and taking the natural logarithm of both sides of Equation (4.6), yields the functional form of:

$$\ln(\beta) \cong -1.052\frac{E}{\Re T} - 5.333 - \ln\left[\left(\frac{E}{\Re \nu}\right)\int_0^{\alpha}\frac{d\alpha}{f(\alpha)}\right] \quad (20 < \frac{E}{\Re T} < 60) \tag{4.11}$$

from which one can find the activation energy, E, by plotting $\ln(\beta)$ versus $\frac{1}{T}$ and finding the slope for different values of α.

The work performed by Dinh's group is important in the investigation into the thermal decomposition of lithium hydride, the study focuses primarily on how controlled amounts of water contamination will affect the amount of hydrogen evolved, and never fully investigates the recovery kinetics for pure lithium hydride. What the work does tell us is that determining the appropriate activation energy barrier for recovery is a vital piece of information when considering isotope reclamation. Other studies have concluded that the inclusion of oxygen in the surface chemistry is important for retention and recovery [33, 34]; however, these experiments were done either using very thin layers of lithium [33] or by looking at retention in the C-Li-O matrix [34]. In both of these cases, the chemistry is significantly different than for a reactor that uses flowing liquid lithium and the loop that would likely be associated with such a scenario. In the extreme case where the treatment option chosen is that where the lithium deuteride and tritide are separated from the Li-D(soln)-LiD-T(soln)-LiT matrix, the activation energy will describe the temperature required to reach the peak hydrogen evolution rate. This rate will need to either match or beat the particle loss rate at the wall described in Chapter 2, so it behooves us to continue the investigation into what exactly will happen to pure LiH when heated to thermal decomposition temperatures.

4.2 Experimental Setup

To measure the rate of thermal decomposition of pure LiH as a surrogate for LiD and LiT, an entirely new temperature-programmed decomposition (TPD) chamber was built at the Center for Plasma-Material Interactions (CPMI). The chamber measured approximately 7 liters in inner volume, and was primarily evacuated using a Varian 550 turbomolecular pump backed by an Alcatel rotary-vein pump. The residual gas analyzer (RGA), which was the primary diagnostic used to quantify the evolved gas analysis, was set apart from this main chamber and was kept differentially pumped using an Osaka TG60FRAB turbomolecular pump, backed by the same Alcatel rotary-vein pump. The ultimate base pressure the system was able to achieve was 2×10^{-7} Torr, with the differentially pumped RGA section able to achieve a base pressure on the order of 9×10^{-8} Torr. Low base pressures are important to eliminating the concerns surrounding water exposure, described by Dinh [18]. The following sub-section will describe the primary chamber in greater detail.

4.2.1 The Lithium Hydride Degassing Experiment (LiHDE) Chamber

A block schematic of the Lithium Hydride Degassing Experiment (LiHDE) can be seen in Figure 4.2. The LiHDE chamber is characterized by three main sections that make LiHDE unique from other chambers. The first key sub-system in the LiHDE chamber is the heating stage, which was manufactured in-house. The heat source was a White Rodgers silicon nitride ignitor, capable of reaching a surface temperature of 1400 °C at full power. The ignitor was surrounded by a hollowed-out rod of the molybdenum alloy commonly known as TZM. TZM was chosen for a number of reasons, the most important being that alloy composition is at or above 99% molybdenum, giving it a very high thermal conductivity while still being fairly easy to machine. The thermal properties for several metals are listed in Table 4.1 [35, 36]. The TZM rod surrounded a custom-fabricated boron nitride sample crucible, which was also directly above the silicon nitride ignitor. This crucible served two purposes: first, it housed the LiH powder, and, second, it contained two concentric electrodes through which the resistance in the sample could be measured. A block schematic of the crucible is illustrated in Figure 4.3. Outside of the molybdenum rod sat an insulating mullite shield, which was in turn surrounded by a stainless steel shim radiation shield to prevent radiative losses. A K-type thermocouple was used to measure the temperature at the

crucible and the temperature at a position halfway up the molybdenum rod. A block schematic of the heater stage assembly can be seen in Figure 4.4.

Table 4.1: Thermal conductivities and linear coefficients of thermal expansion for several metals [35, 36].

Material	k (W m^{-1} K^{-1})	α (x 10^{-6} m $(m K)^{-1}$)
Molybdenum	140	5
Zirconium	23	5.7
Titanium	19-23	8.6
Tungsten	163-173	4.3
Stainless Steel	12-45	16
Lithium	[44 (liquid)]	{46 (solid)}

The second key sub-system that sets LiHDE apart from other TPD chambers is the way in which the RGA section is differentially pumped. While it is true that most chambers remain differentially pumped through the use of limiting orifices, few chambers employ the use of a "sniffer tube" to not only maintain a noticeable difference in pumping between chamber sections, but also to extend the capabilities of the gas analysis diagnostic down to the surface of the sample. The RGA is offset from the sample by approximately 52 cm. The entrance to the RGA sits approximately 25 cm away from the upper boundary of the "sniffer tube", while the tube itself directs the flow of evolving particles 24 cm down to the point where the entrance into the "sniffer tube" sits approximately 3 cm above the surface of the sample. With an entrance orifice diameter of 1.6 mm, the "sniffer tube" helps to effectively direct upward flow toward the RGA, while still maintaining pressures below the 1 x 10^{-4} Torr range, which is the upper limit of the RGA.

The final sub-section of the LiHDE chamber that distinguishes it from other chambers is the diagnostic used for the evolved gas analysis: the Vacuum Technologies, Inc. AeroVac Odyssey 150 Mass Spectrometer [37]. The Odyssey is unique from other quadrupole mass spectrometers (QMS) in that it uses the principles of both time-of-flight and angle of incidence to measure cracking patterns. The detector sits 22.9 cm away from the ionizing filaments and is at a 60° bend

from the ionizer. Along the bend, a permanent magnet, generating a magnetic field of approximately 1000 Gauss, deflects incoming charged particles of various masses toward the detector. This setup gives the Odyssey QMS a distinct advantage over other QMS systems for measuring low-mass species with high resolution. The use of deflection, however, broadens the peaks of higher mass particles, leading to poor resolution of species above approximately 35 atomic mass units (AMU). The reasons for the differences in resolution between low AMU and high AMU species is due to conservation laws, namely those governing energy and momentum. High AMU ions, while still following the magnetic trajectory imposed by the external permanent field, will not be as precisely re-directed to the collector due to the high AMU ion's mass and momentum. A schematic illustrating how the combination of ionization potential and magnetic deflection affect gas measurement can be seen Figure 4.5.

Baking the sample and the chamber prior to experimentation was vital in measuring the most accurate instantaneous recovery rate (or flux) as a function of temperature. The heating stage section is sealable and transferable through the use of a 4.5" Conflat gate valve, which is important for loading the hygroscopic lithium hydride sample and transferring this section to the main LiHDE chamber. Prior to loading the sample, the heater section was attached to the main chamber and the whole system was baked under vacuum for 24 hours at approximately 150 °C using a combination of the ignitor and the external heating ribbon. Both heating sources were powered using external AC variable transformers. After 24 hours, the entire system was flooded with argon (Ar) and the heating stage was detached from LiHDE and transported to a dry box. Approximately 0.16 ± 0.07 g of LiH powder was then loaded under an inert Ar atmosphere. The heating stage was then sealed again and transported back to the LiHDE chamber, where it was re-attached. Prior to opening the heating section up the main chamber, the main chamber was pumped through the Alcatel rough pump and purged with Ar. Once this was done a few times, the heating section was unsealed and the whole system was pumped through the Alcatel rough pump and subsequently through the Varian 550 and Osaka TG60FRAB turbomolecular pumps. The chamber was then once again baked for approximately 36 hours, using the same heating sources described above, prior to initiating the decomposition experiment. This process was very important to maintain hydride integrity and prevent the unwanted buildup of impurity layers, as described by Dinh [18].

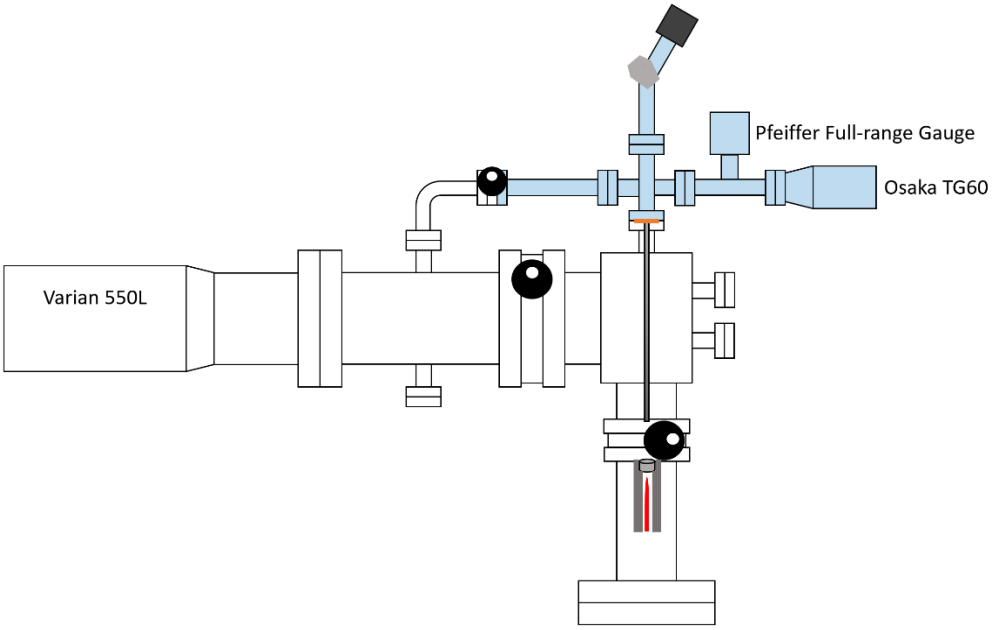

Figure 4.2: A block diagram of the LiHDE TPD chamber. The differentially pumped RGA section is at the top right. The sniffer tube is the long section on the right in the middle. The heating stage is illustrated with a cartoon of the ignitor heating source in the bottom right. The blue highlighted section represents the differentially pumped section.

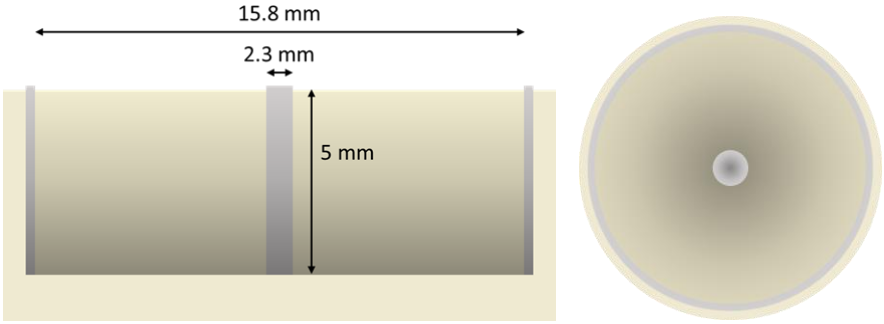

Figure 4.3: An illustration of the crucible in use in the LiHDE TPD system which serves the purposes of holding the sample and measuring resistance through the sample.

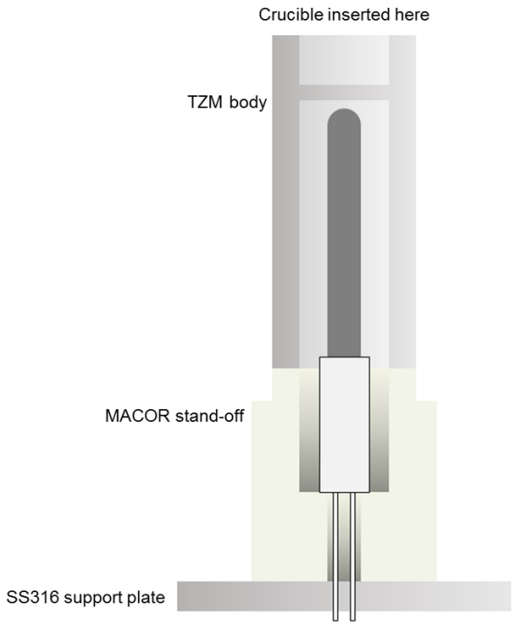

Figure 4.4: A block schematic illustrating the heater stage assembly.

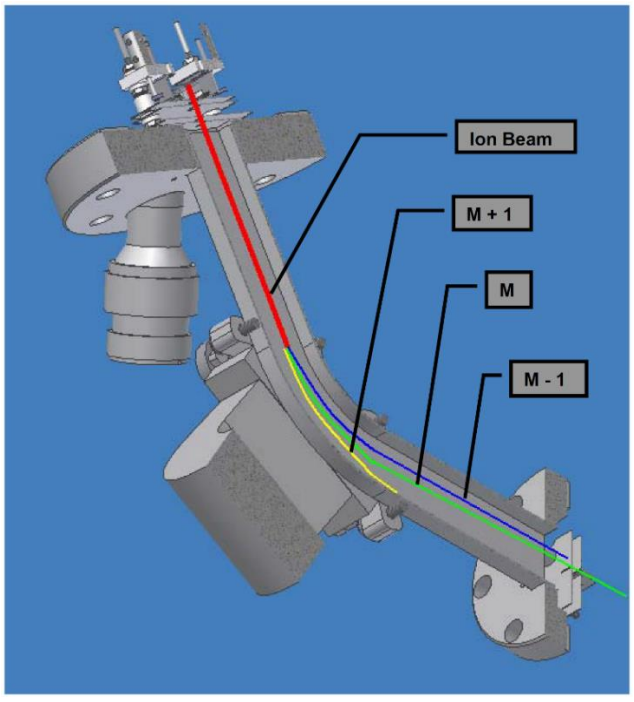

Figure 4.5: A depiction of how the Odyssey QMS system uses a combination of time-of-flight measurements with magnetic deflection to discriminate charged particles based on their mass [37].

4.2.2 Diagnostics

A suite of diagnostics was used to determine the rate of thermal decomposition in pure lithium hydride. Previous studies [18, 35 – 36, 38] on the rate of hydrogen degassing in lithium hydride have reported measurements that are almost entirely based on analyses of the gaseous state, while little has been done to investigate changes that simultaneously occur in the condensed phase. The author wanted to use Li vapor condensation analysis along with an analysis of the condensed phase (solid and liquid LiH) to aid in the investigation of the thermal decomposition rate. The suite of diagnostics and their underlying principles described in this section were chosen to verify one another for direct comparison during the same experimental run.

4.2.2.1 RGA Gas Analysis

Temperature-programmed Decomposition (TPD) analyses are universally accepted as the means with which one can determine the thermodynamic properties of a given compound during its thermal decomposition, either volumetrically or at the surface. Typically this technique is used to look at the surface chemistry of a sample, specifically when it is crucial to determine the species that have absorbed or adsorbed within the first few monolayers. Using the same technique on samples that have been irradiated by plasma may not lead to the same conclusions, as the energetics of bombarding ions are likely to modify the surface and sub-surface chemistry. The same analyses used to investigate surface chemistry may also be flawed when the sample in question volumetrically decomposes into its constituents; however, the same analyses can give insight into the mechanisms by which atomic species may evolve. Regardless of the evolution kinetics, what is true for all TPD measurements is that with increasing temperature, the desorption rate (or degassing rate in our case) will increase until a point where the surface (or system) is sufficiently depleted of the absorbate (or chemical constituent).

TPD spectra can be related back to the chemical mechanisms for release based on the peaks observed during the heating (and cooling) processes. These mechanisms are all based on the breaking of bonds and decomposition volumetrically or along surfaces, so the Arrhenius temperature dependence in Equation (4.2) first described by Friedman [23] is present in all of the

rate equations for decomposition kinetics, regardless of the rate order. Simplified forms of the equations that describe different release kinetics are given by [39]:

$$R(t) = -\frac{d\Theta}{dt} = \nu e^{-E/\Re T} \tag{4.12}$$

$$R(t) = -\frac{d\Theta}{dt} = \nu \Theta e^{-E/\Re T} \tag{4.13}$$

$$R(t) = -\frac{d\Theta}{dt} = \nu \Theta^2 e^{-E/\Re T} \tag{4.14}$$

where $R(t)$ is the rate of desorption, Θ is the surface coverage fraction of the absorbate (from 0 to 1), and ν is the pre-exponential factor similar to that which was reported in the kinetic theory by Dinh [18]. Equation (4.12) describes multilayer desorption, in which the absorbate or chemical constituent evolves from the system volumetrically. Equation (4.13) is more widely considered for TPD analyses of surfaces since it defines monolayer desorption. Equation (4.14) is more complicated both from a physical and mathematical standpoint, since the rate equation governs recombinative desorption. A form of Equation (4.14) was used in the investigation of hydrogen/deuterium release in a study conducted by Baldwin's group [40], which was reported earlier in Chapter 2. Illustrations for each of these mechanisms are seen in Figure 4.6.

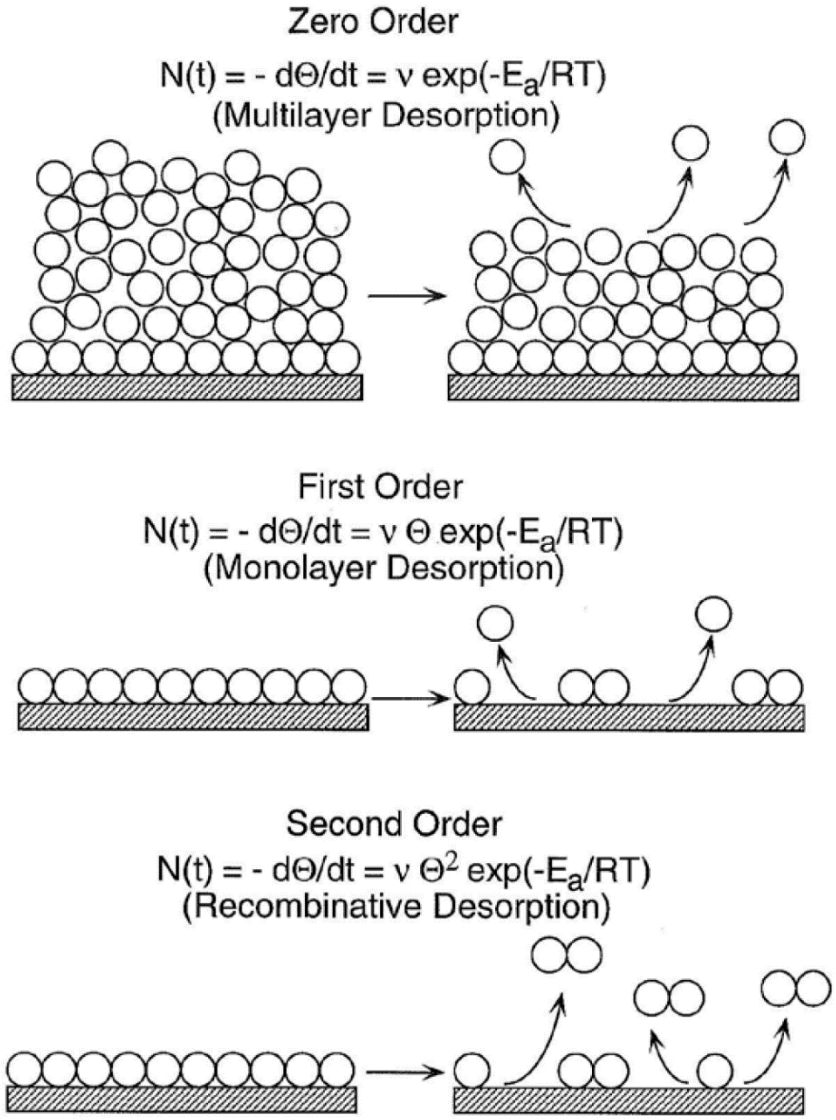

Figure 4.6: Illustrations of the different desorption mechanisms that may occur during TPD experiments [39].

While it is important to understand the mechanism by which hydrogen will be released from pure LiH, the most crucial thermodynamic parameter that can be obtained from the thorough analysis of a TPD spectrum for the thermal decomposition of LiH is the activation energy. The means with which one can determine the activation energy from a zeroth order reaction are not

unlike the methodology Dinh [18] used, which starts with taking the natural logarithm of both sides of Equation (4.12):

$$\ln[R(t)] = \ln(\nu) - E/\Re T \tag{4.15}$$

Therefore, a plot of the natural logarithm of the rate versus inverse temperature will yield a linear relationship where the slope is equivalent to $-E/\Re$.

Calculating the activation energy from first order reaction kinetics is more challenging and requires some manipulation, both experimentally and analytically. Assuming that the activation energy is independent of temperature and surface coverage, the first step in finding the activation energy from the rate equation is defining the heating rate, β [39]:

$$T = T_0 + \beta t \tag{4.16}$$

where T_0 is the initial temperature for the TPD heating process. Stating that $\beta = dT/dt$ and applying this to the left hand side of Equation (4.13), the first order rate equation becomes:

$$R(t) = -\frac{d\Theta}{dt} = -\beta\frac{d\Theta}{dT} = \nu\Theta e^{-E/\Re T} \tag{4.17}$$

Now, differentiating Equation (4.17) as a function of temperature, the result provides:

$$-\beta\frac{d^2\Theta}{dT^2} = \nu\frac{d\Theta}{dT}e^{-\frac{E}{\Re T}} + \frac{\nu\Theta E}{\Re T^2}e^{-\frac{E}{\Re T}} \tag{4.18}$$

The temperature where the rate reaches a maximum and its first derivative goes to zero (T_p = peak temperature), the left hand side of Equation (4.18) also goes to zero. By solving for the temperature derivative of the surface coverage at this point and re-arranging the above result, one can arrive at:

$$\frac{E}{\Re T_p^2} = \frac{\nu}{\beta}e^{-\frac{E}{\Re T_p}} \tag{4.19}$$

where T_p is the temperature at which the evolution rate reaches its maximum. This equation is transcendental and requires approximation for an "analytical" solution. The following approximation is known as the Redhead's peak maximum method [39], and requires the knowledge of the pre-exponential factor to solve for the activation energy from first-order kinetics:

$$E = \Re T_p[\ln\left(\frac{\nu T_p}{\beta}\right) - 3.64] \tag{4.20}$$

The experimental results can also be fit to this function for various values of ν, so long as $10^8 < \nu < 10^{14}$. It is important to note that this is only a special case for first order kinetics. The only other method that can be used to determine the activation energy from first order kinetics is to run the same experiment for different linear heating rates to find the activation energy from the slope of the fit between β/T_p^2 versus T_p.

Finding the activation energy from the second order rate equation can either be simpler or more involved than finding the activation energy from the first order rate equation. Finding E from the second order rate equation may prove necessary due to the fact that recombinative desorption plays an important role in hydrogen recovery and is likely the rate limiting step for isotope reclamation through the use of heat. Again, by knowing the temperature ramp rate, β, Equation (4.14) can be re-written as:

$$R(t) = -\beta \frac{d\Theta}{dT} = \nu \Theta^2 e^{-E/\Re T} \tag{4.21}$$

This equation can be solved quite easily by knowing the desorption rate, $R(t)$, and that the heating rate, β, is held constant. For various values of ν and Θ^2, experimental data can be fit to the following equation:

$$\ln[R(t)] = \ln\left[\frac{\nu\Theta^2}{\beta}\right] - \frac{E}{\Re T} \tag{4.22}$$

From a linear fit between the $\ln[R(t)]$ and $\frac{1}{T}$, the slope will yield $-\frac{E}{\Re}$, which will lead to the determination of the activation energy. The determination of activation energy from this methodology should be done looking by looking at the leading edge of the TPD peak; however, this form may yield inaccurate data. Regardless, this is the form that will be used to look at the second order reaction activation energy for LiH thermal decomposition.

A more involved analysis of the second order rate equation can be done using the Redhead's peak maximum method [39]; however, the same assumptions used in the analysis of first order kinetics are not valid for second order reactions. The second order Redhead equation, where the derivative of the rate at the peak temperature is zero, is of the form [41]:

$$\frac{E}{\Re T_p^2} = \frac{2\nu\Theta|_{T_p}}{\beta} e^{-E/\Re T_p} \tag{4.23}$$

Re-arranging and taking the natural logarithm of both sides of Equation (4.23), the equation then takes the form:

$$\ln\left[\frac{\beta}{T_p^2}\right] = -\frac{E}{\Re T_p} + \ln\left[\frac{2\nu\Re\Theta|_{T_p}}{E}\right] \tag{4.24}$$

Unfortunately, Equation (4.24) cannot be solved from the analysis of a single experiment and instead involves running a number of experiments on similar samples with various heating rates, β, and determining the peak temperature, T_p, from each of these experiments. The activation energy can then be found by finding the slope of the linear plot that relates $\ln\left[\frac{\beta}{T_p^2}\right]$ to $\frac{1}{T_p}$.

Lithium that has been irradiated with a hydrogen plasma will have a different hydrogen release mechanism than that for pure LiH because the Li-H bond requires an extra energy input beyond that which is required for the dissolution, diffusion, and recombinative release of hydrogen at the surface of hydrogenated lithium. The release mechanism of hydrogen from pure LiH, on the other hand, is more aligned with the zeroth order rate equation, since it will be more likely to undergo volumetric decomposition. Hydrogen release from the surface, however, is likely not exclusively volumetric, since H_2 gas molecules must evolve as diatoms. Therefore, some combination of zeroth and second order kinetics will determine release rates from pure LiH. These analytical tools will later be applied to the resultant TPD spectra.

Pragmatically, it is important to note that in order to accurately determine the release rates and compare them to the partial pressure responses by the RGA (and thus determine the associated activation energies), the RGA needed to be calibrated to a known hydrogen flow rate at the pumping conditions used during experiments. To accomplish this, a known flow rate of hydrogen was introduced into the chamber which was controlled by an Alicat MC-50SCCM-D/5M mass flow controller, internally calibrated for hydrogen gas. The gas was fed through a tube, where the outlet was held within the LiHDE chamber in the same position at which samples were held. A cartoon depiction of this setup can be seen in Figure 4.7. The resultant hydrogen calibration is then shown in Figure 4.8, which relates the flow rate to the RGA H_2 pressure response.

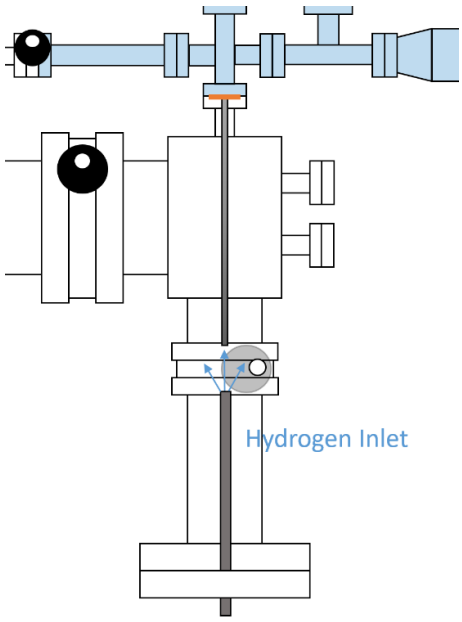

Figure 4.7: A block diagram illustrating how the controlled hydrogen calibration was performed in the LiHDE chamber.

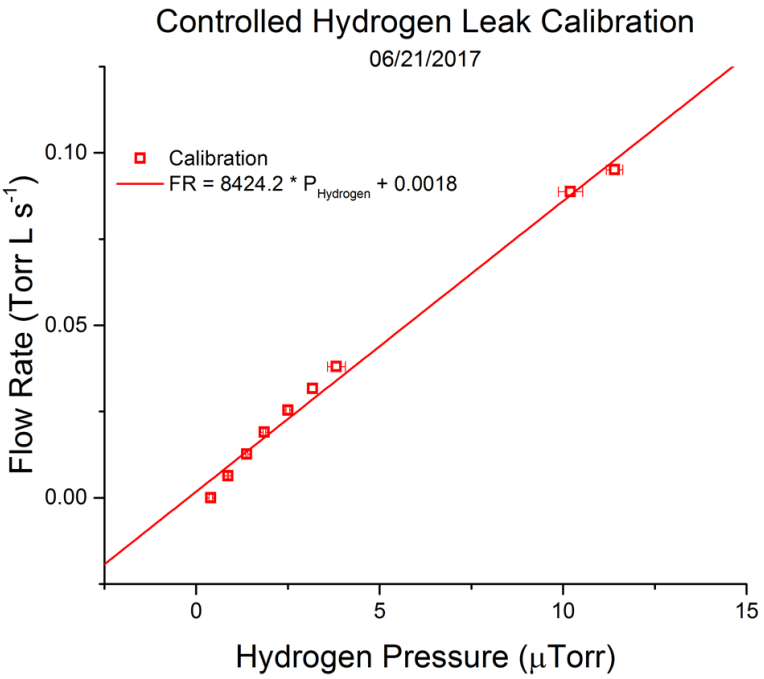

Figure 4.8: The controlled hydrogen leak calibration done in order to take the pressure response from the RGA and convert it to an evolution rate.

4.2.2.2 Lithium Vapor Deposition Analysis

Another analysis technique that can be used to independently measure hydrogen release rates and simultaneously verify those seen in the RGA gas response is by looking at the rate of growth of a lithium layer on a cooled surface as its vapor condenses. This was accomplished by inserting a dual quartz crystal microbalance (QCM) into the chamber with line-of-sight to the sample surface. The principles of the QCM will be discussed and how the changes in oscillation frequency due to the growth of a layer on the surface of the piezoelectric electrode can be related to the deposition thickness. The vapor deposit relates back to the hydrogen release rate by knowing that the thermal decomposition of lithium hydride follows the mechanism:

$$2LiH + energy \rightarrow 2Li + H_2 \tag{4.25}$$

The first extensive study done to illustrate the usefulness and sensitivity of the QCM was done by Sauderby in the late 1950s [42]. The results of this early work culminated in the equation that governs most of the analysis tools used for QCM film measurements. This culmination is embodied in the following equation [42, 43]:

$$\Delta f = -C_f \Delta m \tag{4.26}$$

where Δf denotes the change in frequency of the oscillator, Δm is the change in mass of the deposited film per unit area, and C_f is the sensitivity factor for the crystal. Often the sensitivity factor for a given crystal is taken into account in the electronics which use the change in frequency as the input and the layer thickness as the output. Equation (4.26) is not all-inclusive for every film deposited, however, and the rigidity and global thickness of the foreign layer must be considered because shear stresses may be caused by the crystal vibrations [42, 43]. Reports have shown that if the frequency change is less than 2% of the series resonant frequency of the unloaded crystal, then Equation (4.26) remains valid [44]. In this case, the sensitivity factor can be considered to only be dependent on the properties of the quartz [42, 43]:

$$C_f = 2nf_0^2 / \sqrt{\rho_q \mu_q} \tag{4.27}$$

where n is the number of the harmonic, f_0 is the resonant frequency of the fundamental mode in the crystal, ρ_q is the density of the quartz, and μ_q is the shear modulus of quartz. The results and

analysis of the deposited Li vapor later in this chapter will prove that the frequency change is small enough such that the layer can be adequately described by Equations (4.26) and (4.27).

Often, analyses of QCM outputs concludes in finding the thickness of the deposited layer, rather than the mass or change in mass per unit area. If the film is assumed to be uniformly deposited over the surface of the crystal and it satisfies the conditions for Equation (4.26) to be valid, then the layer thickness can be calculated from the mass change through the relation [43]:

$$T_f = \Delta m/\rho_f \tag{4.28}$$

where T_f is the film thickness and ρ_f is the mass density of the film. A similar relationship was used in calculating the amount of lithium that was deposited on the surface of the dual QCM used in this study.

While the frequency change for the deposited Li layer fell well within the limits defined by Sauderby [42 – 44], a more sophisticated analysis known as the Z-factor analysis takes into account the properties of the deposit and allows for rigid films where the frequency change between the unloaded and loaded crystal can reach as high as 40% [45]. The relationship that defines this Z-factor analysis is given by:

$$\Delta m = \frac{N_q \rho_q}{\pi Z f_l}\ tan^{-1}\left(Z \tan\left[\frac{\pi(f_u - f_l)}{f_u}\right]\right) \tag{4.29}$$

where N_q is the frequency constant for the crystal, ρ_q is the density of quartz, f_l is the frequency of the loaded crystal, f_u is the frequency of the unloaded crystal, and Z is the Z-factor of the film material, which is defined by [43, 45]:

$$Z = \sqrt{\frac{\rho_q \mu_q}{\rho_f \mu_f}} \tag{4.30}$$

where μ_q is the shear modulus of quartz, ρ_f is the mass density of the film, and μ_f is the shear modulus of the film.

From a practical standpoint, QCM film deposition analysis depends highly on the electronics and the load response to the changes in crystal frequency. Simplistically, the QCM circuit is defined by the Butterworth van Dyke model [43, 46]. This model has parallel impedance sections, where one section defines the applicable L-R-C series analysis to the oscillator (motional

section) and the other defines the stray capacitance of the system. The applicable circuit is illustrated in Figure 4.9.

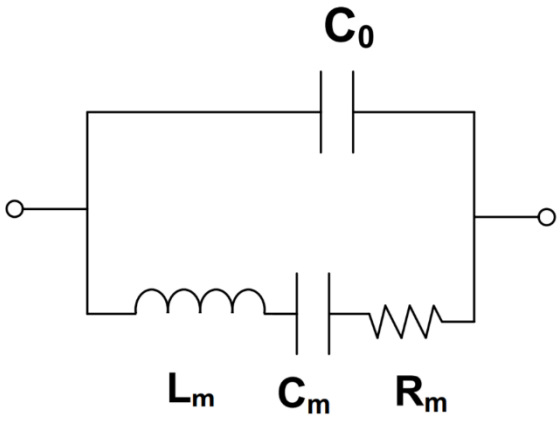

Figure 4.9: The Butterworth van Dyke equivalent circuit for the load of a QCM. The top capacitance, C_0, represents the stray capacitance, while the impedance in the other branch represents the oscillator.

The values denoted as L_m, C_m, and R_m can be effectively used as the measurement load relating the change in series resonant frequency to the change in deposited film mass. The "motional" resistor, R_m, corresponds to the dissipation of the oscillator energy to the surrounding structure as well as the film in contact with the crystal. The "motional" capacitor, C_m, corresponds to the stored energy in the oscillator. The "motional" inductor, L_m, corresponds to the inertial portion of the oscillator, which can be directly related to the mass change during vibration [43, 46]. Added mass increases L_m, and, if the deposit is viscous or a soft film, then R_m is also increased. In the full measurement of the circuit illustrated in Figure 4.9, the stray capacitance requires compensation. Otherwise, this impedance will inject a faulty "leading" current, which will change the properties of the circuit and introduce a false phase shift that skews measurements of the film mass. Most QCM circuits compensate for the stray capacitance by introducing variable components in an effort to "match" and cancel the load of C_0. A simplified circuit diagram, which includes the proper C_0 compensation and a load resistance/amplifier for measurement can be seen in Figure 4.10.

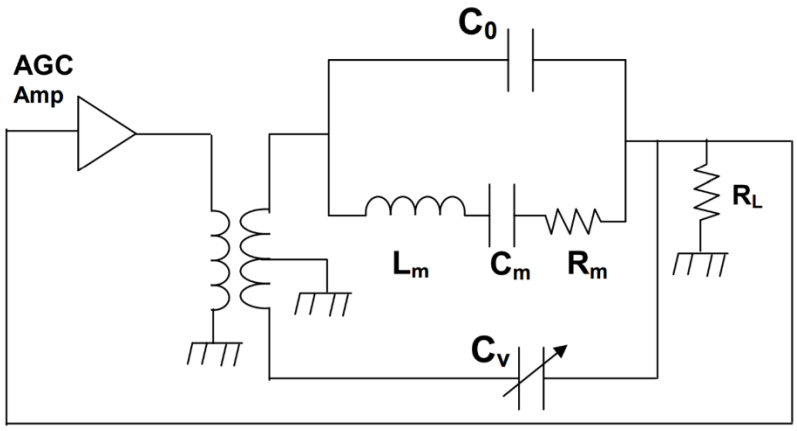

Figure 4.10: A simplified form for the full QCM circuit, with the inclusion of stray capacitance compensation, and the circuitry required for measurement (R_L and the AGC Amp) [43].

A dual QCM was chosen for these experiments in large part because the QCM was being used in a chamber where system components were being heated. Changes in the temperature will change the oscillation frequency of a single crystal. For high accuracy measurements, systems require either careful control of the surrounding or ambient temperature or they require compensation. A second quartz crystal isolated from the depositing vapor can provide correction for the measured frequency change dependence on temperature.

During the actual LiH thermal decomposition experiments, the QCM was positioned such that the open crystal face had line-of-sight to the LiH sample. The crystal was positioned 10° off normal from the surface of the sample at an approximate distance of 6 inches from the surface. Knowing the collection area on the top of an individual QCM crystal, the calculated fraction of the solid angle subtended by the QCM collector was found to be approximately 0.03%. By subtracting the control signal of the closed QCM from the exposed QCM and using the solid angle fraction subtended by the exposed crystal (and assuming that the layer deposited on the surface of the crystal was composed entirely of lithium), Li deposition rates were evaluated. A block diagram depicting how the QCM was positioned during the LiH decomposition experiments can be seen in Figure 4.11.

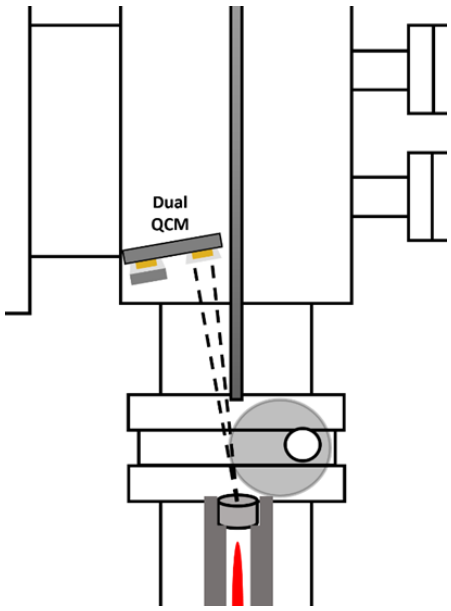

Figure 4.11: A block diagram illustrating the positioning of the dual QCM used during the LiH degassing experiments.

4.2.2.3 Condensed Phase Resistivity Analysis

The studies done to investigate the phase changes and thermal decomposition in various Li-LiH systems up until this point have primarily focused on RGA gas analysis to determine the thermodynamic and kinetic properties in samples [1 – 15, 18, 40]. Only the early works done by Adams' group [16, 17] related hydrogen and deuterium solubility in lithium to a measurable quantity in the condensed phase – resistivity. Adams' group, however, only used this analysis technique to measure the chemical makeup of low-hydrogen concentration systems; whereas, the resistance measurements done in the author's work were made in a system with a starting compound of pure LiH.

Correlating the change in resistance across a sample to its chemical composition and phase is not an easy task. This is especially true when the sample in question thermally decomposes, which is both a chemical and a phase change. For the Li-LiH system, the first place to start is to look at the change in resistivity for each of the constituents and then build up the theory for how the presence of one within the other will affect resistance measurements. The resistivity as a function of temperature for both Li and LiH can be seen in Figure 4.12.

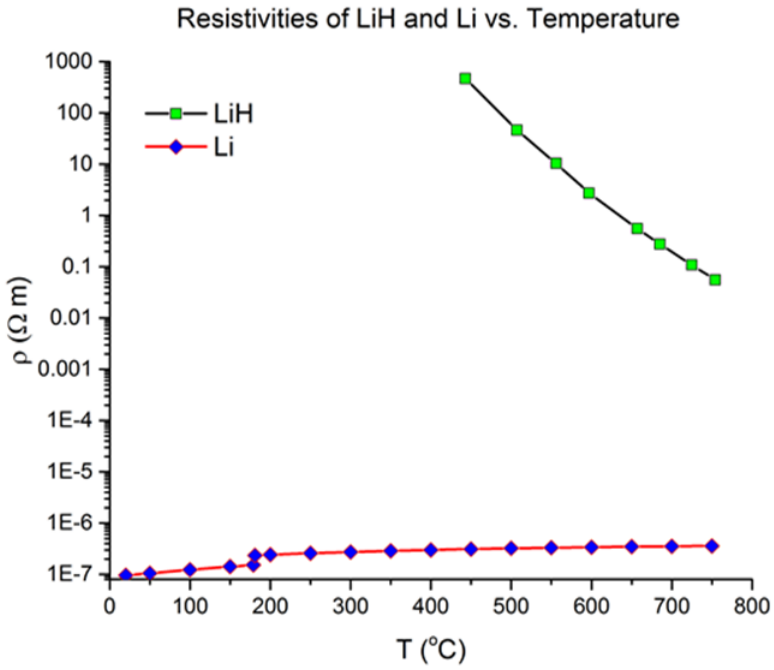

Figure 4.12: A plot illustrating the vast difference in resistivity between Li [47] and LiH [48]. It is important to note that there is a jump in this intrinsic value for Li that occurs at its melting point of 180 °C; however, no such jump was seen in LiH when it reached its melting point at 690 °C [48].

From Figure 4.12 it is clear that the presence of one of these two constituents within the other should drastically alter the resistance measured across the sample with respect to the initial value. Only a few studies have been dedicated to binary systems that include a ceramic and a metal, and even less focus on systems that have the potential for chemical interaction between the two components. Fundamentally, the resistance of a material is caused by electrons scattering on perturbations from an ideal crystal. Scattering events are caused by thermal vibrations of atoms, the presence of impurities, and the presence of grain boundaries (in a polycrystalline solid) [49]. Conductivity is related to these microscopic scattering events through the electron drift mobility, which takes into account the mean time between collisions, the potentials and force fields from the atoms, and the scattering probability, defined through the cross-section. Temperature dependence affects the scattering due to thermal vibrations and can be related to the resistivity through the use of the temperature coefficient of resistivity, which describes temperature perturbations to the

resistivity. In general for a binary system, a dispersed phase within a continuous phase affects the overall conductivity through the Reynolds and Hough rule [49, 50]:

$$\frac{\sigma_{eff}-\sigma_c}{\sigma_{eff}+2\sigma_c} = \chi_d \frac{\sigma_d-\sigma_c}{\sigma_d+2\sigma_c} \tag{4.31}$$

Where σ_{eff} is the effective conductivity, σ_c is the conductivity of the continuous phase, χ_d is the volume fraction of the disperse phase, and σ_d is the conductivity of the dispersed phase. Assuming that LiH is the dispersed phase and Li is the continuous medium, the relation between mass fraction and mole fraction follows as:

$$\omega_{LiH} = x_{LiH} \frac{M_{LiH}}{x_{LiH}M_{LiH}+(1-x_{LiH})M_{Li}} \tag{4.32}$$

where ω_{LiH} is the mass fraction of LiH, x_{LiH} is the mole fraction of LiH, M_{LiH} is the molar density of LiH, and M_{Li} is the molar density of Li. The mass fraction can be related to the volume fraction, assuming an ideal solution, through:

$$\chi_{LiH} = \omega_{LiH} \frac{\omega_{LiH}\rho_{LiH}+(1-\omega_{LiH})\rho_{Li}}{\rho_{LiH}} \tag{4.33}$$

where χ_{LiH} is the volume fraction of LiH, ρ_{LiH} is the mass density of LiH, and ρ_{Li} is the mass density of Li. The effective conductivity as a function of temperature and mole fraction of the dispersed phase (LiH) can then be quantified. A similar analysis can be done that looks at Li as the dispersed phase and LiH as the continuous phase. A graphic for the system that is described by the Reynolds and Hough theory is illustrated in Figure 4.13 [49, 50]. Following the Reynolds and Hough theory [50], the theoretical changes in resistivity for Li-rich and LiH-rich systems are be summed in Figure 4.14.

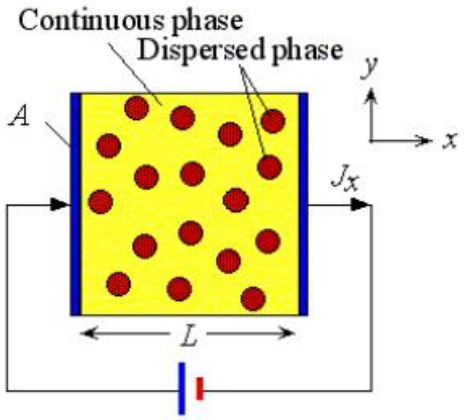

Figure 4.13: The type of system in which the electrical properties are governed by the Reynolds and Hough theory [49, 50]. The variables in the graphic are defined as: L being the length between measurement electrodes, A being the electrode cross-sectional area, and J_x being the current between electrodes.

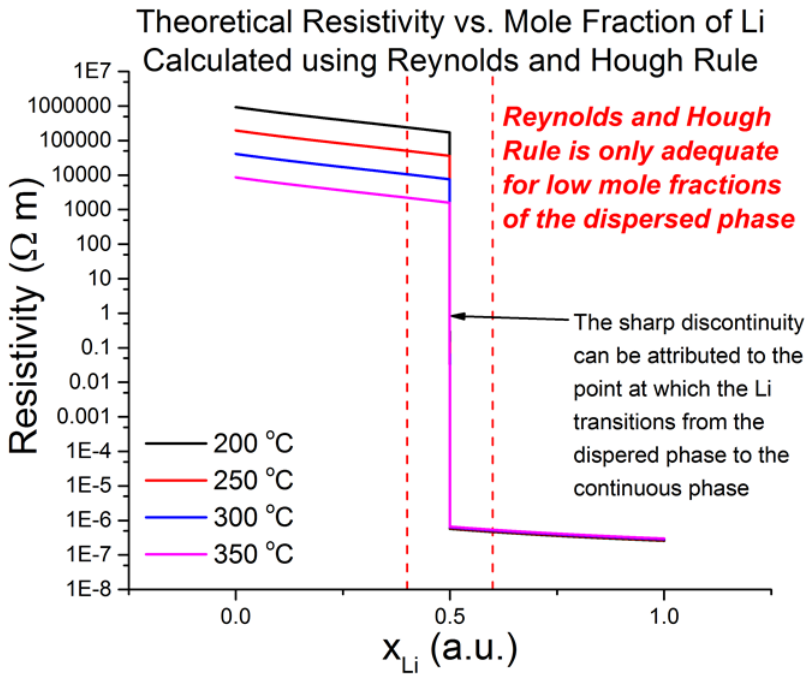

Figure 4.14: The expected changes in resistivity that follow the Reynolds and Hough rule [50] for a dispersed phase within a continuous phase as a function of lithium fraction for various temperatures. While it seems that there is less of a change in the Li-rich system, this is only due to the fact that the ordinate covers a very broad range, even on the logarithmic scale.

The methodology that governs this resistivity analysis and relates it to the sample composition is inherently flawed, however, in that the assumptions made require the system be of a binary composition. In a real-world scenario, the presence of other lithium impurities, such as lithium oxide (Li_2O), lithium hydroxide (LiOH), lithium nitride (Li_3N), and possibly lithium carbonate (Li_2CO_3), will also play a role in the resistance measured through the sample. If the results from Dinh's study are to be believed, the most common of these impurities would be Li_2O and LiOH [18]. The conductivities for a few of these compounds as a function of temperature are shown in Figure 4.15. When applying the theoretical considerations for changes in resistivity and relating these changes to composition, a brief discussion on the presence of these impurities will also be considered. Unfortunately, after an exhaustive literature search, only the electrical properties for Li_2O were found as a function of temperature [51]. This may prove useful, though, as the most probable impurity to affect the resistivity will likely be the oxide that would be directly in contact with the LiH bulk.

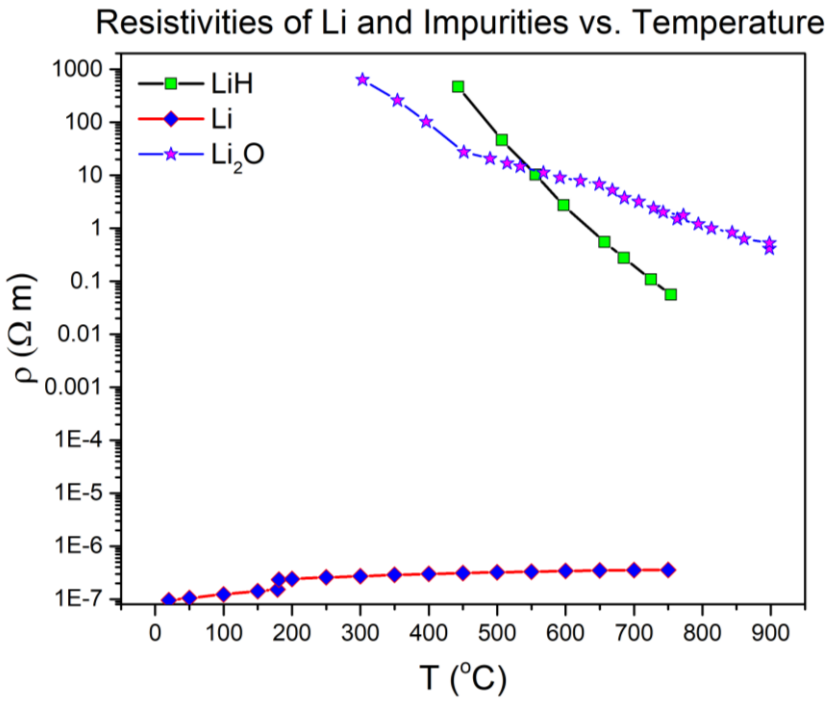

Figure 4.15: Electrical properties of lithium [47], lithium hydride [48], and lithium oxide [51] as a function of temperature.

A unique combination of the three aforementioned analysis techniques can yield a number of interesting results when measuring the thermal decomposition of pure lithium hydride. The conventional RGA gas analysis can be verified by the QCM Li vapor deposition analysis, while the sample composition in the condensed phase can be related to the resistivity and how it is modified by temperature for the constituents in the binary Li-LiH system. The results obtained using these diagnostics and their underlying principles for the thermal decomposition of pure LiH as a surrogate for LiD and LiT will be the topic of the next sections of this chapter.

4.3 Results

Extensive preliminary work went into the investigation of the thermal decomposition of pure lithium hydride prior to the results that will be reported in this section. The data and conclusions described in this section were due to the culmination of several experimental optimizations, which are not fully described in detail in this report for brevity. However, it is worth mentioning that the techniques used to obtain these data are based on experimental trial and error, with the final experimental data sets representing a fully optimized lithium hydride degassing system.

After the chamber was baked using the procedure described in the previous section, an analog base scan was taken with the Odyssey RGA in order to absolutely calibrate it to the base pressure read by the full range gauge that was attached to the same differentially-pumped portion of LiHDE. Once this had been completed, a trend scan in the RGA was then started, with masses equivalent to 1, 2, 6, 7, 18, and 28 AMU tracked during the experiment. These masses correspond to the ions H^+, H_2^+, $^6Li^+$, $^7Li^+$, H_2O^+, and N_2^+, respectively. While all efforts were taken to eliminate leaks, both real and virtual, finite amounts of H_2O and N_2 persisted, but at partial pressures orders of magnitude lower than the atomic and molecular hydrogen, which were the species of interest. The experiments also investigated the evolution of Li vapor by tracking ^6Li and ^7Li signals, but, for most of the test, these signals were only slightly above the background signal. Once the trend scan had begun, the variable transformer that provided power to the ignitor heating source was turned up to accommodate a heating ramp rate of approximately 3.8 K min^{-1}. While the heating ramp did fluctuate during the heating process, great effort was taken to make sure the heating rate was nearly constant, with the largest deviations occurring once the sample had started to

asymptotically approach its maximum temperature. Once the H_2^+ signal began falling (indicating a volumetric depletion of hydrogen from the sample) after having reached and maintained a peak temperature for approximately 5 minutes, the cooling process was started and the test continued until the sample temperature fell below 180 °C. A plot illustrating both the heating and cooling processes and the partial pressure responses of the RGA as a function of time can be seen in Figure 4.16.

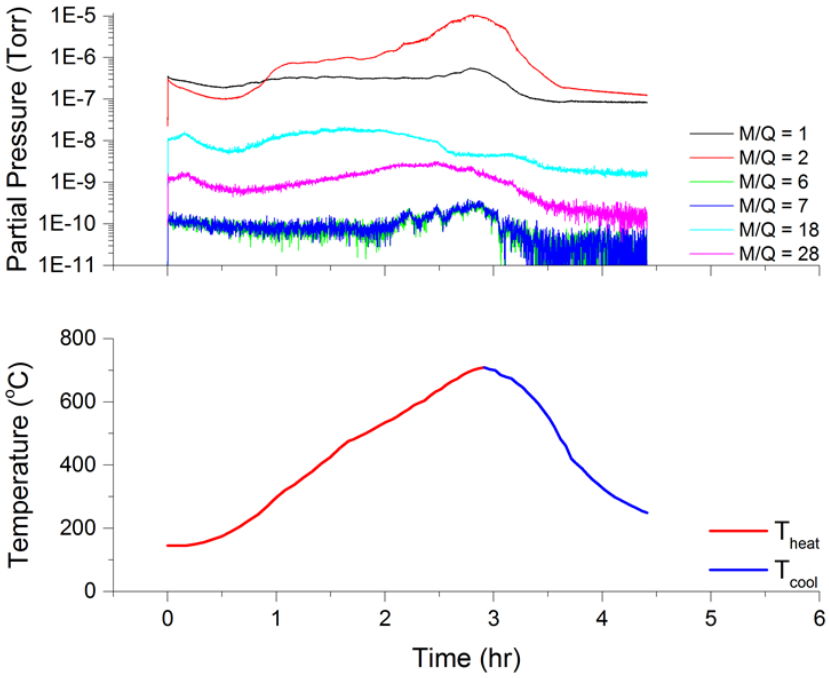

Figure 4.16: The partial pressure responses of the RGA and the temperature ramp rate as a function of time for the entirety of the LiH thermal decomposition test.

The RGA partial pressure trend scan in the top plot has the ordinate in logarithmic scale. The important information is mostly held within the highest two trends, which represent the H^+ and H_2^+ signals. The information contained in the molecular nitrogen trends illustrates the purity of the system, from the gaseous analysis perspective. The water and nitrogen signals never reached values much greater than 1 x 10^{-8} Torr, and were in fact often 3 to 4 orders of magnitude lower than the signals that were used for the majority of the RGA gas analysis. These results help to

justify the level of purity within the LiHDE chamber, which is important when considering the hygroscopic and chemical nature of both Li and LiH.

The results of the LiH decomposition tests will be broken down into individual sections detailing how the data gathered from each diagnostic contributed to the overall set of conclusions. A final, more inclusive, discussion section will confer how each of these individual results relates to the others, and additional information obtained from these comparisons. This chapter will then conclude with a section discussing the implications of this experiment and how it will contribute to the development of a larger scale isotope recovery system.

4.3.1 RGA Gas Analysis Results

The analysis of the components in the gas phase has always been the method of choice when evaluating sample chemistry. Previously described in detail, the ratio of components in this phase and how each evolves respective to temperature can help in determining the activation energy for release (or thermal decomposition in this case). To begin the analysis, one can first draw on the results illustrated in Figure 4.16. Without doing any data manipulation or applying any type of calibration factor, these data already relate two important points, at least from a qualitative standpoint. First, the impurity levels in the gaseous phase seem to be negligible with respect to the data of interest, as was previously stated. Second, the presence of signals representing ^{6}Li and ^{7}Li that climb above background noise at temperatures at or near 500 °C support the claim that decomposition of LiH in vacuum occurs well below even the melting temperature of LiH, at approximately 690 °C. While these points are important in justifying the integrity of the LiHDE system and RGA analysis technique, significantly more information can be found from the proper evaluation of the partial pressures and temperature dependence shown in Figure 4.16.

For the next step in the analysis it is important to note that the RGA pressure response for hydrogen does not represent the actual amount of hydrogen released in the system. Knowing the actual amount of gaseous hydrogen in the system is important because it acts as a check to ensure that the total amount of hydrogen released is not greater than the amount of hydrogen that was initially part of the LiH sample. Granted, some hydrogen will be released from heated surfaces or will be associated with the cracking pattern of water, but the fractions of hydrogen coming from

these species will likely be negligible for these analyses. To factor in that the total amount of hydrogen in the main portion of the LiHDE system was much greater than that which was registered by the RGA, a calibration, not unlike the one described in Section 4.2.2.1, was done with a 20 mTorr MKS Baratron attached to the main chamber. The peak corresponding to a mass of 2 AMU was then tracked and compared to the Baratron pressure in the main chamber using a controlled hydrogen leak. Figure 4.17 shows the consequence of this calibration, with the RGA pressure response shown on the left axis and the actual pressure, calibrated to the Baratron, shown on the right axis.

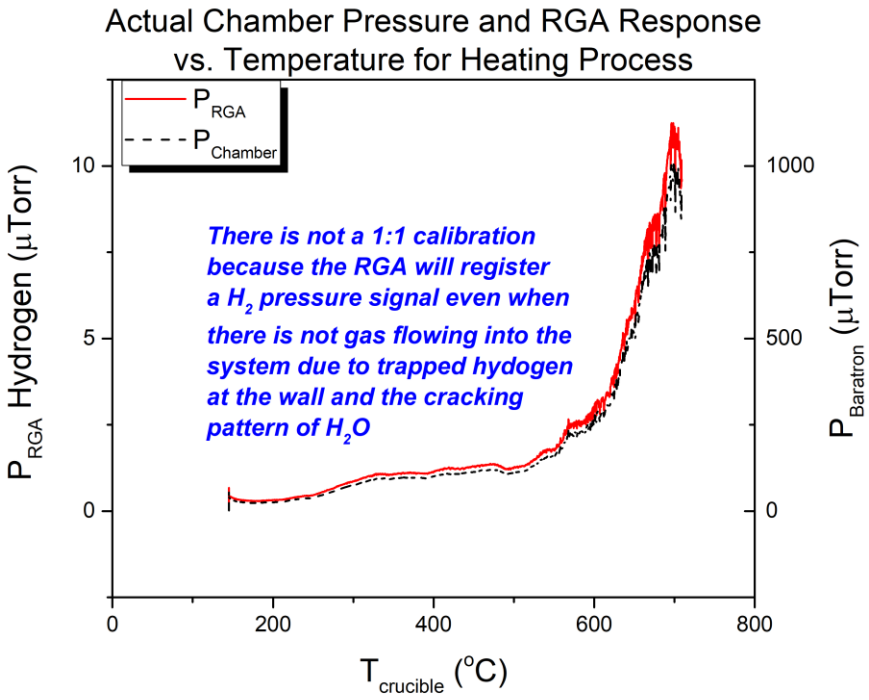

Figure 4.17: A plot of the RGA hydrogen response and the actual pressure in the chamber versus temperature for the heating process. As mentioned in the graph, there is not a direct 1:1 relationship between the two pressures due to the fact that the RGA will never register a zero pressure, whereas the Baratron will read 0.00 at base pressure.

With a sample size previously stated of 0.16 ± 0.07 g of LiH, the total pressure of H_2 that could possibly be released would correspond to 0.010 ± 0.005 moles. This corresponds to a maximum total hydrogen particle release dose of 3.01 ± 1.51 x 10^{21} H_2 molecules which will be

compared to the total amount released by integrating the evaluated release rate over the duration of the experiment, done as a check on the calibration procedure. After having gone through the total amount released evaluation, the amount of hydrogen evolved during the course of the experiment was found to be nearly 2.7 x 10^{21} H_2 molecules, which falls well within the upper limit defined by the total amount of hydrogen within the initial LiH sample. This means that about 88% of the hydrogen within the LiH sample was released during the experiment. This seems higher than what one might expect intuitively, but these calculations are quite approximate. The goal of the experiment, however, was to determine the maximum release rate as a function of temperature at the point where the sample volume started to become sufficiently depleted of hydrogen. This can even be seen in Figure 4.17, where the hydrogen signal began falling after having reached its peak evolution rate.

The next step in the analysis was to take the calibration described in Section 4.2.2.1 and correlate the instantaneous pressure measurement with a respective flow rate in Torr L s^{-1}. These evaluated flow rate data as functions of temperature can then be converted to the respective particle evolution rate by using the appropriate equation of state. For all the particle evolution rate data that will be presented, the molecular hydrogen registered by the RGA was considered ideal, in that the particle conversion rate can easily be related to the flow rate through the equation:

$$\dot{PV} = \dot{n}\Re T \tag{4.34}$$

where the term $\dot{PV}$ denotes the flow rate, $\dot{n}$ denotes the particle evolution rate, $\Re$ is the appropriate gas constant, and T is the gas temperature.

In addition to the application of the flow rate calibration, Dinh [18] reported that the total hydrogen that could have been present within a LiH sample can be considered to be entirely summed up within the molecular hydrogen signal (AMU = 2) and double the water signal (AMU = 18). Dinh's group summed this up by using a simple relationship for the hydrogen flux [18]:

$$\Gamma_{Hydrogen} = \Gamma_{H_2} + 2\Gamma_{H_2O} \tag{4.35}$$

where $\Gamma_{Hydrogen}$ represents the total hydrogen flux from the LiH sample, Γ_{H_2} represents the molecular hydrogen flux registered by the RGA, and Γ_{H_2O} represents the water flux registered by the RGA. Dinh's group [18] used this linear combination of fluxes to determine total hydrogen

evolution because the LiH samles were exposed to controlled amounts of water vapor prior to running TPD measurements. In doing so, the decomposition of the LiOH impurity layers on the surface of the sample will produce water vapor through the reactions [18]:

$$2LiOH(s) \rightarrow Li_2O(s) + H_2O(g) \tag{4.36}$$

$$2LiH(s) + H_2O(g) \rightarrow Li_2O(s) + 2H_2(g) \tag{4.37}$$

This is very important when considering LiH samples that have significant LiOH layers. This analysis, however, is less important for systems where the impurity layers are actively removed and/or minimized through the appropriate purging, evacuation, and baking procedures. This was the case in the data reported here, and it is plain to see from Figure 4.16 that the water vapor signal in the LiHDE system is orders of magnitude lower than the molecular hydrogen signal. The subsequent gas analysis, therefore, will focus primarily on the molecular hydrogen signal and its change with temperature. The results for the particle evolution rate over the duration of the experiment with respect to the crucible temperature can be seen in Figure 4.18.

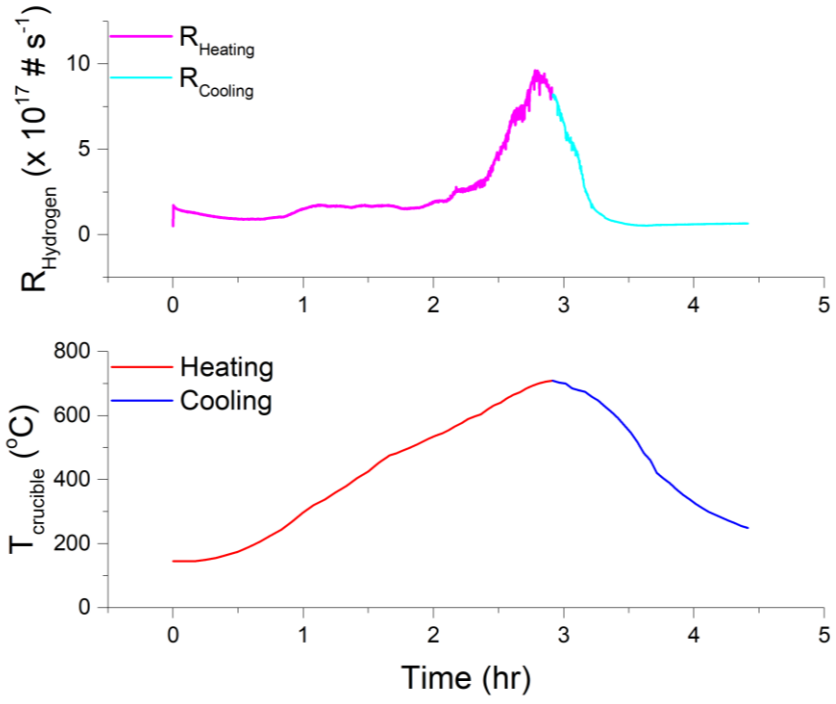

Figure 4.18: Results illustrating the instantaneous hydrogen particle evolution rate over the duration of the thermal decomposition experiment. This plot is stacked on top of the temperature vs. time plot to illustrate how the rates changed with temperature.

The plots in Figure 4.18 help in explaining the actual experiment and the procedure used to investigate the instantaneous evolution rates. The heating portion of the experiment was carried out until the molecular hydrogen signal started to decrease at elevated temperatures. This decrease in pressure, and ultimately particle evolution rate, signaled the point at which the sample volume became sufficiently depleted of hydrogen such that the thermal decomposition reaction mechanism began to be limited simply by the hydrogen atomic fraction in the sample, along with other mechanisms that previously played less of a role such as surface recombination. Essentially the sample went from a pure LiH state to a state where Li, LiH, and trapped hydrogen coexisted, which limited the amount of hydrogen that could be released per unit time. It is important to know what this peak is and how such an evolution peak corresponds to the amount of hydrogen initially within the sample because this will govern how hydrogen can be released.

A much clearer view of the evolution rate dependence on temperature during the heating process can be seen in Figure 4.18. The heating process is by far the more interesting of the processes when it comes to determining the peak evolution rate, because it is during this phase of the experiment that the thermodynamic information of the system can be evaluated. As mentioned before, the cooling phase of the experiment was started once the flux of molecular hydrogen started to decrease at elevated temperatures. A peak temperature of approximately 710 °C was reached and maintained for nearly 5 minutes before the cooling process was initiated. This is illustrated in the plot in Figure 4.19, along with a brief explanation of one of the peaks that is likely to be seen at lower temperatures if impurities within the chamber exist.

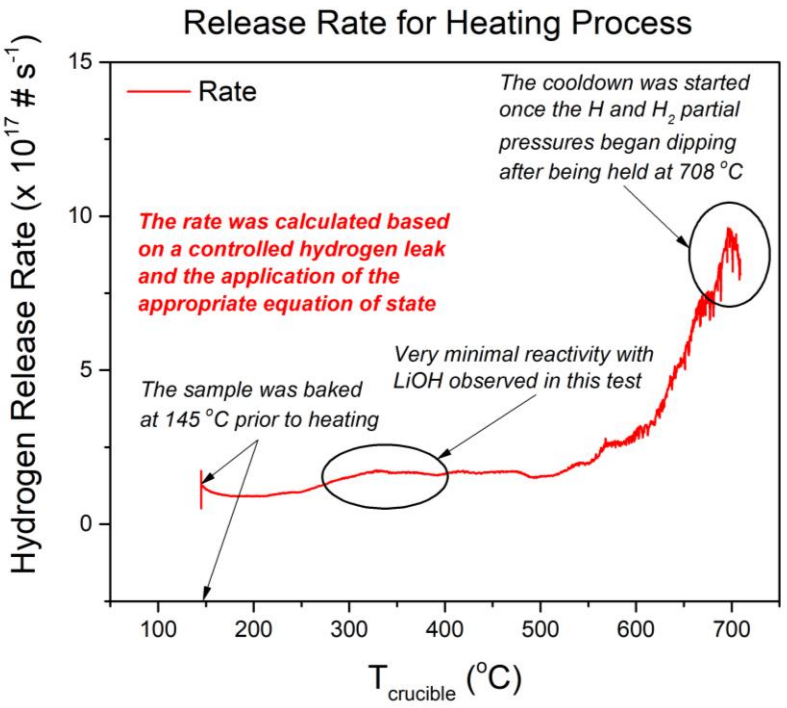

Figure 4.19: A summarizing plot for the hydrogen release rate during the heating process for the LiH thermal decomposition tests.

An important point to be made about the plot illustrated in Figure 4.19 is the fact that while there is a slight increase the evolution rate at around 300 °C, it is insignificant when compared with the primary peak at temperatures around 700 °C. TPD spectra that measure hydrogen evolution for LiH or hydrogenated Li are often plagued by the peak that occurs at temperatures between 300 and 350 °C because this implies a chemical reaction that occurs between LiH and LiOH is acting as a source of hydrogen gas. In these experiments, this peak was found to be minimal, likely due to the efforts taken to make sure the sample was kept as pure as possible, thereby decomposing the impurity layers at high temperatures under high vacuum conditions.

The most important take-away result from Figure 4.19 with regard to isotope recovery is the peak evolution rate seen at a temperature of approximately 696 °C. This rate was evaluated as $(9.6 \pm 1.2) \times 10^{17}$ H_2 particles s^{-1}. With a sample surface area of approximately 1.9×10^{-4} m^2, this equates out to an evolved flux of $(5.0 \pm 0.6) \times 10^{21}$ H_2 particles m^{-2} s^{-1}. The reason this surface area was chosen is that at the peak temperature, the LiH resistivity indicated a singular melt rather than

a powder (discussed in a later section), meaning that hydrogen was evolving from the now fully melted sample surface rather than from the surface of individual granules. These values will be discussed further in following sections, but the main implication from this is that given the wall particle loss rate from Krasheninnikov's work [52] is entirely made of D^+ and T^+ particles and that these ions are well diverted such that an overwhelming majority of them are lost within the divertor strike point, then the recovery flux can balance the loss flux at the wall. This would only be true, however, if the upstream treatment technologies were able to successfully separate pure LiD and LiT from the remaining lithium stream and deuterium and tritium could be recovered from this pure LiD and LiT. It is more likely that while there will be a LiD/LiT-rich stream, this stream will still not be at the 1:1 atomic ratio of hydrogen isotope to Li. This means that the peak evolution rate, while measured at the extreme case of pure LiH, is also a liberal estimate as to the attainable recovery rate.

Manipulating the data in Figure 4.19, one can evaluate the activation energy associated with this thermal decomposition by using the same analysis technique outlined in Section 4.2.2.1. This is done by taking the natural logarithm of the rate shown in Figure 4.19 and plotting this versus the reciprocal of temperature resulting in a decreasing linear trend with a slope equivalent to $\frac{-E}{\Re}$. A similar way of evaluating the same results is by directly relating the evolution rate to the inverse temperature and then fitting an exponential decay function to the resultant plot to evaluate the multiplicative factor in the exponent. This second method was employed for the evaluation of the activation energy for this process and the fit is illustrated in Figure 4.20. The activation energy evaluated using this method was found to be 95.7 ± 2.4 kJ mol^{-1}, which is within 6 % of the standard enthalpy of formation for LiH at 90.65 kJ mol^{-1} [53]. This difference is likely due to the propagation of error through the evaluation along with the error associated with the exponential fit. This value is also significantly lower than the standard bond dissociation energy for the Li-H bond, which is 247 kJ mol^{-1} [54], and the bond energy stored in the Li-H bond, which is reported to be nearly 1000 kJ mol^{-1} [55-57]. Dinh [18] also reported activation energies for his systems, which were composed of lithium hydride, lithium oxide, and lithium hydroxide. His purest hydride sample only had a 93 nm hydroxide, which had an activation energy of approximately 88 kJ mol^{-1}. The energy reported here is 9 % higher than Dinh's value [18], which is likely due to the chemical

reaction between the hydride and hydroxide which would occur in his contaminated samples, lowering the activation energy for hydrogen release.

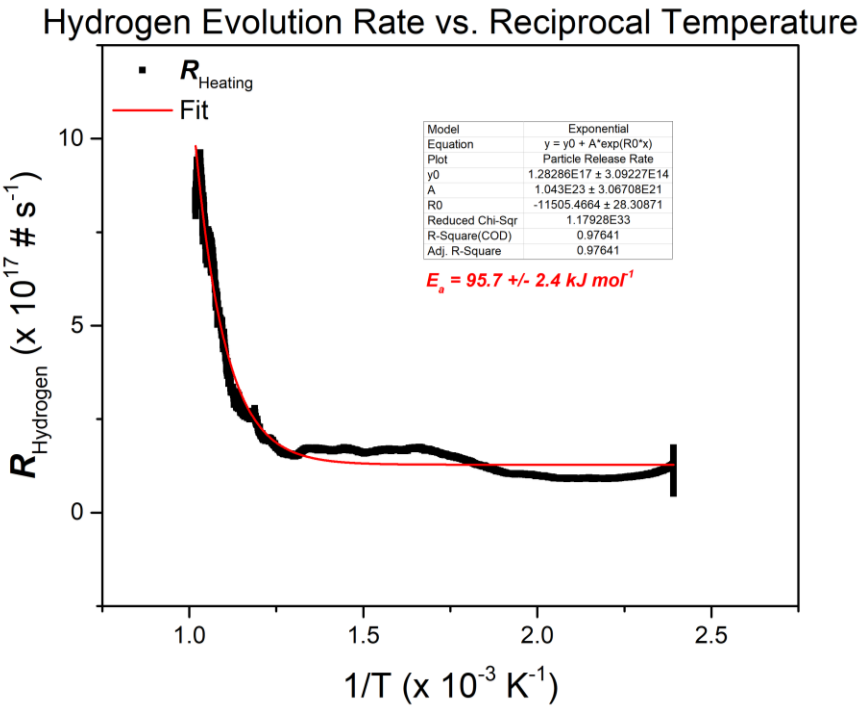

Figure 4.20: A plot illustrating the evolution rate vs. the inverse temperature. The fit of a decaying exponential trend is also displayed, which is used to find the activation energy.

While this gas analysis is very important in understanding a few of the fundamental thermodynamic parameters associated with the thermal decomposition of LiH as a surrogate for LiD and LiT, these measurements alone are not sufficient for obtaining a clear picture of the mechanisms for hydrogen recovery. At the very least, these results should be verified using an independent diagnostic technique with the ability to measure evolved Li vapor along with hydrogen during thermal decomposition. Along with this, using a technique that helps to understand the changes in the condensed phase will lend more credibility to the results obtained from the gas and vapor phase analyses.

4.3.2 Lithium Vapor Deposition Results

As a verification step for the gas analysis, the Li vapor was observed and its rate of condensation was measured through the use of a QCM that had line-of-sight to the surface of the sample. The QCM was not temperature-controlled for the duration of the experiment, which is why the use of a dual QCM was imperative for screening out the effects that thermal noise had on frequency. The QCM used was an INFICON Front Load Dual Sensor and each crystal was measured through the use of an Inficon STM-2 integration and interpretation circuit. The outputs from the STM-2 modules were monitored digitally using the associated Inficon STM-2 software. The software outputs 2 data sets, both based on the changes in frequency, as described in Section 4.2.2.2. Luckily the STM-2 modules already take into account the appropriate analysis methods discussed in the previous section, so no excess interpretation was necessary beyond subtracting the signals of the closed QCM from those of the open QCM.

The STM-2 software returned 2 sets of data, with each scan type being reported as a function of time for the duration of the experiment. The first set of data collected corresponded to the instantaneous deposition rate, which used changes in frequency between the current and previous time step to define the deposition rate. Because of the way this data set is analyzed, it is susceptible to significant noise, with the usable data being drowned out by this same noise. A plot illustrating the instantaneous deposition rate over time for the duration of the thermal decomposition experiment can be found in Figure 4.21.

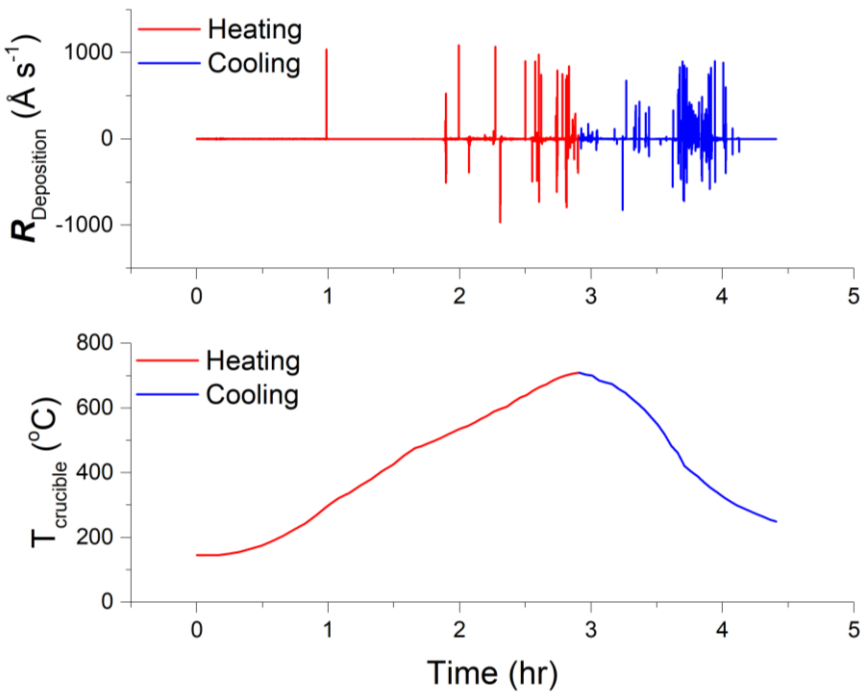

Figure 4.21: Plots illustrating the change in the deposition rate registered by the QCM relative to the LiH decomposition temperature profile.

Unfortunately, not much information can be gained from the plots shown in Figure 4.21. Because the STM-2 modules and the software likely interpret the deposition rate values based on information only from the previous time step, then rate measurements will always be plagued by significant levels of noise. In lieu of these issues, more information can be obtained by looking at a similar plot, showing the thickness as a function of time for the same decomposition experiment. Smoothing this curve and applying an appropriate finite difference evaluation technique, one can obtain much more reasonable deposition rate values. The thickness registered by the QCM as a function of time, along with the associated temperature profile, is shown in Figure 4.22. It is important to state that the material deposited on the surface of the crystal was assumed to be almost purely Li. The reason for this will be explained in detail in a few paragraphs.

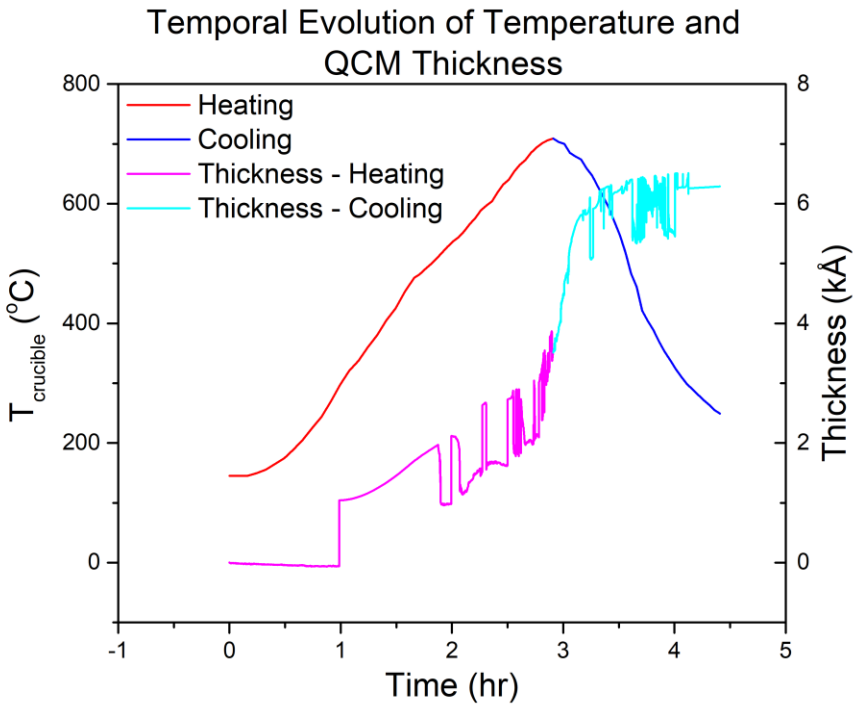

Figure 4.22: A plot describing the temperature profile and the thickness value registered by the QCM for the duration of the LiH decomposition experiment.

While smoothing and applying the appropriate fit to the thickness curve shown in Figure 4.22 gives a set of data that is significantly easier to interpret than either the data from Figure 4.21 or the raw thickness data from Figure 4.22, there are still a couple of assumptions and calculations that need to be made to directly correlate these data to the RGA gas analysis data. The most important assumption used to evaluate the Li evaporation/condensation rate is that the layer deposited on the surface of the QCM is entirely composed of pure Li. This assumption is not farfetched, with a few studies relating that the co-deposited atomic fraction of hydrogen alongside lithium is minimal. After fully flushing out the calculations, it was found that the peak evaporation/condensation rate for Li was approximately (1.7 ± 0.2) x 10^{18} Li particles s^{-1} at a temperature of 701 °C. With the assumption that the entirety of the deposited layer is lithium, this correlates extremely well with the peak hydrogen evolution rate measured with the RGA, when considering the chemical reaction:

$$2LiH \rightarrow H_2 + 2Li \tag{4.38}$$

Therefore, 2 moles of lithium need to be evolved for every one mole of molecular hydrogen. Since the peak molecular hydrogen rate was evaluated to be 9.6×10^{17} H_2 particles s^{-1}, the total amount of lithium that would theoretically be deposited should be closer to 1.9×10^{18} Li particles s^{-1}. The measured rate is therefore 11.5% off from the expected rate. This discrepancy can easily be explained by the evaluation procedures for both sets of analyses and the error that propagates along with each measurement type.

Stated previously was the assumption that the condensate being deposited onto the exposed crystal was very nearly pure Li. Two explanations can be used to justify this claim. First, the oxygen partial pressures in the chamber throughout the experiment were negligible when compared with the presence of other species. This justifies the fact that the oxide does not contribute significantly to the film composition. Another piece of evidence in support of this claim is that after the test had concluded, the QCM thickness was monitored as the chamber was slowly vented with air. Drastic changes in the frequency and thickness readings were observed during the venting process, lending more credibility to the assumption that the deposit could be considered almost entirely composed of Li.

While the RGA gas analysis and the Li vapor deposition analysis are in relatively good agreement, given the number of assumptions made to justify each technique, neither of these techniques directly measure changes that happen in the LiH condensed phase. A few inferences about the composition and phase changes can be drawn from an in-depth analysis from these two data sets, but a more thorough look at how the LiH solid changes phase and/or composition during heating and cooling can aid in diagnosing the entire system. The following section will describe the resistivity measurements made during the thermal decomposition experiment, with resistivity change being the technique chosen for the condensed phase investigation.

4.3.3 Condensed Phase Resistivity Results

As has been mentioned numerous times throughout this chapter, most studies focusing on hydrogen isotope reclamation and how different factors affect retention have used measurements from an RGA as the primary data of interest. While this may well relate to the amount of hydrogen absorbed in lithium exposed to various hydrogen environments, these investigations do nothing to

look at what is happening in the condensed phase during exposure or the subsequent decomposition. These analyses are also often post-mortem, in that the information on the amount retained in the sample is not investigated until after the lithium has been exposed.

Techniques to analyze the changes in the condensed phase during exposure are also quite complicated to implement. Often, surface chemistry analyses such as X-ray photoelectron spectroscopy (XPS) or low-energy ion scattering spectroscopy (LEISS) require that the sample also be examined post-exposure. For this system, the condensed phase diagnostic pioneered by Adams' group [16, 17] can be quite useful in correlating measurements of resistance across a sample to composition and phase changes. sThis same technique can measure real-time sample changes during both exposure and decomposition. For these reasons, along with its ease of use, resistivity was employed during the LiH decomposition experiment described in this chapter and the absorption/solubility experiments described in the next chapter.

The resistance was measured through the LiH sample by using concentric stainless steel electrodes set up positioned within the sample crucible as was shown in Figure 4.3. Resistivity is an intrinsic property of a material and relates to the measurable quantity of resistance through the equation:

$$\rho\ (\Omega\ m) = \frac{R\ (\Omega)\ 2\pi\ h\ (m)}{\ln(\frac{b}{a})} \tag{4.39}$$

where ρ is the resistivity, R is the resistance, h is the height of the sample through which the resistance is being measured, b is the inner radius of the outer electrode, and a is the radius of the inner electrode. By knowing the radii for the two electrodes and the height of the sample placed in the crucible, the resistivity can be determined. This was done for the duration of the LiH thermal decomposition experiment. The resulting resistivity plot with respect to sample temperature is shown in Figure 4.23.

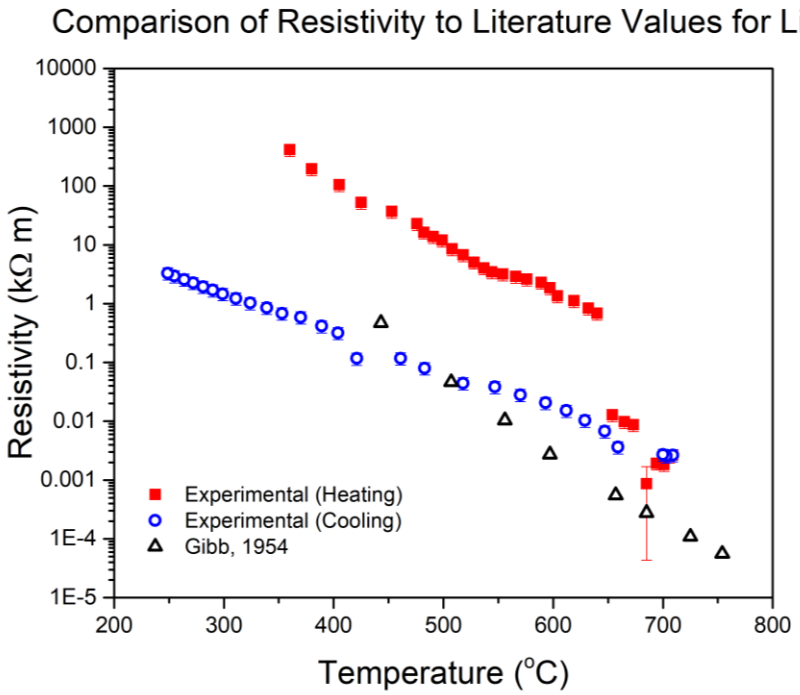

Figure 4.23: The resistivity measurements for the LiH thermal decomposition and how the resistivity for both the heating and cooling processes compares to the literature values for the resistivity of LiH as a function of temperature [48].

Before taking the data from Figure 4.23 and making correlations between it and the previously reported data for the LiH thermal decomposition, it is important to define why there are discrepancies when compared with values reported in the literature [48]. First, the discrepancies between the data measured for the heating phase and the literature will be explained. Up to a point where the sample reached a temperature of approximately 650 °C, the measured resistivity values seemed to a follow a similar logarithmically decreasing trend to the trend reported in Gibb, Jr.'s 1954 report [48]; however, experimental values were still orders of magnitude higher. At a temperature of nearly 650 °C, there was a large drop in the measured resistivity. This drop put the subsequently measured resistivity values within reasonable error of those reported in Gibb, Jr.'s report. At first glance, the experimental values seem to be in error, but the knowledge of the initial state of the LiH sample sheds light on these uncertainties. The LiH that is loaded into the sample crucible is loaded as a very fine powder, while Gibb, Jr.'s samples were single crystals. The fact that the sample remains a powder for most of the decomposition experiment means that the voids

in between LiH granules will affect the measured electrical properties. The reason this becomes a non-issue at temperatures above the 650 °C mark is likely due to a significant phase change, in which the LiH powder melts into a single liquid condensed phase, which puts the measured resistivity values within error of the literature values.

Exploring how the presence of voids between the powder granules affects the electrical properties of the sample requires a bit more investigation. In an analogous system, Marinho's group measured the conductivities for graphite powders relative to those in samples of graphene [58]. Based on the theoretical considerations for powder porosity described in Reference [58] and the effects porosity has on conductivity, the plot in Figure 4.24 was obtained. The value of 0.36 was considered the minimum powdered sample porosity because it represents the closest packing fraction for randomly dispersed spheres [59]. It is important to note that this theory holds well for the graphite systems described in Reference [58], but may not hold well when considering ionic materials such as LiH. The relationship that was applied to compare the electrical properties of the sample to the porosity is given by [58]:

$$\sigma_E = 40.6\ \sigma_0\ \varphi^4\ [\frac{\Gamma(1-\nu^2)}{ED}]^{1/3} \tag{4.40}$$

where σ_E is the effective conductivity, σ_0 is the conductivity of the pure material (LiH in this case), φ is the volume fraction occupied by the LiH powder, Γ is the interfacial energy between individual LiH granules, ν is the Poisson's ratio of LiH, E is the Young's modulus for LiH, and D is the average particle diameter. The interfacial energy was determined to be approximately 200 mJ m^{-2} using the values from Reference [60], while Reference [61] provided the Poisson's ratio (0.08) and Young's modulus (76.2 GPa) for LiH. Sigma Aldrich references that the 99.4% pure LiH powder used in the experiment has an approximate average particle diameter of 100 micrometers.

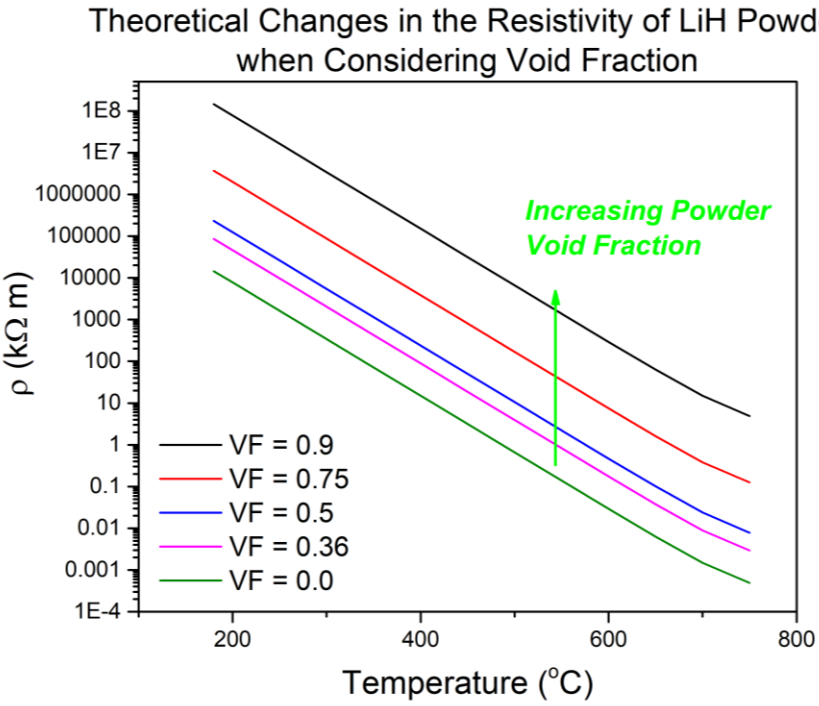

Figure 4.24: A plot illustrating how the void fraction modifies the resistivity for LiH, based on the theory described in Reference [58]. The black line at the bottom follows the same trend reported by Gibb, Jr. [48].

It is clear from Figure 4.24 that as one increases the porosity of the sample the electrical properties drastically differ from single crystal samples (LiH in this case). This can be compared to the experimental resistivity results and can be used to explain the variation between measurements and the previously reported LiH resistivity values [48]. Illustrating this point, the plot in Figure 4.25 is modified from Figure 4.23 to include how the powder void fraction modifies the resistivity.

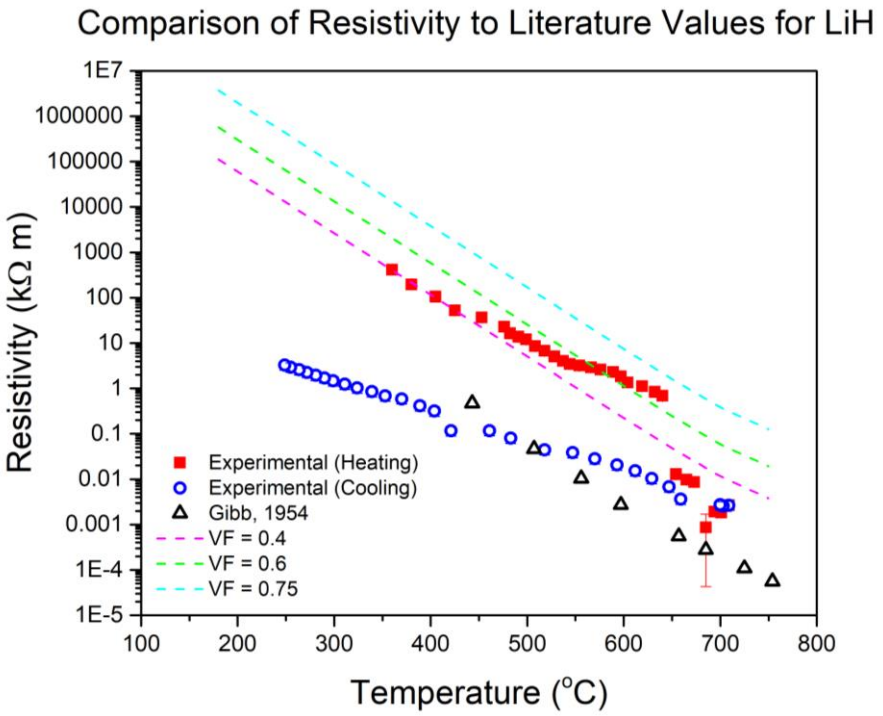

Figure 4.25: A graphic depicting how the initial void fraction [58] in the powdered LiH sample affects the resistivity measurement when compared to Reference [48].

While the discrepancy between the resistivity values during the heating phase of the experiment and those reported by Gibb, Jr. [48] are easily explained by considering that the LiH is initially a powder, there is also interesting information within the measurements made during the cooling phase of the experiment. The phase change that occurred during the heating portion of the experiment at 650 °C permanently changed the sample, which is clear when looking at the hysteresis associated with the differences between the heating and cooling curves. The drop in resistivity at 650 °C brought the measured values closer to those reported in literature; however, even during the cooling phase of the experiment, resistivity values began to significantly deviate from the accepted values. Within this deviation lies a connection to the composition of the sample remaining within the crucible.

Applying the same Reynolds and Hough theory [50] that was mentioned in Section 4.2.2.3, an inference as to the composition of the mixture in the sample may be drawn, specifically for the case of the cooling phase of the experiment. If the Reynolds and Hough theory were to apply to

this system and assuming that the LiH remained the continuous phase even well into the Li-rich regime, then the plots trends shown in Figure 4.26 may demonstrate what is happening to the sample upon cooling. Especially when considering that significantly less hydrogen was being evolved during the cooling process, it is likely that the remaining condensed phase would have a much higher concentration of pure Li, but this is only true at temperatures below approximately 450 °C, when Li evaporation becomes a less dominant loss mechanism. If the shift in electrical properties to the point where Li was the continuous phase were to occur, then it is likely that the drop in resistivity during cooling would be even greater than what was observed, again based on predictions made using the Reynolds and Hough theory.

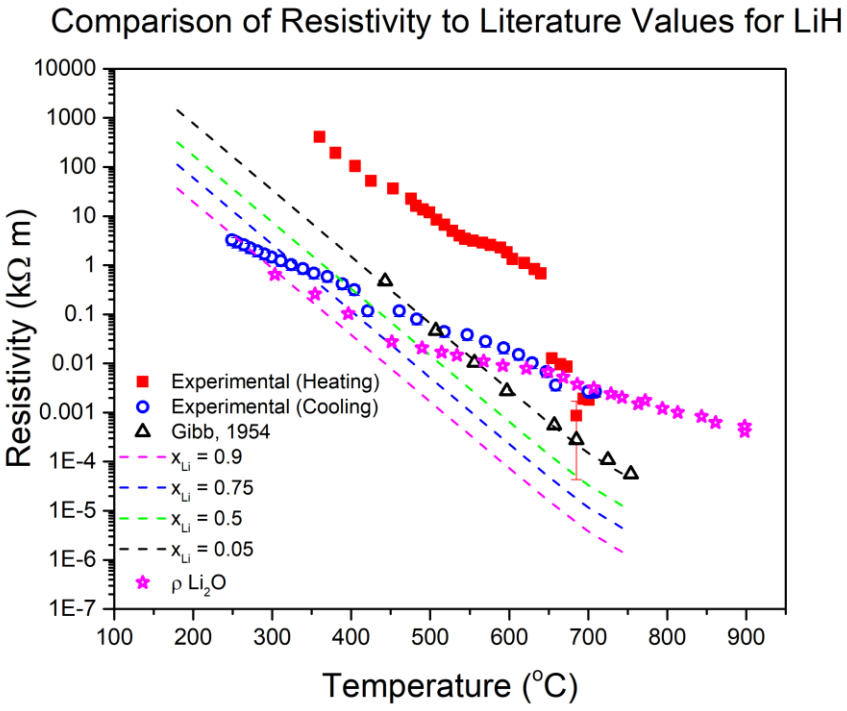

Figure 4.26: Comparing the hysteresis observed in the resistivity measurements during the cooling phase of the thermal decomposition experiment to predictions of the sample composition made using Reynolds and Hough theory [50] and assuming that LiH remained the continuous phase of the sample even well into a Li-rich sample composition. Also plotted is the comparison to the literature values for the resistivity of Li_2O as a function of temperature [51].

From previous discussions, it is obvious that the Reynolds and Hough theory does not extrapolate well to these kinds of systems where a β-rich phase is still considered dispersed and the α phase remains continuous. While a more sophisticated analysis using appropriate composition weighting with temperature may be required, inferences can still be drawn from the application of this incomplete theory to the resistivity measurements made during the cooling process. The most notable conclusion drawn from Figure 4.26 is that upon cooling, the sample does indeed exhibit behavior corresponding to a mixture of Li and LiH, if the system is still assumed binary.

It also seems from the cooling trend that the more the sample is cooled, the more influence the remaining Li has on the electrical properties. This may be due to more Li remaining in the sample than LiH, but it may also be that the Li becomes more of a continuous medium and less of a dispersed phase. Another point of interest from Figure 4.26 is the fact that the effect that Li has on the sample resistivity starts to become more pronounced at temperatures less than approximately 450 °C. Essentially what this is saying is that upon cooling the sample to temperatures below the approximate threshold where evaporation tends to dominate a Li system, the Li that remains within the sample and greatly affects the properties of the sample. The corresponding decrease in the presence of the LiH may be due in large part to the dissolution within the now Li-dominant mixture, as governed by the thermodynamic principles described earlier in the chapter.

While these data may be well described by the presence of both Li and LiH remaining in the mixture, it is difficult to reconcile this with literature values for the resistivity of Li_2O as a function of temperature [51]. The experimental data during cooldown follows the trend for Li_2O too well to ignore, but is counter-intuitive when considering the data in both Figure 4.16 and Figure 4.19. Figure 4.16 indicates that there is only a very small fraction of water in the gaseous mixture, and from Figure 4.19, it is clear that there is minimal influence of LiOH on the hydrogen release process. If the lithium hydride were to have been fully converted to lithium oxide by the time the sample had cooled, then there would likely be significantly more water present in the gaseous mixture and there would be a greater TPD peak at temperatures between 300 and 400 °C, being evidence of chemical interactions occurring between the LiH and the LiOH. Because the system is not binary, as is the case when considering the Reynolds and Hough theory [50], it is too

complicated from resistivity analysis alone to deconvolute the effects that other chemical species may have on the measured resistance. This is especially true since most ceramics exhibit the same trends in electrical properties with respect to temperature, especially if those ceramics are partially comprised of Li. To verify resistivity analyses in future works, the author suggests using a separate surface chemistry analysis technique if available.

While the conclusion that after a sample of pure LiH has reached its peak evolution rate, and the control volume has started to become sufficiently depleted of available hydrogen, there remains Li which begins to dominate the properties at lower temperatures, this conclusion does not hold as much weight with regards to the isotope reclamation process as do other conclusions. This is especially true when considering the presence of other impurity species. Probably the most important conclusion from these resistivity data is that at a temperature of approximately 650 °C, the precipitate will likely agglomerate and melt. In comparison to the results from the RGA gas analysis, this temperature does not mark either the point at which hydrogen evolution begins to dramatically increase nor does it mark the peak evolution temperature; however, it does tell us that a LiH treatment system maintained above this temperature will evolve hydrogen at appreciable rates, with fluxes that evolve from a single molten surface, rather than through the combination of a large number of volumetric processes. Discussion on how these data relate to the data obtained from the RGA gas and the Li vapor deposition analyses will be the topic of the following section.

4.3.4 Correlating Results from Multiple Diagnostics

Each of these results, when considered separately, contains a lot of valuable information to be learned about the process by which pure LiH thermally decomposes. However, combining the results of these diagnostics leads to stronger conclusions, especially when considering what this means for hydrogen isotope reclamation technologies. This section will draw comparisons among the data obtained from previously mentioned diagnostics, and demonstrate how the relationships among them plays a bigger role in obtaining a more fundamental understanding of the system from the macro-scale.

The first conclusion that can be made by including the results gathered from more than one diagnostic was already briefly touched on in Section 4.3.2. This was based on the idea that given

the deposit on the surface of a QCM was entirely composed of Li that the peak evaporation/condensation rate measured through the independent use of the dual QCM system verified the peak hydrogen evolution rate measured by the RGA. For every one mole of molecular hydrogen released, two moles of lithium must also be released, which was very close to the ratio of hydrogen release to lithium deposit. In fact, doubling the peak evolution rate of hydrogen would have only been 11.5% off from the Li deposition rate onto the surface of the QCM. This is quite an amazing result, since the evaluation of the lithium deposition rate from the QCM thickness measurement was very approximate, which is likely where most of the error lies. Essentially, these two independent diagnostics verify each other quite nicely with regard to decomposition rate measurements.

Another conclusion can be drawn from the combination of the RGA gas analyses and the condensed phase resistivity analyses. These data are plotted in Figure 4.27 for the heating phase of the experiment. The previous section describing how the electrical properties of the condensed phase were affected by temperature concluded that reaching temperatures in excess of 650 °C would be important for any future isotope reclamation recovery system. How this temperature relates to the peak evolution rate measured by the RGA becomes clearer when investigating the relationship between the data gathered from the two diagnostics.

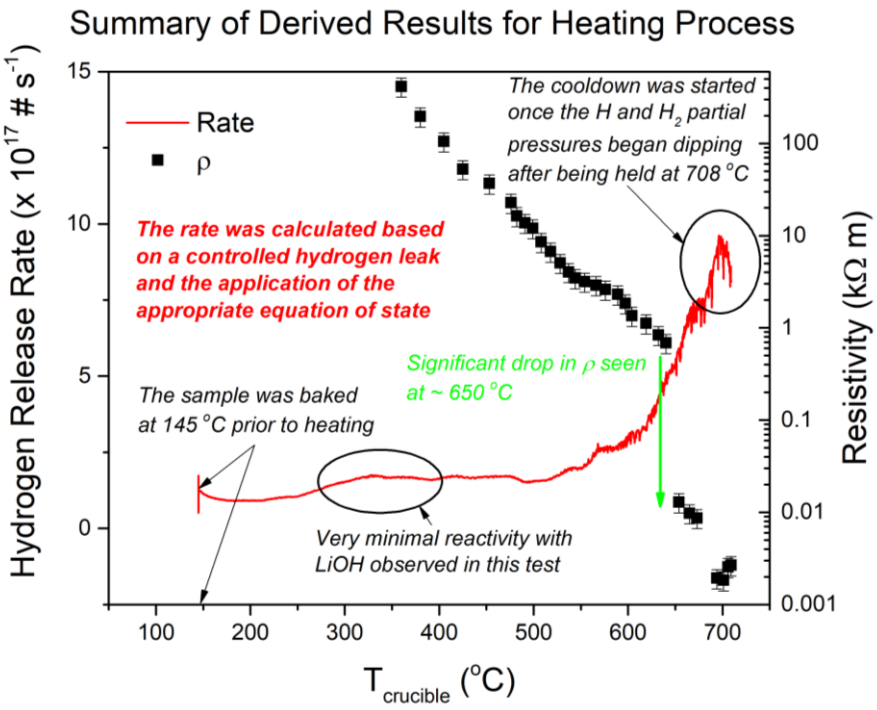

Figure 4.27: A summarizing plot showing the resistivity and release rate as a function of temperature.

A lot of information is embedded within Figure 4.27, but the most important figures of merit are those relating key temperature values, changes in phase, or peak evolution rates. From this plot, we get two key temperatures: the first where the pronounced drop in resistivity occurs at approximately 650 °C and the second at the point where the peak hydrogen evolution takes place at nearly 696 °C. Obviously, the phase change of the sample occurs at 650 °C, with molten LiH being the compound most likely left within the crucible. If Li were to be produced at these elevated temperatures, it would evaporate and escape the crucible along with the hydrogen. If lithium oxide were to be produced, there would be greater evidence of this chemical reaction in the hydrogen and water peaks at temperatures between 300 and 400 °C. Finally, the peak evolution rate registered by the RGA at approximately (9.6 ± 1.2) x 10^{17} s^{-1} corresponds to a temperature of 696 °C. This means that the most hydrogen that can be recovered from pure LiH will occur at temperatures above the melting point of lithium hydride. This temperature will be slightly less for deuterium and LiD, and even less still for tritium and lithium tritide because of the bonding strengths of these materials relative to the LiH surrogate used for these experiments.

A plot similar to Figure 4.27 is shown in Figure 4.28, but these data show the effects that cooling the sample has on both the resistivity and hydrogen evolution rate. While the temperature drop during the cooldown phase of the experiment was slightly faster than the temperature ramp was during the heating phase, it is interesting to see that the hydrogen evolution rate also exhibits some hysteresis. This is evident in the fact that the rate changes much more dramatically with temperature than it did during the heating phase of the experiment. This indicates that the heats that were previously able to produce appreciable evolution rates even at temperatures below the peak value of 696 °C were no longer sufficient to maintain that level of hydrogen release. This is probably due to the sufficient depletion of hydrogen from the sample, whereby lower atomic fractions of hydrogen now exist in the crucible and require more energy to diffuse to the surface, recombine with another hydrogen, and evolve as a molecular species.

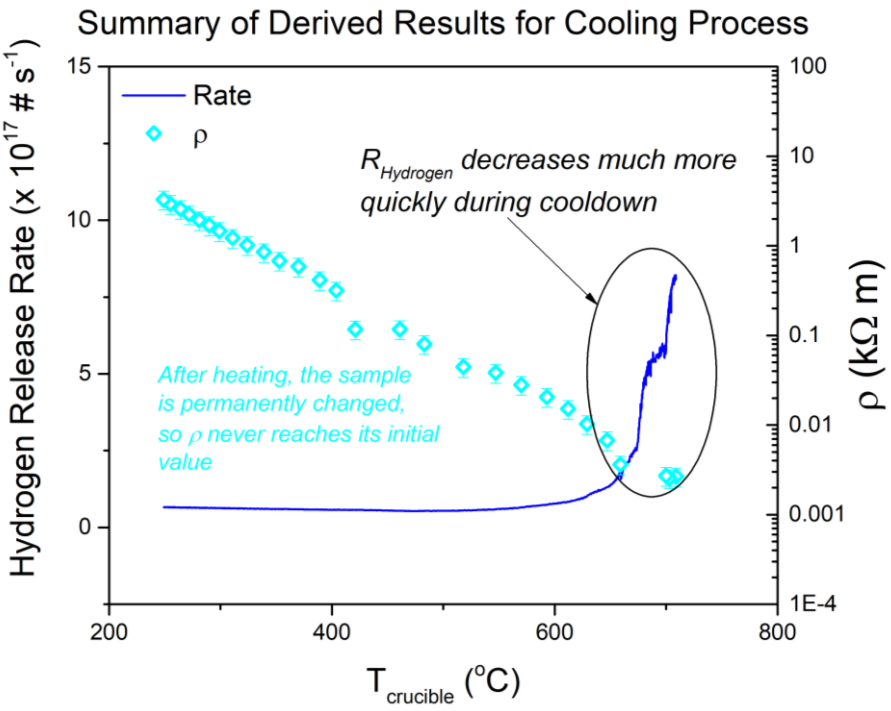

Figure 4.28: The evolution rate and resistivity change versus temperature for the cooldown phase of the LiH thermal decomposition experiment.

The stark drop in evolution rate during cooldown is also corroborated by the Li condensation results. From Figure 4.22, it is plain to see that the deposit on the QCM asymptotically approached a peak thickness of approximately 6.3 kÅ quite rapidly during the cooldown phase of the experiment. Alternatively, the build up to the peak condensation rate during the heating phase of the experiment was much slower, with the dependence on temperature being much more pronounced. This means that the sufficient depletion of hydrogen from the sample volume affects not only the hydrogen evolution rate, but also the accompanying lithium evaporation rate. This is quite an interesting result, since one could infer that below a threshold temperature and with a less-than-sufficient hydrogen atomic fraction, the remaining LiH-Li-H system inhibits lithium evaporation, possibly through a stronger bonding mechanism.

Each of these sets of results corresponding to a combination of diagnostics, along with the results gathered from each diagnostic individually, are quite informative when considering hydrogen recovery from a system with pure, or nearly pure, LiH as the initial material. The implications of these data and how they will affect hydrogen reclamation treatment options will be discussed in the following section. The conclusions that can be drawn from these results are quite promising; however, they need to be discussed within the context of a larger lithium loop system.

4.4 Conclusions and Future Work

The goal of this chapter was to investigate the decomposition and subsequent hydrogen evolution from pure lithium hydride. Of particular interest was the peak value for the flux of molecular hydrogen from the surface of the sample and the sample temperature associated with this flux. A number of diagnostic tools operating in parallel were used during experimentation, and the results from each were analyzed to understand the thermochemistry in hydride decomposition. The goal was to determine if treatment of LiD and LiT would sufficiently compensate the in-vessel loss of tritium and deuterium to the wall.

4.4.1 Conclusions

The most important conclusions from this chapter can be summed up in the following list:

- Lithium hydride (LiH) was heated in a temperature-programmed desorption chamber to investigate the thermochemistry behind the decomposition and desorption of hydrogen in nearly pure samples.
- A stark drop in resistivity, observed at 650 °C, indicates a phase change in the LiH. Beyond this temperature, the sample can be considered as a single molten entity. This allows the release flux to be evaluated based on the surface area associated with the crucible geometry. This surface area was evaluated to be 1.9×10^{-4} m^2.
- The peak evolution rate was found to be $(9.6 \pm 1.2) \times 10^{17}$ H^2 particles per second at a temperature of 696 °C. This evolution rate was corroborated by lithium vapor deposition results, which indicated a nearly ideal stoichiometric lithium deposition rate on a quartz crystal microbalance. Based on the previous point, this evaluates to a release flux of nearly 5×10^{21} H_2 particles m^{-2} s^{-1}.
    - Using the results for wall loss evaluated by Krasheninnikov's group [52] and assuming that the particles that are lost are well diverted and evenly distributed across a 10 m^2 strike point [62], then the loss flux is on the order of 3×10^{21} m^{-2} s^{-1}. The peak recovered flux should be more than sufficient to balance wall losses.
    - The peak release flux from this study is nearly identical to those reported by Baldwin [40], even though his sample was at a mole ratio of 80 % (0.8 mol H : 1 mol Li).

4.4.2 Future Work

- A more decisive study can be done with a sample composed of entirely pure lithium deuteride (LiD). This will eliminate uncertainties associated with residual water and impurities in the chamber.

- Because of the ability to exceed wall loss by heating a sample of pure LiH, the author recommends upstream separation technologies be employed, so that LiD and LiT salts be treated separately from the remaining lithium stream.

4.5 References

[1] E. Veleckis, E.H. Van Deventer, M. Blander, “The Lithium-Lithium Hydride System”, *J. Phys. Chem.* 78 (1974) 1933.

[2] E. Veleckis, “Thermodynamics of the Lithium-Lithium Deuteride System”, *J. Phys. Chem.* 81 (1977) 526.

[3] E. Veleckis, R.M. Yonco, and V.A. Maroni, “SOLUBILITY OF LITHIUM DEUTERIDE IN LIQUID LITHIUM”, *J. Less-Common Met.* 55 (1977) 85.

[4] E. Veleckis, “DECOMPOSITION PRESSURES IN THE (α + β) FIELDS OF THE Li-LiH, Li-LiD, AND Li-LiT SYSTEMS”, *J. Nucl. Mater.* 79 (1979) 20.

[5] C. E. Messer. "A Survey Report on Lithium Hydride." AEC Research and Developrnent Report No. NYO-9470 (1960).

[6] F. K. Heumann, O. N. Salmon, "The Lithium Hydride, Deuteride, and Tritide Systems”, USAEC Report No. KAPL-1667 (1956).

[7] H. R. lhla, C. H. Wu, “Mass-Spectrometric Knudsen Effusion Measurements of Vapor Species in the System Lithium-Hydrogen”, Report No. EUR-4938. p 89, from the 7th Symposium on Fusion Technology, Grenoble. France, Oct 1972.

[8] G. M. McCracken, D. H. J. Goodall, and G. Long, “The Extractlon of Tritium from Liquid Lithium”, IAEA Workshop on Fusion Reactor Design Problems, Culham, United Kingdom, February 1974.

[9] E.E. Shpil’rain, K.A. Yakimovich, T.N. Medl’nikova, A. Ya. Polischuk, *Thermophysical Properties of Lithium Hydride, Deuteride and Tritide*. Springer Science and Business Media, 1987.

[10] H. Katsuta, T. Ishigai and K. Furukawa, “Equilibrium Pressure and Solubility of Hydrogen in Liquid Lithium”, *Nucl. Technol.* 32 (1977) 297.

[11] P. Hubberstey, R. J. Pulham and A. E. Thunder, “Depression of the freezing point of lithium by nitrogen and by hydrogen”, *J. Chem. Soc. Faraday Trans.* 72 (1976) 431.

[12] V. A. Maroni, R. D. Wolson and G. E. Staahl, “Some preliminary considerations of a molten-salt extraction process to remove tritium from liquid lithium fusion reactor blankets”, *Nucl. Technol.* 25 (1975) 83.

[13] E. E. Shpilrayn, K. A. Yakimovich, D. N. Kagan and V. G. Shvalb, *Fluid Mech.-Sov. Res.* 3-4 (1974) 3.

[14] R. Hultgren, R. L. Orr and K. K. Kelly, “Selected values of the thermodynamic properties of metals and alloys”, January 1970 supplement, Inorganic Materials Research Division, Lawrence Radiation Laboratory, Berkeley, University of California.

[15] F. J. Smith, J. F. Land, G. M. Begun, J. T. Bell, “Equilibria in Hydrogen-Isotope-CTR-Blanket Systems”, Chemistry Division Annual Progress Report No. 0ORNL-5111, Oak Ridge National Laboratory, Oak Ridge,Tenn. (1976) 26.

[16] P.F. Adams, M.G. Down, P. Hubberstey, R.J. Pulham, “SOLUBILITIES, AND SOLUTION AND SOLVATION ENTHALPIES, FOR NITROGEN AND HYDROGEN IN LIQUID LITHIUM”, *J. Less-Common Met.* 42 (1975) 325.

[17] P.F. Adams, M.G. Down, P. Hubberstey, R.J. Pulham, “Solutions of Lithium Salts in Liquid Lithium: The Electrical Resistivity of Solutions of Nitride, Hydride and Deuteride”, *J. Chem. Soc., Far. Trans.* 0 (1977) 230.

[18] L.N. Dinh, M.A. Schildbach, R.A. Smith, D.M. Grant, B. Balazs, and W. Mclean II, “Hydrogen Outgassing From Lithium Hydride”, *Report for Lawrence Livermore National Laboratory: Nuclear Materials Research Developments* (2006).

[19] HSC Chemistry software, Outokumpu Research Oy, Finland.

[20] S.M. Meyers, “Ion-backscattering study of LiOH-to-Li_2O conversion on a LiH substrate”, *J. Appl. Phys.* 45 (1974) 4320.

[21] L.N. Dinh, C.M. Cecala, J.H. Leckey, M. Balooch, “The effects of moisture on LiD single crystals studied by temperature-programmed desorption”, *J. Nucl. Mater.* 295 (2001) 193.

[22] L.N. Dinh, W. McLean II, M.A. Schildbach, J.D. LeMay, W.J. Siekhaus, M. Balooch, “The nature and effects of the thermal stability of lithium hydroxide”, *J. Nucl. Mater.* 317 (2003) 175.

[23] C.H. Bamford, C.H.F. Tipper, *Comprehensive Chemical Kinetics: Reaction in the Solid State,* Elsevier, Amsterdam 22 (1980) 41.

[24] K. Heide, W. Holand, H. Golker, K. Seyfarth, B. Muller, R. Sauer, “Die bestimmung kinetischer parameter endothermer zersetzungsreaktionen unter nicht-isothermen bedingungen”, *Thermochim. Acta* 13 (1975) 365.

[25] A.M. Gadalla, “Kinetics of dissociation of hydrated cerium(III) sulfate, nitrate and oxalate in air”, *Thermochim. Acta* 95 (1985) 179.

[26] Galwey A. K., Brown M. E., *Thermal Decomposition of Ionic Solids,* Elsevier, New York, 1999.

[27] H.L. Friedman, “Kinetics of thermal degradation of char-forming plastics from thermogravimetry. Application to a phenolic plastic” *J. Polym. Sci. Part C* 6 (1964) 183.

[28] H.E. Kissinger, “Reaction Kinetics in Differential Thermal Analysis”, *Anal. Chemistry* 29 (1957) 1702.

[29] C-R. Li, T.B. Tang, “Isoconversion method for kinetic analysis of solid-state reactions from dynamic thermoanalytical data”, *J. Mater. Sci.* 34 (1999) 3467.

[30] T. Akahira, T. Sunose, Trans. 1969 Joint Convention of Four Electrical Institutes, paper No. 246; *Res. Report Chiba Inst. Technol.* 16 (1971) 22.

[31] J.H. Flynn, L.A. Wall, “A quick, direct method for the determination of activation energy from thermogravimetric data”, *J. Polym. Sci. Part B* 4 (1966) 323.

[32] T. Ozawa, “Estimation of activation energy by isoconversion methods”, *Thermochim. Acta* 203 (1992) 159.

[33] A.M. Capece, J.P. Roszell, C.H. Skinner, and B.E. Koel, “Effects of temperature and surface contamination on D retention in ultrathin Li films on TZM”, *J. Nucl Mat.* 463 (2015) 1177.

[34] C.N. Taylor, J. Dadras, K.E. Luitjohan, J.P. Allain, P.S. Krstic, C.H. Skinner, “The role of oxygen in the uptake of deuterium in lithiated graphite”, *J. Appl. Phys.* 114 (2013) 223301.

[35] Thermal conductivities and linear coefficients of thermal expansion (values reported at STP). Available from: http://www.engineeringtoolbox.com/linear-expansion-coefficients-d_95.html [accessed: January 13, 2017].

[36] H.W. Davison, “COMPILATION OF THERMOPHYSICAL PROPERTIES OF LIQUID LITHIUM”, *NASA Technical Note* (1968).

[37] *AERO VAC ODYSSEY MANUAL*. Oak Ridge, TN: Vacuum Technology Inc., rev. 1.6.

[38] J.P. Tonks, M.O. King, E.C. Galloway, J.F. Watts, “Corrosion studies of LiH thin films”, *J. Nucl. Mater.* 484 (2017) 228.

[39] A. Teplyakov, “Temperature-Programmed Desorption”, University of Delaware, C-874 (2016).

[40] M.J. Baldwin, R.P. Doerner, S.C. Luckhardt, R.W. Conn, “Deuterium retention in liquid lithium”, *Nucl. Fusion* 42 (2002) 1318.

[41] P.A. Redhead, “Thermal desorption of gases”, *Vacuum* 12 (1962) 203.

[42] G. Sauerbrey, “Verwendung von Schwingquarzen zur Wägung dünner Schichten und zur Mikrowägung”, *Z. Phys.* 155 (1959) 206.

[43] “QCM100- Quartz Crystal Microbalance Theory and Calibration”, Stanford Research Systems (2005).

[44] D.R. Denison, “Linearity of a Heavily Loaded Quartz Crystal Microbalance”, *J. Vac. Sci. Technol.* 10(1) (1973) 126.

[45] K. H. Behrndt, “Long Term Operation of Crystal Oscillators in Thin-Film Deposition”, *J. Vac. Sci. Technol.* 8(5) (1971) 622.

[46] John Henderson, “Electronic Devices. Concepts and Applications”, Prentice Hall, NJ, (1991) p. 357.

[47] G.K. Creffield, M.G. Down, R.J. Pulham, “Electrical Resistivity of Liquid and Solid Lithium”, *J. Chem. Soc., Dalton Trans.* 21 (1974) 2325.

[48] T.R.P. Gibb, Jr., C.E. Messer, “A SURVEY REPORT ON LITHIUM HYDRIDE”, *United States Atomic Energy Comission* (1954) Tufts College: Medford, Massachusetts.

[49] O. Gunes, “Drude theory. Conductivity of metals. Scattering. Matthiessen's and Nordheim's rules. Mixture rules. Conductivity of non-metals. Hall's effect. Electromigration”, *Slides prepared for EE271 Course*: University of Saskatchewan (2017).

[50] J.A. Reynolds, J.M. Hough, “Formulae for Delectric Constant of Mixtures”, *Proceedings of the Phys. Soc. B* 70 (1957) 769.

[51] M. Ohno, S. Konishi, K. Noda, H. Takeshita, H. Yoshida, H. Watanabe, “CONDUCTIVITIES OF A SINTERED PELLET AND A SINGLE CRYSTAL OF Li_2O”, *J. Nucl. Mater.* 118 (1983) 242.

[52] S.I. Krasheninnikov, L.E. Zakharov, G.V. Pereverzev, “On lithium walls and the performance of magnetic fusion devices”, *Phys. of Plasmas* 10 (2003) 1678.

[53] M.W. Chase, Jr., “NIST-JANAF Thermochemical Tables for Oxygen Fluorides”, *J. Phys. Chem. Ref. Data, Monograph 9* (1998) 1.

[54] B. deB. Darwent, *National Standard Reference Data Series,* National Bureau of Standards, no. 31, Washington, 1970.

[55] V.A. Zhdanov, V.V. Polyakov, V.F. Konusov, “BOND ENERGY AND EQUATIONS OF STATE OF LITHIUM HYDRIDE”, Translated from *Teoreticheskayai Eksperimental'naya Khimiya* 10 (1974) 276.

[56] E. A. Hylleraas, “Wellenmechanische Berechnung der Gitterenergie und der Gitterkonstante des Lithiumhydrids”, *Z. Phys.* 63 (1930) 771.

[57] B. F. Ormont, *Structures of Inorganic Substances* [in Russian], GITTL, Moscow-Leningrad (1950).

[58] B. Marinho, M. Ghislandi, E. Tkalya, C.E. Koning, and G. de With, “Electrical conductivity of compacts of graphene, multi-wall carbon nanotubes, carbon black, and graphite powder”, *Powder Tech.* 221 (2012) 351.

[59] H.M. Jaeger and S.R. Nagel, “Physics of the Granular State”, *Science* 255 (1922) 1523.

[60] S.J. Binnie, S.J. Nolan, N.D. Drummond, D. Alfie, N.L. Allan, F.R. Manby, M.J. Gillan, “Bulk and surface energetics of lithium hydride crystal: benchmarks from quantum Monte Carlo and quantum chemistry”, *Phys. Rev. B* 82 (2010) 165431.

[61] T.E. Healy (M.S. Thesis), “Fatigue Crack Growth in Lithium Hydride”, Lawrence Livermore National Laboratory, 1993.

[62] M. Ono, R. Majeski, M.A. Jaworski, Y. Hirooka, R. Kaita, T.K. Gray, R. Maingi, C.H. Skinner, M. Christenson, D.N. Ruzic, “Liquid lithium loop system to solve challenging technology issues for fusion power plant”, *Nucl. Fusion* 57 (2017) 116056.

CHAPTER 5: HYDROGEN ABSORPTION AND DISSOLUTION IN LITHIUM

While the previous chapter focused on the recovery of hydrogen from pure lithium hydride (LiH) as a surrogate for lithium deuteride (LiD) and lithium tritide (LiT), this chapter will focus on the fundamental studies surrounding how lithium consumes fuel particles and what resultant chemical species are formed within the mixture. Similar to the previous chapter, the use of hydrogen, both in its neutral and ionic state, will act as the surrogate species for deuterium and tritium, with the discrepancies between the isotopes having been explained earlier in Chapter 2. Fundamentally, this chapter addresses the concerns surrounding tritium recovery from less-than-saturated lithium solutions. Specific focus will be placed on how various hydrogen exposure conditions will influence the uptake and subsequent release in lithium samples, both in the solid and liquid phases.

The goal of this chapter is to decipher the chemical complexity of hydrogenated lithium. Thermodynamic limitations on the amount of hydrogen dissolved versus that which is precipitated as lithium hydride are based on equilibrium principles. In most cases, the chemistry of hydrogenated lithium can be well-defined by these fundamentals; however, a departure from equilibrium conditions occurs when materials are exposed to both vacuum and plasma environments. In many cases, the energetics of these new environs can influence the properties of materials in unforeseen ways. The property of specific interest here is solubility. The kinetics associated with absorption and desorption will be used to define how much, if at all, the ratio of the hydrogen dissolution rate to hydride precipitation rate changes in these situations.

It is important here to make the distinction in terminology for levels of chemical composition in hydrogen-lithium solutions. The term “saturated” in this and previous chapters refers to samples where an atomic hydrogen to lithium ratio is 1:1, meaning the sample is entirely LiH. This type of sample was the subject of Chapter 4. The term “less-than-saturated” refers to solutions comprised partially of dissolved hydrogen (dubbed the α phase) and partially of precipitated, solid hydride (dubbed the β phase). In contrast to these definitions, the term “far-from-saturated” refers to any sample where the amount of hydrogen in lithium is at or below the thermodynamic solubility threshold, which will be described in the introductory portion of this chapter. The focus of this chapter will be on the less-than-saturated and the far-from-saturated solutions.

The following sections will be outlined in such a way that a bulk of the theoretical considerations not mentioned in Chapter 2 will be detailed first. The section following the background and theoretical work will introduce the TUFCON chamber [1], and the modifications made to it in order to investigate the hydrogenated lithium chemistry. Results from these experiments will then be discussed, with the data from the solid lithium samples being presented first followed by the data from the liquid lithium samples. A detailed design of experiment was done for predictive purposes, but will be described in Appendix B for brevity. Finally, the chapter will conclude with a discussion on the implications of these results, and how they can be used for decisions about lithium loop treatment options.

5.1 Background

Unlike the previous chapter, this chapter focuses on absorption and recovery in the less-than-saturated solutions of lithium and hydrogen. Of particular interest is the determination of the state of the tritium after it has been absorbed. This knowledge is crucial in determining the recovery treatment options. Specifically, does the tritium remain dissolved within the liquid lithium or does it precipitate out as lithium tritide? What is the boundary that separates dissolved tritium from precipitated lithium tritide, and how does it depend on concentration, temperature, and exposure condition? Does the presence of oxygen impurity help or hinder these processes? This chapter aims to answer these questions and then apply this knowledge practically with regards to a hypothetical lithium-walled fusion reactor. To make this connection, this section discusses how tritium interacts with lithium within the reactor and what information exists to help understand hydrogen dissolution in lithium.

5.1.1 Range of Tritium in Lithium

Understanding the sub-surface chemical interactions between deuterium or tritium and lithium requires a bit of preliminary knowledge about the interaction depth, as well as the residence time a given differential element of lithium spends in a hypothetical reactor while being exposed to the fusion plasma. Interaction depths are difficult to determine, since measurable quantities do

not easily relate to particle ranges within a material. Theoretical considerations for such quantities as interaction depth must therefore be taken into account.

Analytical approximations may be used to determine values on the order of the particle range in a material, but these approximations are inaccurate for most systems. This is especially true when the projectile species can chemically interact with the target species. To alleviate some of the concerns associated with the order-of-magnitude analytical estimates, a number of groups have developed software packages to virtually study ion bombardment. The two methods of choice employ Monte Carlo methods and the Binary Collision Approximation (BCA) or Molecular Dynamics (MD) [2]. The BCA portion in the first method defines the projectile-target interactions using elastic, two-body collisions and inelastic electronic stopping [3]. MD simulations are computationally intensive, so Monte Carlo BCA codes, while somewhat inaccurate, are still considered the standard [4].

The most pervasive of these BCA codes used in the ion- or plasma-material interaction fields is the SRIM software. SRIM has been shown, however, to be incredibly inaccurate, especially when considering angular dependences [5]. On top of these pitfalls, SRIM also uses the Ziegler, Biersack, and Littmark (ZBL) interaction potential, which is an entirely repulsive stopping potential [6]. Fractal TRIDYN (F-TRIDYN) is a modification made to TRIDYN, which uses the krypton-carbon interaction potential. F-TRIDYN is modified to investigate effects on surface roughness, but is also uniquely suitable for stochastically determining stopped projectile, stopped primary knock-on atom (PKA), and stopped secondary knock-on atom (SKA) locations within the target [6].

Since F-TRIDYN is a much more capable code, it was chosen for investigating the ion-target interactions between tritium and lithium. A coupled simulation that includes plasma kinetics and bulk material information through the addition of particle-in-cell (PIC) and MD simulations would be significantly more accurate for lithiated fusion reactors. This is beyond the scope of this work, however. Of particular interest is the projected or average range tritium particles with energies adhering to the results presented by Krasheninnikov, et al. [7] will penetrate into a lithium target. In his simulated ignited, Li-Wall ITER scenario, the wall temperatures could reach as high as 7 to 10 keV, while the edge densities would be significantly depressed. Taking this into account,

the range distributions for a variety of incoming triton energies are shown in Figure 5.1. These distributions were also determined as a function of the incoming projectile angles.

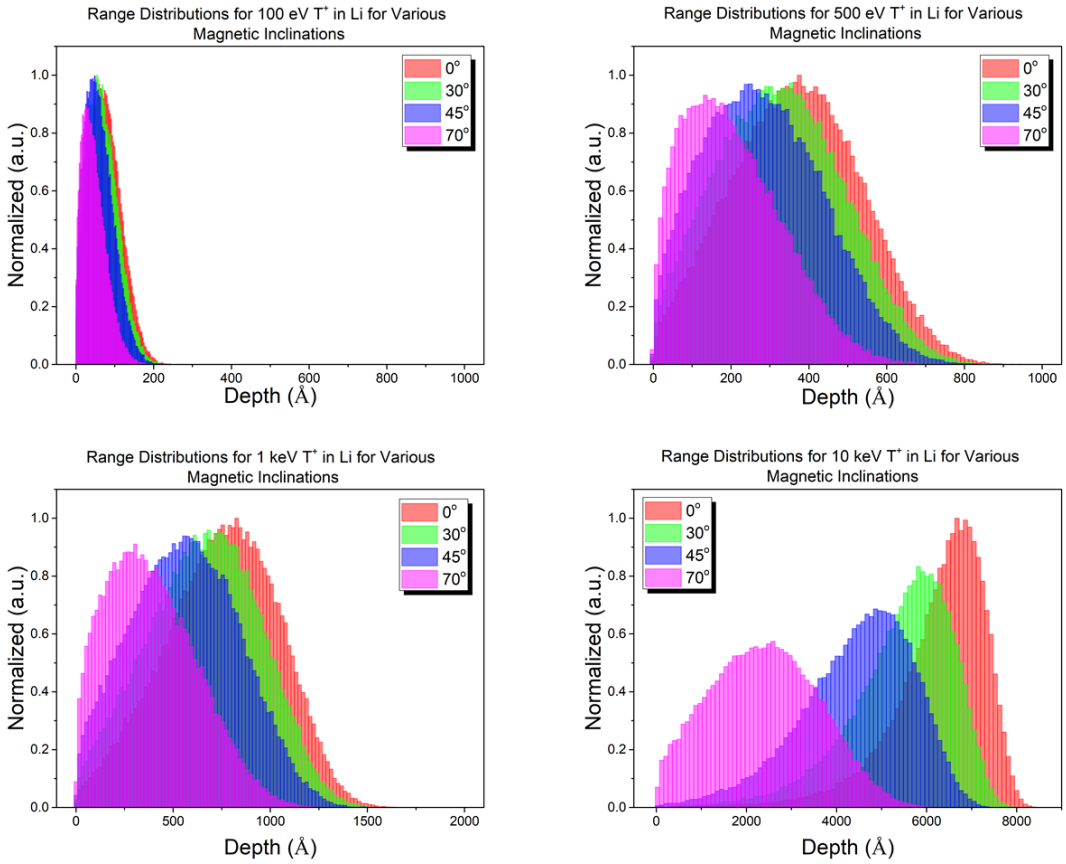

Figure 5.1: The range distributions for tritium ions incident on a lithium target at various projectile energies and angles, evaluated using F-TRIDYN [6]. It is important to note the change in the abscissa for higher energy projectiles.

While these data are quite interesting, showing that at normal incidence, ions at temperatures relevant to those predicted by Krasheninnikov, et al. [7] will penetrate into a lithium target almost up to a micron in depth, they are hard to understand in this form. To make the depth information clearer, a plot in Figure 5.2 was made to summarize the average depths taken from the distributions evaluated in Figure 5.1. The average ranges at normal incidence were compared to analytically evaluated projected ranges for tritons in lithium at the same projectile energies as listed

in Figure 5.1. Projected ranges were calculated following the same procedure defined in Nastasi's book [8], where [8, 9]:

$$\frac{R}{R_p} \approx 1 + B\frac{M_2}{M_1} \tag{5.1}$$

where R is the ionic range, R_p is the projected range, B is a slowly varying function of the incoming projectile energy E and the ionic range, M_1 is the projectile mass, and M_2 is the target mass. In 1964, Lindhard's group [9] was the first to relate this approximation for ionic stopping in a solid, where B was considered approximately 1/3 across a wide range of projectile-target conditions. Substituting this value into Equation (5.1) and rearranging leads to:

$$R_p \cong \frac{R}{1+(M_2/3M_1)} \tag{5.2}$$

The calculation for the projected range in Equation (5.2) requires knowledge of the range a given ion species at a given energy has in a material. Estimating that the nuclear stopping dominates for a given system while ignoring electronic stopping, one can approximate the range using:

$$R \cong \int_{E_0}^{0} \frac{dE}{N\,S_n(E)} \tag{5.3}$$

where E_0 is the initial kinetic energy of the projectile, N is the target number density, and $S_n(E)$ is the nuclear stopping function that varies with particle energy. It is important to note here that approximating the range for the tritium-lithium system as only depending on the nuclear stopping is quite a departure from reality. The electronic stopping for such a system is quite a bit more influential for than for others, since chemical interactions between the target and projectile species will be very important in inelastic collisions, especially at low to moderate energies. At all energies, the electronic stopping for this system will dominate momentum and energy transfer.

By taking a power law approximation for the energy-transfer differential cross-section and applying that to the nuclear stopping function, one arrives at the form for $S_n(E)$ [8]:

$$S_n(E) = \frac{C_m E^{1-2m}}{1-m}\left[\frac{4M_1M_2}{(M_1+M_2)^2}\right]^{1-m} \tag{5.4}$$

where E is the energy, m is a fractional value based on the reduced energy of the system [8, 10], and [8, 10]:

$$C_m = \frac{\pi}{2}\lambda_m a_{TF}^2 \left(\frac{2Z_1 Z_2 e^2}{a_{TF}}\right)^{2m} \left(\frac{M_1}{M_2}\right)^m \tag{5.5}$$

where C_m is a constant used to help describe the energy-transfer cross-section, λ_m is a fitting parameter based on the reduced energy of the system, a_{TF} is the Thomas-Fermi radius, Z_1 is the projectile atomic number, Z_2 is the target material atomic number, and e^2 is 1.44 eV nm [8]. The reduced energy for the system is defined by:

$$\varepsilon = \frac{M_2}{M_1+M_2}\frac{a_{TF}}{Z_1 Z_2 e^2} E \tag{5.6}$$

where [8, 10]:

$$\begin{aligned} &m = \tfrac{1}{3}, \lambda_{1/3} = 1.309 \text{ for } \varepsilon \leq 0.2, \\ &m = \tfrac{1}{2}, \lambda_{1/2} = 0.327 \text{ for } 0.08 \leq \varepsilon \leq 2, \\ &m = 1, \lambda_1 = 0.5 \text{ for } 10 \leq \varepsilon \end{aligned} \tag{5.7}$$

Taking Equations (5.5) and (5.4) and plugging them into Equation (5.3) and integrating over energy, the approximate form for the range evaluates to [8]:

$$R(E_0) = \left(\frac{1-m}{2m}\right)\frac{\gamma^{m-1}}{N\, C_m} E_0^{2m} \tag{5.8}$$

where γ is the reduced mass $\left[\frac{4M_1M_2}{(M_1+M_2)^2}\right]$. Substituting Equation (5.8) into Equation (5.2) will allow for the approximate evaluation of the projected range for a given ion-target system. The values for R_p plotted in Figure 5.2 for the tritium-lithium interactions were all evaluated under the assumption that the system never actually approached a reduced energy value greater than 10 (which is not true for highly energetic tritons).

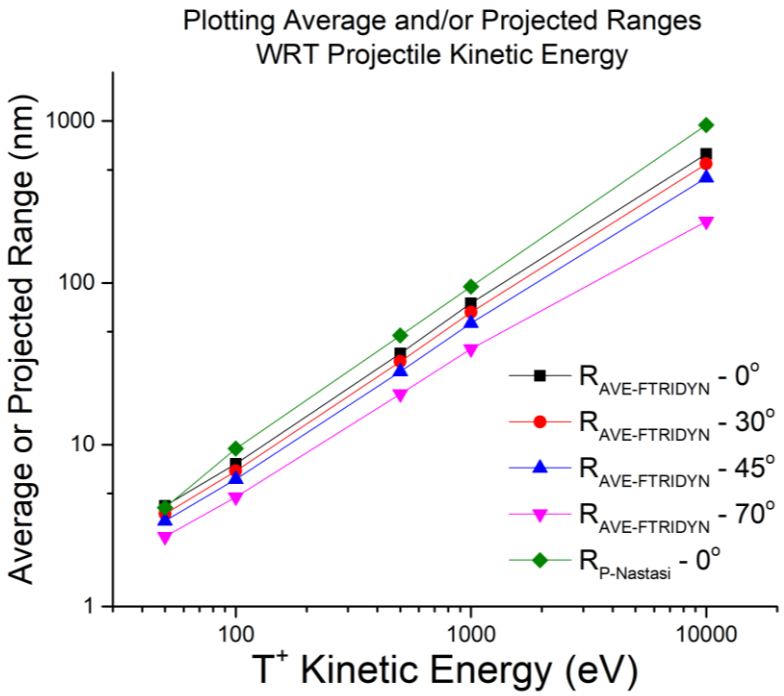

Figure 5.2: Plots of the average ranges for tritium in lithium found by using the F-TRIDYN implantation distribution profiles [6]. These were compared to the projected range calculations for the same energies at normal incidence for tritons in lithium, following the calculation procedure outlined by Nastasi [8 – 10].

It is understandable that the projected ranges calculated using the methodology outlined in Nastasi [8 – 10] are quite a bit larger than those evaluated using the F-TRIDYN code [6]. As mentioned before, the approximations for Nastasi's projected range values are quite unrealistic for this system, where electronic stopping will play quite an important role for the tritium-lithium system. Despite this, the average ranges from F-TRIDYN and the projected range values are quite close. Likely, F-TRIDYN's electronic stopping functionality is also not suitable for this system. The fact still remains, however, that both sets of calculations yield results that high-energy tritons will likely penetrate well into the bulk of any lithium surface, almost up to a micron beneath the surface. This is also quite clear from the bottom, right-hand plot in Figure 5.1, and means that the assumptions that go along with considering the surface chemistry alone will not be valid for this system. It is also important to note that the F-TRIDYN simulations for the tritium-lithium system

also tracked the reflected particles and found that at triton energies relevant to the ignited, Li-Wall ITER scenario, there was a negligible probability that the projectiles would be reflected.

While this work is important and may inspire further studies in determining sub-surface interactions of tritium with lithium, the immediate conclusion that can be drawn is that an overwhelming majority of the tritons and deuterons that do hit the surface of any liquid lithium system will be consumed, since they travel well into the bulk. These theoretical estimates beg further questions. First, if nearly all the tritium that strikes the surface of a lithium target is absorbed, how much tritium is a differential element of flowing liquid lithium subjected to? Second, there are likely quite a few inelastic processes involved in thermalizing a triton on its way into a lithium target. What fraction of thermalized tritons remain dissolved within the lithium and what fraction eventually bond to lithium atoms? Also, to what degree does oxygen play a role in the consumption of tritium? The first of these questions can be easily answered theoretically in the context of a system that serves the LiMIT PFC [11 – 13]; however, the second set of questions remains an active area of research and will be the subject of investigation for this chapter.

5.1.2 Tritium Dose to a LiMIT Lithium Element

As described in the previous section, the tritium particles that travel to the wall in a Li-Wall reactor are expected to be consumed at that boundary. The question that poses the biggest challenge to those that will eventually work with tritium recovery systems is: What is the triton dose that an individual lithium element in any given liquid lithium PFC will be exposed to? This section will answer that question with regards to the LiMIT PFC [11-15].

The LiMIT PFC [11 – 15] has been explained in great detail in the introductory chapters of this thesis, with the bulk of the theoretical work surrounding the practical application of thermoelectric magnetohydrodynamics in this system having been derived in other theses [11 – 12] or articles [13 – 15]. Since this work does not focus on this theory, but only aims to use the results of these theoretical considerations, the full derivation of the fluid dynamics for the LiMIT system will be avoided, primarily for the sake of brevity. The derivations for the fluid physics of the LiMIT system will be left to the reader [11 – 15], while this work will take the resulting velocity

profile equations and use them as the starting point for evaluating the tritium dose to a liquid lithium element flowing in the LiMIT system.

When assuming an infinite trench depth, such as to simplify the LiMIT trench geometry, the trench-width-averaged velocity profile at any given distance along the length of the trench, z, can be defined as [11 – 15]:

$$u_{AVE}(z) = \frac{Ha - \tanh(Ha)}{Ha + C\tanh(Ha)}\left[\frac{S - S_w}{B}\frac{dT}{dy} - \frac{1+C}{\sigma B^2}\frac{dP}{dz}\right] \tag{5.9}$$

where $u_{AVE}(z)$ is the trench-width-averaged velocity at any given point along the length of the trench, S is the Seebeck coefficient for the liquid metal material (lithium in this case), S_w is the Seebeck coefficient of the trench wall material, B is the magnitude of the transverse magnetic field, σ is the electrical conductivity of the liquid metal, $\frac{dT}{dy}$ is the temperature gradient through the depth of the liquid metal, and $\frac{dP}{dz}$ is the pressure gradient along the direction of the LiMIT trench. The variable Ha defines the Hartmann number [16], which relates the ratio of the electromagnetic force to the viscous force in the form:

$$Ha = BL\sqrt{\sigma/\mu} \tag{5.10}$$

where L is the characteristic length scale (in this case the width of the trench), and μ is the dynamic viscosity of the liquid material. The variable C in Equation (5.9) is a ratio of the electrical conductivities for the liquid metal and trench wall materials, weighted by geometrical factors [11 – 15]:

$$C = \frac{a\sigma}{t\sigma_W} \tag{5.11}$$

where a is one half the trench width, σ is the electrical conductivity of the lithium, t is one half the trench wall width, and σ_W is the electrical conductivity of the wall.

Solving Equation (5.9) analytically is no small task, and is often done using finite element analysis through the COMSOL Multiphysics software [11 – 14, 17]. A few simplifying assumptions can be made when approaching this problem analytically for finding an estimate as to the dose of tritons to a differential lithium element flowing within a LiMIT trench. The temperature gradient through the lithium was assumed to follow the straightforward Fourier's law

of conduction, such that $Q = -k_{Li}\ dT/dy$. This heat flux assumption is quite approximate because it assumes that heat is instantaneously transferred from the surface of the lithium through the bulk. More sophisticated analyses would include higher order heat transfer effects, but this calculation was kept simple as an order-of-magnitude estimate. Second, the pressure gradient along the length of the trench, $\frac{dP}{dz}$, was evaluated through a simple convergence algorithm. The pressure-driven term was found to be negligible when compared to the temperature gradient effects for a system with parameters mimicking a Li-Wall reactor.

To find an estimate for the tritium dose to a differential lithium element flowing in a LiMIT PFC, parameters for a virtual reactor scenario were either taken from the work of Krasheninnikov's group [7], or were determined from a few sources relating relevant ITER parameters [18 – 20]. An individual LiMIT trench was assumed to be 2 mm in width and 30 cm in length. The characteristic width value for the trench wall, t, was assumed to be 1 mm. These dimensions correspond to systems that have already been evaluated using the COMSOL Multiphysics software [11 – 14, 17]. Assuming that the particles are sufficiently diverted in a hypothetical reactor, the full-width half-maximum of a Gaussian used to fit the heat and particle flux profiles was assumed to be 5 cm [18]. The peak steady-state heat flux was assumed to be 10 MW m^{-2} [19], while the peak steady-state triton flux was assumed to be 3 x 10^{21} m^{-2} s^{-1}, based on Krasheninnikov's results [7]. The transverse magnetic field was assumed to have a magnitude of 6 Tesla [20]. The geometry for this evaluation was defined as shown in Figure 5.3 [11 – 14], where an inlet velocity of 10 cm s^{-1} was considered for either forced electromagnetic or return flow.

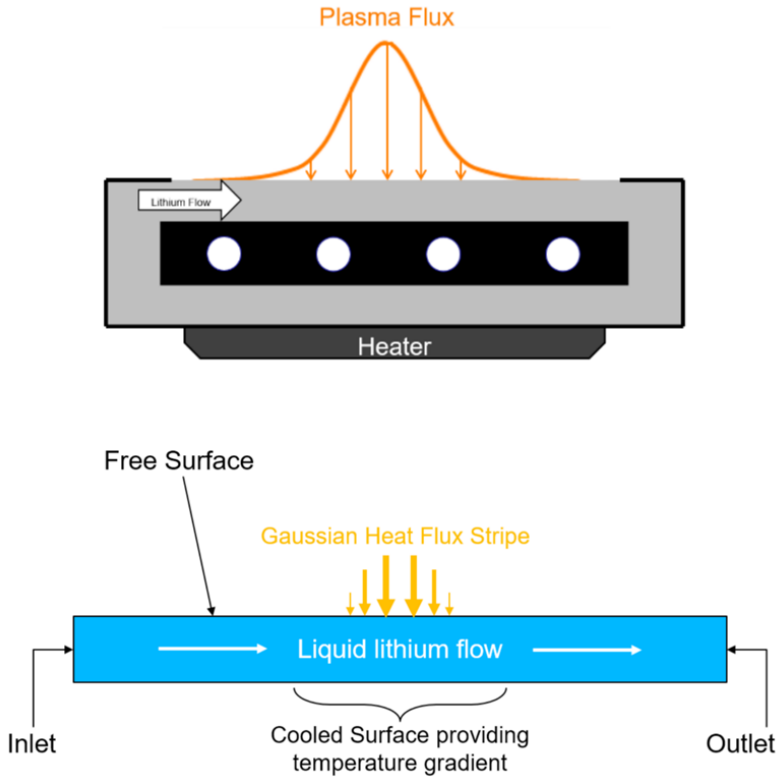

Figure 5.3: The geometry and boundary considerations for the order-of-magnitude dose estimates to a differential Li element in a LiMIT trench reported in this section [11 – 14].

The velocity profile was found to be Gaussian in nature, similar to the profiles considered for the heat and particle fluxes. The peak velocity for this system was found to be approximately 60 cm s^{-1}. The velocity averaged over the length of the trench was found to be nearly 20 cm s^{-1}, with an averaged residence time of roughly 2 s. While these values are not the most useful with regards to the dose evaluation, they do help to serve as a sanity check for the evaluation. While a residence time of 2 s seems quite short when compared with a system that is operating at steady-state, current tokamaks typically operate in pulses on the order of a few 100s of milliseconds. These figures can be used to visualize how quickly a differential lithium element is likely to flow through the LiMIT PFC.

Once the velocity profile had been established over the length of the trench, using Equation (5.9), an integral over the trench width and length was taken to find the tritium dose. This integration followed the equation:

$$N_{trench} = \int_0^w \int_0^L \varphi(z)\, z\, \frac{1}{u_{AVE}(z)}\, dz\, dx \tag{5.12}$$

where N_{trench} is the dose to an element integrated over the dimensions of an individual trench, $\varphi(z)$ is the particle flux profile, z is the length coordinate for a LiMIT trench, and $u_{AVE}(z)$ is the trench-width-averaged velocity profile in z evaluated using Equation (5.9). What is really being said by Equation (5.12) is during a single pass through LiMIT, a trench-sized plasma-facing surface area of 2 mm x 30 cm will be bombarded by greater than 1 x 10^{17} tritons. Under the assumption that all of the tritium ions will be consumed by the lithium, it is then important to figure out how this dose then relates to concentration, because concentration will determine the likelihood that these captured tritons will remain dissolved or will bond to the surrounding lithium.

In this case, the tritium concentration in the lithium exiting the reactor will depend on the trench depth. The value of 1 x 10^{17} only represents a few micromoles of tritium being consumed by an individual trench per pass; however, it is envisioned that there will likely be hundreds of thousands, if not millions, of trenches lining the inner wall of a reactor. This means that in total, the amount of tritium captured per pass will be on the order of moles to tens of moles, but this must be compared to the amount of lithium that has been flowed through the reactor. Assuming a modest trench depth of 0.5 mm, the average volumetric flow rate through an individual trench is nearly 0.2 $cm^3\ s^{-1}$, meaning that the average mass flow rate is roughly 0.11 g s^{-1}. This equates to 15 millimoles s^{-1} of lithium per trench. The sum of an individual trench measuring 2 mm x 30 cm and the accompanying surface area of the trench walls (2x) 1 mm x 30 cm will only cover about 6 x 10^{-4} % of the ITER divertor and 1 x 10^{-4} % of the whole ITER plasma-facing surface. Taking this into account, 175 thousand trenches of this dimension are required to cover the divertor alone, while 710 thousand trenches are required to cover the whole of the ITER plasma-facing surface [21]. If diffusive losses were eliminated and all charged particles were well diverted, then over 2.5 killimoles s^{-1} of Li (greater than 18 kg s^{-1}) would flow through the divertor, and a total of 35 millimoles of tritium would be caught per trench per pass. This molar fraction is well below the thermodynamic solubility limit at all temperatures defined by the works of Veleckis, Adams, and others [22 – 39], meaning that all the tritium absorbed in a single pass will likely remain dissolved.

The reason these results, even if very approximate, are important is that they confirm the chemical state of the tritium as it exits a hypothetical reactor within the lithium. Because the tritium concentration is well below the solubility limit, tritium treatment options need to consider

operation in transient and steady-state situations. Steady-state operation requires that some equilibrium concentration of tritium be continually circulating with the lithium, even after fractions of tritium are removed for treatment. For the transient, tritium will likely remain completely dissolved at very low atomic fractions, meaning that methods using heat for recovery will need to maintain very high heating rates, or supplementary techniques will need to be employed. If a steady-state concentration can be reached, then separation techniques such as surface cold traps and centrifuges can be used to obtain streams with higher concentrations of tritium, both dissolved and as lithium tritide. These higher concentration streams can then be more easily processed. The next sub-section will discuss solubility limitations of LiH in lithium as defined by the thermodynamics, and how the presence of a plasma may end up modifying this property.

5.1.3 Solubility Limitations for Hydrogen in Lithium

As mentioned in Chapter 2 and Chapter 4, a significant amount of work regarding this subject was performed in the 1960s and 1970s by various groups across the globe [22 – 39]. The three studies that best summarize the solubility limitations of hydrogen in lithium were reported by Veleckis' group in 1977 [24], Katsuta's group in 1977 [32], and Adams' group in 1975 [38]. Veleckis' group [24] summarized the findings of a number of groups to help establish the liquidus curve on the Li-LiH and Li-LiD phase diagrams, illustrated in the previous chapter in Figure 4.1. This phase diagram, unfortunately, is incomplete in that it does not fully encapsulate the various changes in phase that are associated with these types of binary systems. Recently, Yakimovich's group has done work to explain the changes in phase more thoroughly, which lead to the phase diagram illustrated in Figure 5.4 [40]. The items of interest in this plot are how the Li-rich phase (α) and the LiH-rich phase (β) separate into their solid and liquid forms based on concentration and temperature.

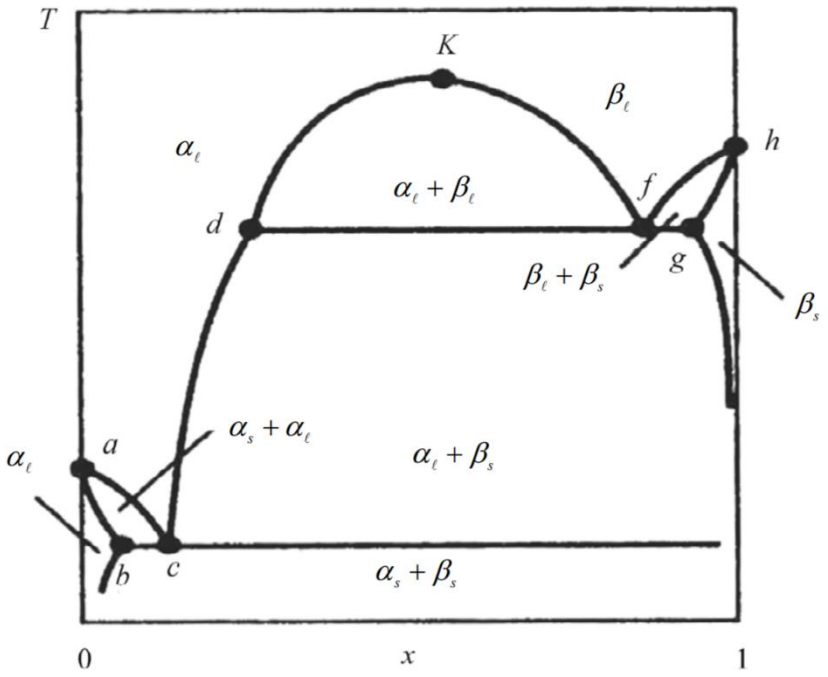

Figure 5.4: A rough sketch of the phase diagram functionality for the Li-LiH, Li-LiD, and Li-LiT systems [40]. The abscissa represents the molar fraction of the LiH, LiD, or LiT, and the ordinate represents the solution temperature. The symbol 'α' represents the Li-rich phase, whereas the symbol 'β' represents the LiH-rich phase. The subscripts 's' and 'l' refer to the solid state and liquid state, respectively.

While the rough illustration in Figure 5.4 only serves to illustrate composition on a very approximate scale, it does help in understanding exactly how the phases are separated what temperatures are required to drive the system toward a given product or set of products. In this case, the α phase represents pure lithium, while the β phase represents LiH, LiD, or LiT. Unless the composition of the mixture follows within the narrow gap on the abscissa between points 'c' and 'd', the increase in temperature will drive a Li-LiH system toward the phase where both constituents coexist as a liquid mixture. In their work, Yakimovich's group also found a relationship for the critical LiH concentration with regards to solubility as a function of temperature using the following relationship [40]:

$$\ln x = A + B\left(\frac{1}{T} - \frac{1}{T_M}\right) + C\ln\left(\frac{T}{T_M}\right) \tag{5.13}$$

where x is the mole fraction of LiH (or LiD or LiT), A is an empirical constant, B is an empirical constant, T is the sample temperature in K, T_M is the monotectic temperature in K, and C is another empirical constant. The group determined the empirical constants for the Li-LiH system to be -1.517 for A, -3998 K for B, and 3.004 for C, with a T_M of approximately 961 K (688 °C). From a practical standpoint, however, where the solution is primarily lithium, there is a finite operating temperature window where lithium does not readily evaporate. The upper limitation on temperature in this case is about 500 °C, with a critical LiH and LiD solubility concentration of slightly less than 4 mol % [40]. This is true for all isotopic species. This means that any more hydrogen, deuterium, or tritium added to the solution from a thermodynamics standpoint would precipitate out as LiH, LiD, or LiT.

The values reported by Yakimovich's group [40] are very similar to those reported in earlier works performed by Adams' group [38], even though the methods for obtaining these results were quite different. This means that in the case of a very pure system, resistivity measurements can indeed produce results that can quantify mixture composition. In light of these similarities, a plot following the result from Equation (5.13) has been generated and is shown in Figure 5.5. This will act as the thermodynamic limit for the results obtained and reported in this chapter. Similar results were obtained by Katsuta, et al. and are plotted in Figure 5.6 [32].

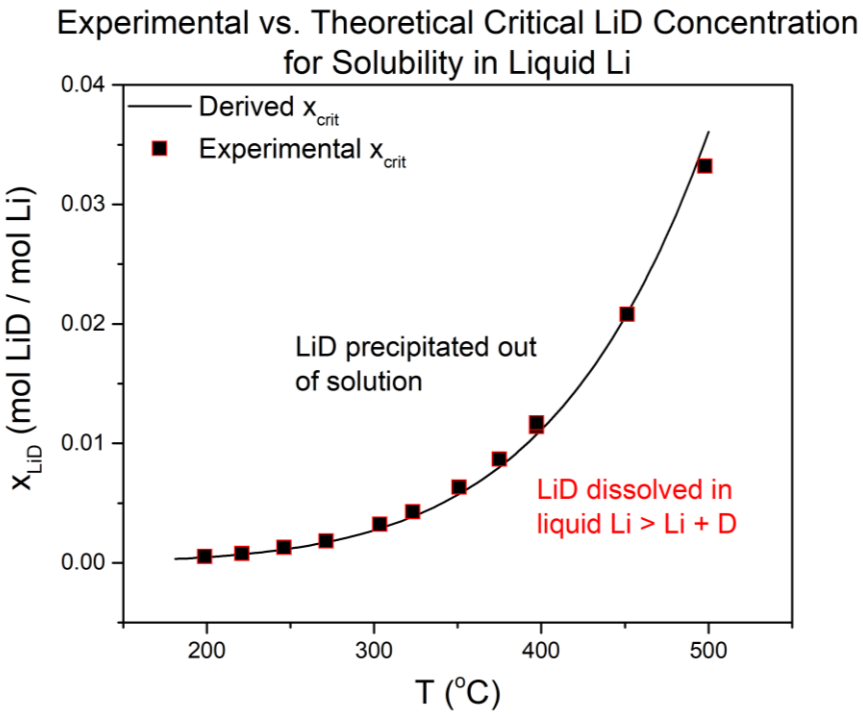

Figure 5.5: The critical concentration line for LiD in Li as a function of temperature [40]. Above this line, any excess deuterium addition will result in the production of LiD.

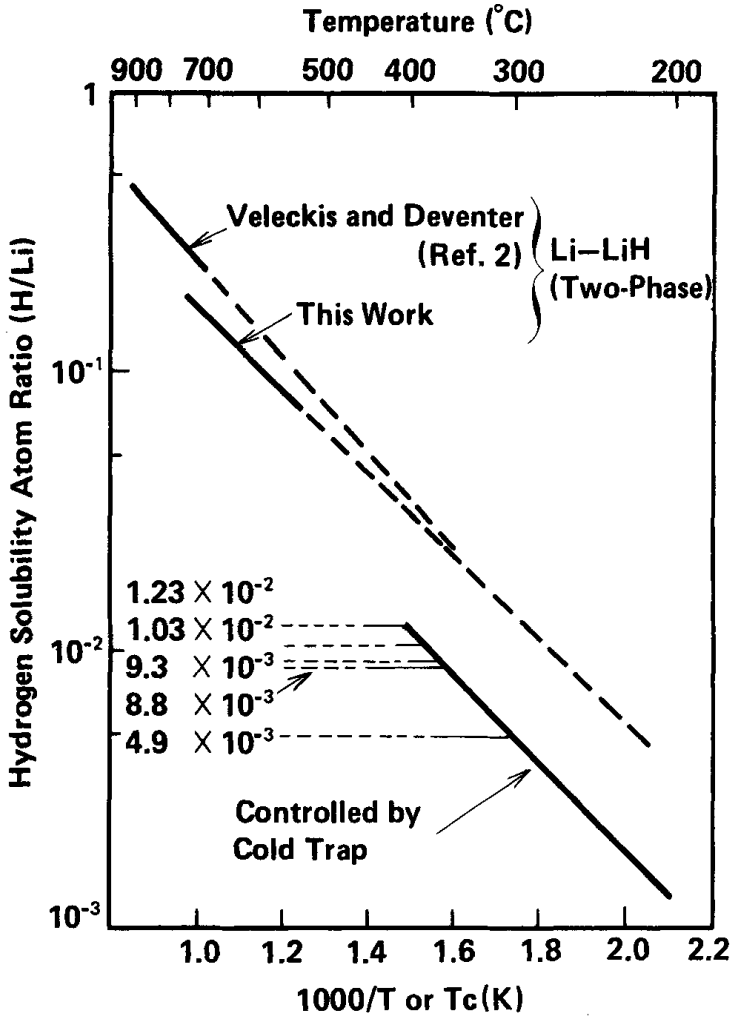

Figure 5.6: A figure illustrating work done by Katsuta's group [32], which confirms the results listed in Reference [40] (note the ordinate of this plot is in logarithmic scale).

The thermodynamic limitations are quite definitive and have been extensively studied. They are hard boundaries when investigation phenomena such as tritium recycling, retention, and recovery. The problem, though, with assuming that any lithium exposed to plasma is bound by these restrictions is that in such an environment there exists a large departure from equilibrium. This is true simply by the virtue that the system must be maintained in ultrahigh vacuum conditions, which constantly drives the system toward non-equilibrium. The combination of this and the energetics and chemical species that make up a plasma modify materials in ways that cannot be explained by thermodynamics alone.

Many studies [41 – 47] have found that the presence of a plasma enhances the solubility of diatomic gases well above the limits predicted by Sieverts' Law [48]. In 1995, Mundra [41] compiled a list of experiments that had previously measured nitrogen, oxygen, or hydrogen concentrations in various liquid metals well above the thermodynamic predictions. His group defined a more universal model for the solubility of diatomic gases in liquid metals. He argued that the reason thermodynamic solubility limits were exceeded was due to the step-by-step process of how charge carriers interact with the metal surface. Those well-versed in plasma physics understand that a floating object in a plasma will initially attract electrons. Once a negative potential has been established along the surface, ions will be attracted to that surface through long-range Coulombic forces. Once at the surface, inelastic collisions will cause the ions to regain electrons and they will become neutral species. Mundra proposed that these species, specifically the monatomic species, are what drive up solubility within the liquid metal. Essentially, the "gas" immediately above the metal surface is at what Mundra referred to as a "superequilibrium concentration". Mundra also went on to explain that it was unlikely for the diatoms to enhance solubility due to the fact that the vibrational energy of these species dampens quickly on impact [44]. Mundra did go on to state that if the delineation between not dissolved and dissolved was determined by the formation of a new species (e.g. LiH, LiD, or LiT), that this limitation may hold from a thermodynamic standpoint; however, if this point is true or not remains unclear. Understanding dissolution properties is especially crucial when considering liquid lithium and plasmas consisting of hydrogen, deuterium, or tritium. From a chemical standpoint, the presence of oxygen may also help to enhance tritium absorption and desorption properties in lithium, which a number of groups claim is responsible for the lithium's superior gettering properties [49, 50]. As such, surface and sub-surface chemistry are critical to understanding tritium allocation within the lithium bulk.

The bulk of this chapter will be aimed at uncovering the truth about these final points. The reason the earlier sub-sections are important is that they give context as to how the knowledge of dissolution rates will practically affect tritium recovery. The next section will discuss the experiments conducted to illuminate the mysteries surrounding how hydrogen behaves within lithium under a variety of low-pressure exposure conditions.

5.2 Experimental Setup

The chamber used to investigate the rate of hydrogen isotope dissolution to hydride precipitate formation was a modified form of the TUngsten Fuzz Characterization Of Nanofeatures (TUFCON) experiment [51, 52]. The primary reason for using TUFCON was that the helicon plasma was driven by a MORI 200 source [53, 54], meaning that the hydrogen plasma striking the surface of the lithium samples would not only have a relatively high ion density (for a low-temperature plasma), but the ions would be confined along field lines in such a way as to imitate impingement in a reactor-like scenario. Granted it should be understood moving forward that this environment is only a surrogate for the reactions expected in reactors; however, the presence of a plasma is significantly more accurate than assuming such interactions can be modeled simply by using an ion beam, which eliminates the effects the electrons and sheath kinetics have on the plasma-surface interactions.

The previous iteration of the TUFCON chamber had not been used for hydrogen plasmas, nor was it capable of performing TDS analyses. The chamber, therefore, went through a major upgrade prior to lithium exposure experiments. To control the inlet flow of hydrogen, an Alicat MC-50SCCM-D/5M mass flow controller, internally calibrated for hydrogen gas, was added to the gas inlet line. Because of hydrogen safety concerns, the exhaust lines for the rotary vane pumps required constant purging with compressed air, which was metered at greater than 20 L min^{-1} for all experiments. Also, the use of hydrogen gas also required a hydrogen-calibrated leak detection/alarm system, which was placed above the TUFCON device. To add temperature-programmed desorption (TPD) capabilities, the TUFCON chamber was elevated above its previous position by nearly an extra 18 inches. This would allow the linear translator arm to have vertical motion, such that the sample could be exposed to plasma near the MORI 200 source, and then be withdrawn by a distance of greater than 3 feet into the TPD antechamber. The addition of the antechamber was paramount in obtaining useful TPD spectra, since no port above this section would allow an RGA direct line-of-sight to the sample. The top portion of the LiHDE chamber, shaded in blue in the block diagram in Figure 4.2, was transferred from LiHDE to the TUFCON antechamber, meaning that the RGA and differential pumping section used in the experiments described in Chapter 4 was also used for the solubility experiments in TUFCON.

A number of diagnostics were utilized to observe the retention and release from less-than-saturated samples of hydrogenated lithium. These diagnostics will be described in greater detail in the following sub-sections. To characterize the plasma, a radiofrequency (RF) compensated Langmuir probe was used to obtain the electron temperatures and densities. For all experiments reported herein, the inlet pressure was held at 50 mTorr (indicated) and the RF power was held at 500 W. A K-type thermocouple was used to measure the crucible temperature before, during, and after hydrogen exposure. Prior to exposure, a resistivity measurement across the pure Li sample was made to compare with a similar post-exposure measurement. These measurements were made in a similar way to the methodology described in Chapter 4; however, because the resistances measured were so low, a Keithley Model 2000 Auto-ranging Multimeter capable of measuring resistances down to the 10s of μΩ's was used. During plasma exposure, a Mikropack PlasCalc-2000-UV/VIS/NIR spectrometer was used to monitor the H_α (656.4 nm), H_β (486.3 nm), Li_I (550.3 nm), and Li_{II} (671.1 nm) spectral lines. The in-vacuo optical fiber cable terminated no further than 1 inch away from the sample and was aligned to look directly at the sample surface during exposure. TPD were monitored using the VTI Odyssey Residual Gas Analyzer (RGA) described in Chapter 4.

In-vacuum heating of lithium during exposure and subsequent TPD runs was not trivial, especially when considering that the heated sample needed to travel more than 3 feet vertically. The other major concern with the system dealt with transporting the lithium sample, and what procedures and equipment were needed to maintain the highest possible purity. For the tests on solid lithium samples described in this chapter, the heat source was provided through the use of a HeatWave Labs, Inc. 0.75" diameter 1200 °C UHV Button Heater. Unfortunately, and after much back and forth conversation with the manufacturer, it was determined that the heat load for this type of source was too great, and the heater was only found to be able to heat samples to approximately 475 °C. This heater was powered through the use of an external variable AC transformer. This design included the use of a custom-manufacture quick connect for easy lithium transfer, but the design had to be re-visited once it was discovered that the heater had an upper limit. The upgraded design used to test liquid lithium samples instead employed the use of two coiled tungsten filaments purchased through the R.D. Mathis Company. Using these elements, the crucible was able to be heated well above 600 °C. The quick-connect system was also re-designed for quick lithium transfer. In both cases, radiative losses were minimized through the use of an in-

house manufactured radiation shield placed around the outside of the heater-crucible body. An image of the initial heater assembly and a half-section Inventor image of the upgraded heater assembly can be seen in Figure 5.7.

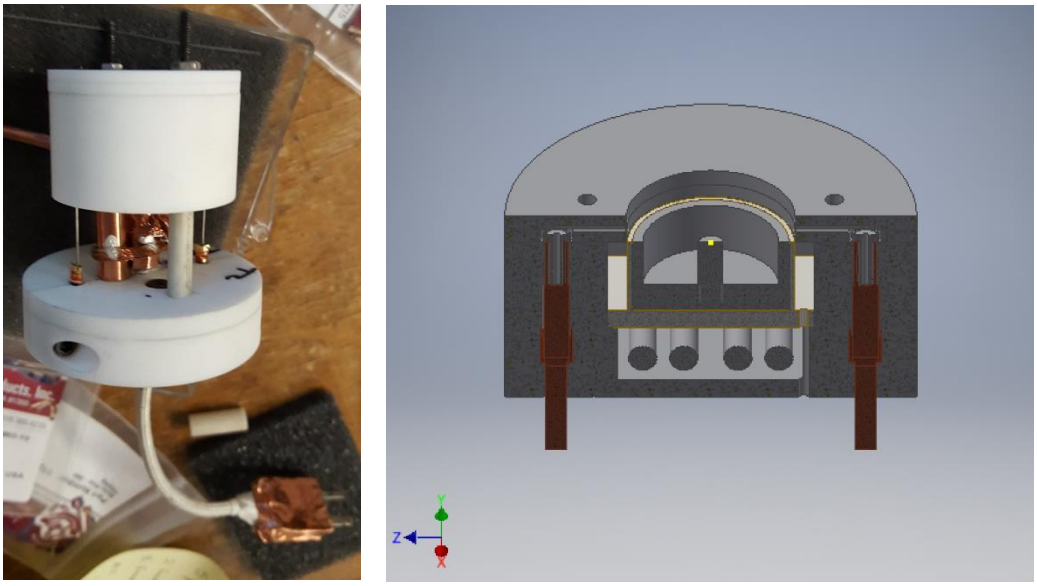

Figure 5.7: (Left) An image of the fully constructed heater assembly and top quick connect that used the HeatWave Labs Button Heater. (Right) A half-section Inventor view of the upgraded heater assembly (rendered by Cody Moynihan).

The lithium exposure and measurement procedure in TUFCON was quite extensive, with the major points being outlined in the block diagrams in Figure 5.8. Great care was taken to ensure the highest possible purity of lithium sample, with the loading, transport, and insertion of the crucible all being done under an argon atmosphere. The amount of lithium loaded for each trial was on the order of 0.20 ± 0.06 g, meaning that the sample number density was on the order of (3.3 ± 0.9) x 10^{22}. The chamber was then evacuated for more than 12 hours to reach acceptable base pressures, with RGA section pressures ranging between 0.2 and 0.5 μTorr and main chamber pressures ranging from 0.9 to 2 μTorr. To make sure that resistance measurements were as accurate as possible, each sample was heated to between 375 °C and 400 °C for more than 10 minutes to make sure the sample had effectively wetted both the inner and outer conductor of the sample crucible, which are illustrated in the previous chapter in Figure 4.3. The sample was then cooled to the pre-determined temperature and a pre-exposure resistivity measurement was taken. The

sample was then exposed to either hydrogen gas or plasma, with a negative floating bias being applied through the sample using the same electrodes used to measure resistance (after having disconnected the Keithley Multimeter). During this time, the Mikropack PlasCalc software was active in tracking the spectral lines previously mentioned (if the sample was indeed being exposed to a plasma). Once the exposure was ended, a post-exposure resistance measurement was taken. During the remainder of the experiment, the Keithley was allowed to continuously sample resistance. The sample was then extracted to the TPD antechamber and the remaining hydrogen was allowed to evacuate from the system. The Odyssey RGA was then absolutely calibrated to the base pressure measured by a Pfeiffer full-range gauge attached to the same differentially-pumped section. The RGA trend scan functionality was then used to track masses of 1, 2, 6, 7, 18, and 28 AMU, with the latter of these masses being used to check impurity level. The sample was then heated from its starting temperature (the temperature maintained during hydrogen exposure) until the Keithley Multimeter read that the sample resistance had elevated to the kΩ range or greater. This was a good indication that the lithium-rich portion of the sample had evaporated.

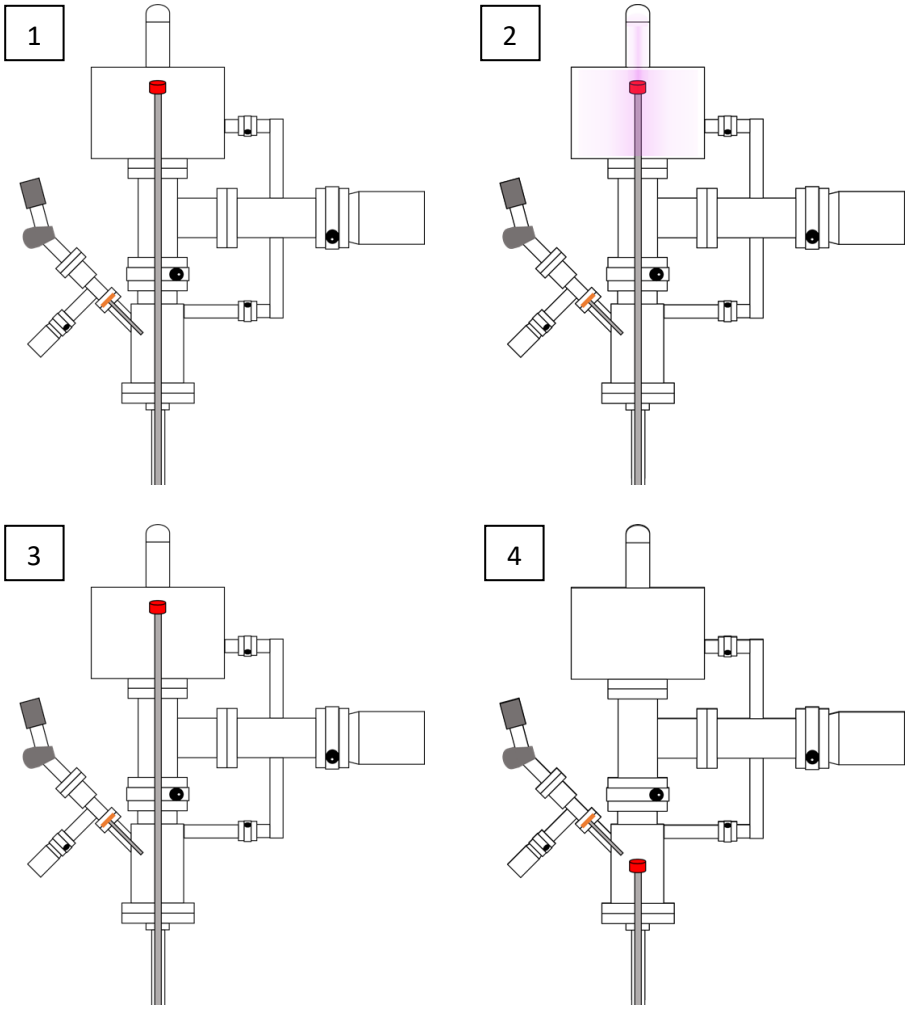

Figure 5.8: A block schematic illustrating the Li exposure and measurement procedure in TUFCON. The procedural explanation for each panel can be found in the preceding paragraph.

The following sub-sections will detail the diagnostics used and explain how each measurement type was used to extract pertinent information about hydrogen retention and evolution. These sub-sections will only contain information about the diagnostics unique to this system/analysis. Some measurement techniques used in the TUFCON experiments were also used when measuring the thermal decomposition of LiH. For brevity's sake, please look to the appropriate section in Chapter 4 for any further clarification about temperature-programmed desorption (TPD or TDS) or resistivity-composition analysis.

5.2.1 Helicon Plasma Source

To understand the results that can be obtained by exposing lithium samples to a hydrogen plasma, it is important to first understand the properties of the plasma in use. Helicon sources for plasma processing and other applications have been investigated since the late 1970s to early 1980s [55 – 65], but no report has been quite as extensive as that published by Chen in 1994 in the book *High Density Plasma Sources* [66]. In this chapter, Chen discussed the work that had been done to fully understand helicon sources and how bound, low-frequency whistler waves (dubbed helicon waves) contributed to the efficiency of the source type. While the details of helicons and how they dissipate power more effectively than other low-temperature plasma source types are beyond the scope of this document, a few of the key points will be briefly discussed.

In the introduction to his chapter [66], Chen relates all of the advantages for using a helicon source over other similar RF-type sources. The primary advantages associated with helicon discharges are coupled, in that there exists a high efficiency for power coupling over other conventional radiofrequency discharges which leads to higher density plasmas [55 – 57]. This was well documented by Boswell [55], Chen [56], and Shoji [57] as they all witnessed stark jumps in plasma parameters when the mode changed from non-resonant RF coupling (an inductively coupled plasma) to helicon coupling. A number of other advantages exist when processing with a helicon source, but one of the more interesting ones is that a self-bias mechanism occurs, which allows samples to obtain negative floating potentials without the need for external biasing [58]. The benefits of using a helicon source for this work are that the source produces high-density plasmas with relatively high ion energies, which can be taken advantage of when simulating higher, reactor-level fluences. These were the reasons the MORI 200 source was used, with the RF antenna powered to 500 W and the focusing electromagnets supplied with 20 A. The pressure was kept constant during exposure at 50 mTorr as indicated by an MKS Granville Phillips Convectron Gauge by manipulating the flow rate using the same Alicat MC-50SCCM-D/5M mass flow controller from the previous chapter. Applying the proper correction factor, this equates to an actual hydrogen pressure of approximately 30 mTorr.

5.2.2 Radiofrequency Compensated Langmuir Probe

While the full examination of a plasma generated using a helicon source is outside the scope of this work, a few fundamental parameters are necessary for understanding the total hydrogen ion dose to the lithium sample. Introduced in 1962 by Mott-Smith and Langmuir [67], the Langmuir probe is still widely considered as the standard for low-temperature plasma diagnosis. Early Langmuir probe theories based on sheath approximations proved inadequate for all plasma regimes, so in 1966 Laframboise [68] extended the earlier theory of Bernstein and Rabinowitz [69] to create a more universal, implicit model for determining plasma parameters. This model is still widely used today [70 – 73], even for RF compensated probes, where the sheath is continuously expanding and collapsing. The chart associated with the Laframboise density evaluation is shown in Figure 5.9 [74]. More information on how to apply this theory can be found in Ref. 74.

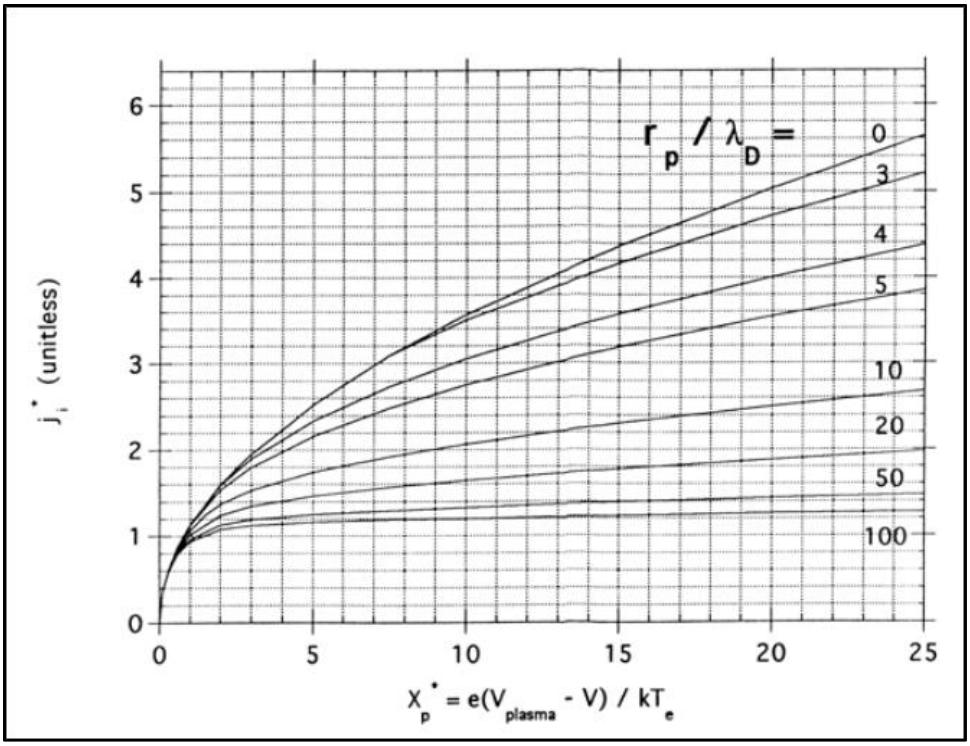

Figure 5.9: A chart showing the iterative scheme associated with the Laframboise evaluation of electron density [74].

Helicon sources are powered using an radiofrequency (RF) power supply. Uncompensated Langmuir probes in RF sources act as antenna, where collected signals are greatly perturbed. Even compensation techniques that use L-R-C chokes for 13.56 MHz can be inadequate for sweeping the RF pickup. This is why Sudit [73] modified his probe circuitry to have a large floating electrode near the probe tip to more accurately sample the plasma potential fluctuations, which can drastically alter measurements. This electrode was connected to the probe body through a large enough capacitor that RF frequencies would view it as a short circuit, but smaller frequency perturbations would be blocked from affecting the signals. In essence, what was done by Sudit and applied in this report is a modified form of a double Langmuir probe to adequately sample an oscillating plasma potential. The circuit diagram for this probe is illustrated in Figure 5.10, where the subscript 'sh' denotes the impedance of the sheath, the subscript 'x' denotes the impedance of the auxiliary electrode, the 'cp' denotes the capacitor which couples the auxiliary electrode to the probe circuit, the subscript 'ck' denotes the impedance of the RF choke, and 's1' and 's2' denote the stray capacitances in the probe.

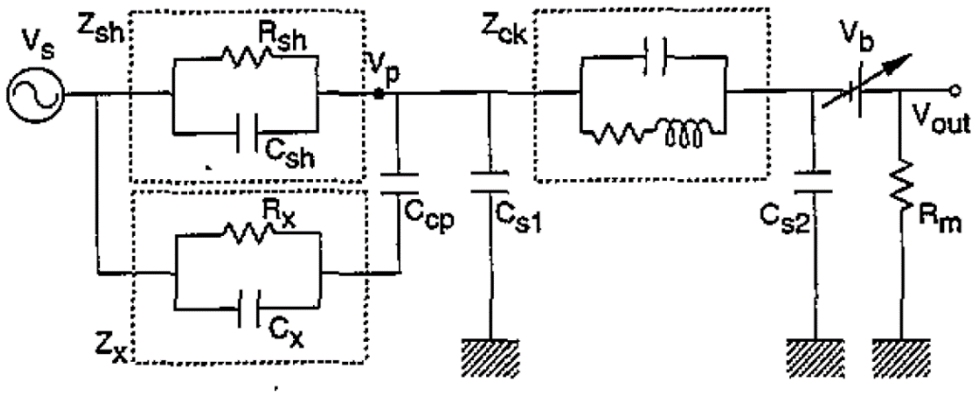

Figure 5.10: The circuit diagram representing the RF compensated Langmuir probe design proposed by Sudit [73], and used for measurements of the hydrogen plasma parameters for this report.

5.2.3 Optical Emission Spectroscopy

One of the more important measurements that can be made when trying to investigate retention in real-time is how the excited hydrogen species interact with lithium at the sample

surface. To do this, a Mikropack PlasCalc-2000-UV/VIS/NIR spectrometer was used to monitor the excited hydrogen and lithium species during exposure. The other diagnostic types used in these experiments were limited to pre- or post-exposure measurements, so the real-time knowledge of how the plasma interacts with lithium sample is invaluable.

As will be explained later, it was found that these measurements could not be used to determine quantitative values with any accuracy. What this analysis could provide were spectral values sampled over the duration of the plasma exposure, which could be examined relative to initial line intensities measured before the plasma was struck. As will be shown in the results portion of this chapter, the hydrogen α and β Balmer lines initially peaked after the plasma was struck and then fell rapidly, indicating that the hydrogen ions and radicals were being absorbed by the lithium. The H_α line is defined by the 656.3 nm wavelength and the H_β line is defined by the 486.1 nm wavelength. At the same time, the wavelengths representing the excited states of the lithium were recorded and rose in time with the fall of the hydrogen Balmer lines. The Li_I line is defined by the 550.3 nm wavelength and the Li_{II} is defined by the 671.1 nm wavelength. The information gleaned from these investigations was three-fold. First, one could identify the total time that the Li sample would absorb. Second, if an absorption threshold existed, this could be identified by observing relative changes in the tracked spectral lines. Finally, the change in intensity relative to the peak initial intensity could be used to investigate if more than one absorption rate existed. The final phenomenon was observed in nearly all samples, likely indicating a change in the bulk chemistry, which would change the absorption rate.

The Mikropack PlasCalc-2000-UV/VIS/NIR spectrometer was connected to a 1.33" Conflat optical fiber feedthrough using an Ocean Optics optical fiber cable. The feedthrough was set quite a ways away from the sample, so a separate vacuum-compatible fiber optic cable was used to extend the capabilities of the feedthrough and spectrometer to within 1" of the sample surface, with the termination of the in-vacuum cable aimed directly at the sample surface. Prior to each experiment, a background spectrum was taken without hydrogen or plasma in order to account for any external emission sources. The in-vacuum setup for the optical fiber transmission is illustrated in Figure 5.11.

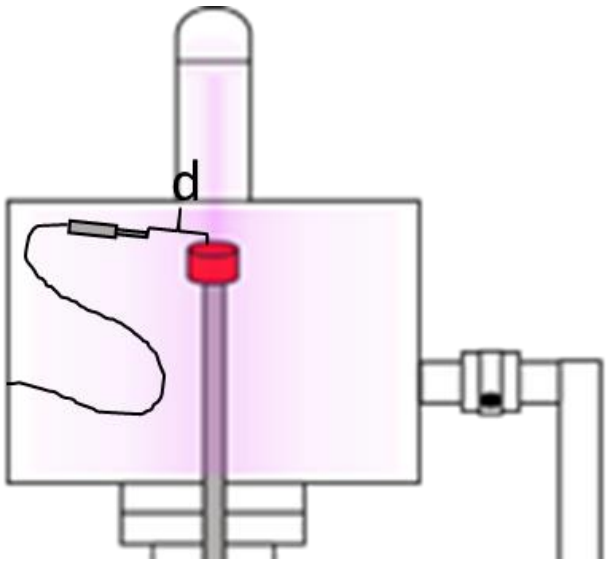

Figure 5.11: A block diagram for the in-vacuum optical fiber cable. The cable terminated at a distance, d, away from the surface of the sample (which was no greater than 1”), while still viewing the sample at a 10° decline.

Optical emission spectroscopy (OES) is often the diagnostic of choice when determining the properties of atmospheric plasma jets, but the method does have its own drawbacks. Often, gated monochromators are used for emission detection, able to block light outside of the wavelength spectrum of interest. The Mikropack does not require section scans to be evaluated in this manner, and can measure signals between 190 and 1077 nm in wavelength. In these experiments, the OES is only being used more so as a relative/qualitative diagnostic to witness the degree of change in the H_{α}, H_{β}, Li_{I}, and Li_{II} and how long these changes are maintained during exposure.

These two diagnostics were used over and above those active in the LiHDE experiments, described in Chapter 4. For more information regarding RGA gas analysis or condensed phase resistivity analysis, the author directs the reader’s attention to the previous chapter. The combination of all these diagnostic types will help to paint a picture of how the retention phenomenon occurs and what species fall out of the hydrogen plasma-lithium interaction.

5.3 Results

The ability of lithium to be able to absorb hydrogen isotope species is a much sought after quality for first wall materials. It allows new forms of the cross-sectional density and temperature profiles within the tokamak reactor that would otherwise be unattainable. For this reason, many demonstration scale reactors, such as NSTX [75, 76] and EAST [77], have employed lithium as a wall conditioner. This wall conditioning technique is where the entire inner vessel plasma-facing surface is covered in a layer of condensed lithium, at temperatures well below the melting point to maintain the lithium coating in the solid phase. Because solid coatings are used quite often in practice, the ability of solid Li samples to retain and release hydrogen was tested in TUFCON. The measurements taken from the solid Li sample experiments were then compared to the same measurements taken from liquid Li samples, exposed under a variety of conditions.

5.3.1 Langmuir Probe Analysis

In order to adequately relate the dose of hydrogen to each lithium sample, it was necessary to define the parameters of the hydrogen plasmas to which each sample was exposed. As stated earlier in the chapter, every sample was exposed to a hydrogen plasma at a Convectron-indicated pressure of 50 mTorr (actual pressure of approximately 30 mTorr) and an antenna radiofrequency power of 500 W. As such, these plasma conditions were given higher priority than what would typically be done for a full sweep of parameters. Since a full characterization of the plasma source is not within the scope of these work, extraneous results will be eliminated in favor of a single plot at the end of this section.

Two probes were used in this analysis. The probe actively sampling the plasma was a radiofrequency-compensated probe oriented so the probe tip faced up and into the bell jar. The tip of the probe was held at approximately the same height that the sample crucible would be held during exposure. A second, uncompensated probe was held in roughly the same position and orientation as the compensated probe, but set radially away from the uncompensated probe by approximately 1.5 inches. This second probe was used to investigate the floating potential in the plasma. A plot of a single representative I-V trace at 50 mTorr (indicated; equivalent to 30 mTorr actual) and 500 W is shown in Figure 5.12.

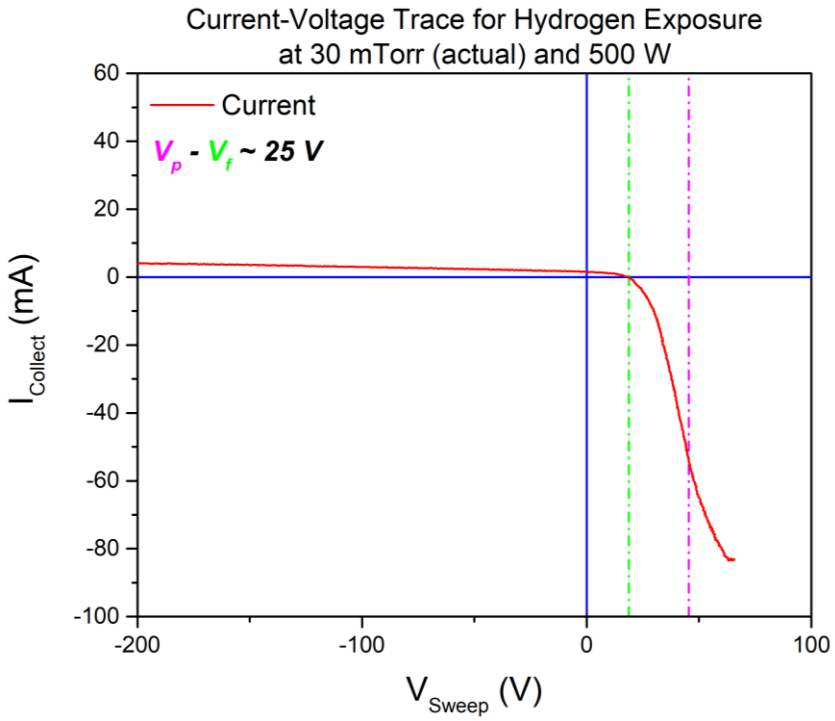

Figure 5.12: A plot of the current-voltage characteristic for a TUFCON hydrogen plasma at 50 mTorr (indicated) and 500 W. The resistor used for the current measurement in this case was 2.181 kΩ.

For the pressure and the RF power used during exposures (30 mTorr [actual] and 500 W), the electron temperature was found to be 5.2 ± 1.0 eV, while the electron density was found to be (3.3 ± 0.7) x 10^{18} m^{-3}. This equates out to an instantaneous, unbiased ion flux of (1.1 ± 0.1) x 10^{22} m^{-2} s^{-1}, which will be used in all future flux and fluence calculations. A -50V bias modifies the flux to (7.2 ± 1.5) x 10^{22} m^{-2} s^{-1}, while a -100V bias modifies the flux to (1.0 ± 0.2) x 10^{23} m^{-2} s^{-1}, based on the ion matrix sheath dependence on sample bias.

5.3.2 Calibration and Controls

Before relaying the information pertaining to the hydrogen that had been absorbed and that which was subsequently released, a calibration needed to be done in order characterize the

pumping capabilities of the TUFCON chamber. The TUFCON characterization test that was performed used a controlled hydrogen inlet flow rate and compared these values to both the chamber pressure read by an MKS Baratron and the RGA AMU = 2 partial pressure response. These results are illustrated in Figure 5.13 and can be used, along with the appropriate equation of state, to find the particle evolution rate from the surface of a sample. In all cases reported here, the gases registered by the RGA were considered ideal. Departures from ideality will be considered in future endeavors.

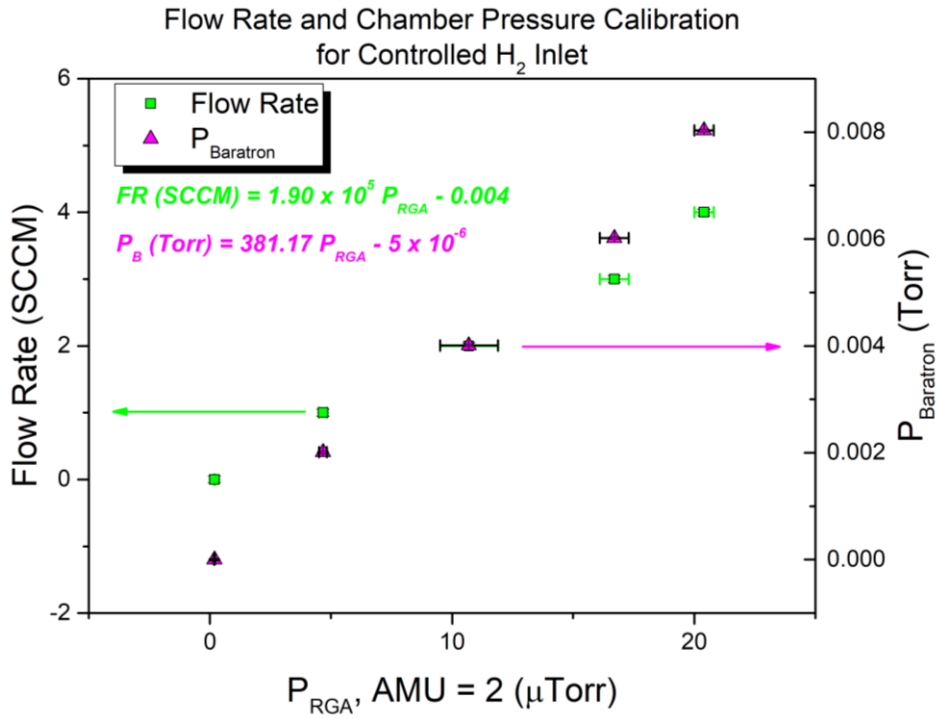

Figure 5.13: A plot illustrating the actual chamber pressure and the RGA AMU = 2 response to a controlled inlet of H_2 gas. Relationships between the pressures and the flow rate are detailed in the plot.

The final step in appropriately evaluating the data collected by the RGA and converting it to useful information, such as the flux evolved from the surface, was to subtract the contributions from the hydrogen background in the chamber. This was done by finding the lowest partial pressure values registered during the RGA trend scan, which were typically observed during the cooldown phase of TPD, and comparing these values to the base partial pressures registered during

the analog base scan taken prior to exposure. These residual hydrogen contributions were then subtracted from the partial pressures in the remaining trend scan. Residual pressures were often found to be 2 or more orders of magnitude lower than typical trend scan pressures.

5.3.3 Solid Lithium Samples

In his report, where he exposed solid and liquid lithium samples to a deuterium plasma in the PISCES-B linear plasma device, Baldwin [78] found that solid samples do not act as the perfectly absorbing plasma-material boundary. This ability, unique to only a few materials apart from lithium, is only achievable if the lithium is in the liquid phase. To make retention measurements in both the deuterated solid and liquid samples, Baldwin used temperature-programmed desorption and directly related the amount of deuterium released to the amount retained in the sample. His results, which relate the 1:1 absorption ratio for liquid lithium samples and the relative inability to absorb for solid lithium samples, were reported in Chapter 2. The aim here is to verify these results by exposing solid lithium samples to hydrogen plasmas and investigate the resultant resistance, spectral response, and gas composition quantities to understand the solution chemistry.

The procedure for solid Li exposition was slightly different than that for liquid lithium samples. To make sure that the lithium completed the circuit for the resistance measurement, lithium was loaded under an argon atmosphere, but, once reaching a reasonable base pressure, was heated beyond the known wetting temperature of lithium on stainless steel to make the best electrical contact possible. This was observed using the Kiethley Model 2000 Multimeter. Once an appropriate circuit had been established and a resistance indicating reasonable ‘conductivity’ had been read, the sample was cooled to room temperature over the course of 4 to 5 hours. After the sample temperature had decayed back to nearly room temperature, the sample was then exposed to a magnetized hydrogen plasma in the TUFCON helicon source. All solid samples were exposed with a constant hydrogen pressure of 50 mTorr (indicated) and an antenna power of 500 W, without the use of an external DC bias. The measurements from the K-type thermocouple indicated that the plasma had a significant heating effect on the sample, with the temperature in the sample able to climb to nearly the melting temperature of lithium. This phenomena is represented in the plot in Figure 5.14, where the spectral signals are plotted on one ordinate and

the sample temperature is plotted on the other ordinate with the sample exposure time plotted on the abscissa. This temperature increase likely had an effect on the absorption rate, at least to some degree, during the sample exposure.

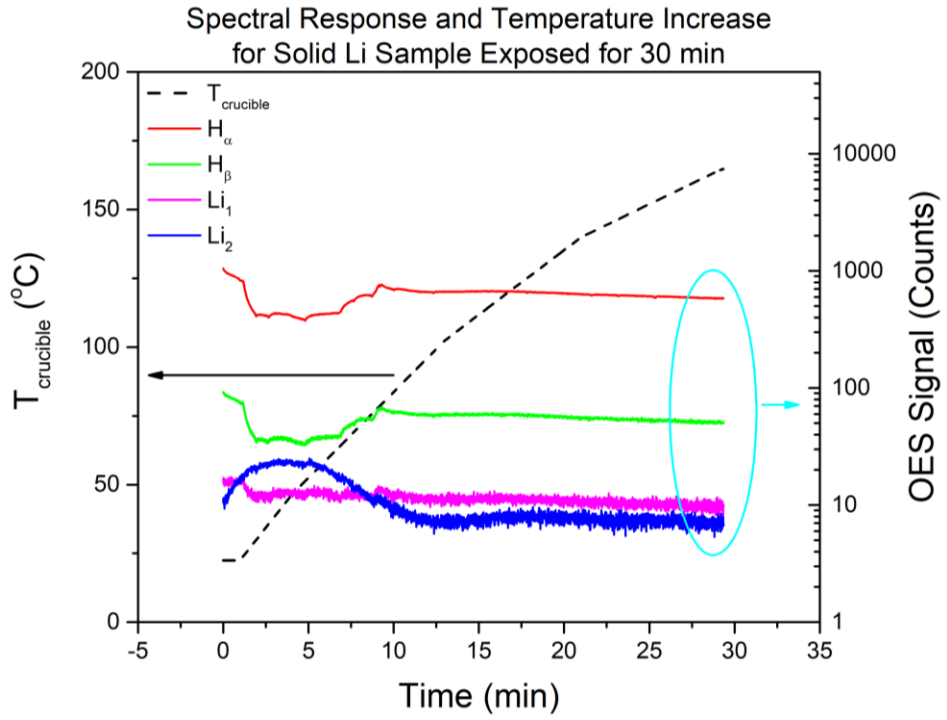

Figure 5.14: The spectral responses (with the background subtracted) and the temperature response in the solid sample exposed to a hydrogen plasma at 50 mTorr and 500 W for 30 minutes, which equates to a fluence of approximately 2 x 10^{25} m^{-2} (and a dose of nearly 3.9 x 10^{21}). By the end of the exposure, the sample temperature almost reached lithium's melting temperature.

Apart from the heating effect of the plasma, the most interesting features from Figure 5.14 are how each of the OES signals changed over time. The hydrogen α and β Balmer lines dropped during the first few moments of the plasma exposure, indicating absorption was taking place at the sample surface. These signals, however, rose back up to nearly their initial values after just under 10 minutes had passed. At the same time, the Li_{II} line showed a reciprocal trend, where the signal rose during these first minutes of exposure and then dropped at the same time the hydrogen lines returned to their initial values. What happened during and after these first 10 minutes have two possible explanations.

First, it may be that after the first 10 minutes lithium begins to absorb hydrogen at a different rate. In essence, the first 10 minutes marks the time during which the hydrogen ions and radicals that are interacting with the lithium are actively modifying the surface and sub-surface chemistry. It is important to remember from Veleckis' plot [23], described in Chapter 2 and 4, that there is a finite amount of LiH (or LiD, LiT) that will remain dissolved within the lithium even below the melting point (at an approximate atomic ratio of 4×10^{-4} H : 1 Li or 0.04 %). Taking this molar ratio into account, a 10 minute dose-equivalent equates to a higher ratio of 3.8 % (0.038 H : 1 Li). This, of course, assumes the entirety of the applied dose is absorbed, which is likely not the case based on the relative drops in the H_α and H_β signals. Regardless, this ratio is much higher than the small dissolved fraction predicted by theory, so hydrides are likely to exist.

If this last statement is true, why does the sample seem to suddenly stop absorbing hydrogen after roughly 10 minutes? The answer may be due in large part to surface saturation. Assuming penetration depths similar to those from Figure 5.2, it is likely that ions that bombard the surface of the sample will only be able to affect the Li up to approximately 1 to 2 nm below the surface. Assuming a conservative depth of 1 nm, the total number of Li particles within this near-surface volume is on the order of 1×10^{16}. The dose of hydrogen particles striking the surface over this exposure time, however, is closer to 1×10^{21}. This is a large discrepancy, but can be explained quite simply in terms of surface coverage. As surface sites become less available due to the overwhelming presence of the bonded hydride, more radicals and ions are rejected from surface positions such that only small fractions of the remaining particle dose are able to absorb and bond. One would expect the buildup of oxide layers to promote absorption, rather than hinder it, meaning that surface oxygen concentration is likely limited or surface availability is drastically reduced. This theory is corroborated by the decay in the Li_{II} signal during exposure. Essentially, the surface becomes saturated and rejects the remaining plasma dose, which is much more likely than the idea that large fractions of dissolved hydrogen can exist within a solid sample.

Similar trends were observed for each solid sample that had been hydrogenated for different exposure times. A plot showing a comparison of how the H_α signals compare for each exposure condition can be seen in Figure 5.15. The sample exposed for 15 minutes did not indicate the same degree of saturation as did the samples exposed for 30 minutes and 60 minutes; however, it may be that if the sample had been exposed for longer a saturation condition may have been

observed. The term saturation is used here, because it appears from jumps in the OES trend scans that the hydrogen signal nearly resumes its initial intensity, which was not consistently observed in the OES scans for the liquid samples described later in this chapter. An interesting observation of trends for the 30 minute and the 60 minute sample is that they appear to eventually start decreasing at longer times, possibly at time scales relevant to hydrogen diffusion away from the surface.

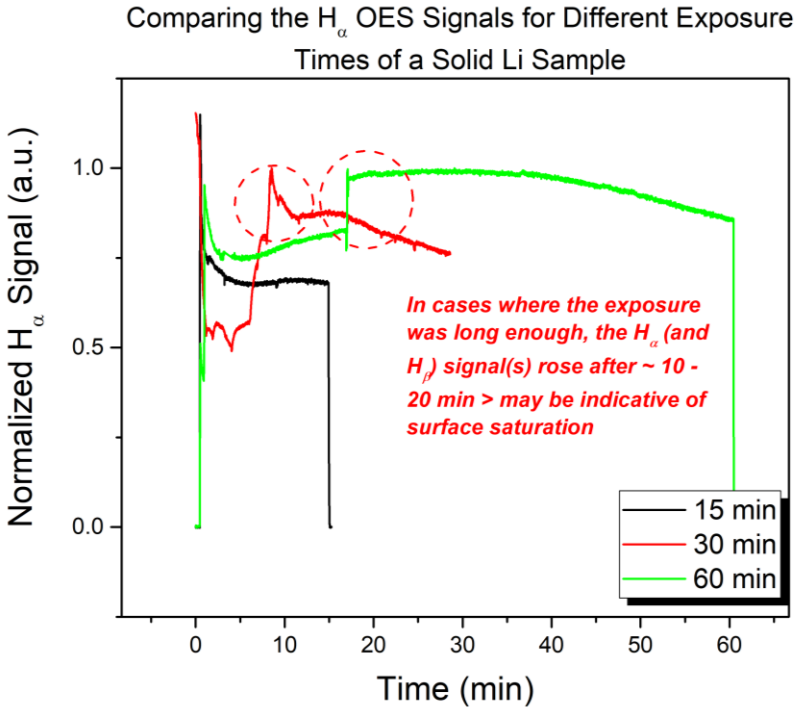

Figure 5.15: Comparing the H_α Balmer spectral lines for solid samples exposed for various times. All signals are normalized to the peak value after what is thought as a saturation event occurred. A sharp rise in these signals occurs after approximately 10 to 20 minutes has elapsed, either indicating a new phase of absorption (a transition from dissolved hydrogen to precipitated hydride) or a surface saturation condition.

Either of these two hypotheses can be either verified or discarded by running the solid samples through TPD scans. TPD results from a similar solid sample exposed to a hydrogen plasma for 15 minutes will be reported and discussed. The raw TPD results for this sample are

shown in Figure 5.16, but the discussion of these results will focus more so on the molecular hydrogen signal (2 AMU).

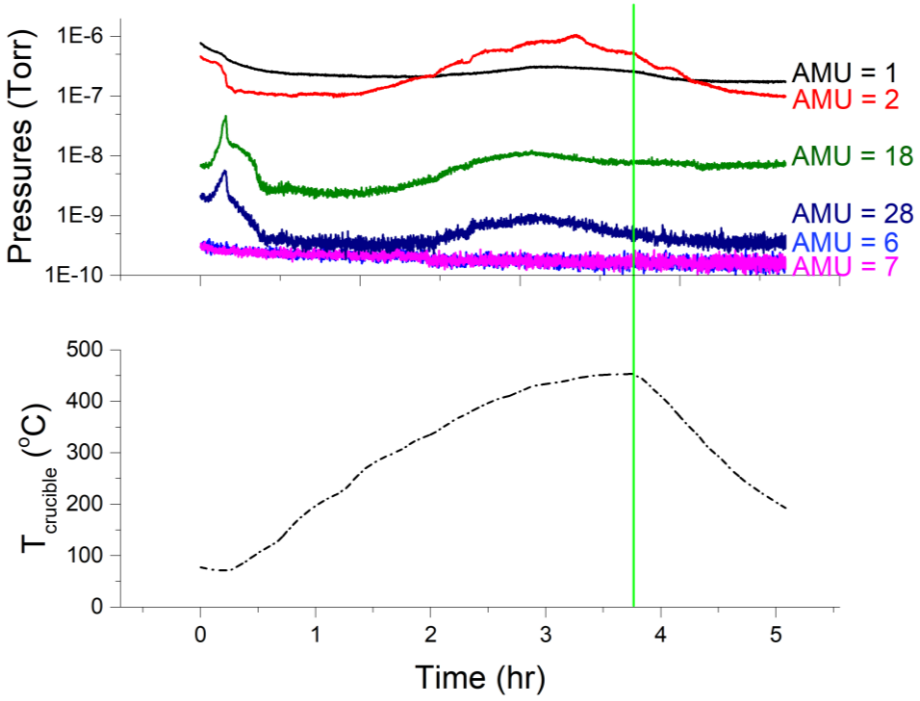

Figure 5.16: The raw TPD results for a solid lithium sample exposed to a 50 mTorr (indicated) hydrogen plasma at 500 W for 15 minutes, without an externally applied sample bias. The vertical green line indicates the point where the cooldown phase starts.

Unfortunately, the TPD scan for the 30 minute sample was taken in error because the appropriate pumping conditions during the first portion of the scan did not match those used for the remaining tests. Another problem with the results presented in this section is that the sample heater was only able to approach a maximum crucible temperature of slightly less than 500 °C for any given TPD experiment. Since hydrogen release from hydride that had been precipitated requires temperatures in excess of 500 °C, the hydrogen absorbed in these samples that was registered by the RGA was likely only the portion pertaining to the dissolved chemical species. The accumulated hydrogen release for the sample exposed for 15 minutes and the sample exposed for 60 minutes were compared. It was found that the total accumulated hydrogen response registered by the RGA was 3.6 ± 0.5 mTorr for the 15 minute sample and 4.2 ± 0.6 mTorr for the

60 minute sample. These values are quite close given the discrepancy in exposure time, again lending credence to the argument that the sample undergoes some form of surface saturation. It is also quite evident from these values that the amount of hydrogen being released from the solid samples far exceeds the dissolved concentration limits. This will be discussed later in this section.

A separate way to look at the chemical modification of the samples is to look at how the resistance change through the sample varied with exposure time. A higher resistance change would likely indicate the presence of hydride, whereas a lower resistance change would be measured if only dissolved hydrogen were present. If surface saturation were to play a role in the hydrogen uptake in solid samples, then the resistance change registered for all three exposure times should be identical, meaning the resistivity change for each is also identical. The resistance rise in the 15 minute and 30 minute samples were nearly identical at $0.008 \pm 0.005\ \Omega$ and $0.009 \pm 0.005\ \Omega$, respectively, meaning that the change in resistivity for both samples was also nearly identical. These resistance changes corresponded to sample resistivity changes of $(2.6 \pm 1.6) \times 10^{-5}\ \Omega$ m and $(2.9 \pm 1.6) \times 10^{-5}\ \Omega$ m, respectively. The sample exposed to a hydrogen plasma for 60 minutes, on the other hand, registered a negative resistance change of $-0.060 \pm 0.005\ \Omega$, which corresponded to a negative resistivity change of $(-19.6 \pm 1.6) \times 10^{-5}\ \Omega$ m. The initial resistance values were 0.232 Ω for the 15 minute sample, 0.197 Ω for the 30 minute sample, and 0.135 Ω for the 60 minute sample.

The changes reported here are well above the dissolved concentration thresholds measured by Adams' group [38], meaning that the presence of the hydride is affecting the electrical properties of the solid solutions. For the 60 minute sample, a number of factors could have contributed to the drop in resistance, chief among them being that the control measurement taken before hydrogen exposure had error. This would have likely been caused by contact resistance if the lithium sample was not making a good connection with either of the electrodes, whether it be because the sample had not fully wetted one of them or that the electrodes themselves had surface contamination layers that may have inhibited proper electrical contact.

While raw partial pressure plots, like those in Figure 5.16, can relate a lot of useful information, further analyses are required for understanding the degree to which each lithium sample absorbed hydrogen and at what rate is it released from the sample volume. Using the information described in Figures 5.13 while also subtracting out the background hydrogen signal

and applying the appropriate equation of state, one can evaluate the evolution rates from each sample. In all cases the gas registered by the RGA was assumed ideal. How other equations of state modify these measurements will be left for future work. The evolution fluxes plotted vs. temperature for the sample exposed for 15 minutes and the sample exposed for 60 minutes are shown in Figure 5.17.

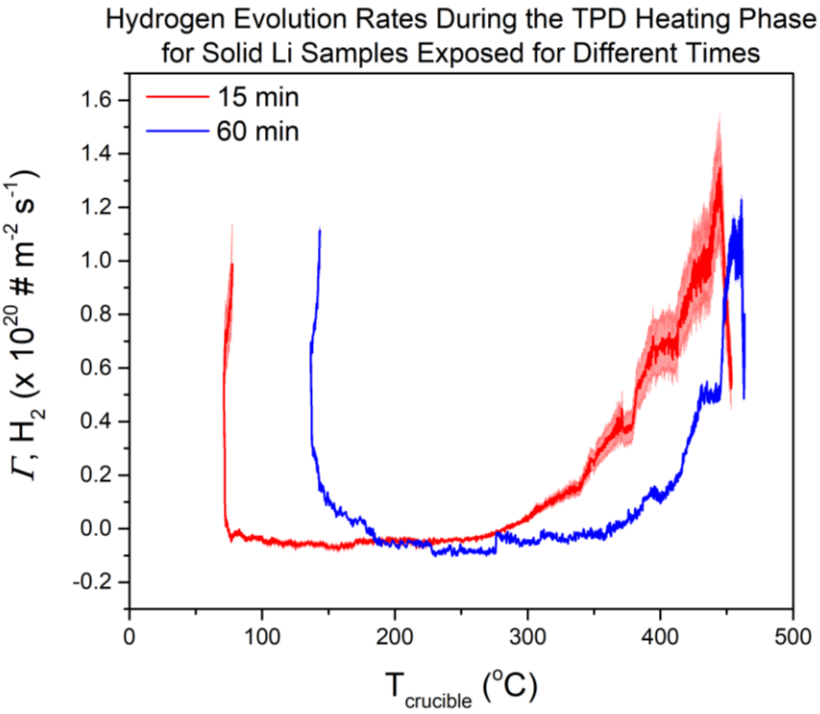

Figure 5.17: A comparison of the hydrogen evolution fluxes for solid lithium samples exposed for different lengths of time to a hydrogen plasma.

The trends in Figure 5.17 have a couple of features that are important, and a couple of features that seem in error. First, the large evolution rate values shown on the left of these trends is due to residual hydrogen gas that remained in the chamber after exposure, which had not been fully evacuated, which was rectified in future tests. Second, it appears as if in both cases the solid sample was at an elevated temperature when the TPD scans were started. This was because of how effectively the plasma was able to heat the sample. Sample temperatures, however, never reached above the lithium melting point. The peak release fluxes from each sample at temperatures that were approximately 20 K apart, with nearly identical amplitudes at approximately 1.2 x 10^{20} H_2

molecules m^{-2} s^{-1}. This value is more than an order of magnitude less than the H_2 release flux from pure LiH witnessed in the previous chapter. What is interesting to note, is the sharper trend that appears in the 60 minute sample as opposed to the 15 minute sample, and what the area under each curve means when deciphering how much hydrogen had been retained in each sample.

At first glance, the evolution rates from the solid samples may appear counterintuitive. If there does indeed exist an insulating layer of hydride along the surface, how is there a peak in recovery at temperatures between 400 and 500 °C? Should not the precipitate be evolving substantial amounts of hydrogen at much higher temperatures – somewhere between 600 and 700 °C? While the details of these answers will be explained in the next section with relation to the liquid samples, what is likely happening is that the insulating precipitate layer is dissolving into the solution as temperature is increased, as predicted by Yakimovich's work [40]. As such, the peak values here represent a combination of the small amount of dissolved hydrogen and the small fractions of atomic hydrogen that are initially formed as hydride but dissolve into solution during the TPD process.

Using the Langmuir probe results from the previous section, the dose to the 15 minute sample was approximately $(1.9 \pm 0.2) \times 10^{21}$ and the dose to the 60 minute sample was $(7.8 \pm 0.7) \times 10^{21}$. Eliminating the effects of the residual hydrogen gas and integrating the evolution rates over time, it was found that the 15 minute sample released approximately $(9.6 \pm 1.6) \times 10^{19}$ H_2 molecules and the 60 minute sample released approximately $(10.9 \pm 0.2) \times 10^{19}$ H_2 molecules. It is interesting that these retention values are so close, proving that solid lithium will indeed undergo saturation. This likely occurs along the surface, preventing further penetration into the bulk. This means that the 15 minute sample retained 10.1 ± 1.7 % of its dose, while the 60 minute sample retained 2.8 ± 0.1 % of its dose. These values are slightly higher than the retained dose reported by Baldwin for his solid sample, which is likely due in large part to the change in temperature the sample underwent during exposure. For reference, Baldwin [78] reported a solid sample retention of 1.7 ± 0.9 % of the applied dose.

The conclusions from the tests in which solid samples are exposed to hydrogen plasmas for different periods of time relate primarily to the efficacy of solid lithium as a sink. From the results obtained in this section, it appears as if the solid state is slightly more effective at retaining hydrogen than previously reported [78], but it still does not come near the amount for a 1:1 atomic

ratio. Lithium in this phase also exhibits evidence of saturation, as demonstrated by the relative change in the OES signals, which does not appear to be compensated by hydrogen diffusion away from the surface at these time scales. The improved uptake when compared with literature may be due in part to the solid sample temperature, the effects of which will need to be explored in future work.

5.3.4 Liquid Lithium Samples

The results that will now be discussed are in relation to the liquid lithium samples that were exposed to a variety of hydrogen environments, while being held at various temperatures and various levels of sample biasing. The goal of these experiments is to observe how each parameter affects the final hydrogenated lithium solution, and, if possible, to identify the ratio of dissolved hydrogen to hydride precipitate for each sample condition. These results will be broken down into sub-sections that describe trends with respect to: sample temperature, sample bias, exposure time, and exposure condition. These results constitute the bulk of the work accomplished in the TUFCON chamber. For the sake of brevity, only the most important results will be discussed in each section.

5.3.4.1 Effects of Sample Temperature

One of the biggest factors in determining the degree to which hydrogen isotopes are absorbed in lithium is the temperature of the lithium sample. Baldwin [78] found that no matter what temperature a liquid lithium sample was held at during exposure, there always existed a 1:1 absorption ratio until the sample had reached saturation. Sample temperature also has an impact on what resultant surface and sub-surface chemistry as described by the curve in Figure 5.5. As mentioned previously, a combination of the spectroscopic response and the resistivity change, along with a deconvolution of the TPD spectrum, allow one to infer the identities and ratios of the chemical products. In all experiments listed here, the only variable modified was the sample temperature. For each test, the hydrogen pressure was held constant at 50 mTorr, the RF power was held at 500 W, and the exposure time was set to 15 minutes. Each sample was biased to -50 V, meaning that the total fluence over 15 minutes was approximately $(6.5 \pm 1.4) \times 10^{25}$ m^{-2}. This

equates to doses of approximately 38 % of the saturation threshold (where $N_H = N_{Li}$). At this level, there should exist both dissolved hydrogen and hydride precipitate with the solution, and the sample is defined by the term “less-than-saturated”.

First, from the spectral responses, the degree of absorption can be broken down into what appears to be two distinct absorption phases. Evidence of two absorption phases is clear in Figure 5.18, where a representative OES scan for a sample held at 250 °C is displayed. From the spectral responses of the H_α and H_β signals, the durations and fluences for each absorption phase are described in Table 5.1.

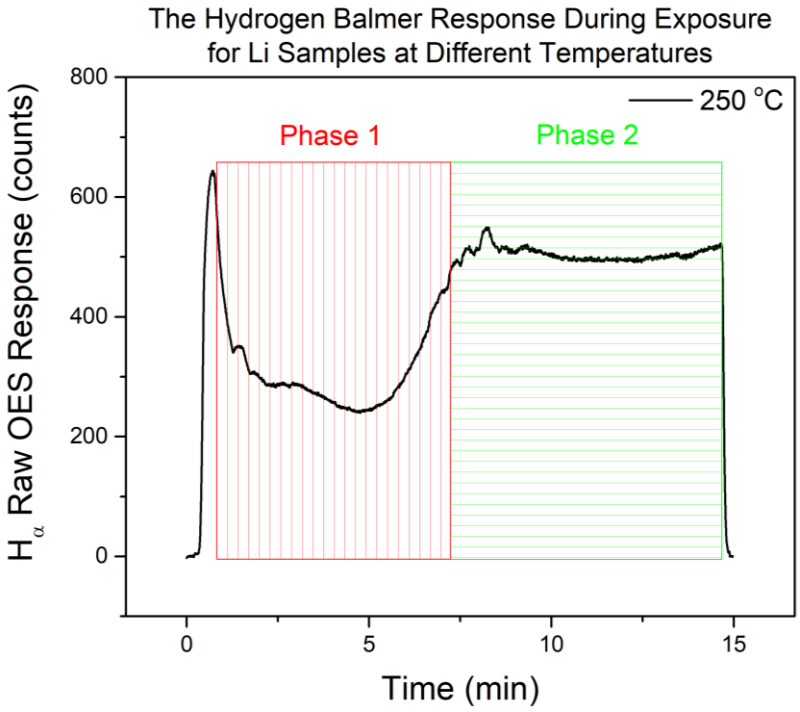

Figure 5.18: A representative H_α trend for the sample exposed at 250 °C to 50 mTorr (indicated) of hydrogen at an RF antenna power of 500 W.

Table 5.1: The different absorption phases and the associated fluences for each sample as a function of exposure temperature.

Sample Temperature	t Phase 1 (min)	Fluence Phase 1 ($x10^{25}$ m^{-2})	t Phase 2 (min)	Fluence Phase 2 ($x10^{25}$ m^{-2})
250 °C	6.8	2.9 ± 0.6	7	3.0 ± 0.6
300 °C	9	3.9 ± 0.8	5	2.1 ± 0.5
350 °C	4	1.7 ± 0.4	9.8	4.2 ± 0.9
400 °C	4.2	1.8 ± 0.4	10.3	4.4 ± 0.9

Based on the spectral responses alone, it appears the absorption phases are broken up such that the samples at lower temperatures tend to absorb more lithium in the first absorption phase than do the samples at higher temperatures. Fluence values corresponded to Phase 1 doses of (5.6 ± 1.2) x 10^{21}, (7.5 ± 1.5) x 10^{21}, (3.3 ± 0.8) x 10^{21}, and (3.5 ± 0.8) x 10^{21}, respectively. These doses account for 45 ± 9 %, 60 ± 12 %, 26 ± 6 %, and 28 ± 6 % of the total dose to each sample, respectively. If the primary absorption phase indicates the amount of bombarding hydrogen that dissolves, then this trend is counterintuitive, apart from the fact that the doses themselves are much higher than what would be expected for the dissolved hydrogen fractions. This initial phase could also be due to the consumption of hydrogen by oxygen along the surface, which then results in saturation along the surface [49, 50]. Based on the information presented in Figure 5.5, if the initial absorption phase were to indeed be representative of the dissolved hydrogen fraction then that fraction should increase with increasing temperature. Figure 5.19 shows the trends for the Li signals, which help to verify the absorption phases inferred from Figure 5.18. The phenomena observed in the OES responses are likely not able to be directly correlated to the species formed in the solution.

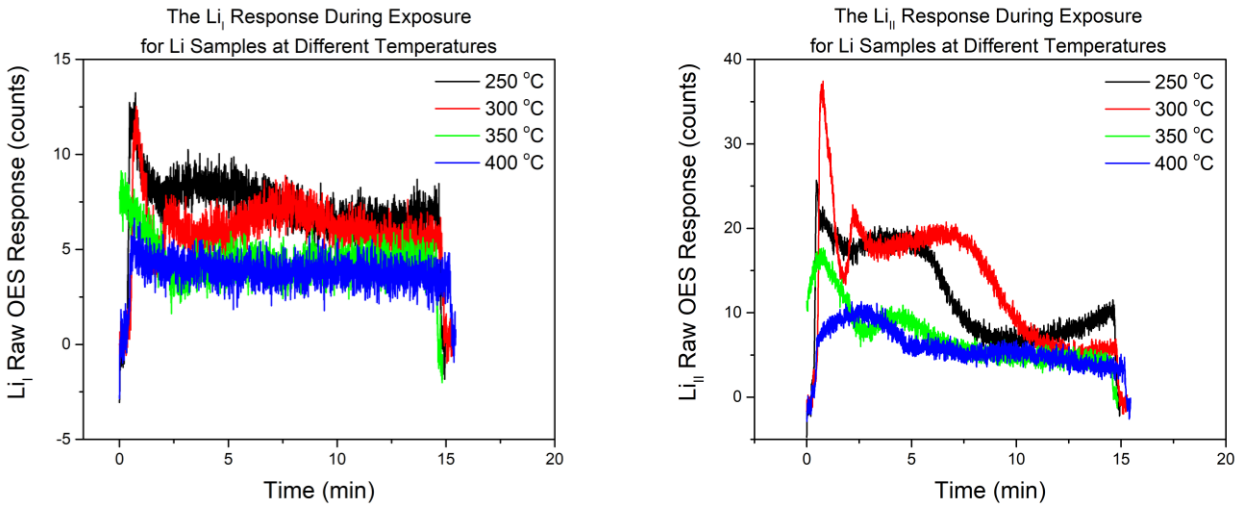

Figure 5.19: The spectral responses for the Li_I and Li_{II} signals as a function of time at each sample temperature. Samples at lower temperatures show a greater positive change in the Li signal, which is sustained for much longer.

From the data in Figure 5.18 pertaining to the 250 °C sample, it appears that even in the second absorption phase the intensity never fully climbs back to its original magnitude. The lithium signal also never completely decays. What differs in these and all liquid samples from the solid samples is that the OES intensities for the solid samples seem to nearly return to their initial values once a certain threshold is crossed. The jump in the solid samples is also much more drastic than in the liquid samples, where the change in absorption phase is much more gradual. The relative level of the intensity change in the H_α and H_β signals in each sample may tell how strongly each sample absorbs hydrogen in each phase. When comparing changes in relative signal intensity, there is not as much of a drastic difference as observed when deciphering fluences for each absorption phase.

Table 5.2: Approximate percent changes in the H_α intensity for the different absorption phases shown in Figure 5.19 with reference to the unperturbed signal from the control sample exposure.

Sample Temperature	ΔI Phase 1 (%)	ΔI Phase 2 (%)
250 °C	62	24
300 °C	84	14
350 °C	58	35
400 °C	59	26

Compiling the data presented in Figures 5.18 and 5.19 and the data in Tables 5.1 and 5.2, what is happening during exposure for increasing sample temperatures becomes clearer. At higher sample temperatures, the energy barrier to form hydride is reduced, a trend which was also reported in Ref. 79. This means that any surface insulating hydride layer will be established faster in liquid samples at higher temperatures. The differences in the Phase 2 absorption described in Table 5.2 is then due to the diffusivity of hydrogen away from the surface, which is also enhanced with temperature. In this way, there exists a tradeoff, especially in samples that are not well mixed.

Ideally, the change in resistivity from pre- to post-exposure would then indicate the level by which the sample had been chemically converted, but a number of these resistivity changes appeared erroneous, often indicating decreases in resistance rather than the expected increases. Resistivity was not used to directly compare the chemical significance between pre- and post-exposure, but was instead used to indicate the degree of desorption and evaporation during the TPD portion of each experiment. One thing that can be identified between the pre- and post-exposure readings is that they often appeared to change very little. What can be concluded from this is that even after exposure there existed a conducting medium between the inner and outer crucibles, meaning that conversion to hydride (or hydroxide) was not absolute. Resistivity values taken during the TPD process are illustrated, along with the raw H_2 partial pressure measurement for the 350 °C sample, in Figure 5.20. Figure 5.20 is a representative result, where all samples

exposed at different temperatures seemed to follow similar trends, the peculiarities of which will be explained shortly.

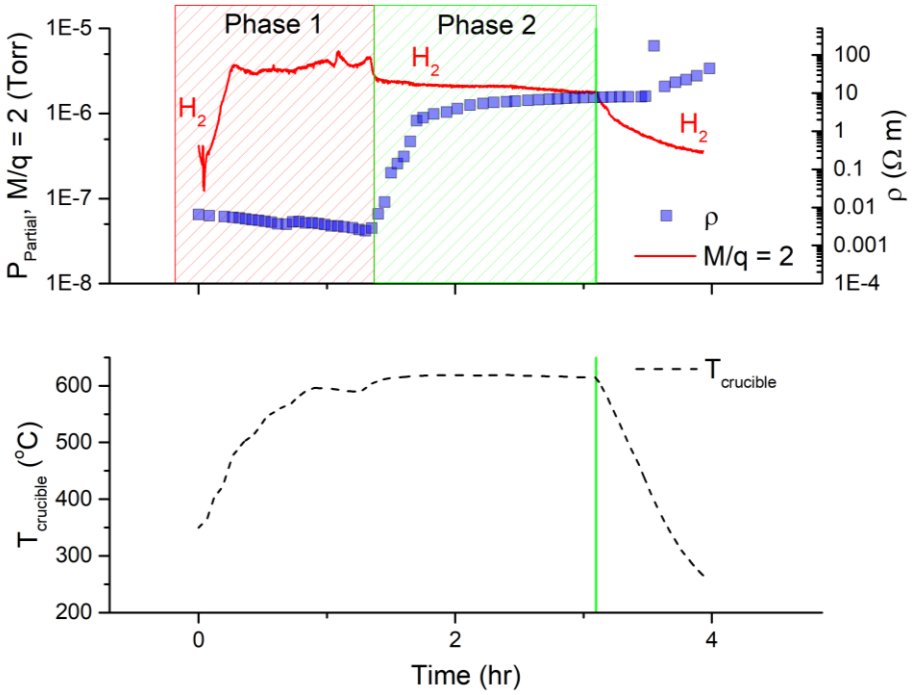

Figure 5.20: Data for the raw 2 AMU RGA signal and the resistivity measurement taken during the TPD portion of the experiment for the sample exposed at 350 °C.

Similar to how the OES signals were indicative of a change in retention, the H_2 trends in the TPD spectra for all samples exhibit what appears to be different desorption phases. This is not uncommon in these systems, and is similar to trends reported by Baldwin [80] in a separate study from the one in Ref. 78. In this work, Baldwin measured retention using TPD as his only metric. The spectra he collected exhibited periods where the Li sample would release relatively high amounts of deuterium, but these signals would eventually fall to plateau pressures. He argued that the initial period, where greater amounts of deuterium gas (D_2) were being registered by the RGA, was due to the amount of deuterium that had remained dissolved within his solution, in what he had labeled as the α (liquid Li-rich) phase. Once this initial concentration had been released, then a pressure plateau, which was still elevated above background pressure values, was observed and could continue for hours or even days, depending on the amount of deuterium in the sample and

at what temperature the sample was held. This plateau section was theorized to be due to the thermochemical interaction where solid deuteride precipitate (the β phase) was dissolving into the solution. The dissolved, atomic deuterium would then migrate to the surface, recombine, and release as either D_2 or HD gas (or HDO or D_2O, depending on the level of impurity). These pressure plateaus are predicted from a thermodynamic standpoint [25], especially when desorption occurs well below the decomposition temperature of the hydride or deuteride salt (typically at or above the melting temperatures of nearly 690 °C). The meaning of this explanation is made clear when looking at Baldwin's representative TPD plot in Figure 5.21. Release at temperatures below the melting point of hydride may also be affected by the presence of oxygen [49, 50].

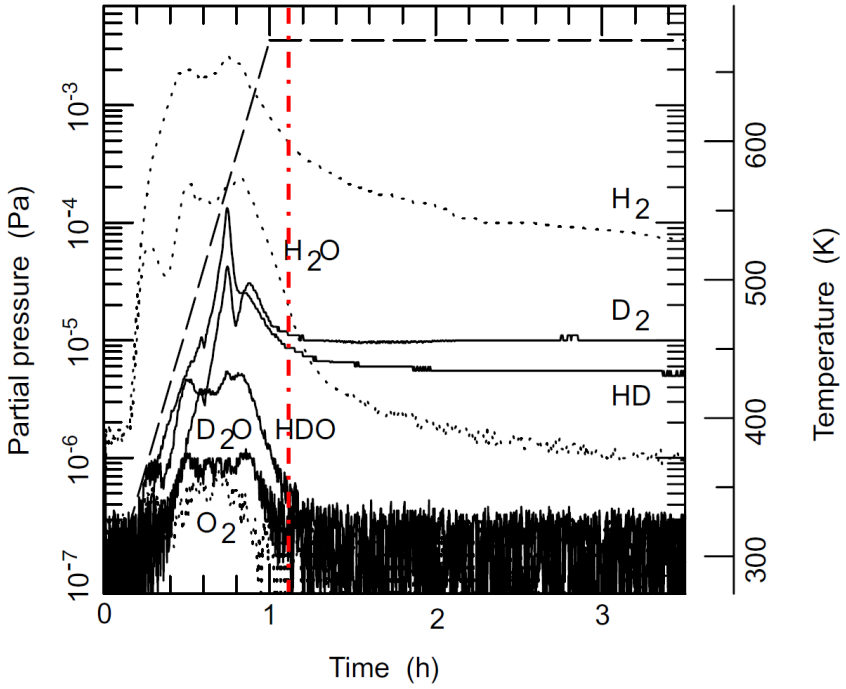

Figure 5.21: A representative TPD plot measuring deuterium retention in a Li sample that was exposed to a PISCES-B deuterium plasma at a sample a temperature of 523 K, a sample bias of -100 V, and for a fluence of 8 x 10^{24} m^{-2} [80]. The vertical, dashed red line indicates the transition between desorption phases.

What Baldwin did not have in order to confirm his claim was the ability to monitor the condensed phase for changes in chemical composition. In the tests reported in this chapter,

resistivity changes were unable to be used for their original purpose – to identify what, if any, chemical changes occurred between pre- and post-exposure samples; however, as is clear from Figure 5.20, monitoring resistivity changes in the sample during TPD scans helps to explain what hydrogen phase is being desorbed. These resistivity changes aid in confirming Baldwin's hypothesis that two desorption phases do indeed exist. Further support of this hypothesis can be seen in the state of the sample after it was removed from the TUFCON chamber, as shown in Figure 5.22. The white flakes that remained in the sample crucible are likely leftover hydride or hydroxide precipitate that did not dissolve into solution during the heating phase of the TPD process.

Figure 5.22: The state of a post-TPD sample after having gone through a 15 minute plasma exposure, where the sample was held at 350 °C and was biased at -100 V. The remaining hydride was not present below what appeared to be an apparent surface structure (empty space in the crucible below what is shown).

Another supporting argument, similar to that which is represented by Figure 5.22, for the presence of the two distinct desorption phases and how these relate to the change in solution resistivity is that lithium evaporation was quite substantial in the main chamber. Significant lithium

signals were not registered by the RGA, however, because of how far the filament was offset from the sample, similar to why there was a lack of lithium signal in the spectra in Chapter 4. Since there is a substantial offset in the RGA filament, a great many condensing surfaces exist for lithium to adhere to prior to interaction with the detector. In the main chamber, lithium did condense on the nearly all of the surfaces, and even deposited onto the bottom of the radiation shield surrounding the crucible. This helps support the claim for two distinct desorption phases from a resistance standpoint, since the depleted presence of lithium in the sample eliminated the conducting pathway which had initially been present between the electrodes in the crucible.

Taking data like that which is presented in Figure 5.21 and extrapolating out the plateau section to the point where the hydrogen source is completely depleted, then the full original dose to the sample should be recovered. This is only true in the case where there exists an absence of an insulating surface hydride or hydroxide layer, and any hydride that forms mixes into the lithium solution. Once established, this insulating layer inhibits further absorption. Even for liquid samples, an insulating layer may exist, as evidenced by the two absorption phases in the OES trends. What is interesting is that performing an extrapolation on the data in Figure 5.20 revealed that the total amount of hydrogen recovered returned approximately 90 % of the dose from Phase 1 absorption.

Recovering the initial dose value can also be achieved by heating the sample up to above 750 °C and fully evaporating the sample; however, this was not done for the experiments within this chapter. Armed with this knowledge, and the knowledge of how the hydrogen pressure relates to an evolving flow rate, one can now separate the TPD spectra to figure out how much of the original hydrogen dose was converted to hydride and how much remained dissolved in solution. To be clear, β phase dissolution as a function of temperature must also be taken into account when analyzing the TPD results.

Another important factor to consider is how quickly the hydrogen in the dissolved phase can be recovered from the sample. Figure 5.23 illustrates the release fluxes for the samples as a function of the temperature they were held at during exposure. Also plotted in Figure 5.23 are the crucible temperatures associated with these peak release fluxes.

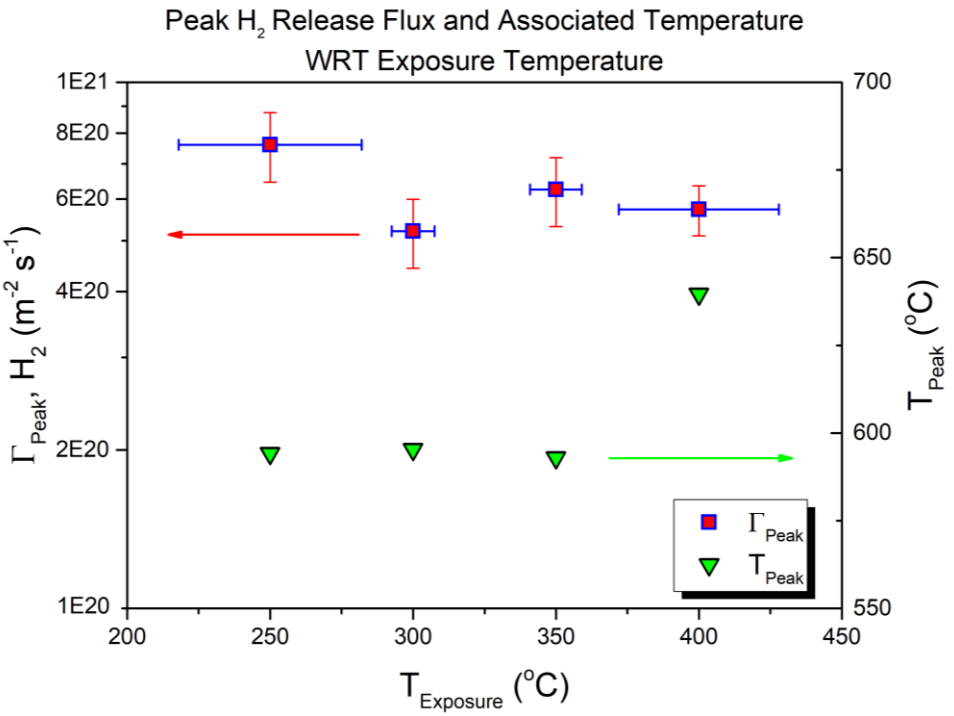

Figure 5.23: The peak release fluxes and the associated temperatures as a function of the sample temperature during exposure.

An interesting, but unsurprising, result from the data in Figure 5.23 is the fact that there exists very little variation in the peak hydrogen evolution fluxes between sample temperatures. If there exists any trend at all, it appears as if the peak fluxes are falling with increasing sample exposure temperature. If there does exist an inverse trend in the evolution flux with sample temperature in hydrogen from the dissolved phase, it may very well be due to the vapor pressure of lithium and its dependence on temperature. The peak fluxes in these tests correspond to the maximum value at which the small amount of hydrogen that remained dissolved within the solution was able to migrate to the surface, recombine, and evolve as molecular hydrogen. After the dissolved hydrogen has been removed, remaining hydrogen in the sample can only evolve once hydride or hydroxide dissolution begins to occur.

In vacuum, the vapor pressure of lithium as a function of temperature is quite high, with noticeable quantities of lithium evolving at temperatures at or in excess of 400 °C. Lower absorption rates and release fluxes may be due directly to the effects of lithium vapor pressure.

Future work should focus on investigating retention as a function of exposure temperature over a broader range of temperatures to establish how, if at all, the vapor pressure of lithium affects absorption and desorption of hydrogen.

Before continuing on to investigate the amount of hydrogen actually retained in the dissolved phase, it is worth briefly mentioning a conclusion that can be drawn from the data in Figure 5.23. The peak flux values from the dissolved phase are not great enough to compensate for fuel losses at the wall, described previously in Chapter 4. This is a very important result, in that it means recovery of tritium in lithium solutions with atomic fractions below the solubility threshold (in the "far-from-saturated" regime) will prove nearly impossible by using heat as the sole impetus, whereas results from Chapter 4 proved that the heating of solutions nearing saturation will indeed be able to compensate wall losses. Many reasons exist for why the heating of "far-from-saturated" solutions will not give a high enough tritium yield, but all of these stem from the same underlying point: the population of hydrogen in samples below the solubility threshold is so low that the probability of two hydrogen atoms diffusing, recombining, and evolving from the surface is not high enough to counteract in-vessel consumption. As such, other supplemental or alternative schemes will need to be tested to aid in recovery from these types of samples. Combining the information from Chapters 6 and 7 of this report will provide an explanation on how this can be done.

Following the theoretical claim laid out by Baldwin [80] and the experimental verification of this claim using the change in resistivity as the marker between desorption phases, the total amount of hydrogen trapped in the lithium in the dissolved state can be evaluated. This was done by integrating the calibrated evolution rates over the time in which the sample undergoes Phase 1 desorption. These values as a function of sample exposure temperature are plotted in Figure 5.24 and are compared to the dissolved concentration curve Yakimovich derived based on thermodynamic principles [40] and the work from previous studies [22 – 39].

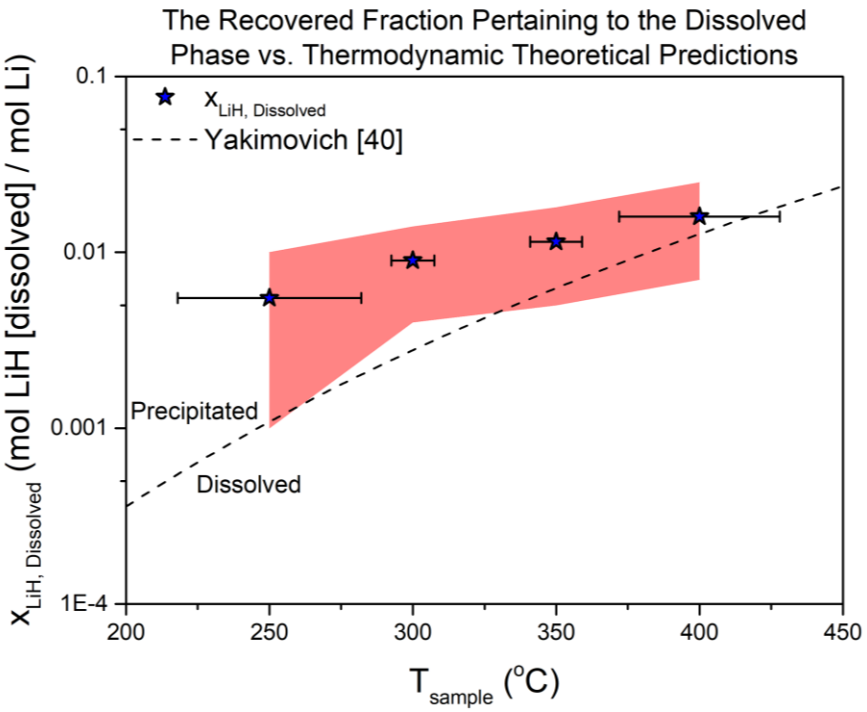

Figure 5.24: A plot illustrating the dissolved fraction of LiH in Li solutions at various temperatures. These are plotted relative to the theory proposed by Yakimovich, et al. [40], which describes the thermodynamic solubility limitations. The red, shaded area represents the experimental compounded error.

Error in the results shown in Figure 5.24 can stem from the simple fact that TPD requires heat to remove material from a sample. As a hydrogenated lithium sample is heated, not only does hydrogen begin to evolve from the α phase, as was predicted by Baldwin [80], but LiH is also able to dissolve into solution to a greater degree. This enhanced, temperature-dependent dissolution of LiH complicates the simple time-integration used to evaluate the dissolved fraction for various exposure temperatures, and makes it appear as if more hydrogen had been absorbed into the α phase than actually had been. Proper evaluation of the true dissolved atomic fraction as a function of exposure temperature requires that one eliminate the contribution of the enhanced hydride dissolution to arrive at the actual amount of hydrogen that was originally absorbed in the α phase.

The contributions from LiH dissolution can be approximated, and can be subtracted from the total α phase evolution. Knowing that the peak hydrogen contribution from the β phase

manifests as the plateau pressure, the β contribution to the dissolved fraction is based on a linear approximation in time between the initial minimum evolution rate and the evolution rate evaluated for the plateau pressure. This portion is then integrated over time and subtracted from the previously evaluated evolution rates. A more sophisticated estimate for the contributions from β phase dissolution would require more in-depth measurements and analysis than what is capable in TUFCON. The approximate contributions were calculated, and the resulting, corrected α phase atomic fractions are shown in Figure 5.25.

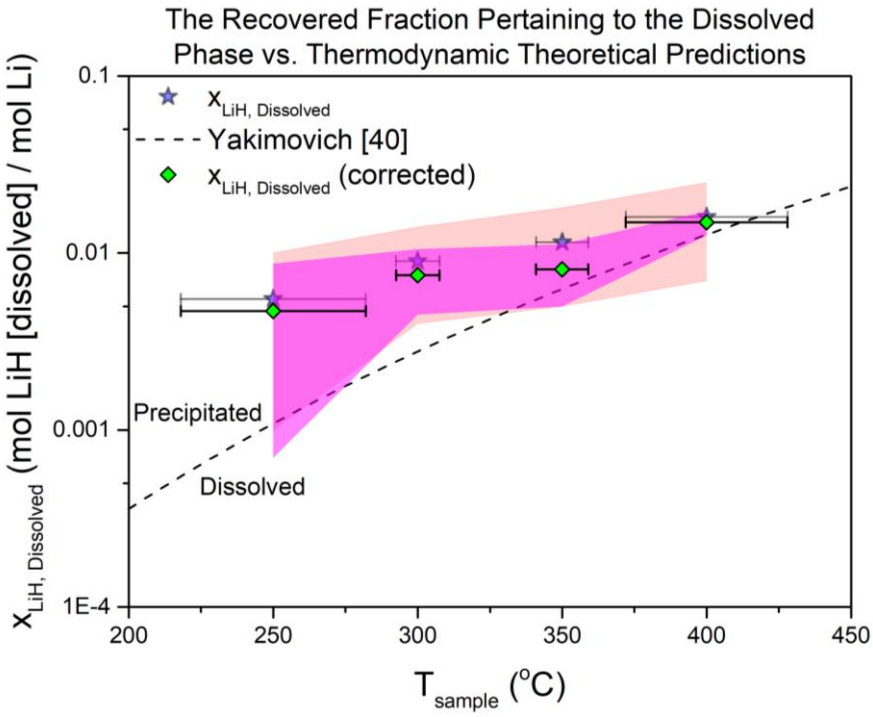

Figure 5.25: A plot illustrating the corrected dissolved fraction of LiH in Li solutions at various temperatures superimposed over the fractional values from Figure 5.24. These are plotted relative to the theory proposed by Yakimovich, et al. [40], which describes the thermodynamic solubility limitations. The magenta, shaded area represents the experimental compounded error.

Figure 5.25, while somewhat unremarkable, is very important when considering what species are likely to be formed when hydrogen, deuterium, or tritium plasmas interact with liquid lithium at various temperatures. The values represented by the diamonds in this plot were obtained by using the stark change in resistivity as a marker, indicating where the upper integration bound

for the release rate over time occurred. The integrated values were then considered to be release doses of molecular hydrogen. Since hydrogen evolves as a diatom, the atomic stoichiometric ratio in each sample needed to be accounted for. The contributions from β phase dissolution during heating were also corrected for.

What can be said about Figures 5.24 and 5.25 is that while it may appear that the amount of hydrogen dissolved in samples exposed to plasmas is greater than what is predicted from thermodynamics, the evaluation of these data is dependent on the accuracy with which the inflection point in resistivity determines the upper bound for desorption from the dissolved phase. The data gathered from this evaluation are quite close to the theoretical predictions for dissolution based on sample equilibrium and thermodynamics, meaning that the thermodynamic principles likely still hold in cases where lithium is exposed to plasma as the medium, instead of to gas alone. This is especially true for the ion energies expected in TUFCON. If there is an improvement in the dissolution fraction due to the presence of a plasma, this improvement is very slight, considering how many sources of error existed when reaching the conclusions illustrated in Figure 5.24, along with the fact that chemical conversion to hydride still remains a hard upper limit in this scenario, as stated earlier by Mundra [41]. Understanding plasma-lithium interactions from the perspective of the dose to a sample, however, is still quite important because this knowledge will determine how to deal with the solution that exits the reactor. What is also important is how oxygen may or may not enhance absorption and desorption, since the oxygen-hydrogen bonds in the presence of lithium have been shown to be weaker than the lithium-hydrogen bonds [50].

We can therefore conclude this section with the knowledge that at these energies, plasma interactions do not enhance hydrogen dissolution over and above what is predicted from thermodynamic principles. During absorption, two phases exist due to the formation of an insulating surface hydride layer. As described earlier, the absorption characteristics in both Phase 1 and Phase 2 are dependent on sample temperature, with hydride formation and hydrogen diffusion being the fundamental phenomena that govern uptake in non-agitated liquid lithium samples. If hydrogen recovery in “far-from-saturated” samples is desired, then methods that aid in supplementing heating drive will be required, which will be revisited in Chapters 6 and 7.

5.3.4.2 Effects of Sample Bias and Exposure Time

The effect that sample temperature had on the hydrogen solubility in liquid lithium in the presence of hydrogen plasmas yielded the most interesting results of this study. It is important, however, to investigate further what various exposure conditions will do the chemical composition of liquid lithium samples. This was done by changing two variables that affected the plasma fluence to the sample surface. The first of these two variables was the voltage the liquid lithium sample was biased to, while the second was the duration a given lithium sample was exposed. The results in this section will be reported with regards to the sample bias first, followed by those with regards to the exposure duration.

Both variables in this section modify the fluence to the liquid lithium sample, and, therefore, the dose. Based on results from the previous section, and intuition about the chemical nature of the Li-LiH system, the hypothesis is that as the dose of hydrogen to the sample increases, there will exist a saturation point at which the entirety of the dose has been converted to hydride, if the sample is well mixed during exposure. This saturation upper limit is defined by the number density of lithium in the sample. Essentially, as long as the experimental dose exceeds the number density of lithium, then the product should be entirely lithium hydride. This means that the recovery rate and recovered amount of hydrogen from samples exposed to higher fluences should be less than those from lower fluences, as long as the peak temperature during TPD remains below the decomposition temperature for lithium hydride. What is meant by this hypothesis is that there exists even less of the dissolved phase in samples exposed to higher fluences, so the total amount recovered should be less and the associated release fluxes at temperatures less than approximately 690 °C should also be less. If oxygen exists, then modifications to the desorption kinetics at these temperatures will be even more evident. The TPD scans should indicate this with lower hydrogen partial pressures at temperatures near 600 °C when compared with the values from the previous section. Again, this is true only if a surface saturation structure is not established while hydrogen is being absorbed.

The question remains, however, of how the energetics of the ions modify the interaction dynamics, if at all. This is something that is explored more so when investigating the effects sample bias has on the chemistry. The question being asked is: do increasingly energetic ions modify the surface, sub-surface, and bulk chemistry of the lithium solution? Does this added energy possibly

give rise to higher hydrogen fractions in the dissolved phase? It is likely that the claims stated in the previous paragraph still hold, but these questions still require an answer, especially in the context of lithium loops and isotope reclamation.

The three sample biases tested were such that the sample was left as a floating object, the sample was biased to -50 V, and the sample was biased to -100 V. These biases correspond to ion doses of $(1.9 \pm 0.2) \times 10^{21}$, $(1.2 \pm 0.3) \times 10^{22}$, and $(1.7 \pm 0.4) \times 10^{22}$, respectively. All doses in this experiment were less than the number density of the lithium sample, so hydrogen should exist in both phases simultaneously. Biases, other than the floating bias of course, were applied using an Electronic Measurements Inc. EMS 7.5-13.0 EMS Power Supply. Five Aerovox 330 μF capacitors were connected together in parallel, and also in parallel with the output of the power supply to maintain the charge applied across the lithium sample during exposure. As in the previous section, the lithium samples were heated to temperatures in excess of 375 °C and held for 15 to 20 minutes before cooling them down to the exposure temperature of 350 °C, which remained the same (within error) between these experiments.

A plot similar to the one in Figure 5.23 is illustrated in Figure 5.26, but the data is with respect to the sample bias. The trends are as expected from a fluence basis, with the released flux decreasing with increasing bias magnitude, meaning that there is an increase in the percentage of hydride in the sample. Interestingly enough, while it was expected that release flux almost vanish with increasing bias from a fluence/dose point-of-view, there was still a substantial signal observed at temperatures previously argued to correspond to the release of hydrogen in the dissolved phase, insinuating that a surface hydride layer was playing a role in both absorption and desorption.

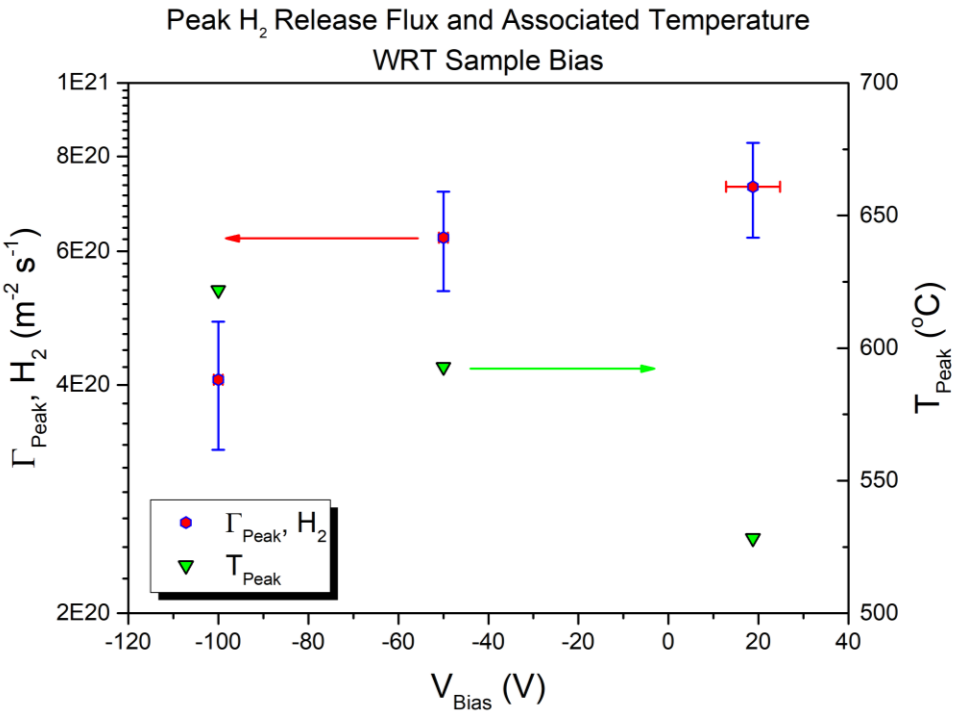

Figure 5.26: The peak release fluxes and associated temperatures as a function of the sample bias during exposure.

The evolved flux of molecular hydrogen from the surface of the sample that was biased at -100 V is surprisingly higher than what was expected from a fluence argument alone. One would expect that since the dose to the sample in this case was slightly less than the number of lithium particles within the sample, then there should exist a greater hydride population. The sample, however, was static, and a protective, insulating LiH layer likely formed at some point during the exposure in the layers at or near the surface. In support of this claim, there is a noticeable difference in the temperatures associated with the peak release fluxes for each sample. The higher temperature for the sample biased to -100 V indicates that more energy is needed for removal of the dissolved hydrogen, which supports the argument that a thicker insulating layer (either hydride or hydroxide) is made in this sample when compared with the others. After the depletion of surface site availability, this layer would have then acted as a barrier for both absorption and desorption, much in the way that it did for the solid samples. An interesting way to look at this is how the hydrogen OES signals were modified during exposure relative to the sample bias, as illustrated in Figure 5.27.

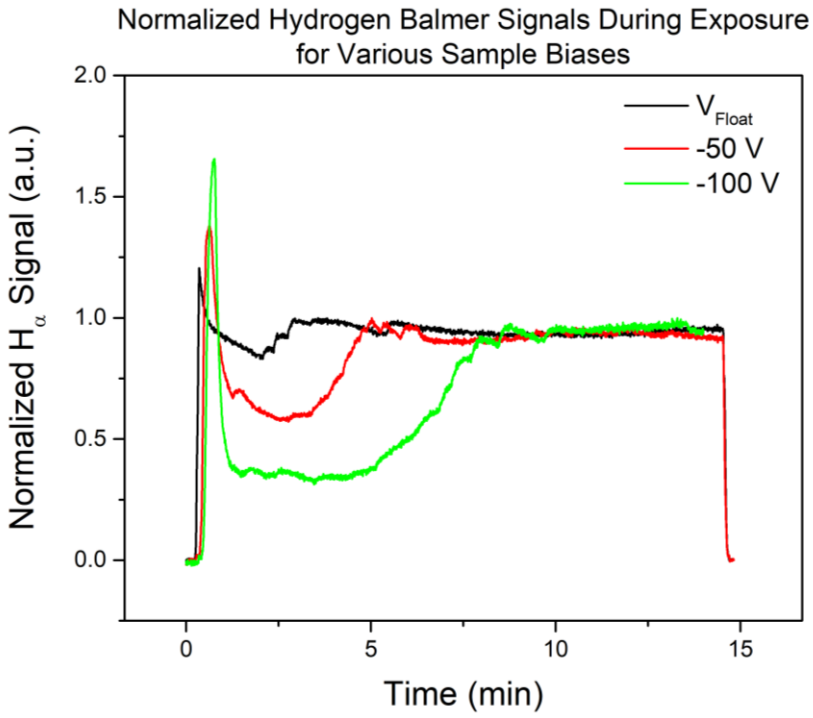

Figure 5.27: The Hydrogen-alpha OES responses, normalized to the peak intensities in Phase 2 absorption, as functions of time for samples subjected to different levels of external biasing.

From the above figure, it appears as though if one were to increase the magnitude of the sample bias then the degree to which absorption in the initial phase occurs is also drastically modified. When comparing the three trends, it looks as if there is a larger change in the H_α signal, which is held for much longer, as the magnitude of the sample bias is increased. What can be inferred is that as the energetics of the ions increase, the important chemical interactions begin shifting away from the surface, deeper into the bulk, as was hypothesized in Figure 5.2. It is likely that this means that a higher amount of lithium below the surface will undergo chemical changes before the effects of "saturation" at or near the surface can be felt.

This leads to another plausible explanation for why there still exists a substantial, albeit smaller, evolution flux for the sample biased to -100 V. While the hypothesis that some form of saturation for these static samples may be taking place may still be valid, it is also likely that an even greater amount of material is converted to hydride. Dissolved hydrogen may still remain

within the volume, but a greater amount has been chemically altered leaving the dissolved phase with a smaller population. Future work will be needed to investigate the validity of this assertion.

In varying the bias applied to the sample, it was found that the sample left floating had a dissolved hydride fraction of 0.9 ± 0.3 %, the sample held to a bias of -50 V had a dissolved hydride fraction of 0.8 ± 0.3 %, and the sample held to a bias of -100 V had a dissolved hydride fraction of 0.7 ± 0.3 %, based on the TPD gas analysis and using resistivity change as an integration upper limit. These are quite close to, but still greater than, the dissolved hydride fraction of 0.65 % at 350 °C, which comes from thermodynamic principles [40].

With regards to sample bias, ions that bombard the surface with higher energies can penetrate deeper into the sample. This means that more time is needed to establish an insulating surface hydride layer, which will increase in size as the magnitude of the sample bias is increased. As this layer grows, it becomes an even greater barrier to both absorption and desorption to and from the α phase. As such, it appears that there exist notable trends in retention and evolution with sample biasing; however, further study is needed to assess the full impact that ion energies have of the lithium-hydrogen chemistry.

Unlike sample bias, the effects that exposure time has on the lithium-hydrogen chemistry should be entirely from a dose/fluence-based point of view. In this case, the energetics remain the same in all samples, with each being biased to -50 V and held at 350 °C during exposure. Changes were made only to the length of time an individual sample was exposed. One would expect that longer exposure times should show significantly depressed hydrogen evolution rates at temperatures below lithium hydride's melting point. This is because longer exposure times equate to higher doses to the sample, wherein the sample should be entirely converted to the hydride if Baldwin's hypotheses are accurate [78, 79], and the sample is well mixed. The presence of oxygen may also be helping to enhance absorption [49, 50]. This, of course, assumes that an insulating hydride layer on the surface of the lithium cannot form, such that the entire volume can chemically interact.

Three samples were exposed to the same plasma conditions (50 mTorr indicated, 500 W) for 15 minutes, 60 minutes, and 90 minutes. These exposure times equate to doses of (1.2 ± 0.3) x 10^{22}, (5.0 ± 1.0) x 10^{22}, and (7.4 ± 1.6) x 10^{22}, respectively. The latter two doses exceed the amount of lithium in a given sample, meaning that the lithium exposed for 60 minutes and 90 minutes

should have been completely converted to hydride, as long as no insulating surface hydride layer had formed to inhibit absorption. Looking to the pre- and post-exposure resistivity measurements as a clue, it was found that the dramatic increase associated with the full conversion to lithium hydride did not occur. Because a conductive pathway remained between the two crucible electrodes, it is likely that none of the samples had undergone full volumetric conversion.

A way to initially compare the effects exposure time has on the chemistry of the sample is to look at the OES responses. Since all samples were held at 350 °C and biased to -50 V during exposure, then one would expect the absorption phases for all three samples be very similar, both in duration and in intensity change. Normalized Balmer α trends for each sample are shown in Figure 5.28.

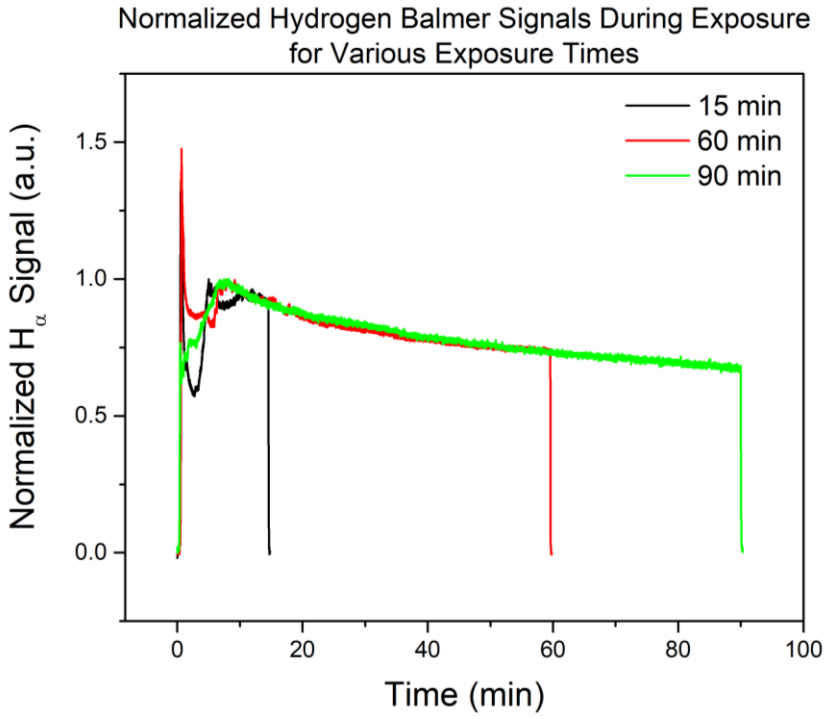

Figure 5.28: The Hydrogen-alpha OES responses, normalized to the peak intensities in Phase 2 absorption, as functions of time for samples exposed for different periods of time.

What is very interesting about the trends in Figure 5.28 that stands out from the rest of the spectroscopy trends is that during the portion of what was previously defined as Phase 2 absorption, there exists a noticeable decrease in the H_α signal as time progresses. Compared to the

samples that were only irradiated for 15 minutes, this is very important because it explains more concisely how fluence changes the sample surface and sub-surface chemistry. What may be happening could be considered a combination of two phenomena. The first of these may be that exposures beyond 15 minutes reach a threshold whereby diffusion of the dissolved hydrogen and dissolution/diffusion of any hydride, hydroxide, or oxide (due to solution equilibrium and density differences) may be occurring.

In 1982, Buxbaum [81] proposed that the diffusion of hydrogen in lithium is related to the diffusion of lithium hydride in lithium. In fact, he found that it is more likely that hydrogen diffuses as higher-order stoichiometric compounds, such as Li_2H, Li_3H, and so on. This is because of the nearest neighbor interactions that occur between hydrogen and lithium in the solution. In any case, the time scales associated with hydride diffusion away from the surface layers and into the liquid lithium bulk are on the order of nanoseconds, assuming that hydrogen only need to transport past the active hydride layer and this layer only extends to the average penetration depth calculated based on F-TRIDYN calculations. For the hydride to travel to depths sufficiently far from the surface (on the order of millimeters), the diffusion process can take minutes to complete, which is on the order of when Phase 2 absorption decay begins to occur as illustrated in Figure 5.28. It is important here to make the distinction between hydrogen diffusing in lithium and hydrogen diffusing in lithium hydride. While diffusion coefficients for hydrogen isotopes in lithium are on the order of 4×10^{-5} cm^2 s^{-1} [81], diffusion coefficients for the same hydrogen isotopes in lithium hydride are on the order of 1×10^{-9} cm^2 s^{-1} [82], meaning that the diffusion process is dominated by hydrogen diffusion into liquid lithium.

The second possible reason that there is a decay in the Phase 2 absorption curve may be due to the effects of surface sputtering. If an insulating surface hydride layer had grown within the first 5 to 10 minutes, OES responses from longer exposure times may be skewed by sputtering of the material at the surface. Sputtering of the inhibiting surface layer over time would allow hydrogen absorption to reach more of an equilibrium state. The correct mechanism can be determined by looking at the lithium OES responses, plotted in Figure 5.29.

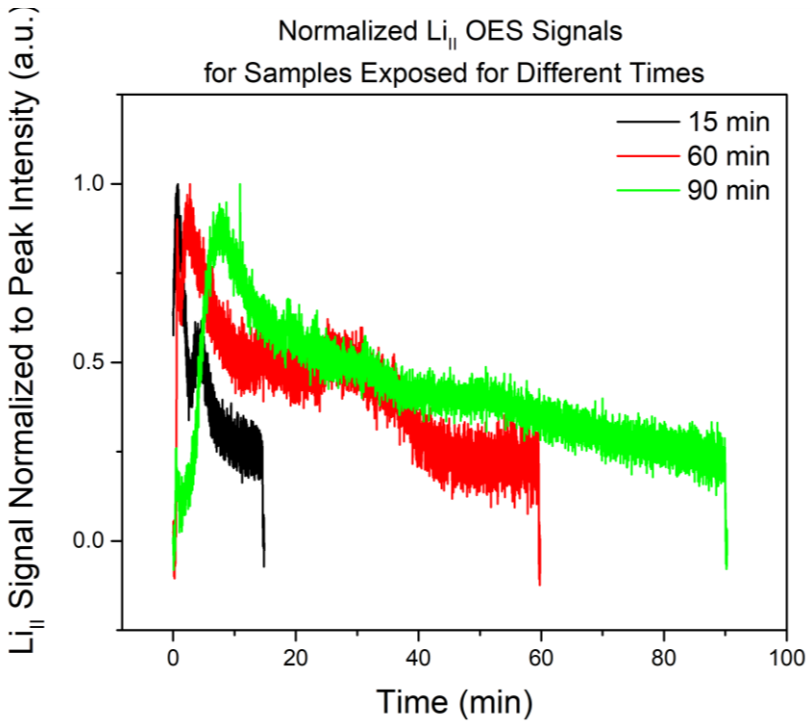

Figure 5.29: The Lithium-II OES responses, normalized to the initial peak intensities, as functions of time for samples exposed for different periods of time.

From the normalized trends of Figure 5.29, it is evident that for the remainder of the irradiation there is never an increase in the lithium signal. This lends more credibility to the first of the previously defined hypothesized mechanisms, where diffusion of the hydrogen away from the surface is affecting absorption at higher fluences. This makes sense from a thermodynamics perspective and may have also been witnessed in the solid samples, but to a lesser extent. This is especially true when looking at the trend in the H_α signals in Figure 5.16, where Phase 2 absorption for solid samples did not exhibit a significant decrease over time like what was observed in the liquid samples in Figure 5.28.

Since lithium samples appear to continue to absorb hydrogen well into the Phase 2 absorption segment, it is likely that these samples have a higher hydrogen atomic fraction. An increased volumetric hydrogen fraction may or may not be reflected in the TPD results, depending on the chemical state of the hydrogen in the mixture. If there is a greater population of hydrogen dissolved into solution, this would be reflected as higher partial pressure readings at lower

temperatures. If this greater hydrogen population is instead divided between the dissolved state and the hydride at the same ratios defined by solubility limits, then this increase in population would only be reflected as a more stable, longer-lived pressure plateau. A way to confirm or deny the first of these claims is to look at the peak surface fluxes and their associated release temperatures, as plotted in Figure 5.30.

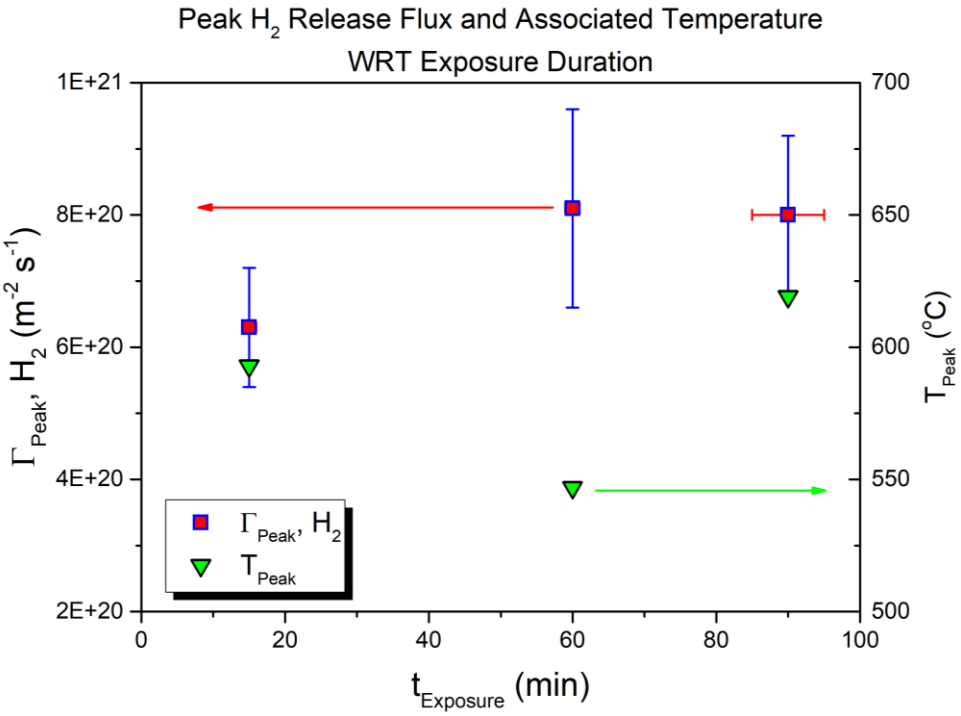

Figure 5.30: The peak release fluxes and associated temperatures as a function of the duration of exposure.

While it does appear that the samples that were irradiated for longer periods of time do have higher release fluxes (likely with higher hydrogen populations within the sample), these values are only slightly greater than the molecular hydrogen release flux associated with the sample exposed for 15 minutes. For a significantly higher population proportionally divided between the two phases, one would expect a higher pressure response at similar or lower temperatures, thus modifying the particle release rate. Assuming particles are released uniformly across the sample surface, which was postulated by Baldwin in Ref. 80 even with significant volumetric concentrations of hydride, then the flux should also be similarly elevated. Since these flux and

release rate values are not substantially greater, what is likely happening is that the insulating surface hydride layer that originally formed is diffusing into the bulk lithium as time passes, and the loss from the surface is being replenished by incoming hydrogen ions and radicals from the plasma, which combine with the lithium or whatever surface oxide layers may have formed. At high enough fluences, this process will reach an "equilibrium" whereby the entire lithium volume is converted to hydride. This is also supported by the OES responses illustrated in Figures 5.28 and 5.29.

Looking to the dissolved hydride fractions for more clues, it was discovered that the 15 minute sample had a dissolved fraction of 0.8 ± 0.3 %, the 60 minute sample had a dissolved fraction of 1.1 ± 0.7 %, and the 90 minute sample had a dissolved fraction of 1.2 ± 0.3 %. These values are nearly identical, likely meaning that the first phase of exposure likely pertains to absorption into the dissolved phase, followed by precipitation of the hydride. At these energies, the hydrogen is only able to penetrate into the first few nm below the surface, where an insulating hydride, hydroxide, or oxide surface structure is set up after a short amount of time has passed. As more time passes, the surface layer begins diffusing into the liquid bulk below, with the hydrogen lost from the surface being replenished by the constant source of the plasma directly adjacent to the surface of the sample. As such, higher fluences should eventually yield a sample that is completely converted to hydride likely mixed with some oxide or hydroxide, but this process is not fast, especially when the liquid lithium samples that are being exposed are not agitated in such a way as to break up the surface layers.

5.3.4.3 Effects of Exposure Environment

There exists a debate within the lithium community about the ability of a plasma to enhance the hydrogen isotope absorption characteristics through modification to the surface and sub-surface chemistry. These enhancements are thought to go above and beyond the thermodynamics and equilibrium conditions that exist between hydrogen gas and lithium. The collection of results supporting this claim is not just limited to the hydrogen-lithium systems, as was earlier described in the results collected and reported by Mundra [41]. Even without the considerations of the energetics of the atomic species, the rate at which diatomic neutrals dissociate and dissolve into lithium is far inferior to the rate at which charged species bombard the surface, due to the

establishment of the complex potential structure adjacent to the surface of an object inserted into the plasma, known as the sheath, and how this affects particle collection well into the plasma domain.

To investigate this claim, two samples of liquid lithium, biased to -50 V and held at an exposure temperature of 350 °C, were exposed for 15 minutes. For the gas, the application of the electric field should have no effect on the degree of absorption. One of these samples was exposed to a hydrogen plasma at an indicated pressure of 50 mTorr and an RF power of 500 W, while the other was exposed to a constant inlet of hydrogen gas. The resultant molecular fluxes are overlaid on top of one another and plotted as a function of temperature for the heating phase of the TPD scans in Figure 5.31.

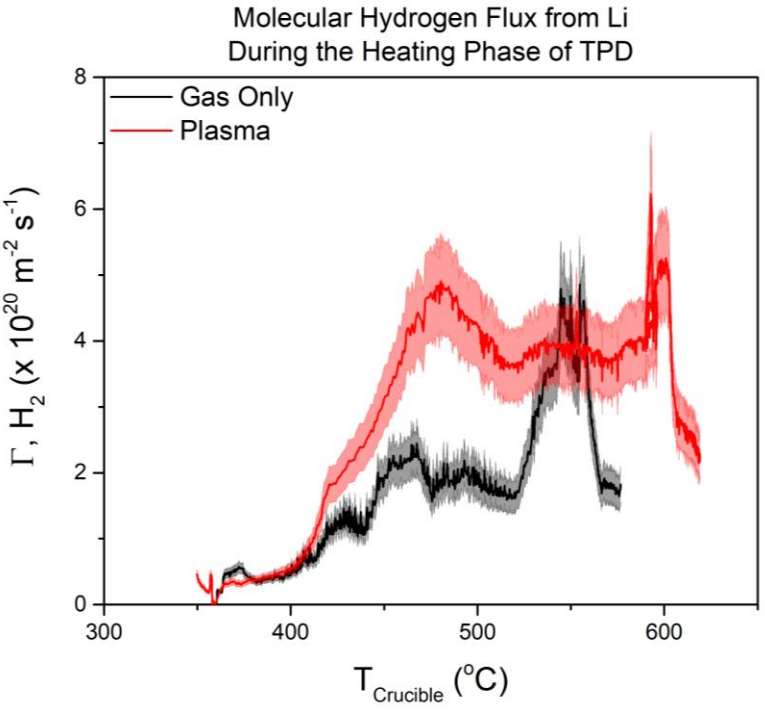

Figure 5.31: The molecular hydrogen evolution fluxes vs. temperature for the heating phase of TPD for each sample type. This plot compares evolution from a sample exposed to purely hydrogen gas and a sample exposed to a hydrogen plasma.

From Figure 5.31 it appears as if exposure to a plasma enhances the hydrogen retention and release chemistry of a sample. Unfortunately, there is no clear way of measuring the amount

of hydrogen gas consumed in these types of experiments which use a constant flow of gas during exposure. This means that the neutral dose to the sample is an unknown quantity, and may fall well below the thermochemical solubility limits even for the sample exposed for 15 minutes, so it is not clear if plasma does indeed enhance retention or not. One thing for certain is that during TPD there was never a glaring change in the resistance across the gas-exposed sample, likely indicating that the dose of neutrals to the sample fell well within dissolution limits. Still, an estimate as to the total amount of "dissolved hydride" for each sample type gave a dissolved fraction of 0.8 ± 0.3 % for the plasma-exposed sample and 0.2 ± 0.1 % for the gas-exposed sample. This estimate was again based on integrating the release rates over time. What can be said conclusively from the data in Figure 5.31 is that the presence of a plasma does change how quickly a lithium sample can absorb hydrogen. This is especially true considering that all gas-lithium reactions would have to occur at the surface, whereas ions and radicals from a plasma can penetrate below the surface. The presence of oxygen will also be affecting surface neutral absorption.

While these results cannot conclusively say that there exists an enhancement in lithium-hydrogen chemistry in the presence of a plasma, what can be said is that plasmas are able to dose a lithium sample at a much faster rate. This, in turn, promotes a quicker chemical response which may give rise to unique bulk properties that have not been observed to exist in the equilibrium condition. These results also help to clarify the degree to which the presence of neutrals play a part during plasma exposure. It should be stressed that in mimicking real reactor environments, absorption timescales are crucial, so it is the author's recommendation that all future experiments investigating these phenomena be carried out using hydrogen or deuterium plasmas rather than gases alone.

5.4 Conclusions and Future Work

The goal of this chapter was to investigate the retention and decomposition chemistry associated with lithium samples subjected to various hydrogen environments. Of particular interest was how the temperature of the lithium, the energetics of the bombarding ions, the duration of exposure, and the exposure condition modified the lithium-hydrogen chemistry. From a hydrogen reclamation focus, the significance of recovery rates and composition cannot be overstated. This

information is vital when developing a technology that will be able to recover tritium at a rate that balances or exceeds the loss rate to the walls of a lithium-walled reactor.

5.4.1 Conclusions

A great deal of effort was put into the work reported in this chapter. In essence, the most pertinent conclusions from this study can be summed up in the following bullet points:

- The triton penetration depth found in F-TRIDYN simulations for reactor-scale energies and densities reaches the micrometer scale, meaning that sub-surface and bulk chemistry must be considered.
- The dose to an individual lithium element travelling through a LiMIT trench on a single pass will remain well below the critical atomic fraction for solubility.
    - The best method for extraction is to allow the lithium to reach an equilibrium concentration of tritium and deuterium in lithium [83]. This can be done by either allowing the system to reach a steady-state concentration, or be pre-loading the lithium with a known quantity of LiD, such that equilibrium can be reached faster.
- Solid and liquid lithium samples were exposed to hydrogen plasmas and gases, and were varied with regards to the sample temperature, the applied bias to the sample, and the exposure time.
    - The work was divided into two main goals: (1) identify if plasmas enhance absorption and solubility chemsitry, and (2) investigate recovery rates from less-than-saturated and far-from-saturated lithium-hydrogen solutions.
- Solid samples exhibited evidence that a saturation phenomenon had occurred.
    - Fractional recovery values (when compared to the applied dose), while still higher than those reported in Baldwin [78], were significantly less than the 1:1 ratio reported for liquid samples.
    - Longer exposure times in solids may approach the point where the diffusion of hydrogen into lithium begins to play a role in the surface chemistry.

- TPD scans taken for the liquid samples revealed two phases of desorption. This was reasoned to be due to the delineation between the dissolved and precipitated phases of hydrogen in lithium.
- The first phase of these TPD experiments was reasoned to be due to the release of the dissolved hydrogen. This claim was corroborated by the reasoning described in Baldwin's work [78], along with a noticeable change in the resistivity experimentally observed in nearly all TPD scans.
- In all cases, the recovered flux in this primary desorption phase, considered to be recovery from the α phase, was found to be insufficient when compared with the loss flux of tritons and deuterons to the wall. Using heat as the sole impetus for recovery in far-from-saturated samples will prove difficult, and supplemental or alternative recovery techniques will be required, which will be made evident when combining Chapters 6 and 7. The author's recommendation is that upstream separation techniques be employed to isolate a Li-rich stream from a LiH-rich stream, the latter of which can be processed using heat alone as evidenced by the results of Chapter 4 and described in Chapter 6.
- It was found that dissolved hydrogen fractions showed little enhancement over the solubility limits described by equilibrium and thermodynamics when lithium samples at various temperatures were exposed to hydrogen plasmas for particle energies relevant to TUFCON discharges. The enhanced dissolution may be the product of compounded error; thus, the dissolved fraction is still likely limited by formation of the hydride precipitate [40].
- In static liquid samples, absorption is controlled by: ion energy, sample temperature, and hydrogen diffusion into the bulk. How these variables affected individual samples was discussed in each respective sub-section. The presence of microscopic oxygen layers may also be adding to enhanced absorption and desorption properties.
- Sample bias appeared to have an effect on retention as evidenced by the raw H_α OES scans. These effects seem to be related to the trends described by the F-TRIDYN penetration depths, and establishment of a thicker hydride surface saturation layer.

- Desorbed hydrogen fractions with respect to increasing sample bias appeared to be based more so on the dose to the sample, rather than the energetics of the ions. The exact effect that the ion and radical energies have on the solution chemistry requires further study.
- The length of time the sample was exposed to a plasma appeared to have an interesting effect on the amount retained and subsequently released. For longer exposure times, diffusion of the insulating, surface hydride layer into the sample bulk is likely the mechanism by which a static sample undergoes volumetric conversion from lithium to lithium hydride in the presence of a hydrogen plasma.
    - The plasma acts to replenish the lost hydride transported away from the surface.
- A hydrogen gas environment promotes less absorption over the same period of time when compared to a plasma environment, with release fluxes and sample chemistry suffering due to what appears to be a significant reduction in absorption.
    - This is caused by the differences in the energetics, as well as the fact that neutral absorption must take place at the surface, meaning that diatomic bonds must be broken before the constituent atoms are absorbed. Ions and radicals from plasmas can penetrate well into the material.
- Plasma environments are required when investigating retention and decomposition/desorption at the laboratory scale.

5.4.2 Future Work

While the bulk of this work aimed at uncovering the truth about how hydrogen in the dissolved phase behaves chemically, future work is required to fully understand the role dissolution and precipitate formation plays in the surface and bulk chemistry for the lithium-hydrogen system. A few recommendations are outlined in the following list:

- More samples should be exposed with even more variability between each exposure condition. For instance, exposing samples with greater variability between biases may help to reveal if the plasma energetics modify absorption.

- Liquid samples should be agitated during exposure, so that inhibiting surface layers are less likely to form.
    - Breaking apart any superficial surface layer that forms, whether it be lithium hydride or some other lithium derivative, can be done using an inert argon or helium plasma during or between hydrogen exposures.
- More work should be done to investigate retention, dissolution, and desorption in solid samples of lithium.
- To eliminate uncertainty surrounding the source of hydrogen, these tests should be repeated with deuterium. Deuterium was not used in these tests due to price and availability constraints.
- Samples should be exposed to a characterized hydrogen radical source to investigate the effects radicals have on retention. These effects need to be compared to the effects that plasmas and neutral gases have on retention and desorption.
- More in-situ diagnoses should be performed on these samples pre- and post-exposure. Surface characterization techniques such as X-ray photoelectron spectroscopy and low energy ion scattering spectroscopy will aid in chemical classification. Using these techniques in tandem with depth profiling would also be quite useful.
- When performing TPD scans, samples should be heated to temperatures in excess of 700 °C to ensure that the entirety of the sample has been evaporated. This should show a stark contrast between the amount of hydrogen in the dissolved phase and that which was converted to hydride. The applied dose should also be completely recovered using this procedure.
- More effort should be made in identifying surface impurities, which would likely inhibit both retention and desorption.
- Experiments should be compared to the results from Ab Initio MD simulations to verify dissolution properties.

5.5 References

[1] P. Fiflis, N. Connolly, and D.N. Ruzic, "Experimental mechanistic investigation of the nanostructuring of tungsten with low energy helium plasmas," *J. Nucl. Mat.* 482 (2016) 201-209.

[2] M.T. Robinson, "The binary collision approximation: Background and introduction", Radiat. Eff. Defects solids (1994) 3.

[3] W. Eckstein, *Computer Simulation of Ion-solid Interactions*, vol. 10, Springer Series in Materials Science, 1991.

[4] W. Mller, W. Eckstein, "Tridyn - binary collision simulation of atomic collisions and dynamic composition changes in solids", Comput. Phys. Commun. 51 (1988) 355.

[5] H. Hofsass, K. Zhang, A. Mutzke, "Simulation of ion beam sputtering with sdtrimsp, tridyn and srim", *Appl. Surf. Sci.* 310 (2014) 134.

[6] J. Drobny, A. Hayes, D. Curreli, and D.N. Ruzic, "F-TRIDYN: A Binary Collision Approximation code for simulating ion interactions with rough surfaces", *J. Nucl. Mat.* 494 (2017) 278.

[7] S.I. Krasheninnikov, L.E. Zakharov, G.V. Pereverzev, "On lithium walls and the performance of magnetic fusion devices", *Phys. of Plasmas* 10 (2003) 1678.

[8] M. Nastasi, J.W. Mayer, *Ion Implantation and Synthesis of Materials*, New York, NY: Springer-Verlag Berlin Heidelberg, 2006.

[9] J. Lindhard, M. Scharff, and H.E. Schiott, "Range concepts and heavy-ion ranges (notes on atomic collisions II)", *Mat. Fys. Medd. Dan. Vidensk. Selsk*. 33 (1963) 3.

[10] K.B. Winterbon, P. Sigmund, and J.B. Sanders, "Spacial distribution of energy deposited by atomic particles in elastic collisions" *Mat. Fys. Medd. Dan. Vidensk. Selsk*. 37 (1970).

[11] M. Szott (2016). Flow control and associated technologies to advance the application of TEMHD-driven liquid lithium in fusion devices (Master's Thesis). University of Illinois at Urbana-Champaign, 2016.

[12] W. Xu (2015). Experimental and numerical analysis of thermoelectric magnetohydrodynamic driven liquid lithium flow in open channels for fusion applications (Doctoral Dissertation). University of Illinois at Urbana-Champaign, 2015.

[13] W. Xu, D. Curreli, D. Andruczyk, T. Mui, R. Switts and D.N. Ruzic, "Heat transfer of TEMHD driven lithium flow in stainless steel trenches", *J. Nucl. Mat.* 438(supplement) (2013) S422.

[14] W. Xu, D. Curreli, and D.N. Ruzic, “Computational studies of thermoelectric MHD driven liquid lithium flow in metal trenches,” *Fus. Eng and Des.* 89 (2014) 2868.

[15] D.N. Ruzic, W. Xu, D. Andruczyk, and M.A. Jaworski. “Lithium-metal infused trenches (LiMIT) for heat removal in fusion devices,” *Nucl. Fusion* 51 (2011) 10200.

[16] J.C.R. Hunt and J.A. Shercliff, “Magnetohydrodynamics and High Hartmann Number”, *Annual Review of Fluid Mech.* 3 (1971) 37.

[17] *COMSOL Multiphysics® Reference Manual*, COMSOL Version 4.3b (2013) http://hpc.mtech.edu/comsol/pdf/COMSOL_Multiphysics/COMSOL_ReferenceManual.pdf, Accessed: 2017-10-20.

[18] A. Loarte, et al., “Transient heat loads in current fusion experiments, extrapolation to ITER and consequences for its operation”, *Phys. Scr.* T128 (2007) 222.

[19] H. Mao, et al., “A multichannel visible spectroscopy system for the ITER-like W divertor on EAST”, *Rev. Sci. Intrum.* 88 (2017) 043502.

[20] S. Äkäslompoloa, O. Asuntaa, T. Bergmansa, M. Gagliardib, J. Galabertb, E. Hirvijokia, T. Kurki-Suonioa, S. Sipiläa, A. Snickera, and K. Särkimäkia, “Calculating the 3D magnetic field of ITER for European TBM studies”, *Fus. Eng. and Des.* 98-99 (2015) 1039.

[21] M. Merola, D. Loesser, R. Raffray, and L. Giancarli, “ITER Internal Components”, presented at MIFED, 23-25 November 2010.

[22] E. Veleckis, E.H. Van Deventer, M. Blander, “The Lithium-Lithium Hydride System”, *J. Phys. Chem.* 78 (1974) 1933.

[23] E. Veleckis, “Thermodynamics of the Lithium-Lithium Deuteride System”, *J. Phys. Chem.* 81 (1977) 526.

[24] E. Veleckis, R.M. Yonco, and V.A. Maroni, “SOLUBILITY OF LITHIUM DEUTERIDE IN LIQUID LITHIUM”, *J. Less-Common Met.* 55 (1977) 85.

[25] E. Veleckis, “DECOMPOSITION PRESSURES IN THE (α + β) FIELDS OF THE Li-LiH, Li-LiD, AND Li-LiT SYSTEMS”, *J. Nucl. Mat.* 79 (1979) 20.

[26] C. E. Messer, "A Survey Report on Lithium Hydride." AEC Research and Development Report No. NYO-9470 (1960).

[27] F. K. Heumann and O. N. Salmon, "The Lithium Hydride, Deuteride, and Tritide Systems", USAEC Report No. KAPL-1667 (1956).

[28] H.R. lhla and C.H. Wu, "Mass-Spectrometric Knudsen Effusion Measurements of Vapor Species in the System Lithium-Hydrogen", Report No. EUR-4938. p 89, from the 7th Symposium on Fusion Technology, Grenoble. France, Oct 1972.

[29] J.P. Tonks, M.O. King, E.C. Galloway, J.F. Watts, "Corrosion studies of LiH thin films", *J. Nucl. Mat.* 484 (2017) 228.

[30] G. M. McCracken, D. H. J. Goodall, and G. Long, "The Extractlon of Tritium from Liquid Lithium", IAEA Workshop on Fusion Reactor Design Problems, Culham, United Kingdom, February 1974.

[31] E.E. Shpil'rain, K.A. Yakimovich, T.N. Medl'nikova, A. Ya. Polischuk, *Thermophysical Properties of Lithium Hydride, Deuteride and Tritide*. New York, NY: Springer Science and Business Media, 1987.

[32] H. Katsuta, T. Ishigai, and K. Furukawa, "Equilibrium Pressure and Solubility of Hydrogen in Liquid Lithium", *Nucl. Technol.* 32 (1977) 297.

[33] P. Hubberstey, R. J. Pulham, and A. E. Thunder, "Depression of the freezing point of lithium by nitrogen and by hydrogen", *J. Chem. Soc. Faraday Trans.* 72 (1976) 431.

[34] V. A. Maroni, R. D. Wolson, and G. E. Staahl, "Some preliminary considerations of a molten-salt extraction process to remove tritium from liquid lithium fusion reactor blankets", *Nucl. Technol.* 25 (1975) 83.

[35] E.E. Shpil'rain, K.A. Yakimovich, D.N. Kagan, and V.G. Shvalb, *Fluid Mech.-Sov. Res.* 3-4 (1974) 3.

[36] R. Hultgren, R. L. Orr and K. K. Kelly, "Selected values of the thermodynamic properties of metals and alloys", January 1970 supplement, Inorganic Materials Research Division, Lawrence Radiation Laboratory, Berkeley, University of California.

[37] F. J. Smith, J. F. Land, G. M. Begun, J. T. Bell, "Equilibria in Hydrogen-Isotope-CTR-Blanket Systems", Chemistry Division Annual Progress Report No. 0ORNL-5111, Oak Ridge National Laboratory, Oak Ridge,Tenn. (1976) 26.

[38] P.F. Adams, M.G. Down, P. Hubberstey, R.J. Pulham, "Solutions of Lithium Salts in Liquid Lithium: The Electrical Resistivity of Solutions of Nitride, Hydride and Deuteride", *J. Chem. Soc., Far. Trans.* 0 (1977) 230.

[39] P.F. Adams, M.G. Down, P. Hubberstey, R.J. Pulham, "SOLUBILITIES, AND SOLUTION AND SOLVATION ENTHALPIES, FOR NITROGEN AND HYDROGEN IN LIQUID LITHIUM", *J. Less-Common Met.* 42 (1975) 325.

[40] K.A. Yakimovich and T. Biryukova, "Thermodynamic Properties of Li-LiH (LiD, LiT) Systems. The Phase Diagram" *Open J. Phys. Chem.* 2 (2012) 141.

[41] K. Mundra and T. Debroy, "A General Model for Partitioning of Gases between a Metal and its Plasma Environment", *Met. & Mat. Trans. B* 26B (1995) 149.

[42] S. Ohno and M. Uda, "Vacuum-extraction Method for Hydrogen Determination in Weld Metals: An Analysis of Hydrogen Behavior in the JIS Type Weld Specimen", *Trans. Nat. Res. Inst. Met.* 23 (1981) 243.

[43] M. Uda and S. Ohno, "Effects of Hydrogen and Nitrogen on Blowhole Formation in pure Nickel at Arc Welding", *Trans. Nat. Res. Inst. Met.* 20 (1978) 358.

[44] J.D. Katz and T.B. King, "Kinetics of nitrogen absorption and desorption from a plasma arc by molten iron", *Metall. Trans. B* 20B (1989) 175.

[45] A. Bandopadhyay, A. Banerjee, and T. DebRoy, "Nitrogen activity determination in plasmas", *Metall. Trans. B* 23B (1992) 207.

[46] G. Den Ouden and O. Griebling, *Recent Trends in Welding Science and Technology*, S.A. David and J.M. Vitek, eds., Metals Park, OH: ASM INTERNATIONAL, 1990, pp. 431-35.

[47] S.A. Gedeon and T.W. Eagar, "MEASUREMENT OF DYNAMIC ELECTRICAL AND MECHANICAL PROPERTIES OF RESISTANCE SPOT WELDS", *Weld. J.* 69 (1990) 264s.

[48] R.D. Pehlke, *Unit Processes in Extractive Metallurgy*, New York, NY: Elsevier 1979, p. 141.

[49] C.N. Taylor, J.P. Allain, K.E. Luitjohan, P.S. Krstic, J. Dadras, and C.H. Skinner, "Differentiating the role of lithium and oxygen in retaining deuterium on lithiated graphite plasma-facing components", *Phys. of Plasmas* 21 (2014) 057101.

[50] A.M. Capece, J.P. Roszell, C.H. Skinner, and B.E. Koel, "Effects of temperature and surface contamination on D retention in ultrathin Li films on TZM", *J. Nucl. Mater.* 463 (2015) 1177.

[51] P. Fiflis, D. Curreli, D.N. Ruzic, "Direct time-resolved observation of tungsten nanostructured growth due to helium plasma exposure", *Nucl. Fusion* 55 (2015) 033020.

[52] P. Fiflis, M.P. Christenson, N. Connolly, and D.N. Ruzic, "Nanostructuring of Palladium with Low-Temperature Helium Plasma", *Nanomaterials* 5 (2015) 2007.

[53] R. Tobe, A. Sekiguchi, M. Sasaki, O. Okada, and N. Hosokawa, "Plasma-enhanced CVD ofTiN and Ti using low-pressure and high-density helicon plasma", *Thin Solid Films* 281-282 (1996) 155.

[54] F. Chen, et al., Final Report on MICRO Project, 1999.

[55] R.W. Boswell, "Effect of boundary conditions on radial mode structure of whistlers", *J. Plasma Phys.* 31 (1984) 197.

[56] T. Shoji, Y. Sakawa, S. Nakazawa, K. Kadota, and T. Sato, "Plasma production by helicon waves", *Plasma Sources Sci. and Tech.* 2 (1993) 5.

[57] F.F. Chen, "Plasma ionization by helicon waves", *Plasma Phys. and Controlled Fusion* 33 (1991) 339.

[58] F.F. Chen and G. Chevalier, "Experiments on helicon plasma sources", *J. Vac. Sci. Technol. A* 10 (1992) 1389.

[59] C. Cui and R.W. Boswell, "Role of excitation frequency in a low-pressure, inductively coupled radio-frequency, magnetized plasma", *Appl. Phys. Lett.* 63 (1993) 2331.

[60] B.J. Davies, "Helicon wave propagation: effect of electron inertia", *J. Plasma Phys.* 4 (1970) 43.

[61] R.L. Ferrari and J.P. Klozenberg, "Dispersion and attenuation of helicon waves in a cylindrical plasma-filled waveguide", *J. Plasma Phys.* 2 (1968) 283.

[62] A. Komori, T. Shoji, K. Miyamoto, J. Kawai, and Y. Kawai, "Helicon waves and efficient plasma production", *Phys. Fluids B* 3 (1991) 893.

[63] J.P. Klozenberg, B. McNamara, and P.C. Thonemann, "Dispersion and attenuation of helicon waves in a uniform cylindrical plasma", *J. Fluid Mech.* 21 (1965) 545.

[64] J.A. Lehane and P.C. Thonemann, "Experimental study of helicon wave propagation in a gaseous plasma", *Proc. Phys. Soc.* 85 (1965) 301.

[65] A.J. Perry, D. Vender, and R.W. Boswell, "Application of the helicon source to plasma processing", *J. Vac. Sci. Technol. B* 9 (1991) 310.

[66] F.F. Chen, "Helicon Plasma Sources", published in: *High Density Plasma Sources*, ed. by Oleg A. Popov, 1994.

[67] H.M. Mott-Smith, I. Langmuir, "The Theory of Collectors in Gaseous Discharges". *Phys. Rev.* 28 (1926) 727.

[68] J.G. Laframboise, "THEORY OF SPHERICAL AND CYLINDRICAL LANGMUIR PROBES IN A COLLISIONLESS, MAXWELLIAN PLASMA AT REST", *UTIAS Report No. 100* (1966).

[69] I.B. Bernstein and I.N. Rabinowitz, "Theory of electrostatic probes in a low-density plasma", *Phys. Fluids* 2 (1959) 112.

[70] F.F. Chen, "Langmuir probes in RF plasma: surprising validity of OML theory", *Plasma Sources Sci. Technol.* 18 (2009) 035012.

[71] P. David, M. Sicha, M. Tichy, T. Kopinczynski, and Z. Zakrzewski, "The use of Langmuir Probe Methods for Plasma Diagnostic in Middle Pressure Discharges", *Contrib. Plasma Phys.* 30 (1990) 167.

[72] M. Tichý, M. Šicha, P. David, and T. David, "A Collisional Model of the Positive Ion Collection by a Cylindrical Langmuir Probe", 1994 *Contrib. Plasma Phys.* 34 59

[73] I.S. Sudit and F.F. Chen, "RF compensated probes for high-density discharges", *Plasma Sources Sci. Technol.* 3 (1994) 162.

[74] D.N. Ruzic, *ELECTRIC PROBES FOR LOW TEMPERATURE PLASMAS*, New York, NY: AVS Press, 1994.

[75] F. Scotti, et. al., "Core transport of lithium and carbon in ELM-free discharges with lithium wall conditioning in NSTX", *Nucl. Fusion* 53 (2013) 083001.

[76] C.H. Skinner, J.P. Allain, W. Blanchard, H.W. Kugel, R. Maingi, L. Roquemore, V. Soukhanovskii, and C.N. Taylor, "Deuterium retention in NSTX with lithium conditioning", *J. Nucl. Mat.* 415 (2011) S773.

[77] J. Li, et al., "A long-pulse high-confinement plasma regime in the Experimental Advanced Superconducting Tokamak," *Nature Physics* 9 (2013) 817.

[78] M.J. Baldwin, R.P. Doerner, S.C. Luckhardt, R. Seraydarian, D.G. Whyte, and R.W. Conn, "Plasma interaction with liquid lithium: Measurements of retention and erosion", *Fus. Eng. and Des.* 61-62 (2002) 231.

[79] R.L. Smith and J.W. Miser, "COMPILATION OF THE PROPERTIES OF LITHIUM HYDRIDE", *NASA Technical Memorandum X-483* (1963).

[80] M.J. Baldwin, R.P. Doerner, S.C. Luckhardt, and R.W. Conn, "Deuterium retention in liquid lithium", *Nucl. Fusion* 42 (2002) 1318.

[81] R.E. Buxbaum and E.F. Johnson, “THE DIFFUSIVITY OF HYDROGEN ISOTOPES IN LIQUID LITHIUM AND SOLID YTTRIUM”, PPPL Report No. PPPL-1960 (1982).

[82] J.N. Spencer, D.S. Catlett, and G.J. Vogt, “Hydrogen transport in lithium hydride as a function of temperature”, *J. Chem. Phys.* 59 (1973) 1314.

[83] M. Ono, R. Majeski, M.A. Jaworski, Y. Hirooka, R. Kaita, T.K. Gray, R. Maingi, C.H. Skinner, M. Christenson, and D.N. Ruzic, “Liquid lithium loop system to solve challenging technology issues for fusion power plant”, *Nucl. Fusion* 57 (2017) 116056.

CHAPTER 6: A DISTILLATION COLUMN FOR HYDROGEN ISOTOPE REMOVAL

The previous chapters focused on the background and fundamental physical results regarding hydrogen isotope retention and release. While these studies were very important in understanding the behavior of saturated or less-than-saturated solutions of lithium and hydrogen when heat is applied, they were performed on small, laboratory-scale samples. To prove that driving tritium recovery using heat is valid for various solutions with different levels of saturation, a demonstration scale device must be designed, constructed, and tested. This chapter will explore the design criteria for, and construction of, a prototype distillation column that will eventually become a part of a full lithium loop. The full loop will be built to accommodate the Lithium Metal-Infused Trenches (LiMIT) plasma-facing component (PFC) [1 – 3] installed in pilot-scale devices such as the Hybrid Illinois Device for Research and Application (HIDRA) [4] or the Experimental Advanced Superconducting Tokamak (EAST) [5 – 7].

The soundness of the design will be evaluated based on the ability of the column to evolve the total amount of hydrogen from a batch mixture of lithium and lithium hydride. These batch mixtures will act as surrogates for samples of lithium that would hypothetically be hydrogenated (or deuterated or tritiated) during exposure within the reactor vessel. These mixtures will also be at varying degrees of saturation, which will represent how different purification technologies upstream of the proposed distillation device will be employed in a given loop scenario. For simplification, the results of this chapter will be presented within the context of the loop and purification technologies proposed by Ono [8] at the Princeton Plasma Physics Laboratory. Ono envisioned the purification technologies to be able to separate a lithium deuteride (LiD) – lithium tritide (LiT) rich phase from the remaining lithium stream. While this enriched stream would likely not be comprised of pure LiD or LiT, it would have significantly higher atomic fractions of deuterium (D) and tritium (T), suitable for adequate recovery. It is also beneficial, albeit not crucial, to be able to recycle clean lithium back into the reactor so that excess lithium did not have to continually be added to the system. This type of purification would be preferential over treating the low-H (or D or T)-atomic-fraction lithium solution in a column on each pass, since adequate recovery rates from these solutions would be much more difficult to achieve. The loop system proposed in Ref. [8] is illustrated in Figure 6.1.

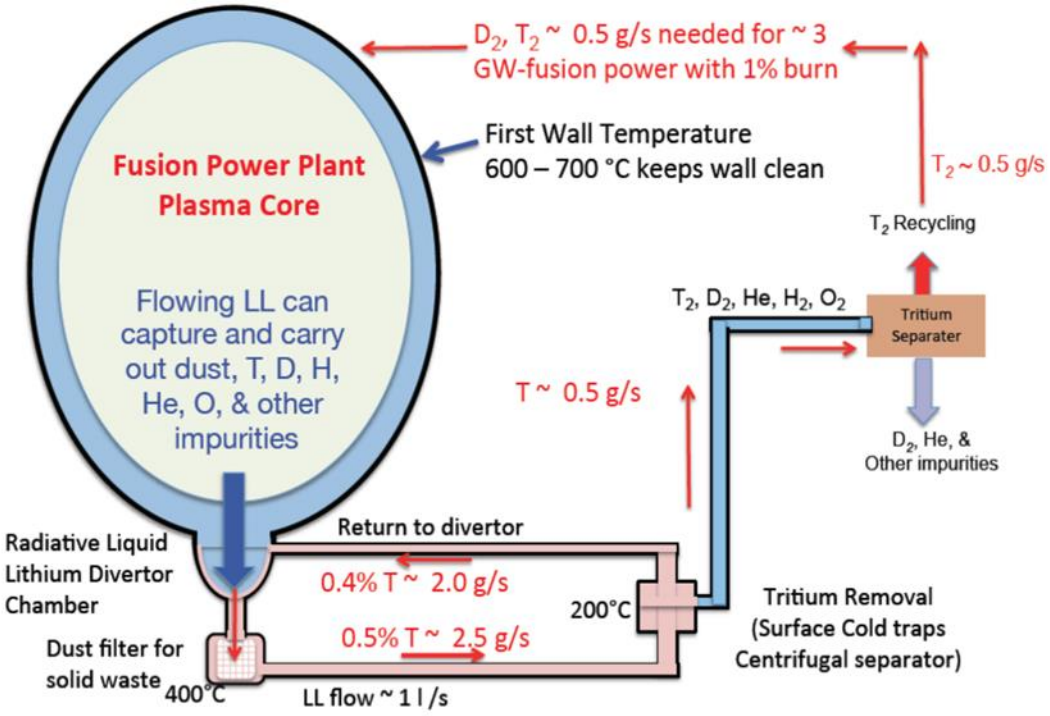

Figure 6.1: The loop system proposed by Ono, et al. [8]. The distillation column would become the "Tritium Separator" module.

It is important to note a few points in the hypothetical lithium loop scenario illustrated in Figure 6.1. First, the liquid lithium would only be active in the divertor within the reactor, with the remainder of the first wall being a different plasma-facing material. Second, this recovery scheme takes into account that a steady-state concentration of tritium must remain within the lithium in order for the recycling rate to balance the loss rate at the divertor surface. The final, and most important point, is that the "Tritium Removal" step does not actually separate the tritium from the lithium, but instead focuses on separating the tritide and deuteride from the remaining lithium stream. The technologies at this step have yet to be proven in a working loop, but they either take advantage of the system thermodynamics (cold traps) or the density difference between the lithium and the precipitates (centrifuge). What currently is unexplored in this scheme is a method for the "Tritium Separator" step. In the context of this proposition, use of the distillation column would be advantageous. For clarification purposes, the purification and tritide/deuteride separation techniques are illustrated in Figure 6.2.

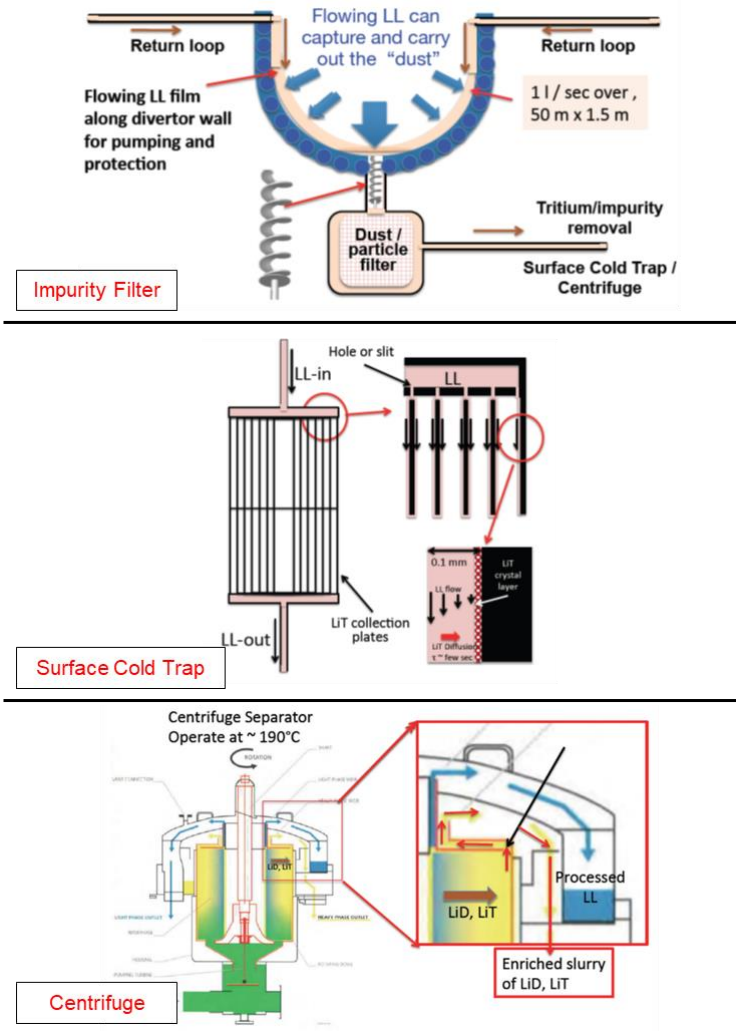

Figure 6.2: The purification and separation technologies for the liquid lithium loop proposed by Ono, et al. [8]. The top depicts filtration as the primary purification step as the lithium exits the reactor. The middle illustrates a surface cold trap, whereby thin layers of tritiated/deuterated lithium are flowed past cooled plates to precipitate out the tritide and deuteride. The bottom graphic illustrates how the use of a centrifuge will create two streams: one that is LiD/LiT-rich and one that is Li-rich.

6.1 Distillation Column Design

Focusing on the prototype column as the subject of this chapter, significant work was done to initially design and model the column components. Multiple design iterations of the column body itself were developed in Autodesk Inventor until a final design was decided on. The column

body was based on the conceptual design for the Lithium Vapor Box developed by Goldston [9], even though the purpose in this case was significantly different. Essentially, the inlet from the lithium loop (or the batch sample in this case) would flow into a bottom bucket, which will have been pre-heated such that the inner walls were at or above 650 °C. Two conical stages are above the bucket, both of which will be held at temperatures between 300 and 350 °C to promote lithium condensation, but be hot enough to inhibit hydrogen co-deposition. The hydrogen will then exit through a top port, which will be differentially pumped. The evolved gases (D_2, T_2, H_2, He, D_2O, etc…) can then be separated by taking advantage of the difference in ionization energies and masses/momentums in the presence of magnetic fields between species.

The novelty of this design comes at the base, where the heating drive will have to continuously overcome the cooling effects from the inlet. To do this, an induction heater using a pancake coil to generate the magnetic fields was placed under the bottom of the 304 stainless steel bucket. To continuously heat to temperatures approaching 700 °C with minimal power draw, while also being able to ramp up to this temperature in the shortest amount of time, the induction heating mechanism was considered superior to all other low-cost heating alternatives. The heating capabilities of such a heater, however, needed to be modelled and tested with the impedance loads it would be subjected to in the prototype column setup.

6.1.1 Induction Heater COMSOL Model

One of the most useful tools for modelling any system with coupled physics is the COMSOL Multiphysics software [10]. Developers of this package have made it possible to model complicated and coupled systems, with the inclusion of various physics modules that cover a wide range of topics. In general, most of the macroscopic physics modelling done in COMSOL is conducted using various solvers for a finite element system domain. For physics modules that are often coupled, COMSOL developers have already allowed for a quick setup of the geometry and physics, as is the case for induction heating. In general, induction heating uses the combinations of Ampere's Law, Lenz's Law, and heat transfer in solids to indicate how the load of a certain induction coil would heat over time. The fundamentals for induction heating are based on how magnetic fields from the working coil induce currents in the metals directly adjacent to the coil. These currents generate heat through Ohmic dissipation in the material, whereby the intrinsic

resistivity in the metal causes heating as a source term. Resistivity, however, changes with temperature, so the two physics modules are coupled in that the results from each inform the other.

The fundamental equations that govern the coupled physics systems in induction heating are given by the thermal energy equation for heat transfer in solids, along with a combination of Ampere's Law and Lenz's Law [10]:

$$\rho\, C_p\, \frac{\partial T}{\partial t} + \rho\, C_p\, u \cdot \nabla T = \nabla \cdot (k\, \nabla T) + Q \tag{5.1}$$

$$(i\omega\, \sigma - \omega^2\, \epsilon_0 \epsilon_r)\, A + \nabla \times \frac{B}{\mu_0 \mu_r} - \sigma\, v \times B = J_e \tag{5.2}$$

$$B = \nabla \times A \tag{5.3}$$

where ρ is the material density, C_p is the constant-pressure heat capacity of the material, T is the temperature in K, u is the advection term for the thermal energy equation, k is the heat conductivity of the material, Q is the heat source, i is the imaginary root, ω is the angular frequency at which the induction coil is driven, $\epsilon_0 \epsilon_r$ is the product of the permittivity of free space and of the specific material, A is the magnetic vector potential defined in Equation (5.3), B is the magnetic field, $\mu_0 \mu_r$ is the product of the magnetic permeability in vacuum and in the material, σ is the electrical conductivity of the material, v is the velocity vector for the Lorentz force, and J_e is the current driven in the material. How Equations (5.1) and (5.2) relate is through the heat generation term, Q. In the physics coupling, COMSOL defines this source using [10]:

$$Q = \frac{1}{2}\, Re(J \cdot E^*) + \frac{1}{2}\, Re(i\omega\, B \cdot H^*) \tag{5.4}$$

where J is the total current, E^* is the conjugate transpose of the electric field, B is the magnetic field, and H^* is the conjugate transpose of the auxiliary field (which takes into account the material response to the magnetic field). Both of the terms in Equation (5.4) describe energy dissipation from the externally applied fields from the working coil of the induction heater. The coupling of these physics allows for the possibility of induction heating.

The COMSOL induction heating model was set up as a 2-dimensional, axisymmetric system, where the geometries for the coil and the sample bucket were generated to mimic the real-life geometries. A virtual pancake coil was generated by simulating 5 concentrically-spaced, hollow coils under the bucket structure, with a pitch of about 1.5 cm. Each coil had an outer

diameter of 8 mm and an inner diameter of 6 mm. This coil is not fully representative of the real pancake coil, as it is generated as 5 separate coils and the real working coil is a single piece of copper with 5 windings. A parameter sweep was done over the current applied (equally applied to each simulated coil winding) to mimic the currents that are available from the actual induction supply. The materials used were copper for the working coil and 304 stainless steel for the bucket/load. A physics-controlled mesh was used, with refinement around the coil determined in the COMSOL software. The frequency parameter was also scanned, again to mimic the frequencies available using the actual induction power supply. All results presented here indicate the peak temperature achieved after 30 minutes of heating. A representative temperature result is illustrated in Figure 6.3, where air is the control volume medium (with an artificially reduced thermal conductivity). A plot of the peak bucket temperatures achievable at 30 minutes of heating at various currents and frequencies is illustrated in Figure 6.4.

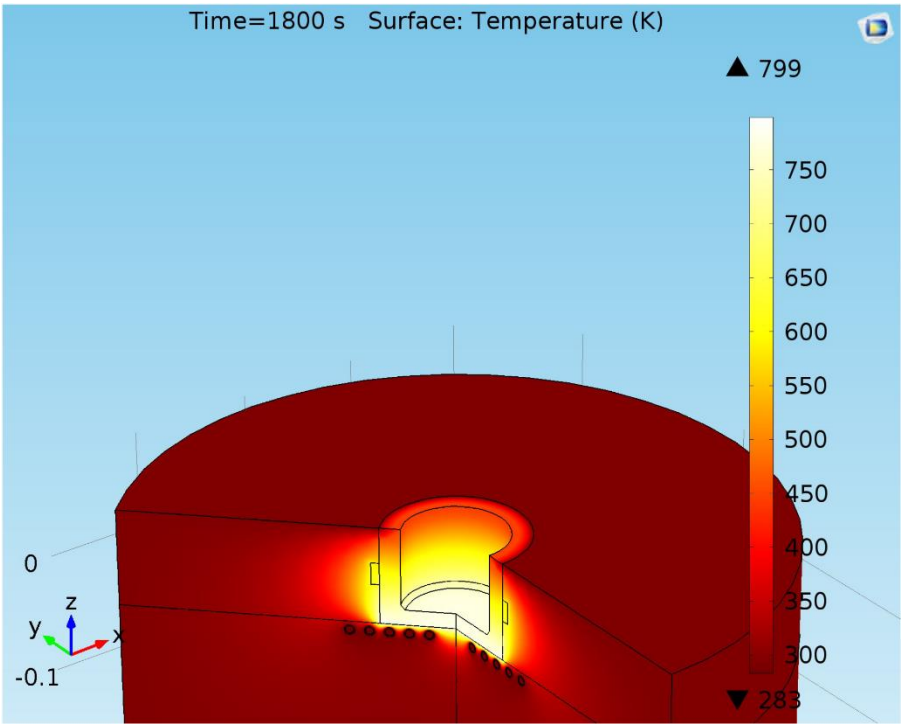

Figure 6.3: A heat map for the COMSOL simulation of the induction heating process as applied to a virtual bucket that mimics a fraction of the real-world load. After 30 minutes of heating at 350 A and 30 kHz, the bucket achieved a peak temperature of 799 K (526 °C).

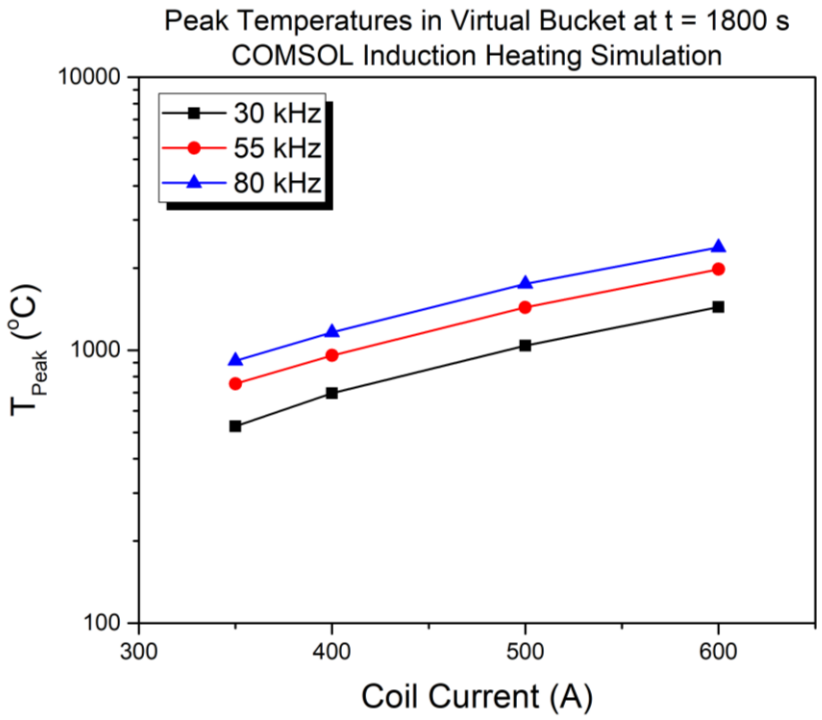

Figure 6.4: The peak temperatures achievable after 1800 s of heating for various currents at various frequencies. These represent the range of operating conditions available with the actual induction heating supply unit. Temperatures above 1000 °C are likely due to the fact that the control volume boundaries are not set to an outflow condition with regards to heat, so the energy is maintained within the control volume. It should also be mentioned that practical operation limited the current to around 400 A or less.

The real induction heater power supply matches the load based on the frequency output. In many other cases where high-frequency induction coils are used for heating, matching networks in series with the supply outlet are used for the most efficient power deposition. The supply used for the distillation column, however, bases the impedance matching for the load on variations in the output frequency, where the frequency can range anywhere from 30 and 80 kHz. Given the results presented in the following sections, it is safe to say that the coil is supplied between 350 and 400 A, at frequencies that are closer to 30 kHz. To validate the COMSOL model, the actual induction heater was tested on a 304 stainless steel dummy load.

6.1.2 Commissioning of the Induction Heating Power Supply

The power supply used for the inductive heating of the base of the distillation column was a Dongguan HaiTuo Machinery Equipment Model HT-15A supply. The supply runs on 110 VAC; however, at maximum the supply will draw nearly 2 kW, meaning that a normal 120 V, 20 A circuit breaker will not accommodate full operation since a 20 A breaker will trip at approximately 18.5 A. The current draw from the supply can be varied, however, by controlling the current output through the working coil. Standard working coils used with this supply had inductances of approximately 8.5 μH (without a load). The standard working coil is hollow to accommodate water cooling, with the water being supplied to the HT-15A through external hosing. In the event of coolant failure, the HT-15A comes equipped with a safety interlock to make sure the power sent through the coil does not melt the copper. A custom pancake coil was manufactured for use with the distillation column, and had an unloaded inductance of 9 μH. The HT-15A manual recommended that the water being used for cooling was filtered, so a filtration/deionizing system was set up in series with the water inlet to the supply to maintain coolant purity.

To test the heating capabilities of the custom manufactured pancake coil, a 304 stainless steel disk measuring 11.4 cm in diameter and 4.2 cm in height was used as a dummy load. K-type thermocouples were spot welded centrally to the top and bottom of the block to measure how quickly the energy from the working coil would dissipate through the steel. Similar peak temperatures to those described in Chapters 4 and 5 were desired, along with the knowledge of the temperature ramp rate at a given output current. The results from this commissioning test are reported in Figure 6.5, which illustrates the two measured temperatures as a function of time for a working coil current of 450 A. Unfortunately, since the supply uses frequency variations to match the load at any given time, the frequency was unknown for all current outputs.

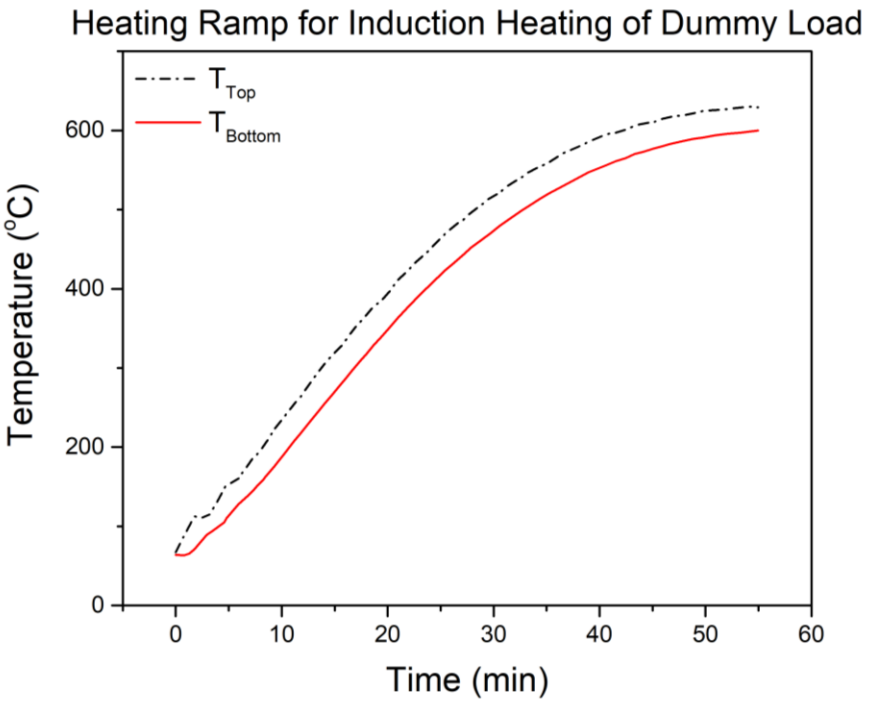

Figure 6.5: The heating test for the inductive heater using a custom manufactured pancake coil. The dummy load was a disk of 304 stainless steel measuring 11.4 cm in diameter and 4.2 cm in height. What is labeled as T_{Top} is the disk face closest to the working coil.

A similar test was done to measure the heating rate of the induction heater on the actual distillation column. This was done to investigate how the load of the actual column structure would affect the ramp rate for given output currents. These data are reported in Figure 6.6. K-type thermocouples measured the temperature rise at the center of the bottom of the bucket and 6.3 cm up along the side of the bucket (near the 8" CF flange). Initially, electrical issues during these commissioning tests prevented the working coil from heating the column at the maximum rate. This was later rectified with a 5 kVA ACME step-down transformer that was able to draw power from a 208 V circuit, which allowed for a greater power draw of closer to 4 kW. This allowed the induction heater supply to operate at full potential, and this difference is illustrated in the commissioning tests in Figure 6.6.

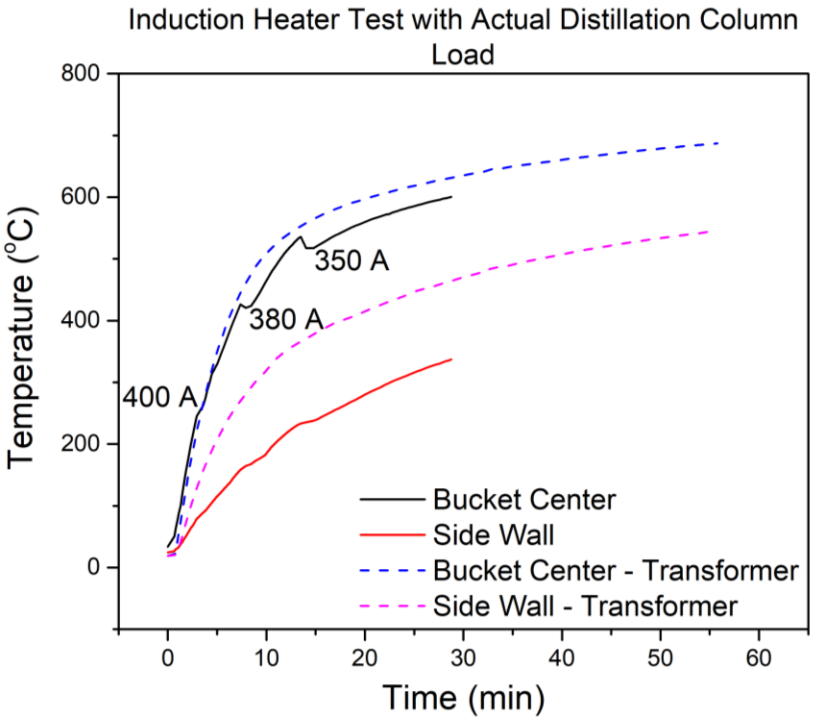

Figure 6.6: The heating test of the pancake coil induction heater with the actual distillation column load. The dashed lines indicate the commissioning test after the addition of a step-down transformer for a higher power draw.

Unfortunately, the heating was somewhat inconsistent during this test with the full column load. Initially, the heater was set such that the output read approximately 400 A. After about 7 minutes, this tripped the 20 A breaker, so the output current was lowered to nearly 380 A. After another 7 minutes, this output value again tripped the 20 A breaker, so the current was again lowered, this time to 350 A. The remainder of the test was carried out at an output current of 350 A. This test was carried out prior to the integration of a step-down transformer that allowed the induction supply to draw more power. From this test, it is evident that supplying an output current between 350 and 400 A will allow the bucket to reach a temperature of nearly 600 °C in roughly 30 minutes. Moving the working coil closer to the bucket by approximately 1/8 inch and adding the step-down transformer allowed for a slightly greater temperature ramp rate. The test with the corrected supply parameters allowed for a peak temperature of greater than 680 °C after an hour of heating. Again, measurement of the output frequency was not available with this supply. This

temperature ramp, however, is fairly close to the results that were predicted by the COMSOL simulations for the case of 350 A and 30 kHz.

6.1.3 Condensation Stages

While tritium recovery within the context of a fully functional lithium loop is the primary focus, it is also important to purify and collect the lithium byproduct to complete the cycle of a fully closed system. A distillation column is perfect for this objective because columns are often outfitted with condensation plates or stages for collection of the less volatile product. The column described in this chapter is no different from these conventional designs, in that condensation stages were also considered for lithium recovery.

The stages designed for the prototype column were based on the design for the condensation stages of the Lithium Vapor Box developed by Goldston, et al. [9]. The condensation stages for the vapor box divertor serve a different purpose and are also oriented with different inclinations than those of the prototype column design. In Goldston's box, the Li is meant to condense and return to the lowest possible sub-section before being vaporized again, with inclinations oriented so the lithium falls back down the central cavity of the box. In this design, the idea is to condense and capture the evaporated lithium and divert lithium flow down to collection ports, which will then transport the lithium out of the column to a separate reservoir. The design of the inner portion of the prototype column is illustrated in Figure 6.7 as an Autodesk Inventor half-section view.

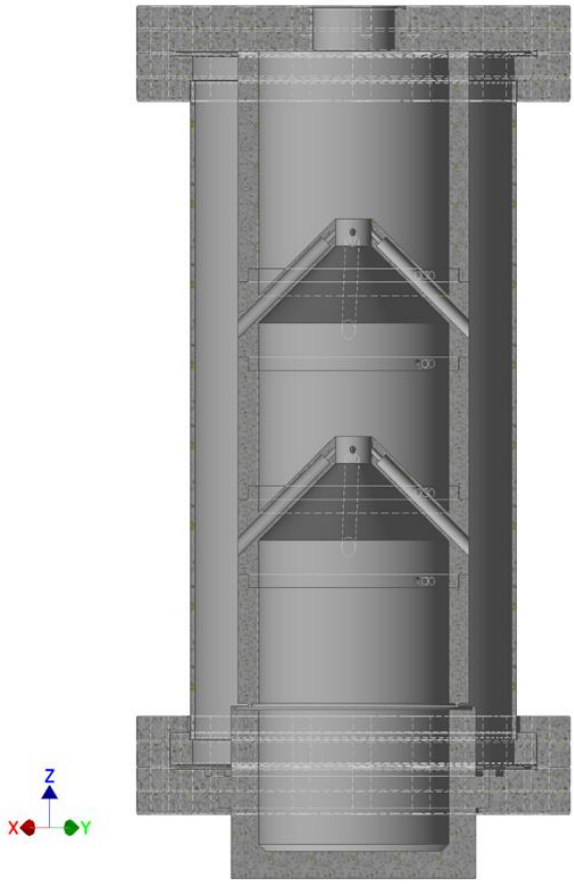

Figure 6.7: An Autodesk Inventor half-section rendering for an internal view of the prototype distillation column (drawing rendered by Cody Moynihan). Two condensation stages, inclined at 45° toward the central cavity, will be the primary means for lithium collection and will be held at temperatures near or in excess of 315 °C using cartridge heaters.

The sample bucket shown at the bottom of the rendering will be where the hydrogenated lithium sample is placed initially. Future iterations will require that the bucket section be modified to allow continuous Li flow, but testing of the prototype column will be performed entirely as a batch process. The bucket will initially be heated from below using the induction heating pancake coil. As the lithium is evaporated and hydrogen is released, both gaseous species will rise to meet the first condensation stage, which will nozzle the flow of both. The lithium will begin condensing on the underside of the first stage and will likely fall back down to the bucket to be vaporized once again. Boundaries at sufficient temperature (likely in excess of approximately 350 °C) have shown

that co-deposition of the hydrogen will be unlikely to occur, with sticking coefficients of 0.01 reported in literature for lithium held at higher temperatures [11]. The gases able to make it up between the first and second stages will likely undergo a similar process as that which occurred between the bucket and the first stage. The collection of lithium on the tops of the stages will eventually lead to an outlet for re-condensed lithium in future iterations of the column. The process will then again repeat between the second stage and the final outlet at the top of the column, which will be the primary exiting point for hydrogen. How to exactly collect the hydrogen and what hardware may need to be employed in order to ensure the outlet flow will have minimum lithium vapor will be discussed at the end of this chapter, while the main focus of the remaining results will be the efficacy of the heating techniques and lithium recovery/purity.

6.2 Proof-of-Concept Experiments

Once the column had been completely constructed and the induction heater supply had been fully assembled and tested, the extraction scheme was tested on a proof-of-concept basis. Three of these proof-of-concept tests were performed, each having mixtures at different ratios of LiH to Li. Initially, hydrogen evolution from pure LiH was tested. This test was performed prior to modifications made to the column that improved the heating and measurement capabilities. As such, this initial test was unable to provide any useful quantitative data. The two tests performed after modifications had been made were conducted with a Li-rich mixture (at an atomic ratio of 0.03 mol H : 1 mol Li) and a LiH-rich mixture (at an atomic ratio of 0.6 mol H : 1 mol Li). For context, the molar ratio for saturation is 1 mol H : 1 mol Li.

In the cases with the pure LiH and the Li-rich sample, an earlier version of the drybox at the Center for Plasma-Material Interactions was used to provide an inert argon environment for loading the bucket with a pre-determined amount of Li granules (99% pure, metals basis, Alfa Aesar) and LiH (99.4% pure, metals basis, Alfa Aesar). Unfortunately, the entire column was unable to fit inside of the drybox, so once the sample had been loaded in the argon environment, the column (positioned immediately outside of the drybox) was continuous purged with argon. A quick transfer and attachment of the bucket from the drybox to the bottom of the column was performed while argon was continuously purging the column body. Once the bucket had been

attached and all valves had been closed, the bucket was transferred to the experimental stand. Loading of the LiH-rich sample was done in a new glovebox, which was able to accommodate the column body and the bucket, which aided in preventing the unwanted introduction of impurities.

The column and bucket assembly was then transferred to the experimental stand and the turbomolecular pumps were attached to the top and bottom of the primary chamber. An image of this physical setup is shown in Figure 6.8. The roughing pump was then opened to the two pumping sub-sections until the pressures in these section had lowered appreciably, at which point the gate valves were opened to evacuate the main portions of the column. Once the gauges read low enough pressures, the two turbomolecular pumps were started and the chamber was evacuated for approximately 14 hours prior to initiating the heating experiment.

Figure 6.8: An image of the actual distillation column experimental setup.

In all experiments, the column was manufactured such that the primary exhaust point is at the top of the column. Gases are still able to escape through a small slit near the bottom, but the manufactured grooves at the points shown in a zoomed image in Figure 6.9 will prevent lithium

vapor from exiting with the hydrogen gas. The exhaust point at the top was choked down to prevent over-saturation of the RGA filament, with the RGA aligned such that it has direct line-of-sight to the bottom of the bucket. This was done by drilling a 0.0625" hole in the center of a blank copper gasket for the pure LiH test, which was attached directly below the 2.75" CF gate valve at the top of the main chamber. The size of this aperture was modified to 0.0465" for the Li-rich and LiH-rich tests. This is important when further referencing the results obtained in the initial proof-of-concept experiment.

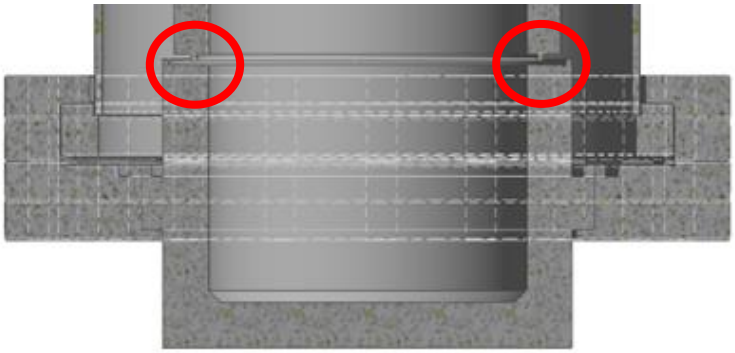

Figure 6.9: A zoomed-in, half-view rendering of the distillation column bottom. The sections in the red circles are manufactured grooves to prevent lithium exhaust at the bottom, but can act as an escape route for other gases.

Apart from measuring the temperatures in the bucket and in the stages, the only other diagnostic used to quantify the success or failure for these proof-of-concept tests was the VTI Odyssey RGA used for gas analysis in the previous two chapters. With the sample loaded, the chamber pumped down, and prior to heating, a base scan was taken to indicate the levels at which any impurities within the evacuated column system may exist. Base scans for each test will be displayed in the respective individual sub-section.

6.2.1 Proof-of-Concept Experiment: Pure LiH

As was mentioned previously, the initial test of the distillation column was conducted with a pure LiH sample. Approximately 1.54 moles of LiH (12.28 g) were loaded into the bucket in the

bucket following the procedure listed in the previous section. After the column had been transported and evacuated for 14 hours, an initial base scan was taken and is shown in Figure 6.10.

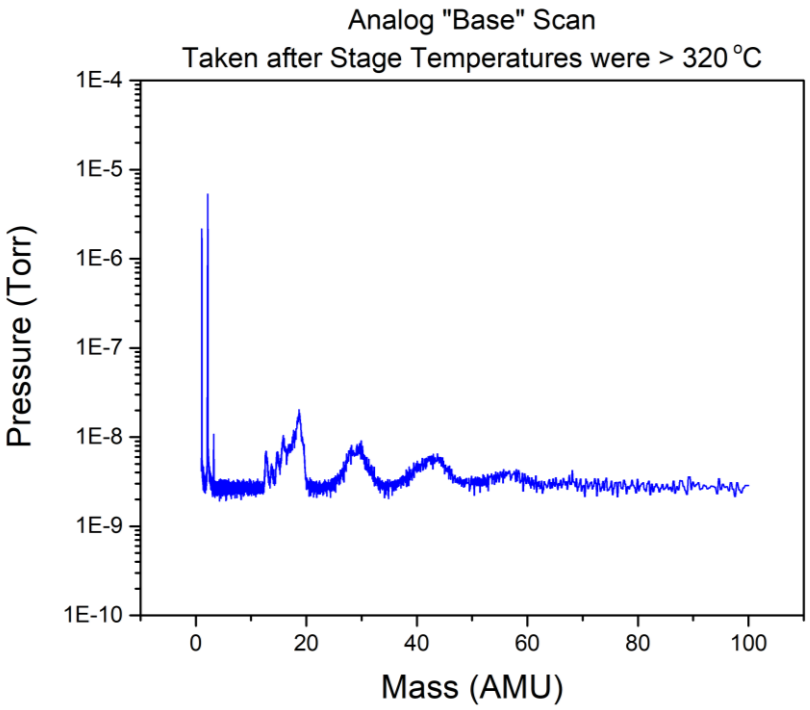

Figure 6.10: The base scan taken for the distillation column before the heating portion of the pure LiH experiment had begun.

Because the stages are resistively heated using embedded cartridge heaters as the source, they take quite a bit longer to heat to temperature. The stages were therefore heated well before the induction heating process was started. During this time, the bucket temperature only elevated by approximately 10 °C, meaning that the bucket and the stages were thermally well isolated. Once both stages had reached temperatures in excess of 320 °C, the induction heater was switched on and set to a current output of 350 A (chosen to try and prevent the circuit breaker from tripping). The bucket then began to rapidly heat, while an RGA trend scan was set to track masses of 1 AMU, 2 AMU, 6 AMU, 7 AMU, 18 AMU, and 28 AMU.

Once the bucket temperature had climbed to values in excess of 330 °C, the 2 AMU signal began to saturate the RGA filament. During this time, there was no detectable increase in the 6 AMU and 7 AMU signals, indicating that hydrogen was being released quite rapidly while the

lithium vapor was condensing before reaching the exhaust point at the top of the chamber. This was a very positive result, in that the lack of any Li vapor signal indicates that the condensation stages are performing their function, while significant amounts of hydrogen were evolving even at relatively lower temperatures. Unfortunately, to protect the RGA filament from over-exposure, the trend scan was halted prematurely, so quantifiable data that characterizes the degree of success for the column were not obtained. The raw trend scan up to the point at which the RGA was turned off is shown in Figure 6.11.

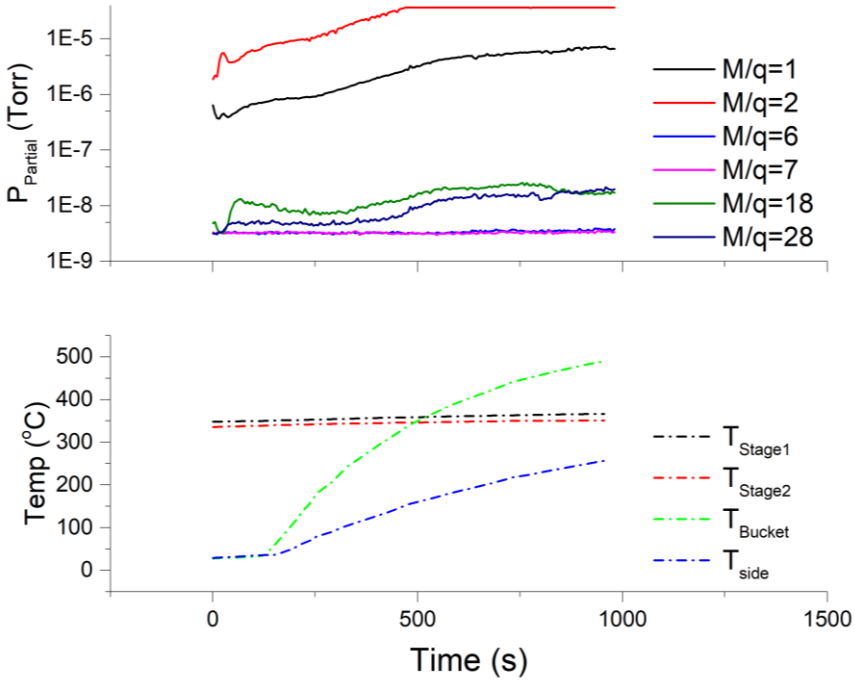

Figure 6.11: The TPD results investigating the hydrogen and lithium release from a sample of 12.28 g of pure LiH loaded into the column bucket. Clearly visible is the flat top on the M/q = 2 trend, indicating filament saturation.

Even though the RGA was turned off to protect the filament, the experiment was continued to see if the induction heater could take the sample bucket up to 700 °C and how quickly this could be achieved. Unfortunately, the during the experiment once the sample bucket reached temperatures in excess of 550 °C, the 20 A circuit breaker powering the induction heater tripped. The breaker was reset and the heater was turned on again, but the temperature was never able to

reach temperatures much above 560 °C without tripping the breaker. The experiment was considered finished at this point and the sample was cooled.

While not much quantitative results can be drawn from this initial proof-of-concept experiment, the initial heating run was still considered successful in that significant amounts of hydrogen were removed from the LiH sample (so much so, in fact, that the filament of the RGA had to be shut down for protection). It was also evident that significant lithium signals were not present in the gas phase at the top exhaust port, meaning that the lithium was condensing in the column stages. It seems evident from the TPD scan that since the molecular hydrogen signal increased substantially at lower temperatures, there likely existed an impurity hydroxide layer on the surface of the sample. The bucket transfer from the drybox to the main chamber would be the cause for the introduction of impurities in the case of this preliminary run. Other than the problem with impurities, it appears as if the column worked as intended.

6.2.2 Proof-of-Concept Experiment: Li-Rich Sample

The Li-rich sample was chosen such that a 3 % molar ratio (0.03 mol H : 1 mol Li) would be tested. This equated to a Li mass of 3 g and a LiH mass of 0.07 g. While this molar ratio was above the solubility threshold for most temperatures, as defined by the liquidus curve by Yakimovich [10] in the previous chapter, it more closely resembled the far-from-saturated solutions that would be expected in the lithium stream exiting from a hypothetical Li-walled reactor, assuming that upstream separation techniques described by Ono [8] were absent. The loading procedure for this mixture was based on the use of the earlier iteration of the CPMI drybox, described previously. After the system was transported to the experimental stand, a base scan was taken with the RGA and is illustrated in Figure 6.12.

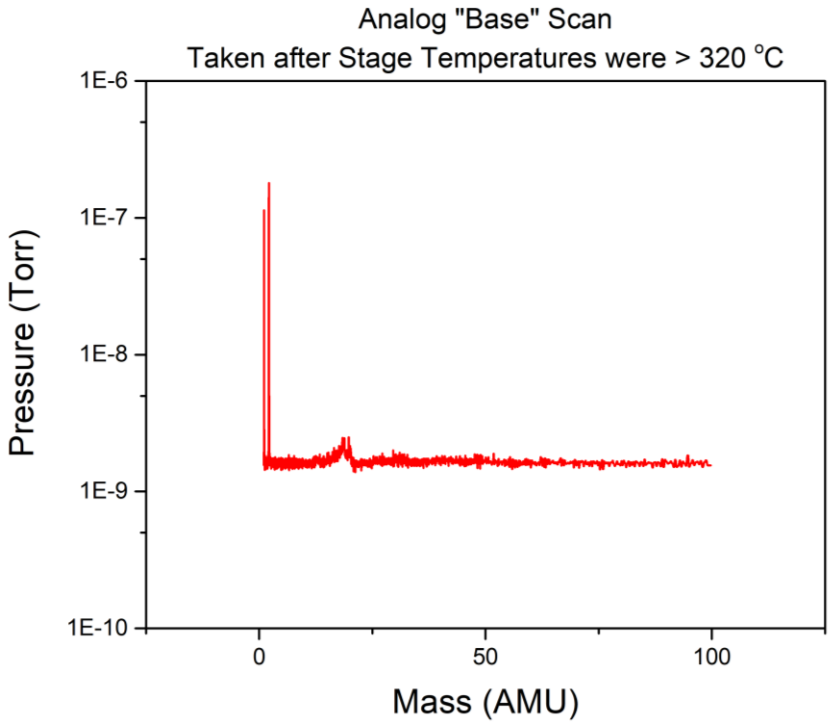

Figure 6.12: The base scan taken for the distillation column before the heating portion of the Li-rich experiment had begun.

In this test, the bucket temperature was able to reach a peak value of approximately 715 °C after nearly 50 minutes of heating. To investigate the effect temperature had on hydrogen and lithium release in this far-from-saturated mixture, partial pressures registered by the RGA were plotted as functions of temperature. These trends are illustrated in Figure 6.13, taken just during the heating phase of the experiment. The trend scan was continued even as the stages and bucket were being cooled, but very little information could be extracted from these data.

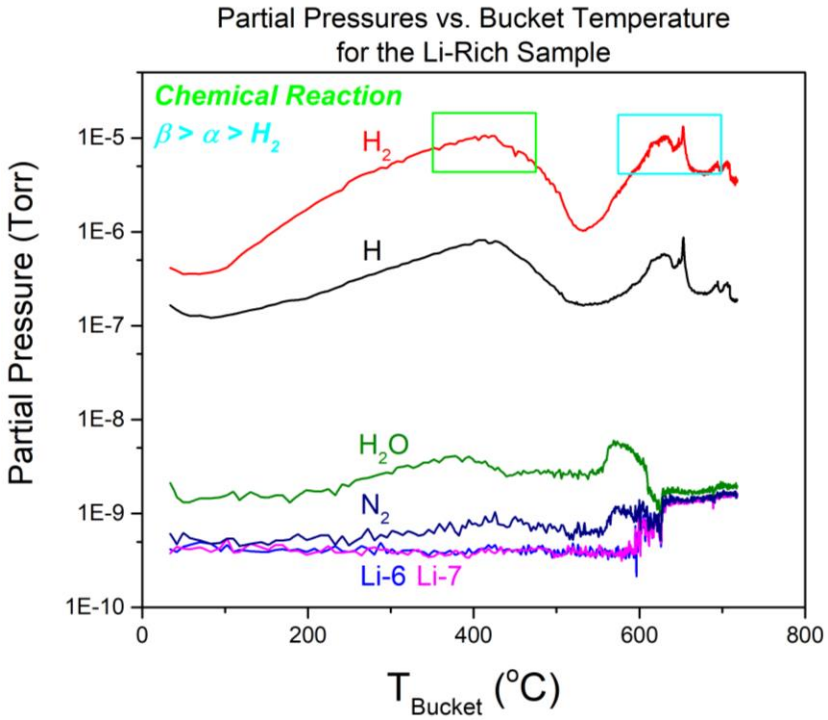

Figure 6.13: The partial pressure vs. temperature plot for the Li-rich proof-of-concept experiment in the prototype distillation column.

While the partial pressure plot does not give relate any significant quantitative information, it can be used to draw a few inferences. First, the broad peak that occurs for both atomic and molecular hydrogen in temperatures between 300 and 400 °C is most likely due to the chemical interaction between either residual water and LiH or LiOH and LiH. This is expected, since the loading procedure for this sample was not ideal, in that the sample in the bucket was briefly exposed to air when attaching the bucket. Second, a rise in the Li signals was observed for temperatures at or greater than 600 °C, indicating significant Li evaporation. Finally, trends that mimicked the β to α LiH phase transition discussed in Chapter 5 are clearly evident from the sharp peak followed by an equally sharp drop in H_2 partial pressure at a temperature slightly greater than 650 °C. A greater degree of quantification could be made with a hydrogen leak calibration for this system, which was done and applied to the hydrogen information in Figure 6.13. The evaluated rates are plotted in Figure 6.14 as functions of temperature. Calculations for these rates were performed similarly to those done in Chapters 4 and 5.

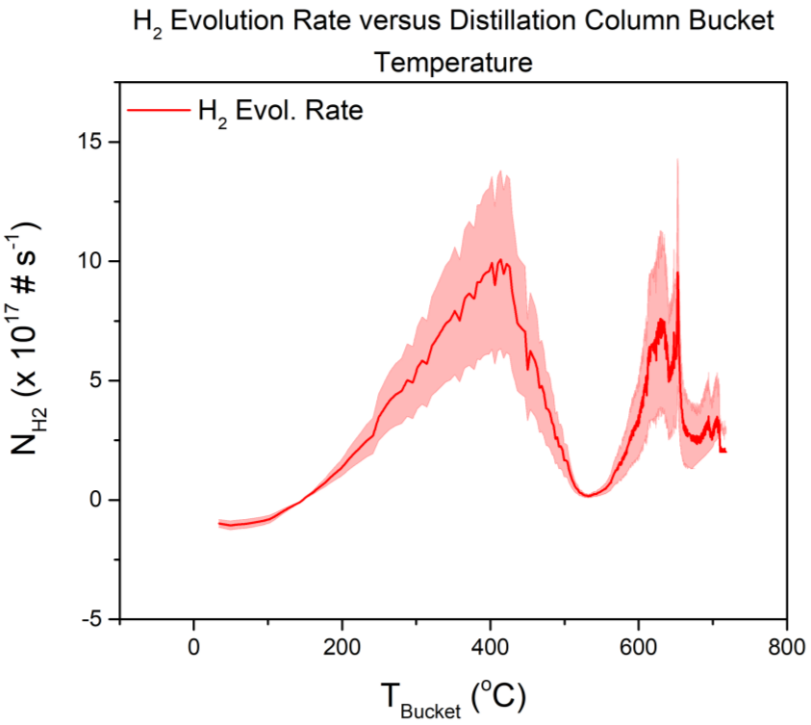

Figure 6.14: The hydrogen evolution rate vs. temperature plot for the Li-rich proof-of-concept experiment in the prototype distillation column.

Taking the information from Figure 6.14 and integrating the hydrogen signal over time, the total amount of molecular hydrogen can be found and compared with the initial amount of hydrogen that was loaded as LiH. The integrated RGA signal yielded a total evolved hydrogen value of 0.004 ± 0.002 moles of H_2, while the initial amount of LiH loaded into the chamber was 0.008 moles. Applying the appropriate stoichiometric ratios, it was found that approximately 50 % of the original hydrogen dose was recovered during this test. For a greater recovery, it would likely be better to allow the system to continue to operate at temperatures above 700 °C to evolve any hydrogen remaining in the hydride precipitate. This also supports the claim that low hydrogen concentration solutions may require supplementary methods more efficient hydrogen reclamation.

The bucket and column stages were also visually inspected post mortem. The whole system was analyzed after the chamber had been vented with laboratory air at a relative humidity of approximately 30 %, meaning that impurities would likely readily form with whatever lithium or lithium derivative remained in the system. It appeared that virtually no lithium remained within

the bucket volume, but had been deposited onto the stages, with the underside of the first stage receiving the highest dose of re-condensed lithium. What did remain in the bucket appeared to be what remained of the LiH, meaning that the H_2 partial pressure at the end of the trend in Figure 6.13 was likely a β phase plateau, similar to what was described in the previous chapter. Sequential images of the interior of the column are shown in Figure 6.15.

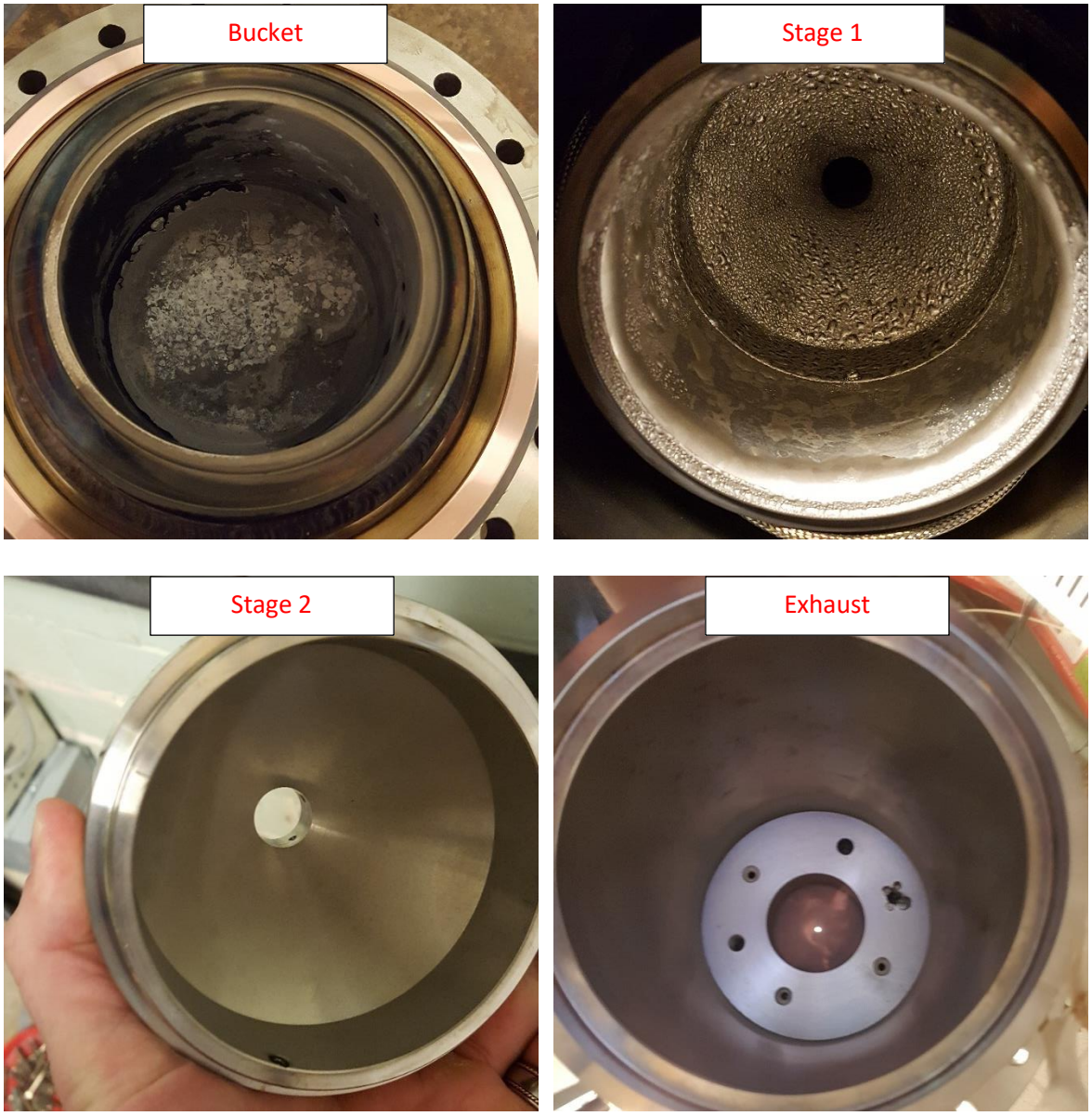

Figure 6.15: Images of the internal components of the column post mortem. The majority of the Li condenses on the bottom of Stage 1; however, some Li residue was noticeable on Stage 2 and the Exhaust.

6.2.3 Proof-of-Concept Experiment: LiH-Rich Sample

The LiH-rich sample was chosen such that 60 % molar ratio (0.6 mol H : 1 mol Li) was tested (actual molar ratio was 59.3 %). This equated to roughly 2.5 g of LiH and 1.5 g of Li. This chemical composition is more representative of the solutions that would be treated in the context of the loop system proposed by Ono [8], where upstream separation techniques are present and able to separate the deuteride and tritide-rich stream from the rest of the lithium exiting the reactor. The loading of this sample was done in the most recent version of the CPMI drybox, meaning that the entire distillation column was able to be held in an inert argon environment while the bucket was loaded and attached to the column body. Having the entire column exposed to an argon environment and being able to isolate the system should allow for a drastic reduction in impurities that plagued the previous tests. A base scan, similar to the one presented in Figure 6.12, was taken for this sample composition and is shown in Figure 6.16.

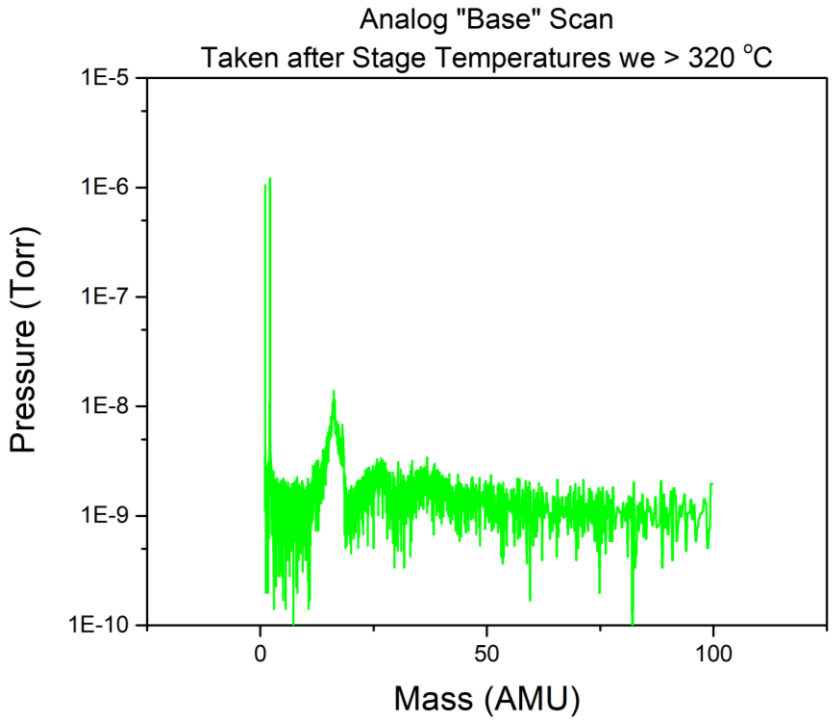

Figure 6.16: The base scan taken for the distillation column before the heating portion of the LiH-rich experiment had begun.

Unfortunately, the results from this sample were unable to be quantified for the entirety of the heating process, due in large part to the fact that so much hydrogen flux was reaching the RGA filament that the filament was getting saturated at temperatures as low as 485 °C. While this seems unfortunate at first glance, it still does relay information about the system, especially when comparing the hydrogen signals between the Li-rich and LiH-rich samples. During the Li-rich test, the hydrogen signal never approached the level of filament saturation, meaning that the maximum evolution rates were limited. This was likely due to the disparity in hydrogen population between the two samples, as was mentioned in the previous chapter. A higher hydrogen population density in the sample results in a higher overall evolution flux, simply by virtue of the increased probability for two hydrogen atoms to diffuse to the surface, recombine, and evolve as a diatom.

Even though the results are again unable to be properly quantified, efforts will be made to relay what information was gathered during the heating process. In doing so, the tracked partial pressures are plotted against temperature in Figure 6.17. Applying the same correction and calibration done for the Li-rich sample, Figure 6.18 illustrates the hydrogen evolution rate versus the temperature. As mentioned in the previous paragraph, since the hydrogen signal saturated the RGA filament, it was impossible to determine exactly how much hydrogen had been evolved during the test. What can be concluded, however, is that higher hydrogen atomic ratios relate to higher evolution rates. As such, the author recommend that future loop systems employ upstream extraction techniques that separate the LiH-rich phase from the Li-rich phase. The investigation of the extraction techniques will act as part of an on-going investigation into a close liquid lithium loop for application on real-world reactors.

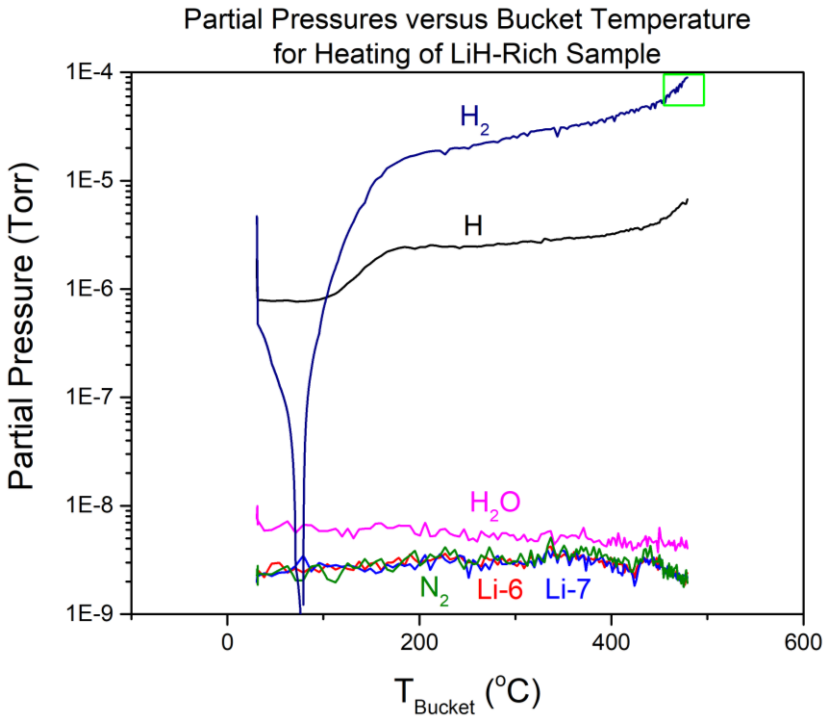

Figure 6.17: The partial pressure vs. temperature plot for the LiH-rich proof-of-concept experiment in the prototype distillation column. The green box illustrates the point of saturation for the RGA filament.

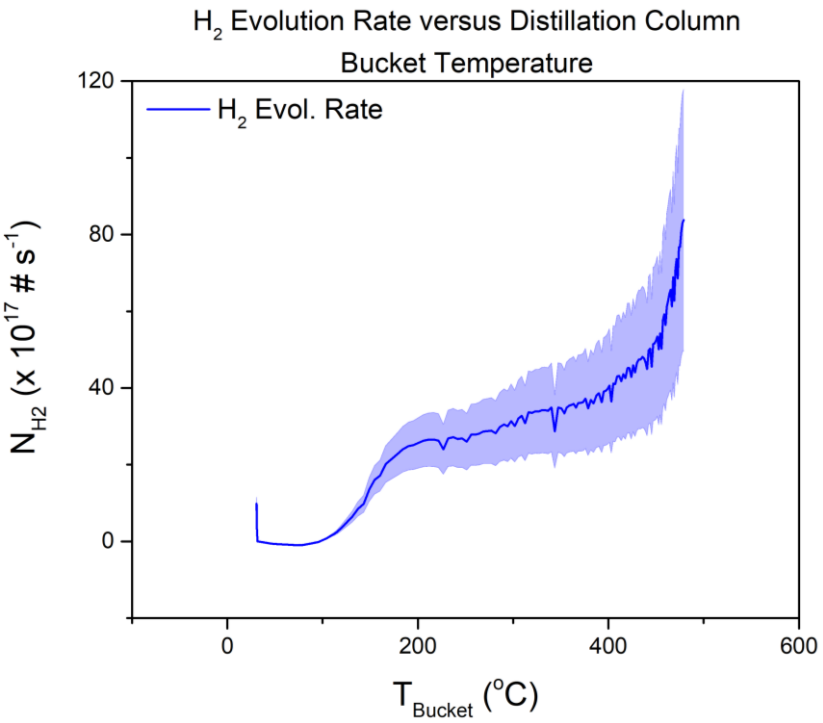

Figure 6.18: The hydrogen evolution rate vs. temperature plot for the LiH-rich proof-of-concept experiment in the prototype distillation column. These data represent molecular hydrogen evolution prior to the point at which the filament saturates. Note that the evolution rates from this sample are nearly an order of magnitude higher than those in Figure 6.14.

6.3 Conclusions and Future Work

The design of a hydrogen isotope extraction tool that can be used within the context of a reactor-scale liquid lithium loop was explored in this chapter. Results from the previous two chapters helped to influence the design process, such that the column could potentially be used in scenarios where the inlet has a near-saturated composition and where the inlet has a far-from-saturated composition. An induction heater was considered as the primary driver for heating, while inclined stages will be used to condense lithium vapor.

6.3.1 Discussion

In a real-world application it is likely that a single column unit with the same measurements listed in this chapter will suffice for separation and recovery based on the mass treatment rates reported by Ono [8]. This means that the power draw will likely be on the order of 2 to 3 kW for a single unit. However, it may be better to have a number of these units working in parallel, or to increase the heating surface area contact of a unit similar to the one described in this chapter. Assuming that 10 units were placed in parallel to maximize thermal recovery, then the power budget for these units would be on the order of 20 to 30 kW. Heating schemes other than induction heating drive could be used, such as siphoning some of the exhaust heat from the reactor for this purpose. Heating possibilities are not limited to induction heating, and must be considered from a power budget standpoint. Induction heating was chosen for this purpose because of its clear advantages over resistive heating. An improvement to this system would be to add a much more efficient induction heater that can provide even more power to heat different loads more quickly.

The induction heating process was modeled in COMSOL using an axisymmetric, finite element solution method. The model was very basic, but helped to gain insight into how quickly the induction heater would be able to heat the column bucket. Errors in the simulation are likely due to the fact that there is not an outflow condition at the boundaries for heat to escape, so all of the heat remains trapped within the domain. This causes auxiliary heating of the air surrounding the bucket. The peak temperatures achievable after an 1800 s heating period were plotted as a function of current and frequency, and the values obtained at low currents and low frequencies matched those obtained during the heater commissioning tests.

Three proof-of-concept tests were then carried out in the fully constructed column to investigate its effectiveness as a hydrogen removal technology. This was done with pure LiH, a Li-rich sample, and a LiH-rich sample. Unfortunately, no quantitative data were obtained during the pure LiH test due to problems surrounding RGA filament over-saturation and the amount of power drawn from the 110V breaker for the induction heater supply. It can be concluded from this test, however, that the column appears to function as predicted, with hydrogen gas being the only species exhausted through the top port and lithium remaining trapped in the condensed phase on the stages below the exhaust port. Future experiments will need an even smaller exhaust port to

help prevent RGA over-pressurization, as well as a larger power source to draw from in order to reach temperatures in excess of 700 °C in relatively short periods of time.

Results from the Li-rich and LiH-rich samples also indicate that the column is functioning as intended, with the stages being able to capture and re-condense nearly all of the lithium, while large amounts of hydrogen were able to be quickly exhausted from the main chamber. Comparing the two sample types helps to prove the hypothesis laid out in Chapter 5, where recovery from Li-rich solutions will be hard-pressed to match wall losses. In contrast, LiH-rich solutions will evolve more hydrogen at faster rates, simply by virtue of the hydrogen population in solution. More work needs to be done to investigate different concentrations of samples, as well as the state of the samples post-mortem. This will be left for future endeavors.

The prototype column will need to undergo further testing before it can be integrated into a fully functional lithium loop. Its efficacy as a removal source for far-from-saturated solutions of lithium and hydrogen require further batch-scale testing, where various ratios of lithium and lithium hydride are mixed together. Once the system has been verified as successful for nearly all real-world solution compositions, physical modifications to the column will need to be done in order to integrate it into a full lithium loop. The column may also require the addition of supplemental recovery techniques, which will require more structural modifications. A supplemental recovery technique will be discussed in more detail in the next chapter.

6.3.2 Conclusions and Future Work

The primary conclusions from these tests can be summed up in the following list:

- A distillation column design was chosen for hydrogen isotope recovery, with its uniqueness coming from the use of induction heating drive and the inclination employed for lithium vapor condensation stages.
- Induction heating was modeled using the Induction Heating physics package in the COMSOL Multiphysics software [10]. Results at low frequency outputs were quite reasonable. Temperatures at higher frequencies were greater than what was intuitively expected, and sources of error may stem from the boundary conditions at the edges of the control volume.

- The induction heater was tested on a dummy load and found to be able to heat a large disk of 304 stainless steel to temperatures in excess of 600 °C in roughly 30 minutes.
- An initial test was performed with pure lithium hydride as the sample to investigate the efficacy of both the induction heater and the condensation stages.
- The only metric for this proof-of-concept test was the Odyssey RGA, situated such that its filament had direct line-of-sight to the center of the bottom bucket. During experimentation for the pure LiH and the LiH-rich samples, enough hydrogen was evolved to oversaturate the RGA filament, so the test was ended prematurely. These tests seemed to prove, however, that the system functioned as intended, since no significant increase in the partial pressures corresponding to the isotopes of lithium were detected by the RGA.
- Li-rich and LiH-rich samples were also tested, and it was found that both compositions evolve appreciable amounts of hydrogen. Comparing the results of both tests helps confirm the hypothesis that LiH-rich solutions (ranging from less-than-saturated to saturated) will be easier to treat than Li-rich solutions (far-from-saturated), simply by virtue of the hydrogen population and probability of interaction.

Since the design, testing, and analysis of the column were only able to be conducted on a proof-of-concept basis, more needs to be done to prove this system will work in a fully functional lithium loop. A few recommendations for future activities are outlined in the following list:

- In order to reduce or eliminate the presence of impurities, the entire column should be placed inside of the drybox along with the sample bucket. The bucket can then be loaded and the column can be assembled in an argon environment to prevent oxide and hydroxide buildup.
- Before integrating the system into a loop, more tests are required with samples that span the range between lithium-rich and lithium hydride-rich compositions. The temperature required for peak flux should be documented for each sample type.
- Post-mortem analysis of the sample in the bucket and the layers on the condensation stages should be done to investigate what species are being deposited, and what the likelihood is that hydrogen gas will co-deposit along with lithium vapor.
- The nozzling of the hydrogen at the exhaust port of the column should be optimized.

- Finally, the entire recovery system should be re-fabricated for integration into a fully functional lithium loop system. This may include outfitting the column with supplementary devices for the treatment of far-from-saturated solutions.

6.4 References

[1] D.N. Ruzic, W. Xu, D. Andruczyk, M.A. Jaworski. “Lithium-metal infused trenches (LiMIT) for heat removal in fusion devices”, *Nucl. Fus.* 51 (2011) 10200.

[2] W. Xu, D. Curreli, and D.N. Ruzic, “Computational studies of thermoelectric MHD driven liquid lithium flow in metal trenches”, *Fus. Eng. and Des.* 89 (2014) 2868.

[3] W. Xu, D. Curreli, D. Andruczyk, T. Mui, R. Switts and D.N. Ruzic, “Heat transfer of TEMHD driven lithium flow in stainless steel trenches”, *J. Nucl. Mat.* 438 (2013) S422.

[4] D. Andruczyk, D. N. Ruzic, D. Curreli, J. P. Allain, and the HIDRA Team, “HIDRA: Hybrid Illinois Device for Research and Applications”, *Fusion Sci. & Tech.* 68 (2015) 497.

[5] J. Li, et al., “A long-pulse high-confinement plasma regime in the Experimental Advanced Superconducting Tokamak”, *Nat. Phys.* 9 (2013) 817.

[6] Y. Sun, et al., “Nonlinear Transition from Mitigation to Suppression of the Edge Localized Mode with Resonant Magnetic Perturbations in the EAST Tokamak”, *Phys. Rev. Lett.* 117 (2016) 115001.

[7] J.S. Hua, J. Rena, Z. Suna, G.Z. Zuoa, Q.X. Yanga, J.G. Lia, D.K. Mansfieldb, L.E. Zakharovb, D.N. Ruzic, EAST team, “An overview of lithium experiments on HT-7 and EAST during 2012”, *Fusion Engineering and Design* 89 (2014) 2875.

[8] M. Ono, R. Majeski, M.A. Jaworski, Y. Hirooka, R. Kaita, T.K. Gray, R. Maingi, C.H. Skinner, M. Christenson, D.N. Ruzic, “Liquid lithium loop system to solve challenging technology issues for fusion power plant”, *Nucl. Fusion* 57 (2017) 116056.

[9] R.J. Goldston, R. Myers, and J. Schwartz, “The lithium vapor box divertor”, *Phys. Scripta* T167 (2016) 014017.

[10] *COMSOL Multiphysics® Reference Manual*, COMSOL Version 4.3b (2013) http://hpc.mtech.edu/comsol/pdf/COMSOL_Multiphysics/COMSOL_ReferenceManual.pdf, Accessed: 2017-10-20.

[11] A.B. Martin-Rojo, E. Oyarzabal, T.W. Morgan, and F.L. Tabarés, “Exposure of liquid lithium confined in a capillary structure to high plasma fluxes in PILOT-PSI – Influence of temperature on D retention”, *Fusion Engineering and Design* 117 (2017) 222.

CHAPTER 7: A SUPPLEMENTARY RECOVERY TECHNIQUE

The distillation column described in the previous chapter will be able to adequately recover hydrogen isotope species from lithium solutions on time scales that balance absorption at the vessel walls of the reactor. This holds true if separation techniques upstream from the column are able to successfully isolate a hydride-rich stream from the remaining lithium. This hydride-rich stream will then be treated in the column to recover deuterium and tritium gas, which will be recycled back to the reactor. It is less certain that the same system will be able to balance absorption losses at the plasma-material interface when upstream purification technologies, such as those proposed by Ono [1], are absent in the context of a larger lithium loop. Heating mechanisms would then be driving deuterium and tritium diffusion, surface recombination, and evolution in far-from-saturated solutions. The ability to then recovery tritium at rates that balance fuel loss at the vessel wall would be significantly less probable, simply by virtue that tritium exists in very low atomic fractions within the lithium solution, which was evidenced by evolution fluxes evaluated for the α phase in Chapter 5.

This chapter addresses a technique that can be used to recover hydrogen isotopes in these far-from-saturation scenarios. This technique is considered as a supplementary technique to the use of heat as the driving force for tritium recovery. The bulk of this chapter will focus on the theoretical and computational framework for how to employ this supplementary method practically. Unfortunately, this same supplemental technique was never experimentally employed in the prototype column; however, the method is already a proven technology in the areas of metallurgy and metal casting. The final sections of this chapter will focus on how this method can be practically applied in the context of the prototype distillation column described in Chapter 6.

This chapter will focus on ultrasonic degassing as a technique that can supplement the distillation column recovery described in the previous chapter. The methodology of this proven technology will be discussed within the context of hydrogen removal from metal castings. The theory will then be extended to the hydrogen-lithium system, where a comprehensive numerical model was developed to investigate growth of an individual cavitation bubble within liquid lithium and how the bubble interacts with the dissolved hydrogen. The results of this model will be reported, along with how these results can be applied practically. The chapter will close with remarks on how each of this technology could be employed in future lithium loop systems.

7.1 Theory and Background

Bubble dynamics is the field of study that forms the basis for the phenomenon known as ultrasonic degassing [2]. Ultrasonic degassing is essentially the practical application of a process known as rectified diffusion, used for the removal of unwanted dissolved gases within liquids. Gas within a liquid forms a two-fluid problem, where the quantities that govern interaction between the two phases are the pressure, temperature, and velocity fields. In the case of ultrasonic degassing, these quantities need to be measured with regards to how the application of an external time-dependent pressure field will modify the physics. Often, the applied pressure field is acoustic in nature, but other forces may be used for bubble nucleation and growth. The conventional theories for bubble dynamics may also be inadequate when the gas phase within the liquid chemically interacts with the liquid, since the mass and energy transfer can be modified by the formation and destruction of chemical bonds. This section will go through the theory and practical applicability of ultrasonic degassing as it pertains to hydrogenated lithium samples, and will then explain the modelling results obtained in an effort to observe the growth of an individual bubble within liquid lithium.

The process of rectified diffusion has been studied quite extensively since the 1940s [2 – 8], with transient cavitation events being observed experimentally as far back as the 1970s [9 – 12]. Rectified diffusion is a modification from conventional bubble dynamics, where the rapidly oscillating fields and the bubble life cycle is governed by cavitation processes. In his book, *Cavitation and Bubble Dynamics*, Brennen [2] described two processes that can rupture a liquid and promote growth of vapor or gas bubbles. The first of these phenomena is known as boiling, where the local temperature is increased drastically while the pressure is held constant. The second is known as cavitation, whereby local decreases in pressure at constant temperature ruptures the liquid, creating a bubble or promoting bubble growth.

Even within quiescent liquids, imperfections may manifest as microbubbles, or nucleation sites for boiling and cavitation. Without an external driving force, these microbubbles may exist in an equilibrium state over very long periods of time. This is especially true when “impurity” gases are dissolved within the liquid medium. Rectified diffusion has the ability to promote bubble growth due to the nonlinearities in bubble dynamics that arise from oscillations in an applied acoustic pressure field. During the expansion portion of the acoustic cycle, the influx of gas from

the liquid to the bubble is higher than the efflux of gas from the bubble to the liquid during the compression portion due to the differences in the surface area of the bubble. From a diffusion layer analysis point-of-view, the liquid diffusion is also thinner during expansion which promotes a higher level of gas influx. Thresholds exist whereby rectified diffusion will promote transient cavitation and growth, and if these thresholds are not met, the bubble may oscillate stably or collapse.

The gas within the bubble, the size of the bubble, and the liquid directly adjacent to the bubble are all rapidly changing, so energy and mass transfer is also oscillating on a similar time scale. In terms of energy, the bubble radiates acoustic energy during oscillation, while the thermal and viscous properties of the liquid act as forces opposing bubble oscillation and growth [13 – 15]. Cavitation may be induced by a number of factors, but this report will focus on how acoustic drive will modify bubble stability and growth. This classification is nonlinear, in that the change in bubble volume is not directly proportional to the acoustic pressure. If the dissolved gas is reactive, then the process becomes physio-chemical and must be modified accordingly.

Ultrasonic degassing is a practical application of rectified diffusion, whereby the gas dissolved in a liquid will diffuse into and out of the bubble generated by the externally applied, oscillating, acoustic pressure field. The threshold for this to occur is based on the intensity of the applied acoustic field and the frequency at which the transducer is set to oscillate. Past this threshold, the bubble will grow over the course of each period, while buoyancy forces will drive the bubble to the surface of the liquid. The dissolved gases in the bubble are then released at the surface. Reactive gases in the bubbles will also appreciably expand more rapidly due to the temperature spike within the bubble during the compression phase of the oscillation [13, 14].

Often, the process of rectified diffusion is thought of in terms of boundary layers. In the liquid, a ‘shell’ occurs where a diffusion layer exists immediately adjacent to the gas bubble [14]. When the bubble goes through the expansion section in the cycle, this shell becomes much thinner and the gradients in the boundary layer increase dramatically. Conversely, as the bubble goes through the compression portion of the acoustic cycle, the boundary layer increases and the gradients within this layer dramatically decrease. This ‘shell’ effect is illustrated by the graphic in Figure 7.1.

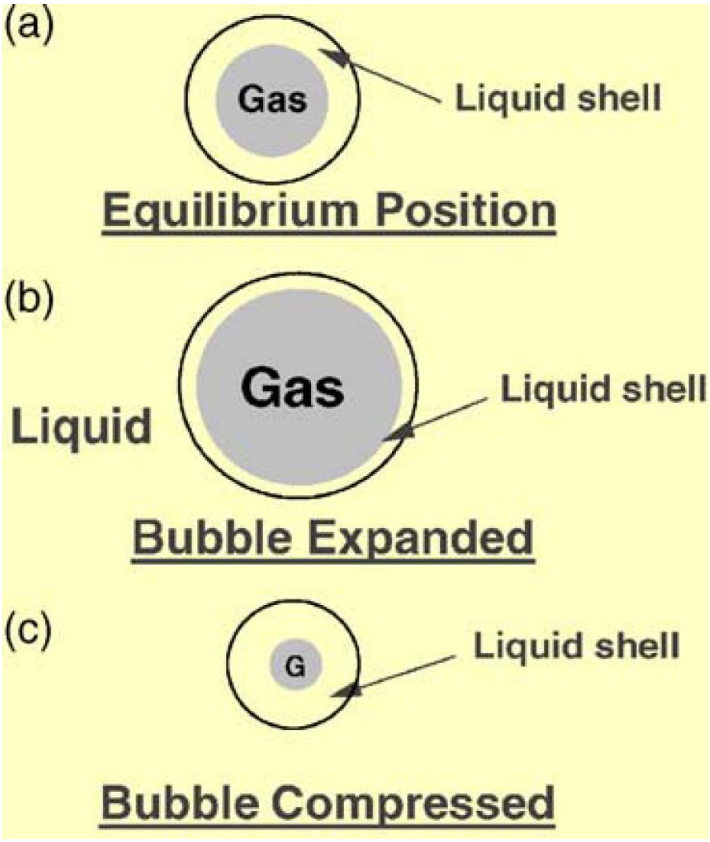

Figure 7.1: A graphic representing rectified diffusion and the liquid boundary layer, or 'shell', which exists directly adjacent to the bubble [13].

The numerical method for solving this problem, modelled after the work done in Ref. 13 – 15, includes a few assumptions that help simplify the problem statement from a macroscopic standpoint. First, a 'stable' nucleation bubble is assumed to already exist by the time an external pressure field is applied to the system. The criteria for bubble stability and growth, as well as what is considered the nucleation process for bubble formation, will be discussed in the next paragraph. Second, the period for bubble growth and collapse is much smaller than the timescale whereby buoyancy forces act on the bubble to accelerate it up and out of the melt. This means that in the assumed scenario, the bubble is considered stationary within the bubble melt. For simplification, the equation of state for the gas within the bubble is the ideal gas law, meaning that the bubble can be considered to be thermally perfect. However, the bubble is considered calorically imperfect, in that energy can be transferred into and out of the bubble from the liquid. In assuming the ideal gas law equation of state for the bubble, it is also assumed that the gas within the bubble is

thermodynamically uniform. Essentially, as soon as energy or mass is transferred to or from the bubble, the entire domain within the bubble takes on the same properties such that there is no gaseous diffusion layer, or 'shell'. The next sub-section will discuss the stability criterion for a nucleation site/bubble to exist and grow.

7.1.1 Nucleation Site Pressure Threshold

The question that remains is: what is the nucleation site for this phenomenon within the liquid and what threshold exists that would allow a bubble to grow from this nucleation site? In order for a nucleation site, which Brennen [2] proposed to be another bubble or void in the liquid, to be a stable point from which an applied pressure field can induce growth, then the initial bubble/nucleation site must be able to overcome not only the metallostatic pressure forces that promote bubble collapse, but also the surface tension and viscosity effects at the interface that act against the bubble. This criterion is described in the equation [13 – 15]:

$$P_g \geq P_{atm} + P_H + \frac{2\,\sigma}{R} \tag{7.1}$$

where the nucleation bubble pressure, equivalent to the sum of the two pressure terms on the left of the inequality, must overcome not only the metallostatic pressure head in P_H, but also the atmospheric pressure applying force on the liquid and the surface tension forces (σ) which oppose bubble stability and growth. In the above equation, R is initial nucleation bubble radius. Often, nucleation bubbles do not purely exist, so other impurities or defects within the melt must be initially present for the nucleation sites to be effective. This inequality satisfies the condition known as the Laplace pressure [13 – 15].

While the inequality described in Equation (7.1) relates the condition for a cavitation bubble nucleation site to form and stabilize, it does not describe the threshold required for bubble growth to occur. The acoustic threshold needed to promote bubble growth beyond what is described by Equation (7.1) is sensitive not only to the amplitude of the applied field, but also to the concentration within the liquid melt and the frequency at which this field is propagated. As will be discussed in the following section, a natural frequency exists for a bubble at any given

radius. The acoustic threshold, defined in Brennen [2] and based on the work of Crum [7] (governed by the Rayleigh-Plesset equation [16]), is given by:

$$P_C^2 = \frac{(\rho_l R_E^2 \omega_N^2)^2 \left[(1-\frac{\omega^2}{\omega_N^2})^2+(\frac{4 \mu_l \omega^2}{3 \eta \omega_N P_0})^2\right](1+\frac{2 \sigma}{R_E P_0}-\frac{c_\infty}{c_s})}{(3+4 \Theta_1)\frac{c_\infty}{c_s}-\left[\frac{3 (\eta-1) (3 \eta-4)}{4}+(4-3 \eta) \Theta_1\right](1+\frac{2 \sigma}{R_E P_0})} \tag{7.2}$$

where:

$$\omega_N = \left[\frac{1}{\rho_l R_E^2}\left\{3 \eta \left(P_0 - P_V(T_\infty)\right) + 2 (3 \eta - 1) \frac{\sigma}{R_E}\right\}\right]^{1/2} \tag{7.3}$$

$$\eta = \frac{1}{3} Re[\Upsilon] \tag{7.4}$$

$$\Upsilon = \frac{3 \gamma}{\{1-(3 \gamma-1) i \chi [(\frac{i}{\chi})^{\frac{1}{2}} \coth(\frac{i}{\chi})^{\frac{1}{2}}-1]\}} \tag{7.5}$$

$$\chi = \frac{\alpha_G}{\omega R_E} \tag{7.6}$$

$$\Theta_1 = \frac{(3 \eta+1-\beta^2)/4+(\sigma/4 R_E P_0) (6 \eta+2-4/3 \eta)}{1+(2\sigma/R_E P_0) (1-1/3\eta)} \tag{7.7}$$

$$\beta^2 = \frac{\rho_l \omega^2 R_E^2}{3 \eta P_0} \tag{7.8}$$

ρ_l – liquid density at T_∞

R_E – equilibrium bubble radius (R_0 for these purposes)

ω – driving angular frequency

μ_l – liquid viscosity (can be modified to include acoustic and thermal effects)

σ – surface tension

$$P_0 = P_\infty + \frac{2 \sigma}{R_E} \tag{7.9}$$

c_∞ – dissolved gas concentration

c_s – saturation concentration

γ – ratio of specific heats for the gas

The plots in Figures 7.2, 7.3, and 7.4 illustrate the critical pressure values normalized to the equilibrium pressure for the nucleation bubble for various conditions. In all cases, the far field pressure, P_∞, is defined by the metallostatic pressure head of the lithium at a depth of 1 inch.

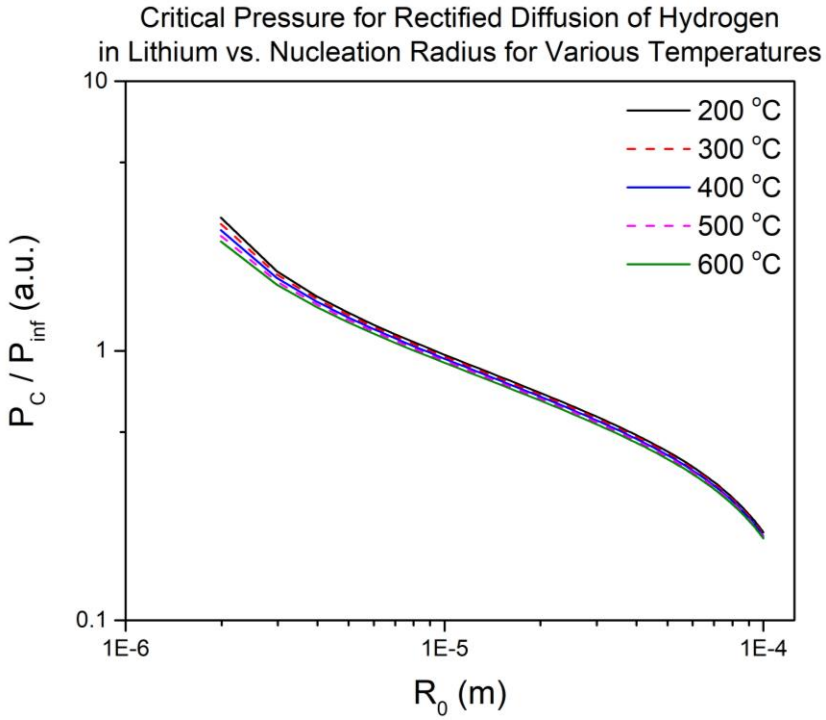

Figure 7.2: A plot illustrating how the acoustic threshold for rectified diffusion in the dissolved hydrogen-lithium system changes with nucleation bubble size and temperature. In this plot, the driving frequency is maintained at 25 kHz and the initial concentration is assumed saturated (at the solubility threshold defined in Chapter 5).

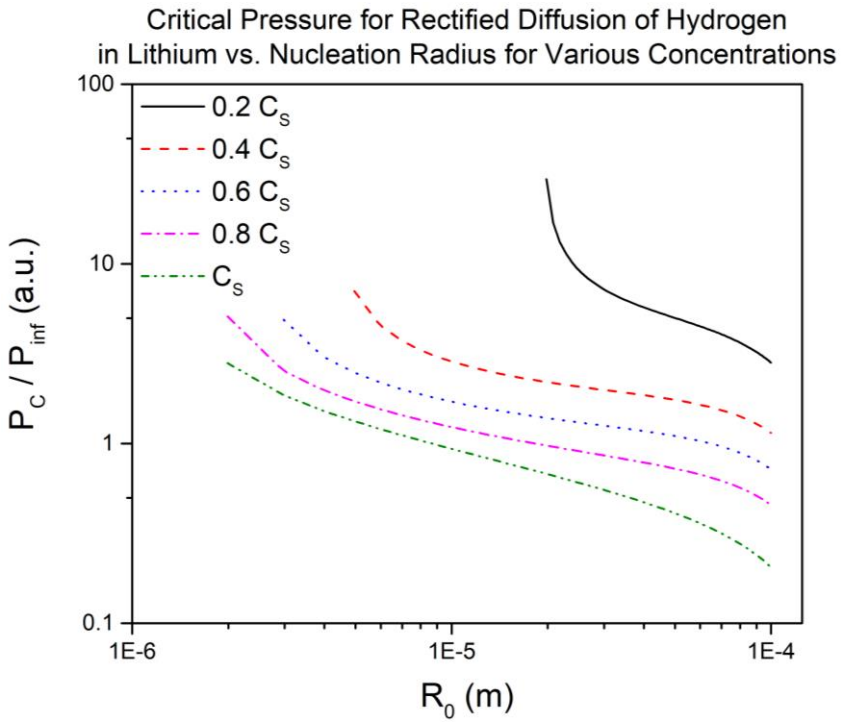

Figure 7.3: A plot illustrating how the acoustic threshold for rectified diffusion in the dissolved hydrogen-lithium system changes with nucleation bubble size and dissolved concentration. In this plot, the driving frequency is maintained at 25 kHz and the system temperature is assumed to be 400 °C.

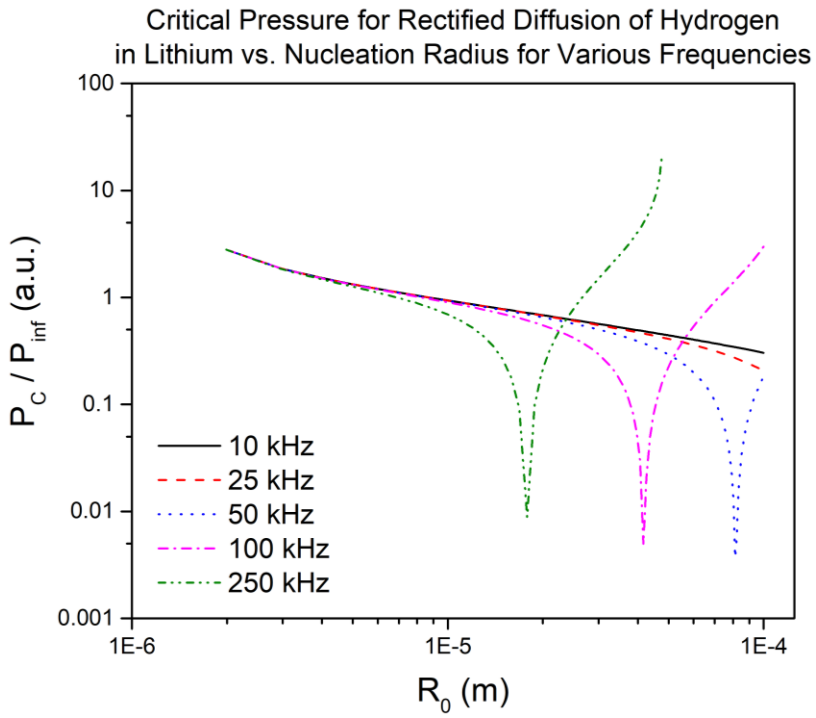

Figure 7.4: A plot illustrating how the acoustic threshold for rectified diffusion in the dissolved hydrogen-lithium system changes with nucleation bubble size and driving frequency. In this plot, the dissolved concentration is assumed saturated and the system temperature is set at 400 °C. Resonant radii, observed at higher frequencies, decrease the critical acoustic threshold substantially.

From these plots, it appears as if the dissolved concentration has the largest effect on the acoustic pressure threshold. Concentrations closer to the saturation point only require P_C values that are below or equal to the initial nucleation equilibrium bubble pressure, P_0. As the concentration gets further from the saturation point, the threshold pressures required for rectified diffusion increase drastically, meaning that concentrations far from the solubility threshold will require a higher driving force. An interesting effect observed in Figure 7.4 are the discontinuities in the critical pressure at higher driving frequencies. Brennen explained in his book that driving frequencies that approach the natural bubble frequency, ω_N, can resonate with the bubble at a critical radius, which causes nonlinear effects such as sudden bubble collapse followed by explosive growth. These resonances can be exploited, since they lower the threshold for transient growth; however, they require significantly higher driving frequencies to achieve. Essentially, the

most ideal transducer will use the combination of high frequencies and high pressure fields to promote bubble growth. In general, the threshold decreases as the nucleation bubble radius increases, but the initial bubble radius is expected to be nearly 10 μm, so it is likely that the threshold amplitude will be near the bubble equilibrium pressure for a given bubble size.

These plots also operate under the assumption that only viscous damping affects growth. For future work, the Rayleigh-Plesset equation [16] can be modified to include thermal and acoustic damping effects for higher accuracy. These effects can be easily incorporated using terms added to the liquid dynamic viscosity in the form [2]:

$$\mu_A = \frac{\rho_l \, \omega^2 \, R_E^3}{4 \, C_s} \tag{7.10}$$

$$\mu_T = \frac{P_\infty + 2 \, \sigma / R_E}{4 \, \omega} \, Im[Y] \tag{7.11}$$

$$\mu_E = \mu_l + \mu_A + \mu_T \tag{7.12}$$

where C_s is the sound speed in the fluid, Y is defined by Equation (7.5), μ_A is the acoustic damping term, μ_T is the thermal damping term, and μ_E is an effective viscosity term. Because these terms act against the bubble, the plots in Figures 7.2 through 7.4 are generous estimates for the critical pressure amplitude. To overcome these added damping effects, practical pressure fields may need to be greater than those indicated in the previous three plots.

7.1.2 Acoustic Wave Propagation and Natural Frequencies

The pressure threshold is not the only value required for stable bubble growth to be predicted. The ability for the acoustic wave to promote bubble growth in the lithium solution is localized to a small, finite area around the source of the force field (likely a pressure transducer). How much energy can be propagated into the melt and how far out the pressure field can extend into the melt is another point of interest in terms of ultrasonic degassing, which can be described through the dispersion relationship for an acoustic wave in a medium. Landau and Lifshitz [17] described the propagation of sound in a fluid by describing the dispersion relation as:

$$k = \frac{\omega}{C_s} + i \, a \, \omega^2 \tag{7.13}$$

which relates the wavenumber (k) to the acoustic frequency (ω), the sound speed in a medium (C_s), and an absorption coefficient (a). In the fluid, the sound speed acts as the maximum velocity magnitude with which a sound wave can travel, which is the upper limit on the group velocity of an acoustic wave.

The derivation if the absorption coefficient is quite involved, but tells a lot about how acoustic power is deposited in the medium. Landau and Lifshitz start the derivation by stating that the maximum mechanical work that can be done in any thermodynamic system is when the process is reversible [17]:

$$E_{mech} = E_0 - E(S) \tag{7.14}$$

where E_0 is the internal energy and $E(S)$ is the change in energy as a function of entropy. The derivative of this system with respect to entropy yields:

$$\dot{E}_{mech} = -\dot{E}(S) = -(\frac{\partial E}{\partial S})\dot{S} \tag{7.15}$$

where the partial derivative is equivalent to the equilibrium temperature, T_0. Assuming that any temperature difference from the equilibrium temperature can be neglected, Landau and Lifshitz found that Equation (7.15) can be rewritten in the form (following the same procedure they had outlined in Chapter 2 of their book):

$$\dot{E}_{mech} = \frac{-\kappa}{T}\int(\nabla T)^2 d\forall - \frac{\mu}{2}\int\left(\frac{\partial v_i}{\partial x_k} + \frac{\partial v_k}{\partial x_i} - \frac{2}{3}\,\delta_{ik}\,\frac{\partial v_l}{\partial x_l}\right)d\forall \tag{7.16}$$
$$-\zeta\int(\nabla\cdot v)^2 d\forall$$

where κ is the thermal conductivity of the medium, T is the temperature, $\forall$ is the fluid volume, μ is the dynamic viscosity of the medium, $\frac{\partial v_i}{\partial x_k}$ is the derivative of the velocity in the i-direction with respect to the k-component, $\frac{\partial v_k}{\partial x_i}$ is the derivative of the velocity in the k-direction with respect to the i-component, δ_{ik} is the delta function, $\frac{\partial v_l}{\partial x_l}$ is the derivative of the velocity in the l-direction with respect to the l-component, ζ is the volume viscosity of the medium, and v is the velocity vector. The volume viscosity term is often neglected in ideal fluids when assuming that the medium

is incompressible; however, compressibility is important when considering the propagation of acoustic waves in a medium.

Assuming the wave is a plane wave travelling in the medium in the x-direction only ($v_x = v_0 \cos(k\,x - \omega\,t)$, $v_y = v_z = 0$), then the final two terms on the right-hand side of Equation (7.13) can be rewritten as:

$$-\left(\frac{4}{3}\,\mu + \zeta\right)\int\left(\frac{\partial v_x}{\partial x}\right)^2 d\forall = -k^2\,v_0^2\,\left(\frac{4}{3}\,\mu + \zeta\right)\int sin^2(k\,x - \omega\,t)d\forall \quad (7.17)$$

where the time-average of this term can be written as:

$$-k^2\,v_0^2\,\left(\frac{4}{3}\,\mu + \zeta\right)\frac{\forall_0}{2} \quad (7.18)$$

The first term in the right-hand side of Equation (7.16) can also be rewritten as (again following an earlier formulation from Chapter 2 of Landau and Lifshitz' book, *Fluid Mechanics* [17]):

$$\frac{\partial T}{\partial x} = \left(\frac{\beta\,C_s\,T}{C_p}\right)\frac{\partial v}{\partial x} = -\left(\frac{\beta\,C\,T}{C_p}\right)\,v_0\,k\sin(k\,x - \,\omega\,t) \quad (7.19)$$

where β is the coefficient of thermal expansion of the material, C_s is the sound speed in the medium, T is the temperature, C_p is the constant-pressure heat capacity, v is the wave velocity, v_0 is the magnitude of the wave velocity, k is the wavenumber, ω is the frequency, and t is the time. The time-average of Equation (7.19) is:

$$-\kappa\,C_s^2\,T\,\beta^2\,v_0^2\,k^2\,\frac{\forall_0}{2\,C_p^2} \quad (7.20)$$

Collecting the time-averaged forms of Equations (7.18) and (7.20) yields:

$$\overline{\dot{E}_{mech}} = \frac{-1}{2}k^2\,v_0^2\,\forall_0\,\left[\left(\frac{4}{3}\,\mu + \zeta\right) + \kappa\,\left(\frac{1}{C_v} - \frac{1}{C_p}\right)\right] \quad (7.21)$$

One can now recall that the total energy propagated in a sound wave is given by:

$$\bar{E} = \frac{1}{2}\,\rho\,v_0^2\,\forall_0 \quad (7.22)$$

where $\bar{E}$ is the time-averaged energy propagated along with the wave, and all other variables retain their previously defined meanings. Knowing that the (plane) sound wave intensity will decrease

through the medium as $e^{-2\,\gamma\,x}$, and the amplitude will decrease through the medium as $e^{-\gamma\,x}$, one can define the absorption coefficient, γ, as [17]:

$$\gamma = \frac{\overline{\dot{E}_{mech}}}{2\,C_S\,\bar{E}} \tag{7.23}$$

where the values listed on the right-hand side of Equation (7.23) retain their previously defined values. Plugging in Equations (7.21) and (7.22) into Equation (7.23), the absorption can then be described by [17]:

$$\gamma = \frac{\omega^2}{2\,\rho\,C_S^3}\left[\left(\frac{4}{3}\,\mu + \zeta\right) + \kappa\,\left(\frac{1}{C_v} - \frac{1}{C_p}\right)\right] \equiv a\,\omega^2 \tag{7.24}$$

where the coefficient a on the right-hand side of Equation (7.24) is the same coefficient listed in the dispersion relationship defined in Equation (7.13). This damping coefficient takes into account processes where the relaxation processes back to equilibrium are fast enough that they follow along with the local expansions and compressions in volume. If the relaxation processes last longer, say in the presence of chemical interactions, the dispersion relationship in Equation (7.13) would need to be modified. A plot relating the square of the index of refraction to the square of the driving frequency is illustrated in Figure 7.5.

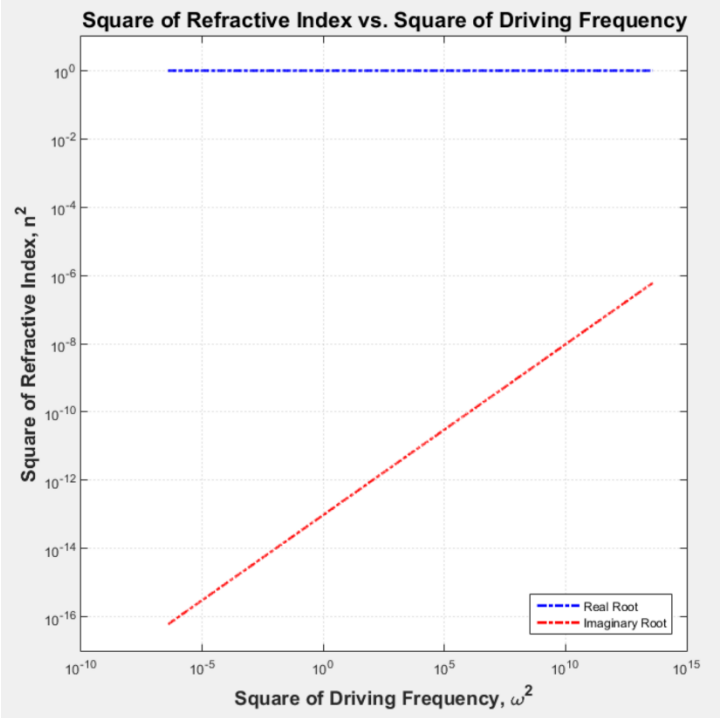

Figure 7.5: A plot illustrating the real and imaginary components of the square of the refractive index with respect to the square of the driving frequency for sound waves propagating through liquid lithium at 400 °C.

The dispersion relationship described by Equation (7.13) is also lacking in mediums that have high thermal conductivities, such as liquid metals. The reason for this is based on the rate of mechanical work done on the system, where it was initially considered that the temperature dissipation from the sound wave into the medium was negligible. To modify the information listed in Equations (7.16) to (7.24), the change in entropy is now considered to be non-adiabatic and is derived from a linearized, non-viscous form of the general equation for heat transfer, defined as [17]:

$$\rho\, T\, \left(\frac{\partial s}{\partial t} + v \cdot \nabla s\right) = \sigma'_{ik} \frac{\partial v_i}{\partial x_k} + \nabla \cdot (\kappa\, \nabla T) \tag{7.25}$$

where s is the entropy, σ'_{ik} is the shear stress tensor, $\frac{\partial v_i}{\partial x_k}$ is the derivative of the ith velocity with respect to the x_k component, and all other variables retain their previously defined meanings.

Without the viscous terms and neglecting the effects of velocity while linearizing the equation leads to a new form for Equation (7.25) [18]:

$$\dot{s}' = \frac{\kappa}{\rho\, T} \nabla^2 T \tag{7.26}$$

where s' represents the non-viscous, linearized, perturbed entropy, $\dot{s}'$ is the time derivative of this new entropy variable, and all other variables retain their previous definitions.

In the same way that the general equation for heat transfer was simplified, the following two equations were also simplified:

$$\frac{\partial \rho'}{\partial t} + \rho_0 \, \nabla \cdot v = 0 \tag{7.27}$$

$$\frac{\partial v}{\partial t} + \frac{1}{\rho_0} \nabla p' = 0 \tag{7.28}$$

where ρ' is the perturbed density, ρ_0 is the equilibrium density, v is the perturbed fluid velocity, and p' is the perturbed pressure. Neglecting the velocity terms in Equations (7.27) and (7.28) and combining the two equations yields [17, 18]:

$$\ddot{\rho}' = \nabla^2 p' \tag{7.29}$$

where $\ddot{\rho}'$ is the 2nd time derivative of the perturbed density. Using thermodynamic relationships and assuming that the variables of interest are the perturbed temperature, T', and the perturbed pressure, p', the perturbed density, ρ', and the perturbed entropy, s', can be rewritten as:

$$\rho' = \left(\frac{\partial \rho}{\partial T}\right)_p T' + \left(\frac{\partial \rho}{\partial p}\right)_T p' \tag{7.30}$$

$$s' = \left(\frac{\partial s}{\partial T}\right)_p T' + \left(\frac{\partial s}{\partial p}\right)_T p' \tag{7.31}$$

By taking the expansion of T' and p' for a plane wave as the equilibrium value multiplied by a perturbative exponential expansion, $e^{i\,(k\,x - \omega\,t)}$, and knowing a few thermodynamic relationships, the combination of Equations (7.30) and (7.31) will produce:

$$k^4 - k^2 \left(\frac{\omega^2}{C_T^2} + \frac{i\,\omega}{\chi}\right) + \frac{i\,\omega^2}{\chi\, C_s^2} = 0 \tag{7.32}$$

where k is the wavenumber, ω is the frequency, χ is the thermometric conductivity, C_s is the sound speed in the medium, and C_T is a thermally-dampened sound speed given by:

$$C_T^2 = \frac{C_s^2}{\gamma} \tag{7.33}$$

where γ is the ratio of the constant-pressure specific heat to the constant-volume specific heat. The roots of Equation (7.32) can be determined to find the characteristic wavenumber vs. frequency relationship.

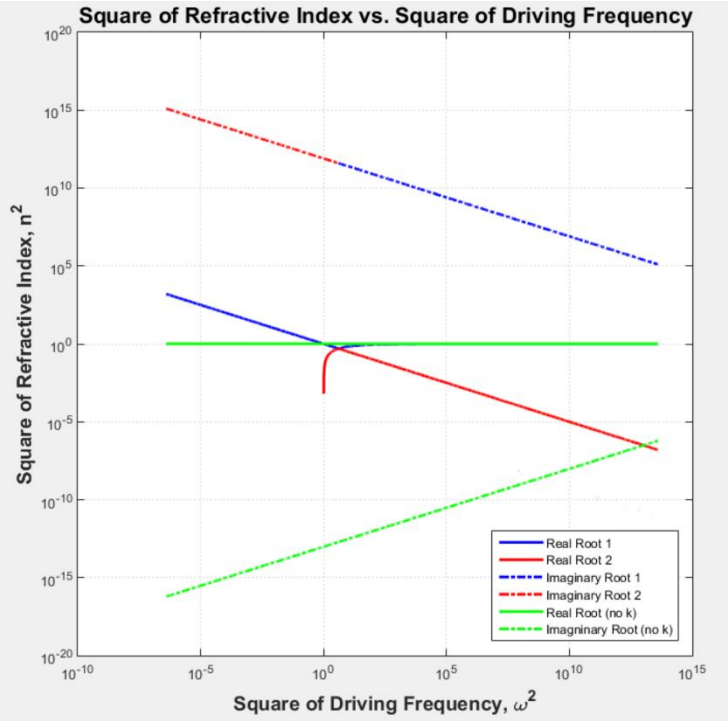

Figure 7.6: A plot illustrating how a high thermal conductivity in lithium affect the branches of propagation in the dispersion relationship. The green lines are the roots from Figure 7.5 superimposed over the roots when considering the high thermal conductivity of lithium.

The dispersion relationships govern how an acoustic wave will affect a given medium; however, the useful information that can be gathered from these relationships is how far out into the medium a wave can propagate before being sufficiently damped. This value will relate how localized the acoustic pressure wave likely is in liquid lithium and will help in determining the pitch between various pressure transducers set up as an array in a far-from-saturated solution of

lithium and hydrogen (or tritrium/deuterium). This information is described by the absorption coefficient, which is related in the imaginary section of the dispersion relationship. To be able to promote growth at distances far from the pressure transducer, the maximum amplitude of the pressure field at the source must be greater than the growth threshold. This will allow for a higher pitch between transducers and a greater overall yield of cavitation/hydrogen in the far-from-saturated lithium solutions.

A concept that was introduced earlier in the chapter was the idea that bubbles at a given equilibrium radius have a natural frequency, ω_N. In his book, Brennen [2] is able to find the natural frequency of an equilibrium bubble by applying the appropriate perturbation theory. The peak frequency, when neglecting thermal effects and liquid compressibility, is defined as [2]:

$$\omega_p = \left[\frac{3\,\eta\,(P_\infty - P_V(T_\infty))}{\rho_l\,R_E^2} + \frac{2\,(3\,\eta - 1)\,\sigma}{\rho_l\,R_E^3} - \frac{8\,\nu_l^2}{R_E^4}\right]^{1/2} \tag{7.34}$$

where ω_p is the peak frequency, $P_V(T_\infty)$ is the liquid vapor pressure at T_∞, and ν_l is the liquid kinematic viscosity. The natural bubble frequency is the point at which there exists zero damping, given by Equation (7.3). The natural bubble frequency defines the response of the bubble to externally applied oscillatory acoustic fields and is thus important in any rectified diffusion study. Resonance with the natural frequency of the bubble causes highly nonlinear effects, such as rapid collapse, explosive growth, and oscillations at subharmonics. A plot illustrating the change in natural bubble frequency with driving frequency is shown in Figure 7.7. The natural frequency seemed to not change much with temperature, concentration, or driving frequency, so this plot is representative of the natural frequency for nearly all variations.

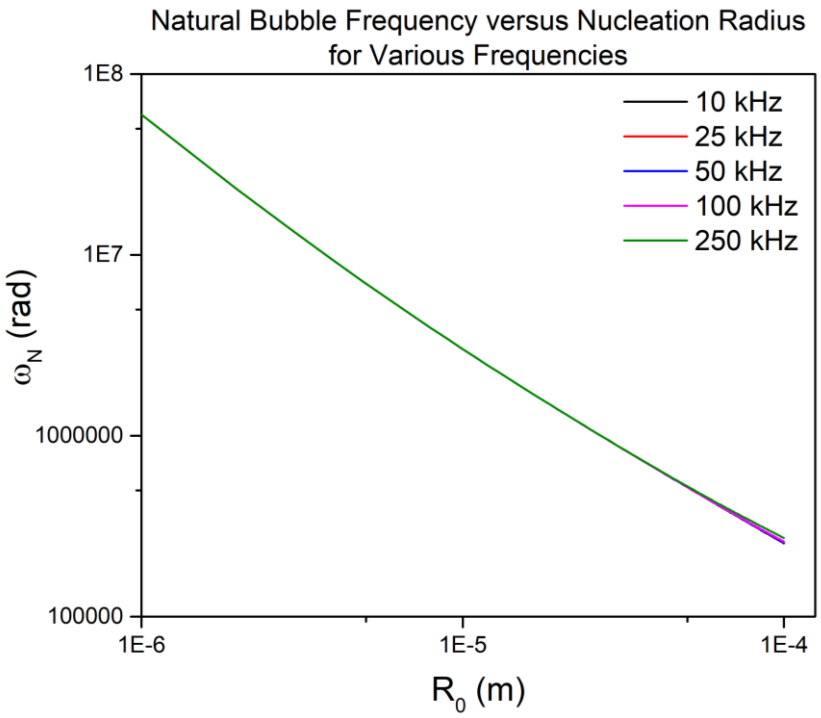

Figure 7.7: A plot illustrating how the natural bubble frequency changes with bubble size and driving frequency. This natural frequency is not greatly affected by changes in solution temperature or the dissolved gas concentration, making this plot representative. For hydrogen in lithium, the natural bubble frequencies for microbubbles is on the order of MHz; however, transient cavitation can be driven by acoustic frequencies much lower than the natural frequency.

From a practical point-of-view the release of hydrogen from the hydrogen-lithium system driven by a combination of heat and acoustic pressure fields should result in a substantial yield of hydrogen gas. As will be explained in detail later, analogous metal systems have seen significant reductions in hydrogen content with the use of heat and ultrasound. The application of these techniques to lithium should be a natural extension from these analogous systems, especially in far-from-saturated solutions. More experimental data is needed to confirm this claim, but theoretically the primary differences between the hydrogen-lithium and analogous hydrogen-metal systems are the liquid properties and chemical reactivity. The liquid metal properties are similar enough between these systems that application to lithium should not require drastic modifications from theory. The time scales associated with reactivity are long enough such that the transient processes in rectified diffusion will not be greatly affected.

As mentioned in previous sections, nucleation bubbles always exist within a liquid volume. Using heat in tandem with acoustic drive is extremely valuable for hydrogen degassing in liquid metals because the use of superheat is a very reliable way to rupture liquid, thereby producing more nucleation sites for cavitation growth. Using heat alone is not as effective as using heat and ultrasonic waves because the ruptures that eventually become vapor bubbles do not necessarily establish concentration gradients that promote hydrogen removal. It is also apparent from previous chapters that removal of hydrogen with the sole application of heat is limited, likely due to the recombination events along the surface that must take place before the diatom can be released. Promoting bubble growth through the combination of boiling and cavitation, however, establishes concentration gradients at the bubble surface within the liquid, along which dissolved gas will flow. Also, the bubble interface serves as a point for recombinative events to occur. Since the surface area is dramatically increased from the formation of many bubbles within the liquid, the limitations imposed by recombination become less drastic during rectified diffusion at elevated temperatures. Taking all of these considerations into account, extension of the established theory to the hydrogen-lithium system should result in higher recovery yields in far-from-saturated solutions.

7.2 Numerical Model and Methodology

As mentioned before, the methodology used to model the growth of an individual cavitation bubble was based on the work accomplished in Ref. 13 – 15. These studies refined earlier works that attempted to look at the process of rectified diffusion and applied the refined model to the process as it pertained to gaseous species dissolved in molten metal castings. The model was not entirely without assumption, however, so the results need to be understood within the context of these assumptions.

The assumptions made when modelling cavitation bubble growth and gas consumption were divided into three primary categories. First, the bubble is assumed to be perfectly spherical and the bubble center is motionless. This assumption is valid only when the time for upward translational for buoyancy forces to dominate is much longer than the time it takes for the cavitation bubble to reach a growth threshold. Meidani [13] related that this is true in most cases. The second assumption is that the bubble gas is thermodynamically uniform and the gas

instantaneously retains all properties except within the diffusion layer near the boundary. Finally, the gas within the bubble is assumed to be ideal, but the heat capacities are temperature-dependent. Essentially, the bubble gas can transfer energy across the boundary, but takes on uniform properties instantaneously.

The governing equations for this process are broken down into a set of coupled ordinary differential equations as functions of time for the gas in the bubble and two diffusion-advection problems for the properties in the liquid immediately adjacent to the bubble. On top of this, the bubble boundary is also constantly in motion, meaning that the boundary conditions must follow along with the boundary. This adds significant complexity to an already complex problem, especially when considering the solutions from the liquid side of the domain.

The most important ordinary differential equation for this system is that which describes how the bubble boundary is modified in time. Mediani [13 – 15] accounted for this by applying an equation of motion for the bubble known as the Trilling equation [19]. The Trilling equation was chosen because it is a modified form of the Rayleigh-Plesset equation [16], but takes into account the compressibility of the liquid [19]. Liquid compressibility becomes important when the gas in the bubble is noncondensable and thermal effects become important. This is especially true when considering that a diffusion layer exists in the liquid near the bubble interface, and that during the rebound phase the bubble radiates a shock wave out and away from the surface. By using the sound speed relationship to replace the derivatives of pressure with respect to the density ($C_s^2 = dP/d\rho$) then the following equation of motion can be used [13 – 15, 19]:

$$\left(1 - 2\,\frac{\dot{R}}{C_s}\right) R\,\ddot{R} + \frac{3}{2}\left(1 - \frac{4\,\dot{R}}{3\,C_s}\right)\dot{R}^2 = \frac{1}{\rho_\infty}\left[P_B(t) - P_{ap} + \frac{R}{C_s}\,\frac{dP_B(t)}{dt}\right] \quad (7.35)$$

where $\dot{R}$ is the bubble expansion velocity, C_s is the sound speed in the liquid, R is the bubble radius, $\ddot{R}$ is the bubble expansion acceleration, ρ_∞ is the far-field density in the liquid (assumed constant at a given temperature), and the bubble pressure acting on the liquid ($P_B(t)$) and the applied pressure (P_{ap}) are given by the following relationships [13 – 15]:

$$P_B(t) = P_g - \frac{2\,\sigma}{R} - \frac{4\,\mu\,\dot{R}}{R} \quad (7.36)$$

$$P_{ap}(t) = P_\infty - P_A \sin(2\,\pi\,f\,t) \quad (7.37)$$

where P_g is the gas pressure within the bubble at a given time, σ is the surface tension of the liquid, μ is the dynamic viscosity of the liquid, P_∞ is the metallostatic pressure head the bubble must overcome, P_m is the acoustic pressure field amplitude, f is the driving frequency in the pressure transducer, and t is time.

The remaining ordinary differential equations describing the gas are two conservation equations and the ideal gas equation of state. Mass conservation for the bubble gas is described by [13 – 15]:

$$\frac{d}{dt}\left(\rho\ \frac{4}{3}\ \pi\ R^3\right) = 4\ \pi\ R^2\ \frac{\partial C}{\partial r}|_{r=R} \tag{7.38}$$

where ρ is the gas density and $\frac{\partial C}{\partial r}|_{r=R}$ is the gradient of the dissolved gas concentration in the liquid at the bubble boundary. The second conservation equation describes conservation of energy for the gas within the bubble and is defined by [13 – 15]:

$$\frac{d}{dt}\left(\rho\ \forall\ C_v\ T_g\right) = -P_B(t)\frac{d\forall}{dt} + 4\ \pi\ R^2\ \kappa_l\ \frac{\partial T_l}{\partial r}|_{r=R} + 4\ \pi\ R^2\ \frac{\partial C}{\partial r}|_{r=R} \tag{7.39}$$

where $\forall$ is the bubble volume, C_v is the constant-volume specific heat of the gas, T_g is the gas temperature, κ_l is the thermal conductivity of the liquid, and $\frac{\partial T_l}{\partial r}|_{r=R}$ is the gradient of the liquid temperature at the bubble boundary. The final equation governing the gas within the bubble is the ideal gas equation:

$$P_g = \frac{\rho\ \Re\ T_g}{M_W} \tag{7.40}$$

where $\Re$ is the universal gas constant and M_W is the molecular weight of the gas.

Equations (7.38) and (7.39) require information about the liquid portion of the domain immediately adjacent to the bubble, in the diffusion layer. Since the liquid properties are not considered uniform, the system is dependent on space as well as time. As such, the concentration in the liquid and the liquid temperature are defined by two separate diffusion-advection problems, which are described by [13 – 15]:

$$\frac{\partial T_l}{\partial t} + V_r\ \nabla T_l = \alpha\ \nabla^2 T_l + \frac{\mu}{\rho_l\ C_{pl}}\ \varphi_\gamma, \quad r > R \tag{7.41}$$

$$\frac{\partial c}{\partial r} + V_r \nabla c = D \nabla^2 c, \qquad r > R \tag{7.42}$$

where V_r is the advection term equivalent to $\frac{R^2}{r^2} \dot{R}$, α is the thermal diffusivity in the liquid, ρ_l is the liquid density (assumed constant for this work), C_{pl} is the liquid constant-pressure heat capacity, φ_γ is the viscous dissipation term equivalent to $12 \frac{V_r^2}{r^2}$, and D is the mass diffusion coefficient. These equations form a set of highly coupled, non-linear differential equations that require implicit schemes for the solution.

The work done by Meidani [13 – 15] used Gear's method of finite differences to solve these coupled differential equations. Essentially, second order finite difference schemes (backward difference in time and central difference in space) were used initially, but were modified to higher order schemes out of necessity when the physics were inadequately captured by the lower order systems. The solution methods used in this work, however, were based on different methods. The diffusion-advection problems were solved using the spherical form of the Crank-Nicholson scheme, while the ordinary differential equations were solved as a state vector system. The entire solution was implicit, in that an initial guess of the bubble expansion velocity was used to solve the diffusion-advection problems and was later solved for from the state vector-Runge Kutta solution in order to define convergence. Generalizing the diffusion and advection terms in Equations (7.41) and (7.42), the Crank-Nicholson scheme takes the forms (in spherical coordinates):

$$v \frac{\partial A}{\partial r} \approx \frac{v}{4\,\Delta r} (A_{i+1}^n - A_{i-1}^n + A_{i+1}^{n+1} - A_{i-1}^{n+1}) \tag{7.43}$$

$$D \frac{1}{r^2} \frac{\partial}{\partial r} \left(r^2 \frac{\partial A}{\partial r} \right) \approx \frac{D}{2\, r_i\, \Delta r} (A_{i+1}^n - A_{i-1}^n + A_{i+1}^{n+1} - A_{i-1}^{n+1}) + \frac{D}{2\,\Delta r^2} (A_{i+1}^{n+1} -$$

$$2\, A_i^{n+1} + A_{i-1}^{n+1} + A_{i+1}^n - 2\, A_i^n + A_{i-1}^n) \tag{7.44}$$

where A is the variable, v is the advection coefficient (V_r in this case), Δr is the radial step, n is the time index, i is the space index, D is the diffusion coefficient, and r_i is the coordinate at index i. Substituting these forms in Equations (7.41) and (7.42), a few constants can be defined as $\alpha = D\, \Delta t / 2\, r_i\, \Delta r$, $\beta = D\, \Delta t / 2\, \Delta r^2$, and $\lambda = v\, \Delta t / 4\, \Delta r$. Using these constants, a spherical diffusion-advection problem with a source can be defined as:

$$\bar{\bar{A}} \cdot \bar{A}^{n+1} = \bar{\bar{B}} \cdot \bar{A}^{n} + \bar{S}\,\Delta t \tag{7.45}$$

where $\bar{\bar{A}}$ is the coefficient matrix for the $n+1$ time step, $\bar{\bar{B}}$ is the coefficient matrix for the n time step, $\bar{A}^{n+1}$ is the solution for the state vector advanced one time step, $\bar{A}^{n}$ is the state vector at the previous time step, and $\bar{S}$ is the source. The $\bar{\bar{A}}$ is defined such that $(1 + 2\,\beta)$ is along the diagonals, $(\lambda - \beta - \alpha)$ is along the first superdiagonals, and $(\alpha - \beta - \lambda)$ is along the first subdiagonals. Conversely, $\bar{\bar{B}}$ is defined such that $(1 - 2\,\beta)$ is along the diagonals, $(\beta + \alpha - \lambda)$ is along the first superdiagonals, and $(\beta + \lambda - \alpha)$ is along the first subdiagonals.

As mentioned before, initial guesses were given for the values of the V_r term (where $V_r = \dot{R}$ at the bubble boundary) and for gas parameters that would influence the boundary conditions at the bubble at each time step. Initial conditions were set such that the bubble gas and the surrounding liquid were in thermal equilibrium and the initial bubble pressure was set such that $P_0 = P_\infty + 2\,\sigma/R_0$. The boundary conditions for the liquid in the far field were set as Dirichlet conditions where the initial temperature, T_0, and the initial dissolved concentration, c_∞, were held constant for the duration of the simulation. The boundary conditions at the bubble were a bit more complicated.

The bubble size changes in time meaning that there exists a complex, moving boundary in this problem. This was captured by using a time-varying radial domain. The bubble size fluctuation is based entirely on the acoustic pressure driver (likely an immersion pressure transducer); however, the interfacial conditions at the boundary are Dirichlet in nature. Dirichlet boundary values are applied to both the concentration and liquid temperature profiles, with the temperature condition being defined by the rate of energy transfer across the bubble boundary [13 – 15]. Following the work done in Ref. 14, the interfacial temperature value is found to be:

$$T_i \approx \frac{T_g + T_0 \sqrt{(k\,\rho\,C_p)_l/(k\,\rho\,C_p)_g}}{1 + \sqrt{(k\,\rho\,C_p)_l/(k\,\rho\,C_p)_g}} \tag{7.46}$$

where T_i is the interfacial temperature, T_g is the gas temperature, T_0 is the initial temperature, k is the thermal conductivity, ρ is the density, C_p is the constant pressure heat capacity, and the subscripts l and g refer to the liquid and gas, respectively.

The interfacial condition for the concentration is different, in that the mass transfer between the gas and liquid has been previously defined for most systems using Henry's law [20]. Henry's law is applicable to gas-liquid systems where the system is in equilibrium and the gases do not chemically interact with the surrounding liquid in which gas species is dissolved. While Henry's law is applicable to most gas-liquid systems at low gas concentrations, liquid metals exhibit behaviors that greatly deviate from expectations for most liquids. In the case of gases in liquid metals (even gas species that are reactive with the metals such as hydrogen and oxygen), Sieverts' law [21] is the applicable analog, which describes equilibrium between the gas pressure directly adjacent to the liquid metal to the dissolved gas concentration within the melt. For the boundary concentration, Sieverts' law is simply given by [13, 15]:

$$c_i = q\sqrt{P_g} \tag{7.47}$$

where c_i is the interfacial concentration (typically reported as mole fraction), q is Sieverts' constant, and P_g is the gas pressure in the layer directly adjacent to the liquid surface (in atm).

Sieverts' law as it pertains to the lithium-hydrogen system was defined by Katsuta [22] in his earlier work defining which helped to define the thermodynamic solubility limits of hydrogen in lithium (and, by extension, deuterium and tritium). Equilibrium physics between the concentration of gas in the dissolved phase and the adjacent gas are summed up within the constant, which was reported by Katsuta to be dependent on temperature in the form [22]:

$$K_S\,[\sqrt{Pa}/(H/Li)] = q^{-1} = 10^{4.92-2.32\times10^3\,/\,T} \tag{7.48}$$

where K_S is the Sieverts' constant in the form defined by Katsuta [22], q is the Sieverts' constant in the form defined by Naji Meidani and Hassan [13, 15], and T is the temperature in K. Another way to determine the Sievert's coefficient is by determining the solubility of hydrogen gas (H_2) in cm^3 per 100 g of lithium and then applying the appropriate weighting based on weight percent. The solubility ratio was found based again on work done by Katsuta [22]:

$$S\left[\frac{cm^3\,H_2}{100\;g\;Li}\right] = 1.6136\times10^5\;\cdot\;(2.02\times10^{-4}\,e^{6.16\times10^{-3}\,T(K)}) \tag{7.49}$$

where S is the solubility of hydrogen in lithium in units of cm^3 H_2 per 100 g of Li. Applying the gas law for appropriate weighting of the solubility, the Sieverts' coefficient in the form presented by Naji Meidani and Hassan is evaluated as [13, 15]:

$$q = 8.9 \times 10^{-5}\, S \tag{7.50}$$

Once the diffusion advection problems were solved, the gradients for the concentration and liquid temperature at the bubble boundary were used to solve the system of non-linear, ordinary differential equations described in Equations (7.34) through (7.39). This was done by using the 'scipy.integrate' python module's built-in 'odeint' function. The inputs to this function used only the state vector values from the previous time step as the initial values. Guesses for the solutions were the same as the guesses for the diffusion-advection problems. The function uses the 'lsoda' method from the FORTRAN library 'odepack' to solve the system of ODEs. The state vector is defined using R, $\dot{R}$, ρ, and T_g, whereas the time derivative of the state vector is defined using $\dot{R}$, $\ddot{R}$, $\dot{\rho}$, and $\dot{T}_g$. As one can plainly see from Equations (7.35) through (7.40) does not exist an equation explicitly for solving for $\dot{R}$ in terms of the other state vector values, so the simulation used the following equation to complete the set of differential equations:

$$\dot{R}_i = \dot{R}_{i-1} + \ddot{R}\, \Delta t \tag{7.51}$$

where Δt is the time step.

Once the solutions for the system of non-linear, ordinary differential equations is found, then the answer for the bubble expansion velocity, $\dot{R}$, is checked against the initial guess for the magnitude of V_r. This check is used as a convergence criterion, such that the entire process is iterative. Upon converging, the simulation exits the loop and starts iterating on the next time step, using the information from the previous time step as the basis for the initial guess values. A diagram illustrating the flow of the simulation is shown in Figure 7.8.

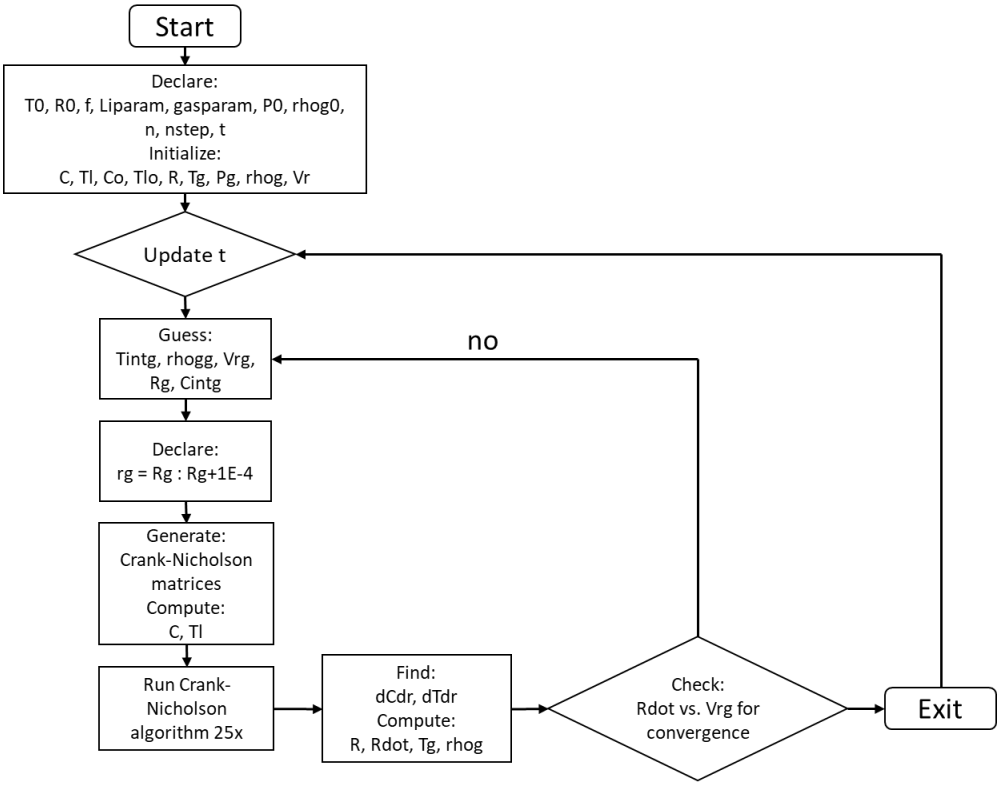

Figure 7.8: A workflow diagram for the rectified diffusion problem simulating hydrogen bubble growth in liquid lithium.

7.3 Results

The results presented in this section will be based on the numerical techniques and formulation described previously, as well as approximate analytical results that relates the maximum bubble radius to real-world parameters in far-from-saturated solutions of hydrogen in lithium. First, the numerical methods, outlined earlier, were verified against the results from similar systems described in Ref. 13 – 15. In matching a variety of these scenarios, the same numerical methods are also indirectly validated, since the work done in Ref. 13 – 15 was validated against experimental results. For the sake of completeness, the results from the methods described herein were also compared to the experimental results reported in Ref. 13 – 15. The numerical techniques were then extended to the lithium-hydrogen system to observe how rectified diffusion could help to remove trapped hydrogen isotopes. Because of the complexity of the problem, it was difficult to follow the simulation out to the point at which an individual bubble would reach its

peak radius at a given metallostatic pressure, so approximate analytical expressions were used to investigate these effects. This complexity will be described later in this section. Finally, the practical application for this type of technique will be discussed in the context of a flowing lithium loop and a distillation column, not unlike that which was described in Chapter 6.

7.3.1 Transient Simulation Results

The first step when looking at the ability of the numerical model to mimic real-world situations is to compare results from a few simplified simulation runs to data reported in literature. This can be done in two ways. The model can be tested against other numerical schemes that describe similar physics. This process is called verification. Second, the model can be tested against experimental data to prove it adequately mimics real-world phenomena. This process is called validation.

In his doctoral dissertation [15], Meidani relates bubble dynamics and talks about the nonlinearities that arise from acoustic radiation propagating through a liquid medium. In doing so, he shows the functionality of a stable bubble which oscillates about some equilibrium radius value. The excitation of subharmonics gives rise to peaks that are not directly correlated with the acoustic wave, which Meidani showed to manifest itself in Figure 7.9. Also in Figure 7.9 are the results from the numerical model in which an air bubble is oscillating in water. The plot from the numerical model is based on a nucleation radius of 0.3 mm, a driving frequency of 38.5 kHz, and an acoustic amplitude of 0.3 times the hydrostatic pressure.

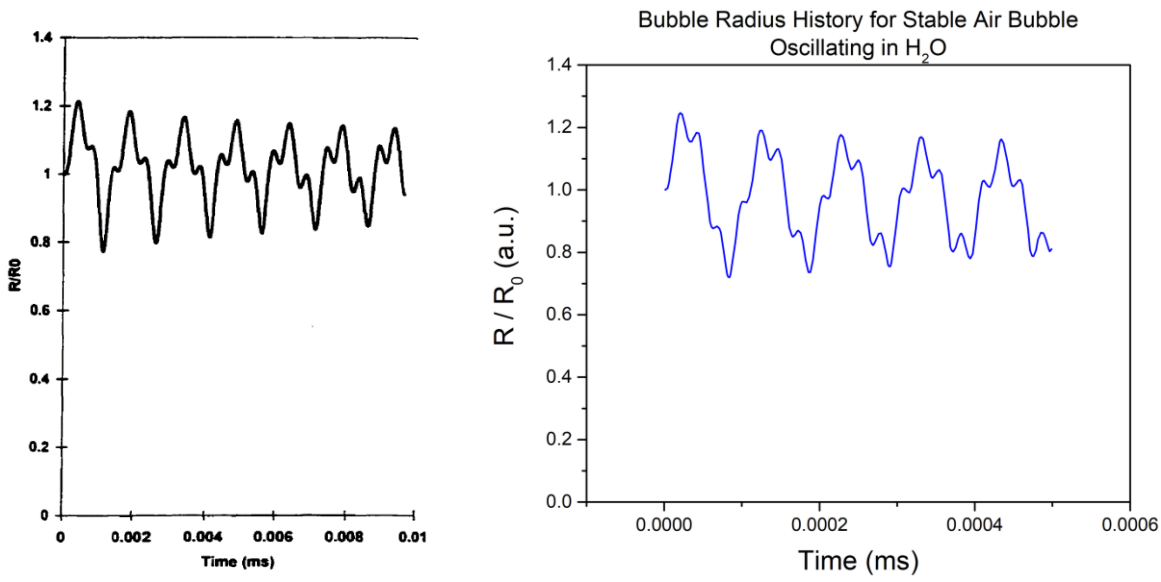

Figure 7.9: (Left) An image of a typical bubble history for a stable cavitating bubble presented in Meidani's doctoral dissertation [15]. (Right) An image of a stable air bubble in water oscillating about an equilibrium radius. This result was evaluated using the numerical model described in this chapter. Nonlinearities in the physics manifest as subharmonic oscillations.

While this result does not directly prove verification of the model, it does support the fact that the simulation is appropriately capturing the nonlinearities in the oscillatory behavior of a stable bubble, albeit over a much broader timescale (this may be due to the driving frequency for Meidani's figure, which is not explicitly stated in Ref. 15). A more apparent verification is illustrated in Figure 7.10, where the bubble radius history and gas temperature for an argon bubble in water are compared between the current model and the numerical method outlined in Ref. 14. The model was set to run with a nucleation radius of 5 mm, an initial temperature of 298 K, and a constant applied pressure of 8 bar (no oscillatory behavior was implemented for this trial).

Distinct differences are noticeable between the two plots in Figure 7.10. First, it appears as if the results from the numerical model are dilated with respect to time when compared with the data reported in Ref. 14. Second, while the amplitudes for both the radius and the temperature seem to be within relatively good agreement, disparities do exist between the two. Finally, the gas temperatures evaluated by the model seem to be plagued by numerical error that will eventually crash the simulation. The reason for these differences can be summed up in two points. First, the

time scales and magnitudes may be skewed since the parameters for the gas evaluated in Ref. 14 are never explicitly stated. Second, the model employed in Ref. 14 also takes into heat supplied by exothermic reactions, which is described in their governing equations. The physics for the transient cavitation model for this chapter did not employ this reactionary heating, which would likely change the bubble dynamics. Regardless, this simplified model appears to capture the physics of the transient cavitation of argon in water quite well.

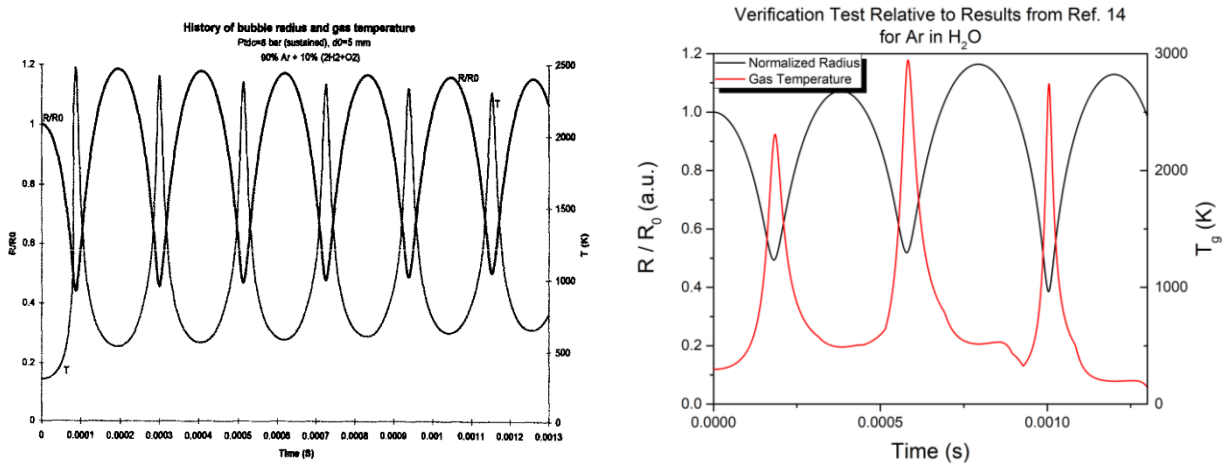

Figure 7.10: (Left) A plot of the bubble radius history and gas temperature for the simulations reported in Ref. 14, where the initial bubble had a 5 mm radius and the applied pressure was sustained at 8 bar. These data assumed the gas was composed of 90 % argon and a 10 % mixture of 2 H_2 + O_2. (Right) A plot of the bubble radius history and gas temperature results from the model reported in this chapter for argon in water, where the initial bubble had a 5 mm radius and the applied pressure was sustained at 8 bar. The initial dissolved gas concentration was assumed to be 90 % of the saturation value.

While discrepancies exist between the current model and results from Ref. 15, the comparison shown in Figure 7.10 illustrates that the current numerical approach adequately captures the complicated physics of transient cavitation. While verification is important, it does not entirely prove that any numerical approach will be able to accurately predict real-world physics. To do this, the model must be compared with experimental data. Unfortunately, little to no data exists where numerical methods have been compared to rectified diffusion in liquid metals because the dynamics of a single bubble are nearly impossible to observe. Because of this, the

current numerical approach was compared against the growth of an air bubble in water, observed in Ref. 13. The numerical approach in Ref. 13, which also looked at transient cavitation and rectified diffusion of hydrogen in liquid metals, was benchmarked against these results. A plot showing how the current model and the model proposed in Ref. 13 compare against the growth of an air bubble in water is shown in Figure 7.11, where the nucleation bubble size was observed to be 0.3 mm, the driving frequency of the acoustic radiator was set to 38.5 kHz, and the acoustic pressure field amplitude was set to 0.9 bar. Relatively good agreement exists between the current model and the model from Ref. 13; however, some discrepancies do exist between both models and experimental observations. Both models predict faster growth than what was empirically observed, meaning that the dampening effects that inhibit growth are stronger than what was initially predicted.

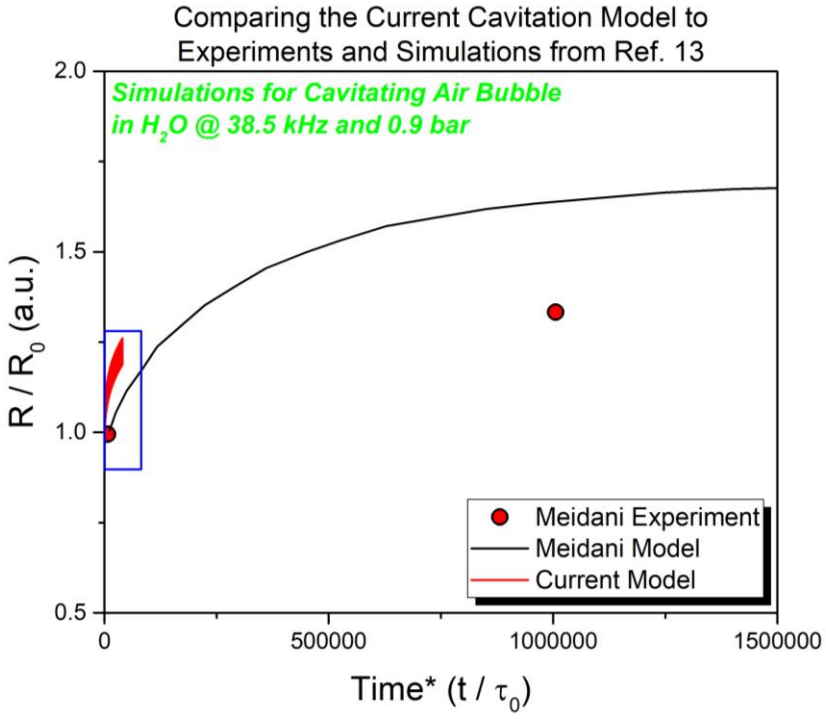

Figure 7.11: A comparison between the current model, the model of Ref. 13, and experiments in Ref. 13 which observed the single bubble dynamics for air in water. The blue box highlights the section of comparison. The current model is quite computationally intensive, so it was difficult to extend the results beyond this section. The abscissa is plotted as a normalized time variable, where the normalization factor is the acoustic period.

Since the model has been shown to be able to adequately capture the physics of cavitation growth, focus was then shifted to the application to the hydrogen-lithium system. The results from a simulation investigating the transient growth of hydrogen in lithium is shown in Figure 7.12. The acoustic frequency was set to 25 kHz, while the pressure amplitude was set to 1.1 times the metallostatic pressure head in the liquid at a depth of 1 inch. The liquid temperature was set to 400 °C, while the initial nucleation radius was set to 15 μm. The results in Figure 7.12 are very nearly what is expected from most systems, but a few features of interest arose as the simulation progressed. First, the excitation of subharmonics from the nonlinearities in the system, described as an expected occurrence by Brennen [2], are evident as the bubble undergoes growth. Second, real-world phenomena measured in Ref. 3 – 12 are mimicked in the results, in that the bubble seems to undergo a rapid collapse during the transient growth phase. Typically, this is followed by extremely explosive growth, but the simulation methodology was not robust enough, even at time steps less than 1 nanosecond, to capture this phenomenon. This behavior is different from the air-water system because the properties of liquid metals are radically different than those of common liquids. For instance, the surface tension and thermal properties of lithium are significantly higher than those for water, which greatly impact the bubble dynamics. As such, other methods were employed to evaluate the hydrogen bubble once it had reached a maximum, steady-state radius. A sequence of images illustrated bubble growth and collapse is shown in Figure 7.13.

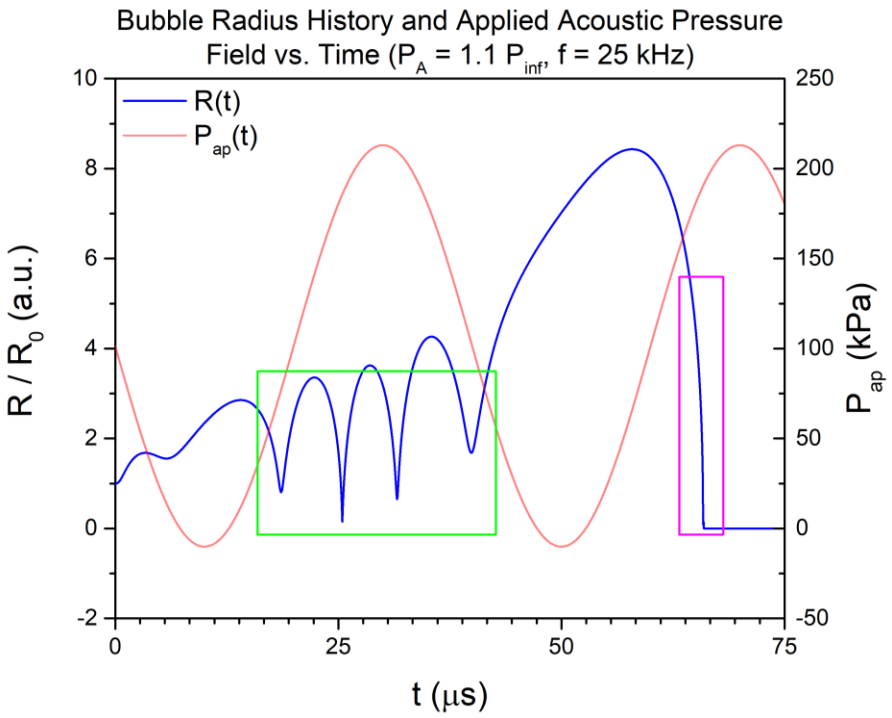

Figure 7.12: An image of the results pertaining to the bubble history and applied pressure for a hydrogen bubble (R_0 = 15 μm), oscillating at a frequency of 25 kHz. These conditions pertain to parameters near the threshold for cavitation. The green box illustrates the excitation of subharmonics due to the nonlinearities in the system [2], and the magenta box shows the point at which the bubble appears to fully collapse but will be followed up by a real-world explosive expansion. The actual collapse is a real discontinuity observed in many studies [2 – 12], but the physics beyond this point were difficult to model since the solution method was unable to recover from the discontinuity.

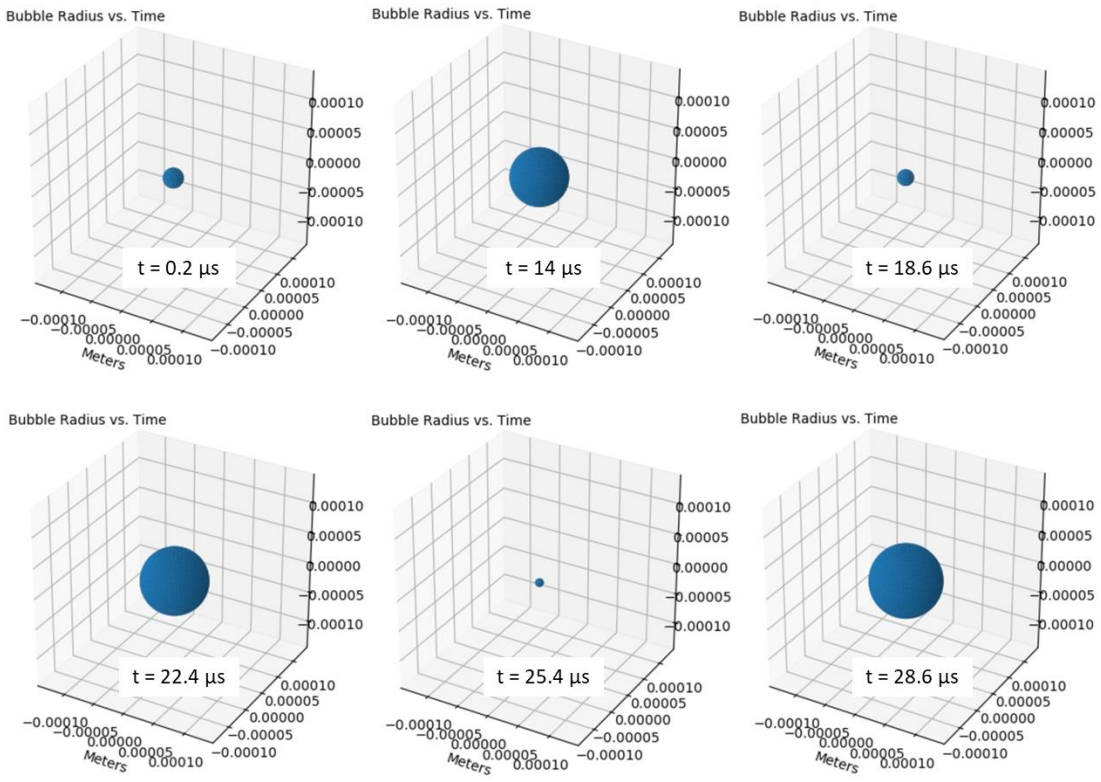

Figure 7.13: A sequence of images illustrating a cavitating hydrogen bubble in liquid lithium as it goes through different phases of expansion and collapse. Collapse is followed up by rapid rebound, the result of which is a shock wave that propagates into the liquid medium. Once a resonance radius is reached, a catastrophic collapse will occur followed by explosive growth where the bubble expands to many times its original size.

To put Figures 7.12 and 7.13 in practical context, the results must be explained with regards to what would happen in the real-world system. Figure 7.12 is unable to capture what would happen after approximately 70 μs, but the bubble will then undergo explosive growth, where, after a very short time, the bubble will oscillate stably about a new, larger equilibrium radius. The size of this new equilibrium radius will be explored in the next sub-section, but it is dependent on parameters such as the initial nucleation bubble radius, the driving frequency, and the acoustic amplitude. It is at this new equilibrium size, and these time scales, that the bubble will then be driven to the surface and rupture, releasing the captured hydrogen. As such, buoyancy forces for long-term processes must be taken into account and will be re-examined later.

7.3.2 Steady-State and Maximum Size Results

While the results described above focused primarily on how a hydrogen cavitation bubble in a far-from-saturated solution of lithium will expand, the simulations used were computationally intensive and were only able to show rectified diffusion in a portion of the transient stage. The knowledge desired is what size the bubble grows to once it reaches an equilibrium condition, and, by extension, how much hydrogen has been consumed by an individual bubble by the time this equilibrium is reached. In a simplified approach to this problem, Brennen [2] broke the maximum bubble radius into two thresholds: that where the driving frequency was much less than the natural frequency and that where the driving frequency is much greater than the natural frequency. Assuming a 15 micron hydrogen bubble in lithium, the natural frequency (illustrated in Figure 7.7) of the bubble is greater than 2 MHz. A driving frequency of 25 kHz puts the system in the first of the two aforementioned regimes, meaning that the Rayleigh-Plesset equation needs to be solved to the point where the bubble expansion velocity, $\dot{R}$, goes to zero. Before going through this complicated process, one can explore the maximum bubble radius for the second regime [2]:

$$R_M = f(\beta)\ \frac{\pi}{\omega}\ \left[\frac{P_A - P_\infty}{\rho_l}\right]^{1/2} \tag{7.52}$$

where:

$$f(\beta) = \left(\frac{4}{3\,\pi}\right)\ (2\,\beta)^{\frac{1}{2}}\ \left[1 + \frac{2}{3\ (1-\beta)}\right]^{1/3} \tag{7.53}$$

$$\beta = 1 - \frac{P_\infty}{P_A} \tag{7.54}$$

P_A – amplitude of acoustic pressure field

P_∞ – pressure of the liquid in the far-field (metallostatic pressure)

In this case, the maximum bubble radius is only dependent on the pressure amplitude, the metallostatic pressure head, the driving frequency, and the liquid density. With these parameters in mind, Figures 7.14, 7.15, and 7.16 were generated. It is important to note here that these values are very approximate, whereas solving the Rayleigh-Plesset equation [16] up to the point where $\dot{R}$ goes to zero will result in a much more accurate result for the maximum bubble radius. In all cases, except for the trends with respect to pressure amplitude, the pressure was set for 1.1 times the equilibrium pressure.

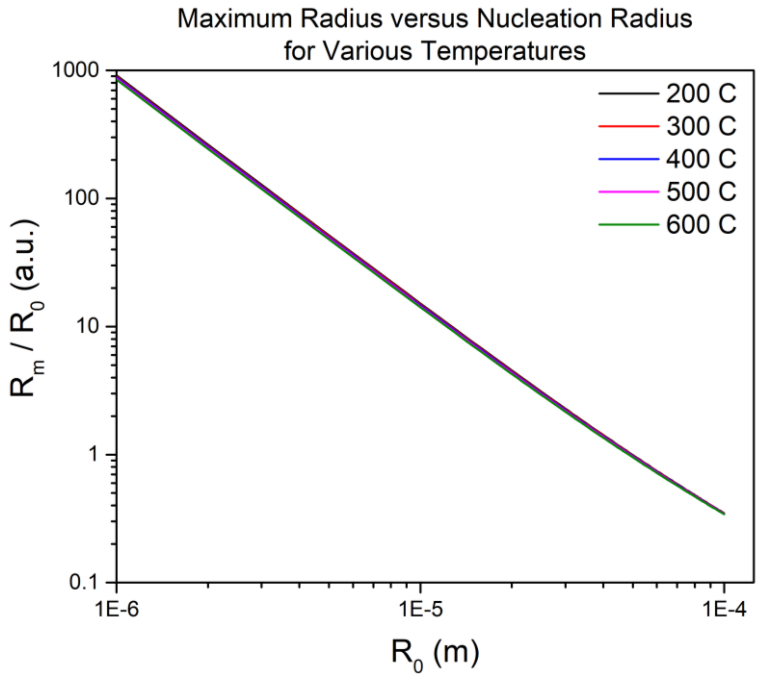

Figure 7.14: Maximum bubble radius values normalized to the initial nucleation bubble radius for various temperatures evaluated using Equation (7.52) [2].

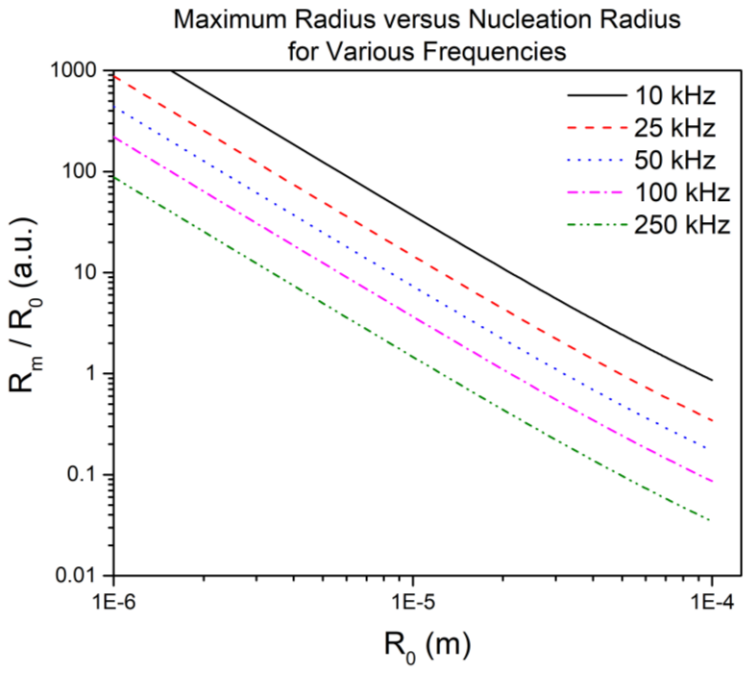

Figure 7.15: Maximum bubble radius values normalized to the initial nucleation bubble radius for various frequencies evaluated using Equation (7.52) [2].

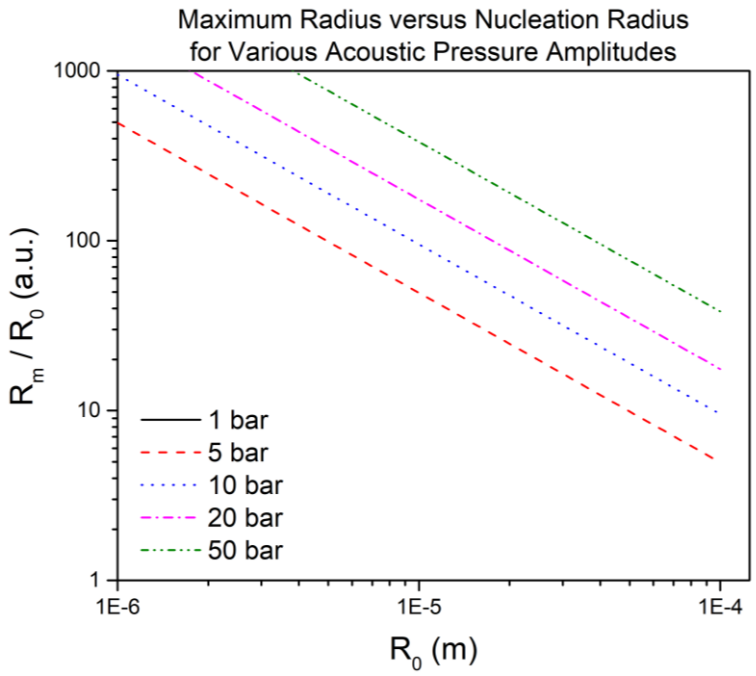

Figure 7.16: Maximum bubble radius values normalized to the initial nucleation bubble radius for various acoustic pressure amplitudes evaluated using Equation (7.52) [2]. Results for a P_A of 1 bar are not observed because this value is below the critical pressure, P_C, for growth.

While the information in Figures 7.14, 7.15, and 7.16 is only based on a few operating parameters, it gives an order-of-magnitude estimate for how large a hydrogen bubble in lithium may grow under certain acoustic pressure conditions. Under these assumptions, the bubble will expand to anywhere between 10 and 100 times its original size, depending on the acoustic parameters and the nucleation bubble radius. As mentioned in the paragraph preceding this analysis, a more accurate way for determining the maximum bubble size is to solve the full Rayleigh-Plesset equation, along with the thermal energy equation and the mass conservation equation for the bubble gas. Following the work of Hilgenfeldt [23], Louisnard [24] found an approximate solution for the maximum bubble size more robust than that which was previously proposed. By neglecting the gas pressure, radiation, and viscous terms during the expansion phase, an approximate analytical form for the maximum bubble radius was found as [24]:

$$\frac{R_M}{R_0} = f(p, x_M) + g(p, x_M)\left[1 - \frac{4}{9\sqrt{3}}\frac{\alpha_s}{p-1}\right]\frac{R_{res}^2}{R_0^2} \tag{7.55}$$

where:

$$f(p, x_M) = \zeta^2\left[1 + 2\left(x_M + x_+\right)\right] \tag{7.56}$$

$$g(p, x_M) = \frac{2}{3}\left[2 - p\cos x_M - \frac{1}{2}\left(x_M^2 - x_+^2\right) + \frac{1}{3}\left(p\sin x_+ - x_+\right)\left(x_M + 3\,x_+\right)\right] \tag{7.57}$$

$$x_M = \frac{\pi}{2} + \frac{\sqrt{1 + p\left(Q(p) - \pi\,\zeta^2\frac{R_0^2}{R_{res}^2}\right) - 1}}{p} \tag{7.58}$$

$$Q(p) = 2\,p + \frac{2}{3}\left(p\sin x_+ - x_+\right) \tag{7.59}$$

$$\alpha_s = \frac{2\,\sigma}{P_\infty\,R_0} \tag{7.60}$$

$$R_{res} = \sqrt{\frac{3\,P_\infty}{\rho_l\,\omega^2}} \tag{7.61}$$

$$x_+ = \arccos\frac{1}{p} \tag{7.62}$$

$$p = \frac{P_A}{P_\infty} \tag{7.63}$$

P_∞ – metallostatic pressure head

ζ – constant typically set to 1.6 [23]

While the approximation in Equation (7.55) is more robust than that which is listed in Equation (7.52) in that it includes the effects that nonlinearities have on bubble growth, it does not take into account the initial concentration of dissolved gas and how this parameter affects growth. Hilgenfeldt's approximation [23] assumes a mixture at or near saturation, so the maximum growth may be dampened by the lack of mass transfer across the bubble interface. This means that the maximum radii are likely less than what is predicted by Equation (7.55). The plots in Figure 7.17 illustrate the maximum bubble radius evaluated using Hilgenfeldt's [23] and Louisnard's [24] approximation for varying acoustic amplitude, driving frequency, and nucleation bubble size. For both plots, the initial equilibrium temperature was assumed to be held at 400 °C and the

metallostatic pressure head was calculated for 1 inch below the lithium surface. Interesting discontinuities were observed in the trends for radius values that approached the resonant radius and frequencies that approached the natural bubble frequency.

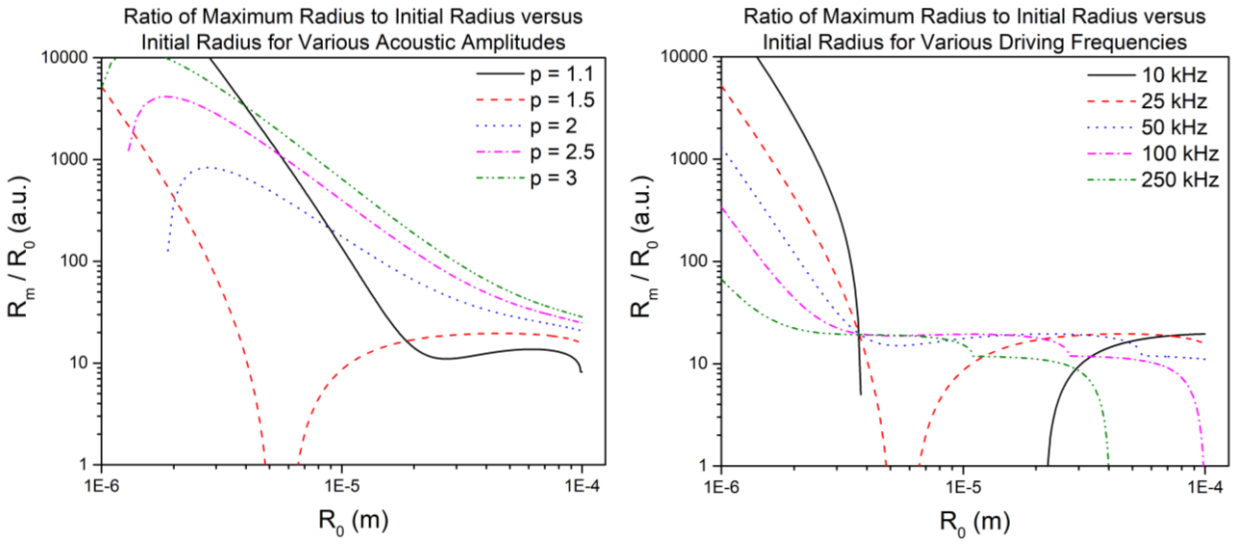

Figure 7.17: (Left) The maximum bubble radius normalized to the nucleation bubble radius as a function of nucleation bubble radius at various acoustic pressure amplitudes. In all cases, the driving frequency was set to 25 kHz. (Right) The maximum bubble radius normalized to the nucleation bubble radius as a function of nucleation bubble radius at various acoustic pressure amplitudes. In all cases, the acoustic pressure amplitude was set to 1.5 times the metallostatic pressure head. The nonlinearities are more accurately captured in this approximation; however, the effects of dissolved concentration are eliminated and the solutions are assumed to be at or near saturation.

For practical considerations, it is likely that a piezoelectric pressure transducer will be able to oscillate between 10 and 50 kHz and the acoustic field generated by the transducer oscillations will be able to provide localized field amplitudes that range between 1 and 1.5 times the metallostatic pressure head. This means that looking at the red dashed lines in both plots that the bubbles will likely grow between 10 and 20 times their original size, given that most nucleation bubbles exist at or less than 10 micrometers in size [25]. Most nucleation bubble radii will exist in equilibrium in the melt at or below 10 micrometers. Using the associated approximate analysis,

the time it takes for this maximum size to be achieved is on the order of 1 to 3 seconds. This was taken into account in the x_M variable, which is the time to reach maximum size.

7.3.3 Practical Application and Future Experimental Validation

The results listed previously lay out the theoretical groundwork from which the practical application of ultrasonic degassing may be integrated into hydrogen recovery schemes, such as the distillation column described in the previous chapter. While ultrasonic degassing alone has been observed to remove dissolved gases in appreciable amounts [26, 27], the combination of heat and a cavitating acoustic force has been shown to reduce dissolved concentrations in light metals such as aluminum and magnesium by greater than 50 % [27 – 29]. On top of these two driving forces, the degassing effects of reduced pressure has also shown to improve this reduction [27], allowing for up to and greater than an 80 % reduction in dissolved hydrogen in a molten aluminum alloy. Ref. 26 also related how heat will affect the reduced-pressure degassing process, with higher heats and lower vacuum levels relating to the greatest observable reduction in dissolved hydrogen content. These experimental observations lend credibility to the use of this technique to supplement the distillation column, but extension to the hydrogen-lithium system requires a bit more evaluation.

First, the total hydrogen mass that can be consumed by an individual bubble needs to be evaluated. In doing so, one must first look to the maximum radius to which a bubble can grow. From Figure 7.17 and assuming the nucleation bubble radius is 10 μm, the driving frequency is 25 kHz, and the acoustic amplitude is 1.5 times the value of the metallostatic pressure head (evaluated to be slightly greater than 1 atm at a depth of 1 inch), then the maximum radius the bubble will grow to will be on the order of 0.1 mm or greater. Based on the work of Hsieh and Plesset, the expectation value for the rate of mass transfer into the bubble is given by [30]:

$$\langle \dot{m} \rangle = \frac{8\,\pi}{3}\, D\, c_\infty\, R_0\, \left(\frac{P_A}{P_0}\right)^2 \tag{7.64}$$

where $\langle \dot{m} \rangle$ is the expectation value for the mass transfer, D is the diffusion coefficient for hydrogen in lithium, c_∞ is the dissolved concentration in equilibrium with the metallostatic pressure, P_0, R_0 is the equilibrium radius, and P_A is the acoustic pressure amplitude. Knowing that the radius

expands to approximately 10 times the nucleation radius, the amount of mass transferred to an individual bubble during rectified diffusion growth would be on the order of 1000 times the initial hydrogen mass. While this means an individual bubble will be able to capture and evolve hydrogen on the part-per-billion scale, what really defines the total amount of hydrogen that can be degassed in far-from-saturated solutions is the bubble number density.

In order to remove hydrogen on scales similar to the dissolved concentrations in far-from-saturated solutions, the bubble number density must approach 10^6, such that the total mass removed nears the amount dissolved. Brennen relates a homogeneous nucleation site production rate in the form [2]:

$$J = J_0 e^{-Gb} \tag{7.65}$$

where:

$$J_0 = N \sqrt{\frac{2\,\sigma}{\pi\, m}} \tag{7.66}$$

$$Gb = \frac{W_{CR}}{k\,T} \tag{7.67}$$

$$W_{CR} = \frac{16\,\pi\,\sigma^3}{3\,(\Delta P_C)^2} \tag{7.68}$$

N – liquid number density

σ – liquid surface tension

m – mass of an individual molecule

ΔP_C – liquid tension

In a completely ideal liquid, there do not exit imperfections that act as typical nucleation sites, except for at the solid-liquid boundary of the container. However, the presence of heat aids in generating nucleation sites, thereby increasing the probability that a nucleation bubble of critical radius will be forced to undergo transient cavitation growth. Because both phenomenon are very difficult to quantify, evaluating the bubble number density also proves quite challenging. Work done in Ref. 27 – 29 and Ref. 31 prove that removal of dissolved gases in molten metals will approach values necessary for the hydrogen-lithium system.

The third consideration for the practical application of this method is how many pressure transducers are required for optimal degassing. Work done earlier in the chapter was related to how an acoustic wave propagates through a liquid medium and was based on the theory provided by Landau and Lifschitz [17]. Kobayashi [25] arrived at a similar result and found the acoustic attenuation coefficient to be similar in functionality to that described in Equation (7.24). With the knowledge that the acoustic intensity falls off as $\exp(-2\,a\,\omega^2\,x)$, where x is distance, then the acoustic intensity falls to one half its original value in approximately 4 x 10^7 m, meaning that acoustic damping in the medium can be ignored. The pitch, however, is still important, since Xu [27] found that growth and transport is localized to areas near the ultrasonic radiator, which is why his group also looked at using inert gases as a means for more efficient degassing and transport. In doing so, it is likely the pitch between transducers be on the order of 1 to 10 centimeters to prevent bubbles from re-dissolving.

One final factor that must be taken into account is the effect buoyancy has on bubble growth, and how the bubble will travel through the liquid to rupture at the surface. The transport of gas within the bubble through the liquid is important because it relates how long the acoustic pressure field will be affecting bubble growth. As such, the characteristic transport time and velocities are also important quantities. Using the terminal velocity correlation defined by Jamialahmadi [32] for low density liquids, the terminal rise velocity for a 10 μm hydrogen bubble in liquid lithium at 400 °C is approximately 0.4 mm s^{-1}. This value holds across a broad temperature range. By comparison, the same correlation reveals that a 100 μm bubble hydrogen bubble in liquid lithium at 400 °C is approximately 3 cm s^{-1}. This means that a bubble has ample time to reach its maximum radius within the bulk lithium, but as it approaches this size it will quickly transport to the surface and rupture, releasing the absorbed hydrogen.

To test the validity of the claims laid out in this chapter, future experimental investigations into the efficacy of ultrasonic degassing of hydrogen from lithium must be carried out. In his findings, Xu [27] found that temperature had a profound impact on degassing efficiency, meaning that the integration of a piezoelectric transducer into the distillation column described in Chapter 6 will act as the perfect test bed for this combined technique. What should be done is that a normal degassing run with a pre-determined mixture of Li and LiH be carried out using heat as the sole driver for evolution. A second test with a mixture of the same chemical makeup should be carried

out and heated in a similar fashion, only the second run will pulse the transducer during the heating process to observe any shift in partial pressures registered by the RGA. Multiple runs will then be carried out while varying the pulse length, the temperatures corresponding to each pulse, the acoustic frequency, and the acoustic amplitude. The combination of heat, ultrasound, and vacuum should all help drive hydrogen evolution in far-from-saturated solutions beyond what would normally be achievable using heat and vacuum alone. An enhancement in hydrogen degassing of more than 50 % has been measured in similar systems [28 – 29, 31], which may actually allow the peak fluxes from the α phase described in Chapter 5 to approach values on the order of the wall losses described in Krasheninnikov's work [33].

Taking into account all of the information presented in this chapter, it is estimated that the rate at which hydrogen can be evolved from far-from-saturated solutions using an ultrasonic radiator in the distillation column will be enhanced by 50 % or more. Assuming the peak release flux from the α phase measured in Chapter 5 at approximately 8 x 10^{20} H_2 m^{-2} s^{-1}, then the appropriate application of acoustic drive should result in an enhanced rate, with an added 4 x 10^{20} H_2 m^{-2} s^{-1} or more. This means, conservatively, that the enhanced release flux should be nearly 1.2 x 10^{21} H_2 m^{-2} s^{-1}, which equates to 2.4 x 10^{21} H m^{-2} s^{-1} stoichiometrically. This conservative value is within 20 % of balancing the loss flux evaluated from Krasheninnikov's work [33]. Further optimization may be applied to improve upon this estimate, so that evolution using the combination of heat and acoustic drive under vacuum will be able to balance in-vessel losses.

7.4 Conclusions and Future Work

The goal of this chapter was to investigate the theory for a technique that could supplement the removal of hydrogen from hydrogenated solutions of lithium in systems where heat is used as the sole impetus for recovery. To be clear, this technique is proposed in an effort to aid in the recovery of hydrogen in far-from-saturated solutions (where the atomic concentration of hydrogen is at or below the solubility threshold). Also, ultrasonic degassing alone will not be suitable to remove quantities of hydrogen that balance losses within the reactor vessel. It is because of these reasons, the author proposes that ultrasonic degassing techniques be integrated into the distillation column described in Chapter 6 of this report.

7.4.1 Conclusions

This chapter focused on laying the theoretical groundwork for thermally-assisted ultrasonic degassing of hydrogen from lithium. In essence, the most pertinent conclusions from this study can be summed up in the following bullet points:

- The theory of rectified diffusion for degassing of liquid metals was investigated and extended to the hydrogen-lithium system.
- Critical acoustic pressure amplitudes were evaluated for the hydrogen-lithium system based on the work outlined in Brennen's book, *Cavitation and Bubble Dynamics* [2].
- A numerical simulation method was developed to investigate the transient effects that acoustics played on the growth and decay of an individual hydrogen bubble in liquid lithium. The goal for this simulation was to find the maximum bubble radius a hydrogen bubble would grow to for a given set of initial parameters; however, nonlinearities present in governing equations (and in the real-world phenomena) gave rise to discontinuities that were unable to be temporally resolved, even with very fine time steps.
- The numerical method was verified against results presented in Ref. 14 and 15 for the air-water and argon-water systems. Discrepancies between results are likely due to slightly different physical models that were employed.
- Practical information was evaluated based on a number of approximate analytical solutions. This information included, but was not limited to: maximum bubble radius, the mass of hydrogen consumed by an individual bubble, and the acoustic dampening in liquid lithium.
- Future validation experiments were described in detail. An ultrasonic radiator is proposed to be used in tandem with the distillation column described in Chapter 6.

7.4.2 Future Work

- The simulation should be re-visited to look at the validity of the underlying physical model. Portions of the governing equations may overcomplicate the problem unnecessarily.
- More effort should be placed in verifying and validating the model, especially once experimental results for the hydrogen-lithium system have been obtained.

- Validation experiments should be carried out within the distillation column described in Chapter 6. A basic procedure for these experiments was outlined in the final paragraph of the Results section.

7.5 References

[1] M. Ono, R. Majeski, M.A. Jaworski, Y. Hirooka, R. Kaita, T.K. Gray, R. Maingi, C.H. Skinner, M. Christenson, D.N. Ruzic, "Liquid lithium loop system to solve challenging technology issues for fusion power plant", *Nucl. Fusion* 57 (2017) 116056.

[2] C.E. Brennen, *Cavitation and Bubble Dynamics*, New York, NY: Cambridge University Press, 2014.

[3] F.G. Blake, "The tensile strength of liquids; a review of the literature", *Harvard Acou. Res. Lab. Rep. TM9* (1949).

[4] M.S. Plesset and T.P. Mitchell, "On the stability of the spherical shape of a vapor cavity in a liquid." *Quart. Appl. Math.* 13 (1956) 419.

[5] A. Eller and H.G. Flynn, "Rectified Diffusion during Nonlinear Pulsations of Cavitation Bubbles", *J. Acoust. Soc. Amer.* 37 (1965) 493.

[6] L.A. Crum, "Measurements of the growth of air bubbles by rectified diffusion", *J. Acoust. Soc. Amer.* 68 (1980) 203.

[7] L.A. Crum, "Rectified diffusion", *Ultrasonics* 22 (1984) 215.

[8] F.R. Young, *Cavitation*, New York, NY: McGraw-Hill Book Company, 1989.

[9] D. Frost and B. Sturtevant, "Effects of ambient pressure on the instability of a liquid boiling explosively at the superheat limit", *ASME J. Heat Transfer* 108 (1986) 418.

[10] T.B. Benjamin and A.T. Ellis, "The collapse of cavitation bubbles and the pressures thereby produced against solid boundaries", *Phil. Trans. Roy. Soc., London, Ser. A* 260 (1966) 221.

[11] W. Lauterborn and H. Bolle, "Experimental investigations of cavitation bubble collapse in the neighborhood of a solid boundary", *J. Fluid Mech.* 72 (1975) 391.

[12] M.S. Plesset and A. Prosperetti, "Bubble dynamics and cavitation", *Ann. Rev. Fluid Mech.* 9 (1977) 145.

[13] A.R. Naji Meidani and M. Hasan, "A study of hydrogen bubble growth during ultrasonic degassing of Al-Cu alloy melts", *J. Mater. Process. Technol.* 147 (2004) 311.

[14] A.R. Naji Meidani and M. Hasan, "A numerical study of the complex dynamic behavior of a reactive gas bubble in water", *Appl. Math. Modelling* 21 (1997) 127.

[15] A.R. Naji Meidani (2001). A Study of Bubble Dynamics and Some Metals Processing (Doctoral Dissertation). McGill University, 2001.

[16] M.S. Plesset, "The dynamics of cavitation bubbles" *ASME J. Appl. Mech.* 16 (1949) 228.

[17] L.D. Landau and E.N. Lifshitz, *Fluid Mechanics*, trans.: J.B. Skyes and W.H. Reid, Elmsford, N.Y.: Pergamon Press, 1987.

[18] M.A. Isakovich, "On the propagation of sound in emulsions", *Zh. Eksp. Teor. Fiz.* 18 (1948) 907.

[19] L. Trilling, "The collapse and rebound of a gas bubble", *J. Appl. Phys.* 23 (1952) 14.

[20] W. Henry, "Experiments on the quantity of gases absorbed by water, at different temperatures, and under different pressures", *Phil. Trans. R. Soc. Lond.* 93 (1803) 29.

[21] A. Sieverts, "The Absorption of Gases by Metals", *Zeitschrift für Metallkunde* 21 (1929) 37.

[22] H. Katsuta, T. Ishigai, and K. Furukawa, "Equilibrium Pressure and Solubility of Hydrogen in Liquid Lithium", *Nucl. Technol.* 32 (1977) 297.

[23] S. Hilgenfeldt, M.P. Brenner, S. Grossman, and D. Lohse, "Analysis of Rayleigh Plesset dynamics for sonoluminescing bubbles", *J. Fluid Mech.* 365 (1998) 171.

[24] O. Louisnard and F. Gomez, "Growth by rectified diffusion of strongly acoustically forced gas bubbles in nearly saturated liquids", *Phys. Rev. E* 67 (2003) 036610.

[25] M. Kobayashi, C. Kamata, and K. Ito, "Cold Model Experiments of Gas Removal from Molten Metal by an Irradiaation of Ultrasonic Waves", *ISIJ International* 37 (1997) 9.

[26] E.A. Hiedemann, "Metallurgical effects of ultrasonic waves", *J. Acoust. Soc. Amer.* 26 (1954) 831.

[27] H. Xu, Q. Han, and T.T. Meek, "Effects of ultrasonic vibration on degassing of aluminum alloys", *Mater. Sci. Engrg. A* 473 (2008) 96.

[28] G.I. Eskin, "Cavitation mechanism of ultrasonic melt degassing", *Ultrasonics Sonochemistry* 2 (1995) S137.

[29] G.I. Eskin, "Influence of cavitation treatment of melts in the processes of nucleation and growth of crystals during solidification of ingots and castings from light alloys", *Ultrasonics Sonochemistry* 1 (1994) 59.

[30] D.-Y. Hsieh and M.S. Plesset, "Theory of rectified diffusion of mass into gas bubbles", *J. Acoust. Soc. Amer.* 40 (1966) 106.

[31] T.T. Meek, Q. Han, and H. Xu, “Degassing of Aluminum Alloys Using Ultrasonic Vibration”, *Oak Ridge Final Technical Report No. ORNL/TM-2006/61* (2006).

[32] M. Jamialahmadi, C. Branch, and H.N. Steinhagen, “Terminal bubble rise velocity in liquids”, *Chem. Eng. Res. Des.* 72(A) (1994) 119.

[33] S.I. Krasheninnikov, L.E. Zakharov, G.V. Pereverzev, “On lithium walls and the performance of magnetic fusion devices”, *Phys. of Plasmas* 10 (2003) 1678.

CHAPTER 8: CONCLUSIONS AND FUTURE WORK

The primary goal of this thesis was to investigate the fundamental phenomena that drive retention and recovery of hydrogen isotopes in lithium. In all cases, hydrogen was used as the surrogate species for the fusion reactor fuel species of deuterium and tritium. While many studies have been conducted to answer the questions surrounding tritium retention in both solid and liquid lithium, very little effort has been dedicated to the back-end process of recovering and recycling trapped tritium back into the reactor. The focus of this work surrounded this back-end process. Of specific interest was the knowledge of if heat-driven recovery methods could adequately balance tritium loss to lithium walls within a reactor.

In order to reach the standard for reactor recovery, a number of laboratory-scale experiments were conducted to obtain better insight into the fundamentals that govern tritium retention and release. These experiments were conducted on a number of different machines to investigate phenomena such as the thermal decomposition of lithium hydride, the retention of hydrogen in lithium under different plasma or neutral exposure conditions, and the evolution rates from saturated and sub-saturated solutions of hydrogen in lithium. The reason for this division of work was based on necessity, where each sample type was selected to mimic solutions from different lithium loop/pre-treatment scenarios. These studies were necessary to fill in the knowledge gaps left by earlier groups when studying the lithium-lithium hydride, lithium-lithium deuteride, and lithium-lithium tritide systems. In all case studies, it was assumed that the upstream purification technologies in any hypothetical liquid lithium loop system will be sophisticated enough to remove extraneous lithium impurities, such as lithium hydroxide, lithium oxide, lithium nitride, lithium carbonate, and others.

The benefits of these fundamental experiments were ample. No previous study has reported the peak hydrogen evolution rate from nearly pure, bulk lithium hydride in applicable units, even though many groups have looked into the material. The work done while investigating less-than-saturated solutions proved a number of things that were formerly hypothesized, but had never actually been tested. The consequences of these experiments aided in the designing and testing of a prototype distillation column that will eventually be employed in a liquid lithium loop, manufactured for use with the LiMIT-style PFC.

The bulk of these fundamental experiments were aimed at supplementing the gaps in the literature with regards to hydrogen retention in, and recovery from, solid and liquid lithium. An understanding of these phenomena was critical in the design and development of the prototype distillation column described in Chapter 6. The design process was also guided by liquid lithium loop systems that had previously been studied [1 – 2] or proposed [3]. The column body was also based on the Lithium Vapor Box developed by Goldston [4], which is envisioned to be used for a different purpose within the reactor, but ultimately aims at decomposing, evaporating, and re-condensing lithium. The column was developed based on these theoretical models and tested with various types of hydrogenated lithium samples.

Quite a bit of preliminary tests were carried out to commission individual components of the distillation column. One of the more novel aspects of this design was that the primary heating component was inductive, instead of resistive. The reason this was chosen is that inductive heating will have a variety of advantages over conventional resistive heating. The stainless steel vessel that holds the sample was heated quite rapidly, regardless of the sample type/hydrogen concentration. The vessel temperature will be quite important when considering heating the deuteride, tritide, or hydride salt-rich solutions. If the solutions are predominantly lithium, however, the currents that are induced in the column can also travel through the lithium, which will further help in heating the lithium.

Throughout the course of these experiments, it became apparent that far-from-saturated solutions of hydrogen in lithium may require methods that supplement thermal decomposition to aid in approaching a point where recovery balances wall loss. These types of solutions would need treatment if the upstream purification technologies were either non-existent or were much less effective than those proposed by Ono, et al. [3]. The supplemental technique proposed in Chapter 7 of ultrasonic degassing/rectified diffusion is an industry-tested process in metallurgy and metals casting, in which hydrogen is removed improve the cast quality. As of yet, this has not been applied to the tritium-lithium problem, which was done theoretically in the chapter.

The initial sections of this chapter will discuss the major conclusions from each chapter and how they were applied to later studies or can be applied to future work. Each of these conclusions will be put into the context of the viability of recovery using these methods within the

timescale limitation described by Krasheninnikov's results [5]. This chapter will then conclude with how this work can be extended to future loop systems.

8.1 Major Conclusions

As mentioned above, this section will be sub-divided based on the major results obtained from each chapter and what they mean with respect to isotope recovery technologies and future lithium loop systems. The conclusions will first be drawn from Chapters 4 and 5 based on the fundamental results obtained from each. Major results from Chapters 6 and 7 will then be discussed and what the implication of these results mean for future loop systems.

8.1.1 Thermal Decomposition of Lithium Hydride

Chapter 4 looked at the thermal decomposition of lithium hydride as a surrogate for lithium deuteride and lithium tritide. This was done to examine what recovery rates could be expected in the extreme scenario where the precipitate salts were completely purified and separated from the rest of the lithium stream exiting a hypothetical lithium-walled fusion reactor. To look at if the recovery rates from this species would be able to balance tritium wall losses, a standard was needed as a metric to measure against. For these studies, the results provided by Krasheninnikov's group [5] were used. His results found that the time-averaged particle loss rate to the wall in a Li-Wall ITER-FEAT scenario was on the order of 3×10^{22} s^{-1}. This value, however, needs to be normalized by the area or volume over which the particles impinge and absorb. To do this, this time-average particle loss was divided by an assumed divertor strike point of 10 m^2 [3], assuming the fuel species were evenly distributed across this surface area. In doing so, the standard to measure against was given as a flux at 3×10^{21} m^{-2} s^{-1}.

Hydrogen release from the thermal decomposition of lithium hydride was measured in the Lithium Hydride Degassing Experiment (LiHDE). The peak evolution rate was found to be nearly 9.6×10^{17} s^{-1} (for molecular hydrogen, H_2) at a temperature of 696 °C. Taking into account the small sample surface area and the fact that the lithium hydride at this temperature was likely a single, molten phase (as indicated through resistivity measurements), the flux from the surface of

this sample was found to be nearly 5 x 10^{21} H_2 particles m^{-2} s^{-1}. This release flux is more than sufficient to balance the standard imposed by Krasheninnikov in the ITER-FEAT scenario [5]; however, the results from this assume that the phase being treated is complete saturated. Even in the case where the purification technologies can separate a LiD- and LiT-rich slurry from the rest of the lithium stream, the LiD- and LiT-rich phase is still not completely saturated. Work needed to be done to confirm what level of hydrogen release flux could be expected in less-than-saturated and far-from-saturated solutions of hydrogen and lithium.

8.1.2 TUFCON Hydrogen-Lithium Solubility Experiments

Chapter 5 described the procedure and results used to identify the chemical composition and absorption/desorption kinetics in lithium samples exposed to a variety of hydrogen environments. The primary goal was to investigate how ions and radicals in plasmas modify the surface and sub-surface chemistry in the hydrogen-lithium systems. This work was important because it has been observed in analogous systems that solubility in liquid metals can be enhanced beyond thermodynamic limitations under plasma irradiation. Specifically, the increased atomic radical density at the surface of the liquid metal has shown to be very influential in changing the system solubility properties. While Baldwin's work [6] showed that liquid lithium absorbs deuterium at nearly a 1:1 ratio up to the point of saturation, the study did not relate any sort of compositional analysis. In the same work, Baldwin concluded that the consumption of the deuterium manifests itself in the systematic conversion of the entire lithium sample to lithium deuteride, but this likely occurs over a long time scale. Even in these situations, small fractions of the deuterium striking the lithium surface will remain dissolved in the liquid metal. However, there is a chance that as the sample is converted to lithium deuteride over large fluences, more and more dissolved deuterium will precipitate out as the deuteride salt since the fraction of lithium will decrease over time. It is important to note that these fluences are likely much greater than those a single lithium volume element will experience during its time within a reactor, so the chemical makeup of the stream exiting the reactor will hold more weight than the results that Baldwin reported.

The main outcomes of Chapter 5 surround how lithium will retain and release hydrogen under a variety of exposure conditions. The parameters that were scanned were sample bias,

sample temperature, and exposure time. This was done for static (not agitated) liquid lithium samples, and a smaller parameter scan was explored for solid samples. Each of these independent variables were predicted to influence the absorption properties and chemical composition in the lithium solution in different ways. For all sample variants, the release flux was considered with respect to the dissolved (α) phase, since temperature-programmed-desorption had an upper limit of 650 ° which is well below the melting point for the hydride. As such, release fluxes from this phase were not observed to be able to match loss rates evaluated by Krasheninnikov [5].

Solid samples were observed to undergo what appeared to be a very stark surface saturation event, as evidenced by the spectroscopic trend scans. Release fluxes for these samples were significantly lower than what was measured for the liquid samples. The amounts recovered from the solid samples related to very small fractions of the applied dose, even though these fractions were slightly greater than those reported by Baldwin [6].

It was found that with increasing sample temperature, absorption does not a follow a monotonic trend based on the comparison between spectroscopic measurements. Reasons for why this was occurring were stated in Chapter 5, but in essence had to do with enhanced reactivity and diffusion at higher temperatures. Also with increasing sample temperature, the solubility threshold appeared to still be limited by solution thermodynamics at particle energies relevant to the TUngsten Fuzz Characterization of Nanoparticles (TUFCON) helicon source. Release fluxes appeared to be relatively unaffected by this variable.

The effects of sample bias and exposure time were coupled, in that both influenced the hydrogen ion dose to the sample. Samples biased more negatively showed evidence of enhanced absorption, considered to be due to increased particle penetration depth. The exact effect that the ion and radical energies have on the solution chemistry requires further study. For longer exposure times, diffusion of the insulating, surface hydride layer into the sample bulk is likely the mechanism by which a static sample undergoes volumetric conversion from lithium to lithium hydride in the presence of a hydrogen plasma, whereas the plasma act to replenish the lost hydride transported away from the surface.

Another factor that was explored, but originally not set as one of the independent variables was how plasma affected absorption over and above the effect neutrals (as hydrogen gas) had on absorption. It was observed that plasmas do indeed play a role in absorption *rate*, which is

enhanced beyond cases where lithium is exposed to hydrogen gas. Since it was difficult to determine the fluence of gas particles to the surface, a direct comparison between the two exposure environments proved difficult. The primary conclusion drawn in this comparison, however, was that plasmas increase the amount absorbed likely because neutral absorption is limited by the breaking of diatomic bonds at the sample surface.

From a very general perspective, peak release rates in far-from-saturated solutions were found to be appreciably lower than the in-vessel loss rates. From a flux balance perspective, the peak fluxes from these less-than-saturated and far-from-saturated solutions would not be able to balance the losses at the inner vessel walls, meaning that purification and separation steps are required in any reactor-scale lithium loop system upstream from the hydrogen reclamation step. As mentioned before, these purification and separation steps have already been proposed by Ono, et al. [6], so the application of thermally-driven recovery technologies would go well with systems that exist or have been proposed. If one were to get rid of the purification and separation steps, then methods that supplement thermally-driven recovery would be required.

8.1.3 Prototype Distillation Column Design and Testing

Using information from Chapters 5 and 6, and taking into consideration the entirety of the lithium loop/hydrogen recovery provided by Ref. 3, a prototype distillation column was designed, constructed, and tested. The column was designed to take advantage of the thermophysical properties of solutions of hydrogen and lithium at various molar concentrations. The novelty of this design is most apparent at the base, where the heating drive will have to continuously overcome the cooling effects from the inlet. To do this, an induction heater using a pancake coil to generate the magnetic fields was placed under the bottom of the 304 stainless steel bucket. To continuously heat to temperatures approaching 700 °C with minimal power draw, while also being able to ramp up to this temperature in the shortest amount of time, the induction heating mechanism was considered superior to all other low-cost heating alternatives.

An ulterior motive for developing a distillation column of this type was to condense and recycle clean liquid lithium back into the reactor. Other reclamation techniques that have been considered are often chemical in nature; however, either the yields for these methods are too low

or they produce unwanted byproducts, such as lithium oxide or lithium hydroxide. As such, condensation stages were developed for lithium re-circulation based on the design of the Lithium Vapor Box by Goldston [4].

Prior to running a few proof-of-concept experiments, where mixtures of lithium hydride and lithium were tested in the fully constructed column as batch processes, the induction heating system was modelled and commissioned. Modelling was done using the COMSOL Multiphysics software [7], which showed that at practical output frequencies and currents the sample bucket portion of the column would be able to heat to temperatures in excess of 600 °C in 30 minutes or less. Higher frequencies and currents were also modelled, but these seemed to result in erroneous temperatures, which may be a fault of the simplified virtual geometry as well as the boundary conditions imposed on the control volume. The heating capabilities of the working induction coil was then tested on a dummy load and the actual column. Temperatures and heating rates for these tests were found to be in good agreement with the COMSOL [7] results for the cases that modelled practical output frequencies and currents (nearly 30 kHz and between 350 and 400 A).

Proof-of-concept tests were then conducted to investigate hydrogen recovery rates in saturated, less-than-saturated, and far-from-saturated samples. The difference between these sample types was described in the beginning of Chapter 5, but saturated samples refer to mixtures with a 1 mol H : 1 mol Li atomic ratio and far-from-saturated samples refer to mixtures with atomic ratios less than the thermodynamic solubility limit. Recovery rates were determined for the far-from-saturated solution, with the time-integrated recovered dose calculated to be nearly 50 % of the original hydrogen molar content. In contrast, the less-than-saturated and saturated samples released enough hydrogen quickly enough to saturate the RGA filament, rendering further evaluation impossible. What can be confirmed when comparing the results between the LiH-rich samples and the Li-rich sample is that mixtures with higher hydrogen concentrations will be able to evolve greater amounts of hydrogen more quickly, simply by virtue of the population density and probability of recombinative diatomic release at the sample surface.

Results from the condensation stages also seemed to point to the fact that the system was working as intended, with large amounts of hydrogen being captured by the primary stage. The secondary stage was also able to capture some lithium deposit, but in significantly smaller quantities, while there was no evidence of lithium deposit on the primary exhaust. The RGA

filament registered very little in the way of lithium signal, which helps to support the claim the column system was working properly. While more work needs to be done to fully characterize the distillation column and its capabilities, it the results from this chapter prove that the prototype design functions as intended.

8.1.4 Ultrasonic Degassing: A Supplementary Technique

Chapter 7 addressed a technique that can be used to aid in recovering hydrogen from lithium in far-from-saturated solutions. The distillation column, described in Chapter 6, will be able to adequately recover hydrogen isotope species from lithium solutions on time scales that balance absorption at the vessel walls of the reactor if separation techniques upstream from the column are able to successfully isolate a hydride-rich stream from the remaining lithium. In the absence of these upstream separation techniques, the sole use of heat will need to drive deuterium and tritium diffusion, surface recombination, and evolution in solutions with hydrogen molar ratios below the solubility threshold. As evidenced by the results from Chapters 5 and 6, it is unlikely that the use of heat alone will be able to drive recovery to the point of balancing in-vessel wall losses. In these scenarios, where upstream separation technologies are absent, methods that help to promote hydrogen desorption need to be used in tandem with the distillation column.

One such method, which has proven itself as a viable technology in the fields of metallurgy and metal casting, is ultrasonic degassing. Chapter 7 explored the theory associated with the practical application of acoustic cavitation to solutions of hydrogen in lithium. To do this, a numerical model was developed to investigate the transience of rectified diffusion based on previous work accomplished in Ref. 8 through 10. This model was used to solve a set of 3 stiff, non-linear ordinary differential equations and 2 diffusion-advection equations, with the state of the gas inside the cavitation bubble assumed to be uniform and ideal. Techniques employed in the model differed from those in Ref. 8 through 10, so the results were verified against those reported in these references. The current model appeared to capture the physics quite well; however, computational complexity hindered the numerical approach from obtaining the final expansion radius for a single hydrogen bubble in lithium driven at various acoustic parameters.

Since real-world singularities exist during rectified diffusion and transient cavitation, whereby bubbles will undergo a violent collapse to sizes much smaller than the initial nucleation microbubble size followed by a rebound where the bubble undergoes explosive growth, the numerical model was unable to proceed to completion. As such, the final radius after explosive growth was not observed, so approximate analytical methods were used to evaluate the final radius and pressure thresholds that needed to be surpassed for such growth to occur. These approximate analytical solutions were used as a means to guide the practical integration of acoustic pressure transducers into the distillation column system. During these analytical analyses, the method was deemed viable based on evaluation and work accomplished in previous studies on the degassing of light metals [11 – 13]. While no experimental data was taken to investigate the effects ultrasonic degassing would have on hydrogen recovery, the bulk of the chapter was used to lay the theoretical groundwork and build an outline for future research.

8.2 Extension and Recommendations

While significant effort was dedicated to the fundamental studies along with the design and construction of a prototype hydrogen recovery unit, a few unanswered questions remain. A few of these were brought about by some of the more unusual results observed during the course of this work; however, the majority of these questions are part of the natural extension from the conclusions previously stated. In essence, this work served to fill in the knowledge gaps surrounding the back-end process of tritium recycling for a lithium-walled fusion reactor and to report on the development of technologies that could be integrated into future lithium loop systems.

The work done to investigate the thermal decomposition and release of lithium hydride as a surrogate for lithium deuteride and lithium tritide was quite conclusive. The next step for these investigations would be to use pure lithium deuteride, rather than lithium hydride, to look at any isotopic differences that may occur. Also, heating future samples past the 710 °C mark, until the entire sample was evaporated, may prove useful in determining the exact temperatures needed for thermally-driven recovery systems. Evolving deuterium or hydrogen from an agitated deuteride- or hydride-rich slurry, rather than from a static deuteride or hydride sample may prove beneficial. Finally, it would be advantageous to further characterize the condensed phase chemistry before,

during, and after temperature-programmed desorption to get a handle on the exact thermochemistry, so that treatment options will be optimized in terms of heating.

Similar to the first recommendation from the previous paragraph, lithium exposures to deuterium plasmas and gases will improve the quality of the results. The reason for this is that within a chamber there will exist residual hydrogen, which must be taken into account when looking at hydrogen desorption and the resultant chemical phases in the condensed phase. This study would also benefit from the ability to agitate the samples, which would break up any insulating surface hydride or deuteride layer that may form during absorption. A higher degree of sample diagnosis will also aid in the compositional analysis. Enhanced sample diagnosis could even be as simple as heating the crucible up to temperatures in excess of 700 °C during temperature-programmed desorption to delineate the fraction desorbed from the α phase and that which is desorbed from the β phase. Finally, this study would benefit from a much broader parameter scan over those variables listed in Chapter 5. This would help in truly flushing out the dependencies on sample temperature, ion energy, exposure duration, and exposure environment. Of particular interest are the effects of ion energy, since sample biasing was limited in the TUFCON chamber.

Chapter 6 went in to detail on the design, development, construction, and proof-of-concept testing of a prototype distillation column unit as a means of exploring the viability of using thermochemical properties to recover tritium. While initial runs prove that the column is operating as predicted, upgrades to the RGA diagnosis capabilities (along with the "sniffer tube" aperature that limits gas flow to the filament) would prove beneficial in acquiring more accurate quantitative data. On top of this, characterization of the heating and degassing capabilities requires that more tests be done with various solution mixtures at different isotope atomic ratios. This extended proof-of-concept testing would profit from the use of deuterium and lithium deuteride, similar to the reasoning why deuterium was recommended for the other studies. More post-mortem analysis would also aid in determining the effectiveness of each column sub-section. Finally, the integration of supplementary techniques into the column structure, and the integration of the fully characterized column into a larger-scale liquid lithium loop would finalize the extension of the work reported in Chapter 6.

Results from Chapter 7 laid the theoretical groundwork for the incorporation of an ultrasonic degassing technique into treatment units like the distillation column mentioned in Chapter 6. The natural extension of this is to take the results and recommendations from this chapter and compare them to experimental observations, where the distillation column is outfitted with an ultrasonic pressure transducer. On top of this, applying optimization techniques to the numerical model will improve its performance and allow for more accurate predictions with regards to hydrogen bubble dynamics. Further verification and validation are required for this model; however, this may be as simple as changing a few of the thermodynamics properties for the liquid and gas phases.

In conclusion, the work accomplished in this report completes the vital initial steps toward the realization of fully functional liquid lithium loop, complete with back-end reprocessing technologies. It has been shown that the appropriate treatment of tritiated liquid lithium exiting a lithium-walled ignited fusion reactor will result in recovery fluxes that balance fuel losses at the in-vessel plasma interface. As such, future endeavors will be needed to complete the work initiated in this dissertation to provide fusion a viable path toward sustainable energy production. To conclude this report, an image of a fully integrated loop, complete with the technologies described in previous chapters, is shown in Figure 8.1.

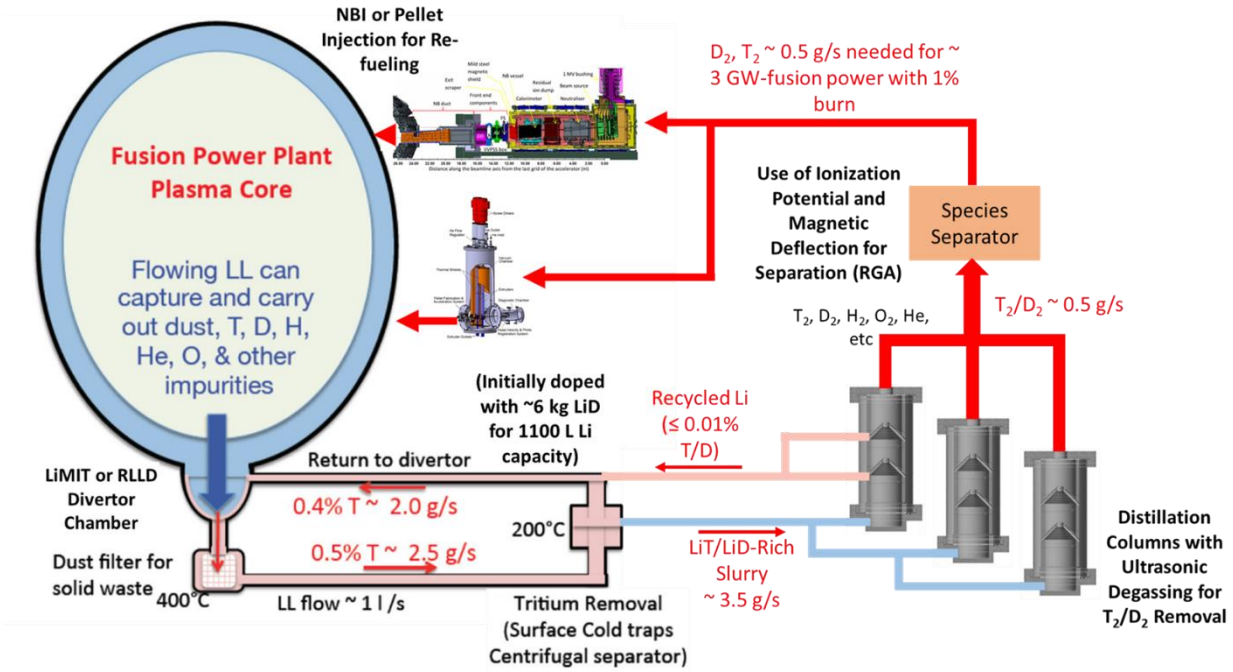

Figure 8.1: An image of the loop system envisioned for use with a 3 GW fusion power plant, based on work done by Ono [3], Hemsworth [14], and Vinyar [15]. Separation technologies will remain as those reported by Ono [3]; however, the inclusion of distillation columns outfitted with ultrasound transducers is the unique addition from this dissertation. Gas species will be separated based on the same principles on which an RGA operates. Fuel will be recycled into the reactor using an NBI [14] or a pellet injector [15], or a combination of the two. The advantage of using the distillation columns is the ability to recycle lithium back to the inner vessel wall, along with the ability to re-fuel.

8.3 References

[1] E. Wakai, et al., “Engineering validation for lithium target facility of the IFMIF under IFMIF/EVEDA project,” *Nucl. Mater. Energy* 9 (2016) 278.

[2] J.S. Hu, et al., “First results of the use of a continuously flowing lithium limiter in high performance discharges in the EAST device”, *Nucl. Fusion* 56 (2016) 046011.

[3] M. Ono, R. Majeski, M.A. Jaworski, Y. Hirooka, R. Kaita, T.K. Gray, R. Maingi, C.H. Skinner, M. Christenson, D.N. Ruzic, “Liquid lithium loop system to solve challenging technology issues for fusion power plant”, *Nucl. Fusion* 57 (2017) 116056.

[4] R.J. Goldston, R. Myers, and J. Schwartz, “The lithium vapor box divertor”, *Phys. Scripta* T167 (2016) 014017.

[5] S.I. Krasheninnikov, L.E. Zakharov, G.V. Pereverzev, “On lithium walls and the performance of magnetic fusion devices”, *Phys. of Plasmas* 10 (2003) 1678.

[6] M.J. Baldwin, R.P. Doerner, S.C. Luckhardt, and R.W. Conn, “Deuterium retention in liquid lithium”, *Nucl. Fusion* 42 (2002) 1318.

[7] *COMSOL Multiphysics® Reference Manual*, COMSOL Version 4.3b (2013) http://hpc.mtech.edu/comsol/pdf/COMSOL_Multiphysics/COMSOL_ReferenceManual.pdf, Accessed: 2017-10-20.

[8] A.R. Naji Meidani and M. Hasan, “A study of hydrogen bubble growth during ultrasonic degassing of Al-Cu alloy melts”, *J. Mater. Process. Technol.* 147 (2004) 311.

[9] A.R. Naji Meidani and M. Hasan, “A numerical study of the complex dynamic behavior of a reactive gas bubble in water”, *Appl. Math. Modelling* 21 (1997) 127.

[10] A.R. Naji Meidani (2001). A Study of Bubble Dynamics and Some Metals Processing (Doctoral Dissertation). McGill University, 2001.

[11] H. Xu, Q. Han, and T.T. Meek, “Effects of ultrasonic vibration on degassing of aluminum alloys”, *Mater. Sci. Engrg. A* 473 (2008) 96.

[12] G.I. Eskin, “Cavitation mechanism of ultrasonic melt degassing”, *Ultrasonics Sonochemistry* 2 (1995) S137.

[13] G.I. Eskin, “Influence of cavitation treatment of melts in the processes of nucleation and growth of crystals during solidification of ingots and castings from light alloys”, *Ultrasonics Sonochemistry* 1 (1994) 59.

[14] R.S. Hemsworth, D. Boilson, P. Blatchford, M. Dalla Palma, G. Chitarin, H.P.L. de Esch, F. Geli, M. Dremel, J. Graceffa, D. Marcuzzi, G. Serianni, D. Shah, M. Singh, M. Urbani, and P. Zaccaria, “Overview of the design of the ITER heating neutral beam injectors”, *New J. Phys.* 19 (2017) 025005.

[15] I. Vinyar, J. Hu, A. Lukin, J. Li, X. Yao, C. Li, Y. Chen, and P. Reznichenko, “50 Hz deuterium pellet injector for EAST tokamak”, *Fus. Eng. and Des.* 98-99 (2015) 1898.

APPENDIX A: DEGASSING EXPERIMENTS IN IGNIS

For the degassing of hydrogen from lithium hydride, a series of auxiliary tests was performed on the Ion-Gas-Neutral Interactions with Surfaces (IGNIS) chamber, which is part of the Radiation Surface Science and Engineering Laboratory (RSSEL). These tests were meant to investigate the thermochemistry involved with the decomposition of lithium hydride (LiH) in the presence of a controlled hydrogen background. As was the case in the bulk of this report, hydrogen and lithium hydride were used as surrogates for deuterium, tritium, lithium deuteride, and lithium tritide, respectively. Literature studies have been done to investigate thermal decomposition of LiH when exposed to a controlled amounts of water [1, 2], but very little has been done to examine the role hydrogen gas plays in the desorption chemistry. This is important from a tritium recycling perspective because if the evolved gas is not exhausted quickly enough, it may begin to interact with the remaining deuterated/tritiated lithium solution and prevent desorption. The level at which the neutral background affects release was therefore the focus of this ancillary study.

Intuitively, a hydrogen environment should inhibit the decomposition of lithium hydride and modify the release kinetics to inhibit desorption. This is based on the concept of Le Chatelier's principle [3], whereby an excess of either products or reactants will shift the chemical equilibrium of a reaction. Since the thermal decomposition of lithium hydride yields lithium and hydrogen gas, an added background environment should drive the reaction back toward the reactants. This would manifest as an increase in the activation energy barrier, which would result in shifts in the peak release temperatures observed during temperature-programmed desorption (TPD).

Procedurally, each sample tested in the IGNIS facility was loaded under an argon environment in a crucible made by inverting a Materials Analysis Particle Probe (MAPP) sample holder. Approximately 0.1 to 0.2 g of LiH powder was loaded for each sample. An image of the sample holder is shown in Figure A.1. A grid was placed over the top of the sample holder to prevent mass scale lithium erosion from coating sensitive in-vacuum equipment. The crucible was then packaged under argon and transferred from the Center for Plasma-Material Interactions (CPMI) to the RSSEL facility. The sample was loaded into an antechamber, which had previously been purged with argon. Once closed, the chamber was evacuated to ultra-high vacuum pressures (at or less than 1×10^{-7} Torr) before the antechamber was opened to the primary chamber and the sample was transferred via manipulator arm to the primary stage. A pre-determined flow rate of

hydrogen gas was then introduced into the chamber through precise control of a leak rate valve prior to initiating the TPD scan. The variable that was changed between samples was the amount of background hydrogen introduced into the chamber. Scans were completed after the sample had been held at temperatures slightly greater than 690 °C for no more than 2 minutes. An image of the crucible being heated within the IGNIS device is shown in Figure A.2. The Odyssey RGA that was used in Chapter 4, 5, and 6 was during each scan to track species corresponding to masses of 1 AMU, 2 AMU, 6 AMU, 7 AMU, 18 AMU, and 28 AMU. The Odyssey RGA was offset from the sample stage by roughly 16 inches, at an angle of roughly 30° off normal.

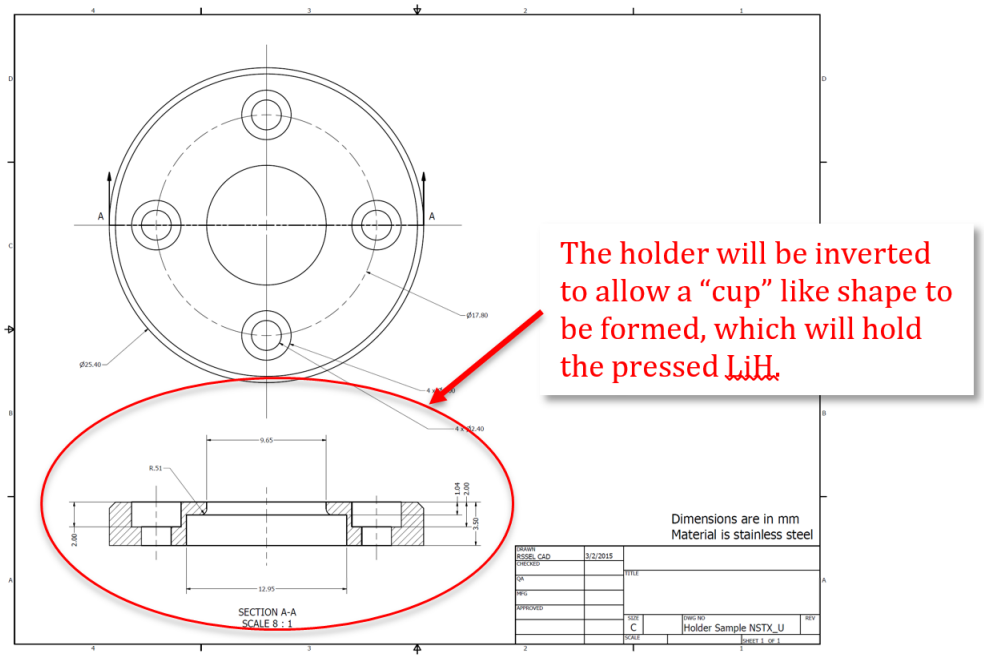

Figure A.1: A CAD drawing of the sample holder used in the MAPP device (rendered by Dr. Felipe Bedoya). The holder was inverted to make a sample crucible, which held LiH.

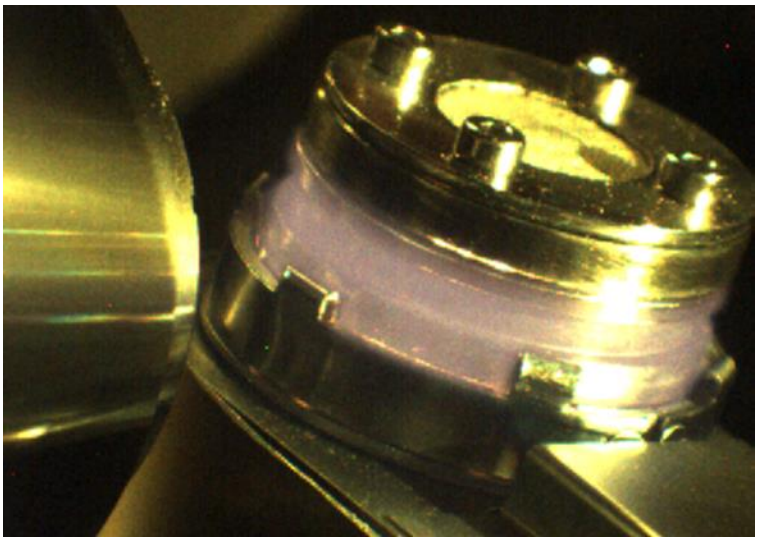

Figure A.2: An image showing the heating of the sample crucible within the IGNIS device. The glow from the stainless steel was observed for temperatures near the peak temperature.

Results comparing the molecular hydrogen signals from three different samples are shown in Figure A.3. In this plot, the effects of the hydrogen background manifest as an increase in the threshold temperature at which a critical "inflection point" occurred. This is most prevalent between the control sample and that with a 2 x 10^{-5} Torr L s^{-1} hydrogen background, indicating a significant change in the activation energy barrier for the thermochemical decomposition of lithium hydride. Other interesting features were observed when changing the background hydrogen pressure. It appeared as if the order of the desorption kinetics was changing, with a secondary feature appearing at temperatures between 670 and 690 °C. This was likely due to the fact that even as hydrogen was evolving an equilibrium was being established between the gas and the condensed phase, with the kinetics no longer being governed solely by the forward reaction. Another interesting feature was that it appeared that at the highest hydrogen leak rate that the primary peak characteristic of LiH decomposition had been almost completely suppressed. It is likely that between the 2 x 10^{-5} Torr L s^{-1} hydrogen background and the 1 x 10^{-4} Torr L s^{-1} there exists a point where typical decomposition becomes almost completely obstructed. While future work should be done to help clarify the exact effects that background hydrogen gas has on the degassing of lithium hydride, some interesting chemical observations were made during the auxiliary tests performed in IGNIS.

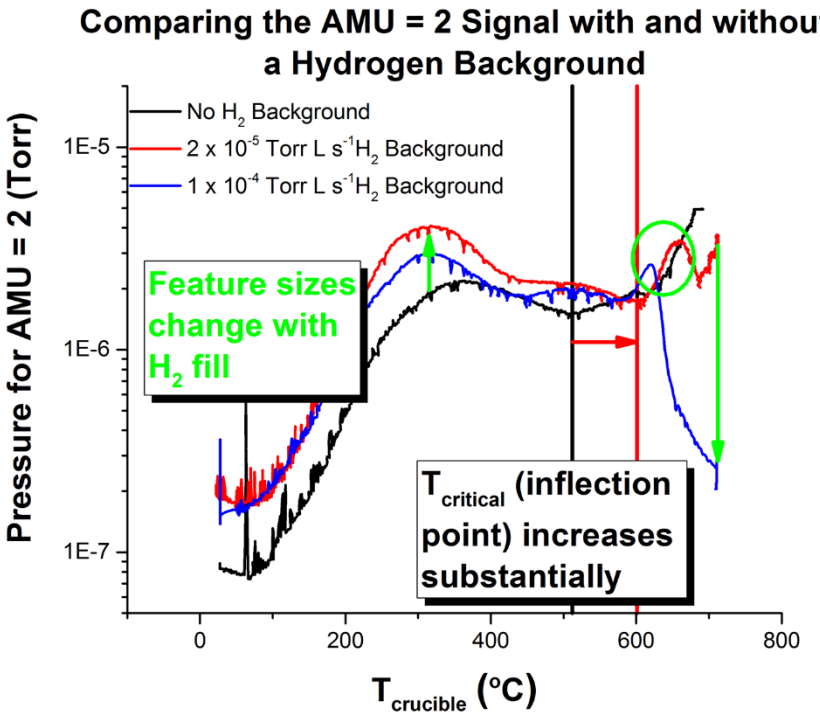

Figure A.3: A plot comparing the molecular hydrogen trends versus temperature for varying amounts of background hydrogen in IGNIS.

A.1 References

[1] L.N. Dinh, M.A. Schildbach, R.A. Smith, D.M. Grant, B. Balazs, and W. Mclean II, "Hydrogen Outgassing From Lithium Hydride", *Report for Lawrence Livermore National Laboratory: Nuclear Materials Research Developments* (2006).

[2] J.P. Tonks, M.O. King, E.C. Galloway, J.F. Watts, "Corrosion studies of LiH thin films", *J. Nucl. Mater.* 484 (2017) 228.

[3] H. Le Chatelier and O. Boudouard, "Limits of Flammability of Gaseous Mixtures", *Bulletin de la Société Chimique de France* 19 (1898) 483.

APPENDIX B: DESIGN OF EXPERIMENT FOR SOLUBILITY TESTS

In the case of the solubility experiments, a design-of-experiment analysis was performed prior to the setup and testing in the TUFCON chamber. Design of experiment analyses are often done before experimental production runs begin to understand the expected variation in the results based on a number of statistically relevant factors. The study performed to investigate the expected outcomes of the solubility experiments in TUFCON is of the full-factorial classification. It is important to relate that this study also required at minimum a guess of the plasma parameters for the experimental exposure conditions, so estimates of T_e and n_e were made from prior knowledge of helicon plasmas produced by a similar MORI 200 source. The flux to the surface was calculated with the knowledge of these values.

These types of predictive analyses are not only used to look at the expected responses from various types of measurements, but they are also used to give an operating range when multiple parameters need to be scanned. In the prediction for the solubility experiments in TUFCON, three parameters were chosen as the independent variables for establishing dissolution rates: exposure time, sample bias, and sample temperature. All other variables that could affect the outcome were considered to be constant within a reasonable degree, but these "nuisance factors" could also affect the outcomes and, thus, need to be taken into account. Both solid and liquid lithium samples will be exposed, so a separate design-of-experiment analysis needs to be done for each phase.

Predicting the outcomes from these experiments first requires a hypothesis about how each of the chosen independent variables will affect the final outcome. Exposure time affects the fluence of the ions (or neutrals for some of the tests) to the sample. As more hydrogen ions impinge the surface, it becomes increasingly likely that these ions will recombine with electrons on the surface, form energetic radicals, and absorb into the lithium. The longer this happens, the more likely it is that the solubility threshold of the sample at a certain temperature will be reached and hydride precipitate will begin to form and affect the measured quantities. Exposure time will affect the spectral response, resistivity response, and RGA pressure response. The change in intensity with respect to the initial value will decrease over time as precipitate forms and the sample approaches saturation. The change in resistivity between the pre- and post-exposure measurements will increase as the atomic fraction of dissolved and precipitated hydrogen increases. Finally, the accumulated evolved hydrogen pressure registered by the RGA should increase, and the evolution

rate should also increase simply by virtue that more hydrogen exists within the sample. This all assumes that there is not some thermodynamic or absorption limit, which would register as a change in the spectral and RGA responses.

The sample bias should affect the lithium in the same manner as the exposure time, since both increase the fluence to the sample. A more negative sample bias will attract more positively charged species to the sample surface, thereby increasing the flux. The flux over time yields the fluence. Assuming that the exposure times between two samples with different biases were the same, the sample with the larger negative bias will be exposed to and consume more hydrogen. This will affect the measured responses in similar ways to what was described in the previous paragraph.

The influence that the sample temperature will have on absorption and desorption will likely be the most interesting factor to explore, as little to no data exists for how retention in a plasma environment is affected by the temperature of the lithium sample. As the temperature increases, more precipitate will dissolve into solution as described in Chapter 2. This will likely result in a smaller change in resistance being measured between pre- and post-exposure, since the presence of dissolved hydrogen changes the solution resistivity less than the presence of precipitate. The total amount absorbed should be less affected by the change in sample temperature; however, as the sample approaches temperatures where lithium readily evaporates then the result would likely be that less overall hydrogen would be absorbed. This is something that definitely requires further exploration. The spectral response may show a higher Li_I and Li_{II} signal, since lithium neutrals will be more likely to evaporate and then excite or ionize. The change in the hydrogen Balmer lines may also be less drastic than at lower temperatures for the same reason that the total amount absorbed will likely be less. What can be said with confidence is that the amount of hydrogen dissolved in higher temperature samples will likely be higher. Of the three independent variables under investigation, the one that may produce the most interesting absorption and desorption results is the sample temperature.

These predictions were all taken into consideration when performing the full factorial design of experiment analysis for the TUFCON absorption experiments. For ion flux to the surface (without an external negative bias), the electron temperature was predicted to be approximately 5.2 eV and the electron density was predicted to be approximately 3.3×10^{18} m^{-3}. These values are

typical for low-AMU species confined in a helicon plasma source. Without sample biasing, these values gave a predicted instantaneous flux of approximately 1.1 x 10^{22} m^{-2} s^{-1}. Each independent variable was set to an interval between pre-determined minimum and maximum values. Table B.1 outlines the intervals for each independent variable, assigning the minimum value to a '-1' and the maximum value to a '1'.

Table B.1: The three independent variables analyzed for the TUFCON Solubility DOE.

Factor	Name	Unit	Low (-1)	High (+1)
A	Temperature	°C	200	400
B	Sample Bias	V	V_f (0)	-100
C	Exposure Time	s	600	7200

The outputs of these analyses are typically reported as response surfaces. These surfaces are predictions of how the measured dependent variables will change as one or more independent variable is varied over a pre-determined interval. Typically, the result most sought after in these experiments is how the measurements will change between the minimum and maximum of each input to determine the least number of experiments necessary for verification. The total accumulated RGA H_2 pressure response curve can be seen in Figure B.1.

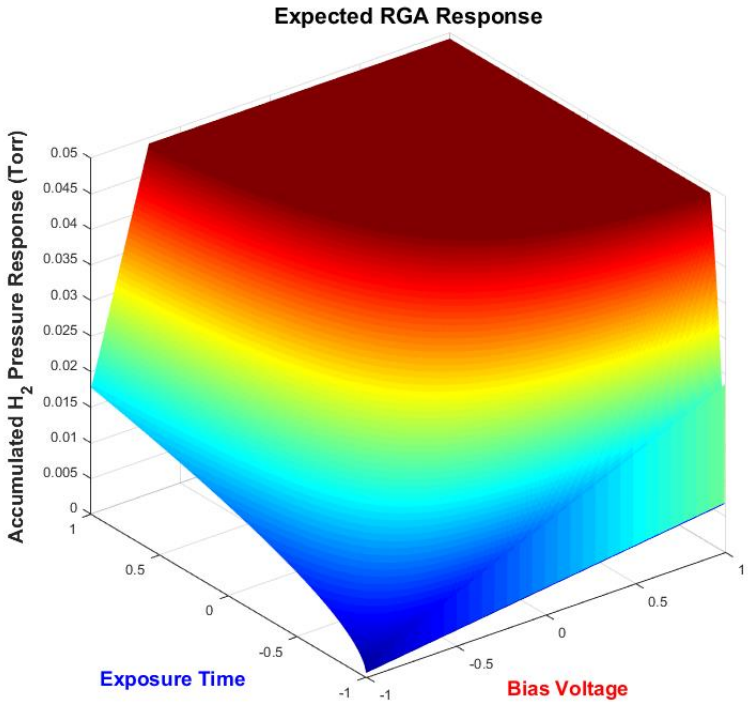

Figure B.1: The predicted total accumulated (integrated over time) H_2 pressure response surface as a function of the exposure time and sample bias. The flat top on the response surface exists, because at this point the lithium solution is completely saturated (converted to LiH).

A few interesting features exist within the plot in Figure B.1. First, and as would be expected, the total RGA H_2 response increases with both increasing exposure time and increasing sample bias. It appears as if the sample bias has a slightly greater influence over the total accumulated amount of hydrogen absorbed, and subsequently released, than does the exposure time. This is due to each variable's influence on the fluence to the sample. What is also interesting to see is that while the accumulated hydrogen seems to always increase with an increasingly negative sample bias, the amount of hydrogen accumulated with respect to exposure time does not exhibit this same trend. The final interesting feature from Figure 5.12 is the fact that there exists a peak amount of hydrogen that should be registered by the RGA. This corresponds to a solution that is saturated with hydrogen, in that there exists 1 mole of atomic hydrogen for every 1 mole of lithium. This is under the assumption that approximately 0.2 cm^3 of lithium has been loaded into the sample crucible.

A similar type of response plot can be predicted based on the assumption that the amount of dissolved hydrogen will follow the thermodynamic trends posed by Yakimovich's group [1]. This plot is illustrated in Figure B.2, where the dependent value is reported as the ratio of dissolved hydrogen to the total amount of hydrogen absorbed by the sample as a function of temperature and exposure time for a constant -50 V bias.

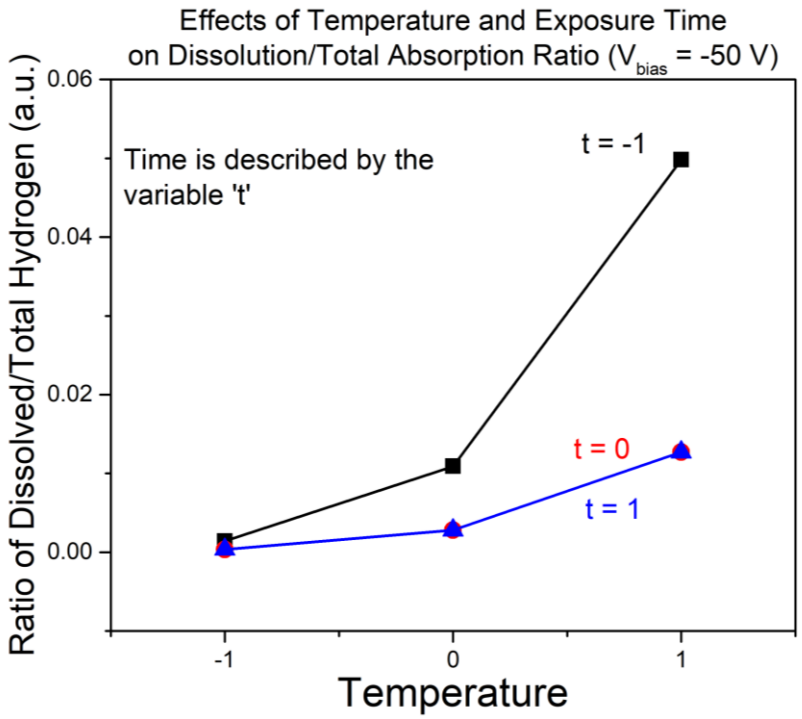

Figure B.2: A predictive response plot for what ratio of dissolved hydrogen to total hydrogen is expected when lithium samples biased at -50 V are exposed to hydrogen plasmas. This prediction was made as a function of sample temperature and exposure time. For the minimum and maximum values associated with each independent variable, the author refers the reader to the information in Table B.1.

This plot follows what is intuitively expected with regards to hydrogen absorption/dissolution in liquid lithium. At low sample temperatures, the mole fraction of dissolved hydrogen (or LiH) is much less than at higher sample temperatures, as defined by the thermodynamic limits reported by Yakimovich, et al. [1]. Smaller exposure times relate to lower fluences, meaning the overall amount of hydrogen absorbed is much less. At the same temperature

this means that as exposure time goes down the likelihood that the hydrogen in solution will remain dissolved increases, which is what the plot shows. The values of '-1', '0', and '1' referred to for each parameter refer to the intervals described in Table 5.1. The trends in Figure 5.13 would likely be inverted for the measured quantity of $\Delta\rho$ (the change in resistivity before and after exposure). The reason for this is that higher concentrations of dissolved hydrogen only modify the resistivity in the sample in very small increments, as described in Adams' work [2]. Alternatively, the presence of the hydride salt will drastically alter the resistivity from the pre-exposure condition, as described in Chapter 4. In summary, the lower the ratio of dissolved to total absorbed hydrogen, the higher the ratio of precipitated hydride to total absorbed hydrogen. The greater this latter ratio is, the greater the change in resistivity should be measured. This ratio can also be verified using the temporal spectral response, where differences in the change in the Balmer spectral lines will relate to different levels of absorption and chemical formation.

The results obtained in the TUFCON solubility experiments will take the predictions listed in this appendix under consideration. A similar analysis was made for solid samples; however, there was not found to be much variation in the responses since the eutectic point of the Li-LiH system is at the melting point of lithium, meaning that there likely will not be a significant change in the amount absorbed between the independent variable intervals. The experimental results for the TUFCON solubility tests were presented in Chapter 5.

B.1 References

[1] K.A. Yakimovich and T. Biryukova, “Thermodynamic Properties of Li-LiH (LiD, LiT) Systems. The Phase Diagram” *Open J. Phys. Chem.* 2 (2012) 141.

[2] P.F. Adams, M.G. Down, P. Hubberstey, R.J. Pulham, “Solutions of Lithium Salts in Liquid Lithium: The Electrical Resistivity of Solutions of Nitride, Hydride and Deuteride”, *J. Chem. Soc., Far. Trans.* 0 (1977) 230.